

Air Force Institute of Technology

AFIT Scholar

Theses and Dissertations

Student Graduate Works

9-6-2007

Optimal Control Strategies for Constrained Relative Orbits

David J. Irvin Jr.

Follow this and additional works at: <https://scholar.afit.edu/etd>



Part of the [Aerospace Engineering Commons](#)

Recommended Citation

Irvin, David J. Jr., "Optimal Control Strategies for Constrained Relative Orbits" (2007). *Theses and Dissertations*. 2903.

<https://scholar.afit.edu/etd/2903>

This Dissertation is brought to you for free and open access by the Student Graduate Works at AFIT Scholar. It has been accepted for inclusion in Theses and Dissertations by an authorized administrator of AFIT Scholar. For more information, please contact richard.mansfield@afit.edu.



OPTIMAL CONTROL STRATEGIES FOR
CONSTRAINED RELATIVE ORBITS

DISSERTATION

David Jonathan Irvin Jr., Major, USAF

AFIT/DS/ENY/07-03

DEPARTMENT OF THE AIR FORCE
AIR UNIVERSITY

AIR FORCE INSTITUTE OF TECHNOLOGY

Wright-Patterson Air Force Base, Ohio

APPROVED FOR PUBLIC RELEASE; DISTRIBUTION UNLIMITED.

The views expressed in this dissertation are those of the author and do not reflect the official policy of the United States Air Force, Department of Defense, or the U.S. Government.

AFIT/DS/ENY/07-03

OPTIMAL CONTROL STRATEGIES FOR
CONSTRAINED RELATIVE ORBITS

DISSERTATION

Presented to the Faculty
Graduate School of Engineering and Management
Air Force Institute of Technology
Air University
Air Education and Training Command
In Partial Fulfillment of the Requirements for the
Degree of Doctor of Philosophy


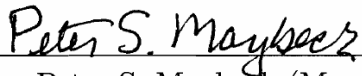

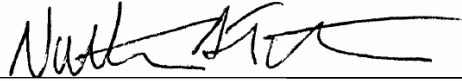
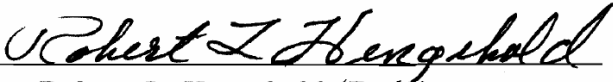
David Jonathan Irvin Jr., BS, MS
Major, USAF

September 2007

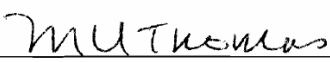
APPROVED FOR PUBLIC RELEASE; DISTRIBUTION UNLIMITED.

OPTIMAL CONTROL STRATEGIES FOR
CONSTRAINED RELATIVE ORBITS
David Jonathan Irvin Jr., BS, MS
Major, USAF

Approved:

 _____	<u>17 Aug 07</u> Date
Dr. Richard G. Cobb (Chairman)	
 _____	<u>17 Aug 07</u> Date
Dr. Peter S. Maybeck (Member)	
 _____	<u>17 Aug 07</u> Date
Dr. William E. Wiesel (Member)	
 _____	<u>17 Aug 07</u> Date
Lt Col Nathan A. Titus, PhD (Member)	
 _____	<u>17 Aug '07</u> Date
Dr. Robert L. Hengehold (Dean's Representative)	

Accepted:

 _____	<u>6 Sep 07</u> Date
Dr. M. U. Thomas Dean, Graduate School of Engineering and Management	

Abstract

The US Air Force’s ability to protect space assets is enhanced by a proficiency in satellite proximity operations and Space Situational Awareness (SSA). In pursuit of that proficiency, this research develops a key capability of interest to mission planners; the ability of a deputy satellite to “hover” within a defined volume fixed in the vicinity of a chief satellite for an extended period of time. Previous research has developed initial methodologies for maintaining restricted teardrop hover orbits that exist in a plane fixed within the chief’s local reference frame. These methods use the natural drift of the deputy satellite in the relative frame and impulsive thrust to keep the deputy in a bounded volume relative to the chief, but do not address fuel-optimality. This research extends and enhances that work by finding optimal trajectories, produced with discrete-thrusts, that minimize fuel spent per unit time and stay within the user-defined volume, thus providing a practical hover capability in the vicinity of the chief. The work assumes the Clohessy-Wiltshire closeness assumption between the deputy and chief is valid, however, elliptical chief orbits are allowed. Using the new methodology developed in this work, feasible closed and non-closed relative orbits are found and evaluated based on a fuel criterion and compared to an easily calculated continuous-thrust baseline. It is shown that in certain scenarios the discrete-thrust solution provides the lowest overall fuel cost. These scenarios are generally constrained to a smaller total time-of-flight. A simple check is proposed that enables the mission planner to make the correct strategy choice.

Acknowledgments

Life's greatest challenges are rarely solo endeavors; a fact especially true for those striving towards a doctoral degree. A great debt is owed to many people for shepherding me through this effort. First and foremost, I would like to thank my wife for her understanding, patience, and especially her bravery in returning with me to AFIT. Supporting an AFIT student is difficult in an of itself but knowing what you're getting into and still supporting just as strongly is near heroic. You are the reason I had a smile on my face every day. I also thank my boys who were to young to understand why their dad had to work some Saturdays instead of playing with them but were always there when I could play.

Next a big thanks to my advisor and committee chair, Dr. Richard Cobb whose uncanny planning put just the right number of conferences and sponsor updates at just the right times to optimize performance and push me to get results. I've truly enjoyed working with you; you made it fun. I am also indebted to my committee: Dr. Peter Maybeck, Dr. William Wiesel, Lt Col Nathan Titus, and my dean's representative Dr. Robert Hengehold. You probably don't realize it, but through our interaction, each one of you lead me to a significant breakthrough or kept me from going down a fruitless path. I could have never completed this research on time without you. And of course a special thanks to my unofficial committee member and sponsor Dr. Alan Lovell at AFRL/Space Vehicles, I've enjoyed our close collaboration.

And last but certainly not least my fellow classmates who kept it fun and never boring. Vinnie, Kevin, Jason, John, and of course Tim; the Lando to my Han, the Arthur Dent to my Ford Prefect, the Gonzo to my Kermit. Your blend of arcane \LaTeX commands and precision billiard shooting make you a force to be reckoned with...but try and watch Star Wars just once okay?

David Jonathan Irvin Jr.

Table of Contents

	Page
Abstract	iv
Acknowledgments	v
List of Figures	x
List of Tables	xiv
List of Symbols	xv
List of Abbreviations	xix
I. Introduction	1
II. Literature Review	4
2.1 Background	4
2.2 Dynamic Analysis	5
2.3 Formation Establishment, Maintenance, and Reconfiguration	6
2.4 Effect of Perturbations	7
2.5 Extension to Elliptical Chief Orbits	7
2.6 Constrained Formation Geometries	8
2.7 Summary	9
III. Methodology	10
3.1 Notation	11
3.2 The Equations of Motion	14
3.2.1 Initial & Final Relative Velocities	19
3.2.2 Equilibrium Points of the EOM	21
3.2.3 Symmetries of the Circular Chief Relative EOM	23
3.2.4 Error Analysis	25
3.3 The Cost Function	31
3.4 Interior Thrust Points	34
3.5 Units	35
3.6 The Constraint	35
3.6.1 Calculation of \tilde{T}_{\max}	37
3.6.2 Invariance of the Constraint Surface to y_L	39
3.6.3 Symmetries Between Constraint Surfaces in the Right and Left Hand Planes	40
3.6.4 Lobes Symmetric About Their Horizontal Axis	43

	Page
3.6.5 Lobes that Intersect the \hat{Y} Axis	43
3.6.6 Sensitivity of the Constraint Surface to Lobe Size	46
3.6.7 Sensitivity of the Constraint Surface to x_L	47
3.6.8 The Constraint Surface for Elliptical Chief Orbits	48
3.6.9 Other Constraints	50
3.6.10 Summary	50
IV. The Optimal Trajectory	51
4.1 The Optimal Trajectory in the $\hat{X}\hat{Y}$ Plane	52
4.2 The Optimal Trajectory in the \hat{Z} Direction	52
4.3 Entry Condition Definitions	55
4.3.1 Defined Entry Condition	55
4.3.2 Open Entry Condition	56
4.3.3 Entry from a Closed-Relative Orbit	56
4.4 Exit Condition Definitions	57
4.4.1 Defined Exit Condition	57
4.4.2 Open Exit Condition	58
4.4.3 Exit to a Closed-Relative Orbit	58
4.4.4 Repeating Hover Orbit	59
4.5 Research Cases	60
4.6 The Continuous-Thrust Solution	60
4.6.1 Entry Leg	61
4.6.2 Exit Leg	63
4.6.3 Hover Time	64
4.6.4 Summary	65
V. Results and Analysis	66
5.1 The Persistent Hover Orbit	67
5.2 Case 1: Defined Entry Condition/Open Exit Condition	70
5.3 Case 2: Entry From a Closed-Relative Orbit/Exit to a Closed-Relative Orbit	80
5.4 Case 3: Open Entry Condition/Repeating Hover Orbit	85
5.5 Trajectory Changes Due to Increased x_L	92
5.6 Trajectory Changes Due to Increased Lobe Size	93
5.7 Trajectory Check in Other Quadrants	94
5.8 Addition of \hat{Z} Axis Motion	94
5.9 Results from Elliptical Chief Orbit	98
5.10 Summary	98

	Page
VI. Conclusions and Recommendations	99
6.1 Contributions	100
6.2 Topics for Future Research	101
Appendix A. Math Preliminaries	102
A.1 Theorem: Radius of an Ellipse	102
A.2 Theorem: The Inertial Derivative	103
A.3 Theorem: The Harmonic Addition Theorem	106
A.4 Theorem: Partial Derivative of $u'RR'u$ with Respect to a Scalar (u is a Function of the Scalar)	108
A.5 Theorem: Partial Derivative of $u'RR'u$ with Respect to a Scalar (R is a Function of the Scalar)	110
Appendix B. The User-Defined Lobe	112
B.1 In the Orbit Plane	112
B.2 Out of the Orbit Plane	116
Appendix C. The Two Body Problem	117
Appendix D. Orbital Mechanics	121
D.1 True Anomaly (ν)	121
D.2 Ellipse Radius (r)	123
Appendix E. General Relative Motion Derivation	125
Appendix F. Chief Orbit Fractions as the Independent Variable	133
Appendix G. A Closed-Form Solution of the Linear Clohessy-Wiltshire Equations	136
G.1 Units Analysis	143
Appendix H. Transformations between the Inertial and Relative Reference Frames	145
Appendix I. Circular Chief Relative Velocities	150
I.1 Initial Relative Velocity	150
I.2 Final Relative Velocity	154
Appendix J. T_{\max} of the \hat{Z} Motion for a Circular Chief	159

	Page
Appendix K. The Derivation of ΔV	163
K.1 The Derivation of ΔV^2	163
K.2 Specific ΔV	167
K.3 The Derivation of ΔV for \hat{Z} Motion	168
K.4 ΔV Expressed in the Inertial Frame	171
Appendix L. The Continuous-Thrust Solution	173
Appendix M. The Persistent Hover Orbit	176
M.1 Maximum ρ and b	178
Appendix N. The Teardrop Hover Orbit	180
Appendix O. The Truth Model	185
O.1 Propagation of the Truth Model	185
O.2 The J_2 Perturbation	185
O.3 Atmospheric Drag	189
Appendix P. The Gradient of the Cost Function	192
P.1 The Gradient of ΔV^2	193
Appendix Q. MATLAB [®] Algorithm	200
Bibliography	201

List of Figures

Figure		Page
1.	General Problem Formulation	11
2.	Lobe Parameters	12
3.	Types of Relative Trajectories	17
4.	Plot of $f(\tilde{T}) = 8 - 6\pi\tilde{T}\tilde{S} - 8\tilde{C}$	21
5.	Time Between the Zeros of $f(\tilde{T}) = 8 - 6\pi\tilde{T}\tilde{S} - 8\tilde{C}$	21
6.	Symmetry of the Circular Chief Equations of Motion	25
7.	Trajectory Integration Errors Over One Chief Period	26
8.	Numerical Error Due to Inertial to Relative Frame Rotations	27
9.	Linearization Error in a Closed Relative Orbit ($a = 0$ km)	28
10.	Linearization Error in a Drifting Relative Orbit ($a = 2$ km)	29
11.	Maximum Linearization Errors Over One Chief Period	29
12.	Perturbations Due to J_2 (Orbital Altitude = 250 km)	30
13.	Perturbations Due to Atmospheric Drag (Orbital Altitude = 250 km)	31
14.	Notional Time-of-Flight Comparisons	36
15.	Maximum Time-of-Flight ($\alpha = 45^\circ, \gamma = 2$ km, $\tau_x = 1$ km, $\tau_y = 0.5$ km)	37
16.	Points of Zero Maximum Time-of-Flight	38
17.	Flowchart for Finding \tilde{T}_{\max}	39
18.	Invariance of the Constraint Surface to y_L	40
19.	Symmetric Lobes and Reflective Trajectories	41
20.	Equivalent Constraint Surfaces ($\alpha = 135^\circ, \gamma = 2$ km, $\tau_x = 1$ km, $\tau_y = 0.5$ km)	43
21.	Equivalent Lobes	44
22.	Lobe Symmetric About Horizontal Axis ($\alpha = 0^\circ, \gamma = 1.414$ km, $\tau_x = 1$ km, $\tau_y = 0.5$ km, $\eta = 0^\circ$)	45

Figure		Page
23.	Trajectories of Nearly One Chief Orbit Period	45
24.	Lobe Intersection of the \hat{Y} Axis ($\alpha = 90^\circ, \gamma = 2 \text{ km}, \tau_x = 1 \text{ km}, \tau_y = 0.5 \text{ km}, \eta = 20^\circ$)	46
25.	Constraint Surfaces for Varying Size Lobes ($\alpha = 45^\circ, \gamma = 2 \text{ km}, \eta = 45^\circ$)	47
26.	Constraint Surfaces for Varying Distances from the \hat{Y} Axis ($\tau_x = 1 \text{ km}, \tau_y = 0.5 \text{ km}, \eta = 45^\circ$)	48
27.	Elliptical Chief Constraint Surface $e = 0.7, \nu_o = 0 \text{ rad}$	49
28.	Elliptical Chief Constraint Surface $e = 0.7, \nu_o = \pi \text{ rad}$	49
29.	Notional $\Delta\check{V}$ vs Z Period	55
30.	The Continuous-Thrust Trajectory	62
31.	Lobes of the Results Section	66
32.	Optimization Algorithm Results for Lobe 1	67
33.	The Persistent Hover Orbit	68
34.	Persistent Hover Orbit Test: $\psi_1 = \frac{\pi}{4}$	69
35.	Persistent Hover Orbit Test: $\psi_1 = \frac{3\pi}{4}$	69
36.	Case 1, Lobe 2, Single Leg	71
37.	Case 1, Lobe 3, Single Leg	71
38.	Case 1, Lobe 4, Single Leg	72
39.	Case 1, Lobe 3, The Trivial Solution	72
40.	Case 1, Lobe 2, Legs = 1	74
41.	Case 1, Lobe 2, Legs = 2	74
42.	Case 1, Lobe 2, Legs = 3	75
43.	Case 1, Lobe 2, Legs = 4	75
44.	Case 1, Lobe 2, Legs = 5	76
45.	Case 1, Lobe 3, Legs = 1	76
46.	Case 1, Lobe 3, Legs = 2	76
47.	Case 1, Lobe 3, Legs = 3	77
48.	Case 1, Lobe 3, Legs = 4	77

Figure		Page
49.	Case 1, Lobe 3, Legs = 5	77
50.	Case 1, Lobe 4, Legs = 1	78
51.	Case 1, Lobe 4, Legs = 2	78
52.	Case 1, Lobe 4, Legs = 3	78
53.	Case 1, Lobe 4, Legs = 4	79
54.	Case 1, Lobe 4, Legs = 5	79
55.	Case 2, Lobe 2, Legs = 1	81
56.	Case 2, Lobe 2, Legs = 2	81
57.	Case 2, Lobe 2, Legs = 3	82
58.	Case 2, Lobe 3, Legs = 1	82
59.	Case 2, Lobe 3, Legs = 2	82
60.	Case 2, Lobe 3, Legs = 3	83
61.	Case 2, Lobe 4, Legs = 1	83
62.	Case 2, Lobe 4, Legs = 2	83
63.	Case 2, Lobe 4, Legs = 3	84
64.	Case 3, Lobe 2, Legs = 3, Teardrop	85
65.	Case 3, Lobe 2, Legs = 2, Bounce	86
66.	Case 3, Lobe 3, Legs = 3, Teardrop	86
67.	Case 3, Lobe 4, Legs = 3, Teardrop	86
68.	Case 3, Lobe 4, Legs = 4, Teardrop	87
69.	Lobe 2 Teardrop Analysis	89
70.	Lobe 3 Teardrop Analysis	90
71.	Lobe 4 Teardrop Analysis	91
72.	Defined Entry/Defined Exit, Legs = 2	92
73.	Defined Entry/Defined Exit, Legs = 2	93
74.	Comparison of Lobe 2 Results to its Mirror Lobe	94
75.	Case 1, Lobe 3, Legs = 3, $\beta = 45^\circ$, $h = 0.5$ km	95
76.	Case 2, Lobe 2, Legs = 2, $\beta = 45^\circ$, $h = 0.5$ km	96

Figure		Page
77.	Case 3, Lobe 2, Legs = 4, $\beta = 45^\circ$, $h = 0.5$ km	97
78.	Case 1, Lobe 2, Legs = 1, Elliptical Chief Orbit	98
79.	Ellipse Centered on the Origin	102
80.	Derivatives of the $\hat{X}\hat{Y}\hat{Z}$ Frame Unit Vectors	105
81.	The Lobe in Two Dimensions	112
82.	Conversion from Cartesian to Polar Coordinates	115
83.	The Lobe in Three Dimensions	116
84.	Two Body Problem	117
85.	The General Elliptical Orbit	121
86.	General Relative Motion Setup	125
87.	Relative Orbit Types	139
88.	Relationship Between the $\hat{X}\hat{Y}\hat{Z}$ and $\hat{I}\hat{J}\hat{K}$ Frames	145
89.	Cylindrical Lobe	160
90.	T_{\max} vs z_{\min}/z_{\max}	162
91.	ΔV Derivation Setup	163
92.	Notional $\Delta\check{V}$ vs Z Period	172
93.	Persistent Hover Orbit Setup	177
94.	Notional Teardrop Orbit	180
95.	Oblate Earth Coordinate Frame	187

List of Tables

Table		Page
1.	Lobe Parameters	67
2.	Atmospheric Model	191

List of Symbols

Symbol		Page
\hat{X}	Chief centered reference frame: radial direction	11
\hat{Z}	Chief centered reference frame: out-of-plane	11
\hat{Y}	Chief Centered reference frame: in-track direction	11
x_i	The i th position of the deputy in the \hat{X} direction	11
y_i	The i th position of the deputy in the \hat{Y} direction	11
z_i	The i th position of the deputy in the \hat{Z} direction	11
x_L	Position of the lobe center in the \hat{X} direction	12
y_L	Position of the lobe center in the \hat{Y} direction	12
z_L	Position of the lobe center in the \hat{Z} direction	12
α	Angular position of the lobe center in the $\hat{X}\hat{Y}$ plane	12
β	Angular position of the lobe center measured from the \hat{Z} axis	12
γ	Distance from the chief to the lobe center	12
γ_{XY}	Projection of γ in the $\hat{X}\hat{Y}$ plane	12
η	Angular orientation of the lobe with respect to the \hat{X} axis	12
τ_x	Length of the lobe axis in the \hat{X}' direction	12
τ_y	Length of the lobe axis in the \hat{Y}' direction	12
h	The half height of the elliptical cylinder	12
ψ_i	Deputy angular position $\hat{X}\hat{Y}$ plane	12
r_i	Deputy radial position in the $\hat{X}\hat{Y}$ plane	12
$T_{i,i+1}$	Time-of-flight between the i th and $[i + 1]$ th points	13
t	Time	13
P	Period of the chief orbit	13
a_{SMA}	Semi-major axis of the chief orbit	13
μ	Gravitational parameter	13
n	Mean motion of the chief orbit	13

Symbol		Page
G	Fundamental gravitational constant	13
m	Mass	13
\tilde{T}	Time-of-flight expressed in fractions of a chief orbit	13
\dot{x}_i^-	Incoming velocity at the i th point in the \hat{X} direction	13
\dot{y}_i^-	Incoming velocity at the i th point in the \hat{Y} direction	13
\dot{z}_i^-	Incoming velocity at the i th point in the \hat{Z} direction	14
\dot{x}_i^+	Outgoing velocity at the i th point in the \hat{X} direction	14
\dot{y}_i^+	Outgoing velocity at the i th point in the \hat{Y} direction	14
\dot{z}_i^+	Outgoing velocity at the i th point in the \hat{Z} direction	14
e	Eccentricity of the chief orbit	15
r_o	Instantaneous inertial orbit radius	15
ν	True anomaly	15
\tilde{t}	Time expressed in fractions of a chief orbit	16
\tilde{x}	\hat{X} position where time is in fractions of a chief orbit	16
\tilde{y}	\hat{Y} position where time is in fractions of a chief orbit	16
\tilde{z}	\hat{Z} position where time is in fractions of a chief orbit	16
$\tilde{\nu}$	True anomaly where time is in fractions of a chief orbit	16
ρ	Relative orbit parameter: size of relative orbit	18
a	Relative orbit parameter: \hat{X} offset term	18
b	Relative orbit parameter: \hat{Y} offset term	18
θ	Relative orbit parameter: phase angle	18
l	Relative orbit parameter: $\hat{X}\hat{Z}$ plane slope	18
q	Relative orbit parameter: $\hat{Y}\hat{Z}$ plane slope	18
\tilde{z}_{\max}	Relative orbit parameter: maximum \hat{Z} position	18
ϕ	Relative orbit parameter: \hat{Z} motion phase angle	18
\tilde{M}_o	Matrix mapping initial/final relative positions to initial velocity	20
\tilde{M}_f	Matrix mapping initial/final relative positions to final velocity .	20
R_e	Radius of the Earth	29

Symbol		Page
X	Inertial coordinate in the \hat{I} direction	29
Y	Inertial coordinate in the \hat{J} direction	29
Z	Inertial coordinate in the \hat{Z} direction	29
V_{rel}	Velocity relative to the atmosphere	30
B_C	Ballistic coefficient	30
ρ_o	Nominal density	30
h_o	Reference altitude	30
h_d	Satellite altitude	30
H	Scale height	30
J	Cost function: ratio of fuel spent to time-of-flight	31
ΔV_i	Instantaneous change in velocity at the i th point	31
k	Number of legs in the $\hat{X}\hat{Y}$ plane	31
ΔV_C	Continuous ΔV	32
x_{min}	Minimum x coordinate of the lobe	32
\tilde{T}_T	Total time-of-flight expressed in fractions of a chief orbit	32
$\Delta\check{V}$	Specific ΔV	33
$\Delta\tilde{V}$	ΔV where time is in fractions of a chief orbit	33
\tilde{T}_{max}	Maximum time-of-flight expressed in fractions of a chief orbit	50
\tilde{z}_{min}	Minimum allowable \hat{Z} coordinate	53
\tilde{z}_{max}	Maximum allowable \hat{Z} coordinate	53
\tilde{P}_z	Period of the \hat{Z} oscillation	53
k_z	Number of legs in the \hat{Z} direction	54
$\Delta\check{V}_Z$	Specific ΔV required in the \hat{X} direction	54
τ	Radius of a circular lobe	114
p	Semi-latus rectum	123
ϕ	Geocentric latitude of the satellite	187
λ	Geographical longitude	187
ω_e	Rotation rate of the Earth	187

Symbol		Page
t_e	Epoch time	187
J_n	Zonal harmonic coefficients of order 0	187
P_n	Legendre polynomial of degree n and order 0	187
P_{nm}	Legendre polynomial of degree n and order m	187
C_{nm}	Tesseral harmonic coefficients for $n \neq m$	187
S_{nm}	Sectorial harmonic coefficients for $n = m$	187
C_D	Coefficient of drag (unitless)	189
A	Area	189
ρ_d	Atmospheric density	189

List of Abbreviations

Abbreviation		Page
USAF	United States Air Force	1
OCS	Offensive Counterspace	1
DCS	Defensive Counterspace	1
CW	Clohessy-Wiltshire	4
DARPA	Defense Advanced Research Projects Agency	4
AFRL	Air Force Research Laboratory	4
NASA	National Aeronautics and Space Administration	5
LVLH	Local-Vertical/Local-Horizon	11
EOM	Equations of Motion	14
DEnC	Defined Entry Condition	55
OEnC	Open Entry Condition	56
EnCRO	Entry from a Closed-Relative Orbit	56
DExC	Defined Exit Condition	57
OExC	Open Exit Condition	58
ExCRO	Exit to a Closed-Relative Orbit	58
PHO	Persistent Hover Orbit	67

OPTIMAL CONTROL STRATEGIES FOR CONSTRAINED RELATIVE ORBITS

I. Introduction

The dawn of the 20th century saw humanity's first hesitant steps from the surface of Earth, setting off a technological and engineering explosion that put a manmade object into space a mere 54 years after that first flight. The US Military has made enormous strides in utilizing the space environment to provide capability and multiply overall military effectiveness in combat operations. As the world's technological base has grown, our allies and enemies are also taking advantage of the opportunities gained with their own assets in space. Although doctrine is changing, space has historically been viewed mostly as a medium of non-interference due in large part to an inability to affect assets on orbit. This could be viewed as a modification of the "Big Sky" theory of early powered flight in which opposing forces merely waved at each other as they passed by on their way to the fight. In today's military environment this simple philosophy is no longer viable. Recent events have proven that our space assets are not beyond our enemy's reach and therefore must be protected. This new mission for the USAF is called Counterspace and is defined in Air Force Doctrine Document 1 [10] as

those kinetic and nonkinetic operations conducted to attain and maintain a desired degree of space superiority by the destruction, degradation, or disruptions of enemy space capability

Counterspace is separated into two pieces: Offensive Counterspace (OCS) and Defensive Counterspace (DCS). DCS preserves space capabilities from enemy threats while OCS operations seek to affect non-US space assets negatively. On the DCS side, there are a number of scenarios in which it would be advantageous for a friendly micro-satellite to stay within the local area of a larger friendly satellite in a protection or inspection role. The feasibility of this type of mission using closed orbits with the

target satellite in the center was investigated by Thomas et al [54]. The protective “sentinel” mission may require the microsat to remain in an orbit near the target satellite but transition to a defined relative location for defensive mode upon indication of attack.

In addition to DCS measures, there are a host of capabilities that will be essential for maintaining critical space systems in the future. These include repairing, refueling, upgrading, augmenting, and otherwise servicing on-orbit space assets. The linchpin for all of these capabilities is the ability to perform close-proximity operations. A specific type of close-proximity operation, as mentioned briefly above, is the ability to “hover” in a specific zone relative to the target satellite. Hover capability has been demonstrated for a few constrained cases (i.e., in specific places relative to the target satellite) or missions about smaller planetary bodies such as asteroids. The goal of this dissertation research is to extend hover capability to anywhere within the target satellite’s local area and for a target satellite on any closed Keplerian orbit. Note that, since hovering will typically not be on a natural, drift-free relative orbit, thrusting will be required. Thus the research will focus on maximizing the time of hover for a given amount of fuel and, in doing so, will address the feasibility of a variety of potential scenarios under consideration by military planners. For the purposes of this research, the target satellite of interest, which is located at the center of the relative frame, will be called the “chief” satellite and the satellite operating in proximity to the chief is the “deputy”. The problem statement addressed in this dissertation is to

develop a control strategy to place a deputy satellite inside a specific lobe defined in the chief body-fixed frame and keep it there in a fuel-optimal manner.

Solving this problem will allow us to answer two questions:

1. Can a discrete-thrust trajectory be found that outperforms a benchmark continuous-thrust solution for a fuel criterion of optimality?
2. Can we quickly and robustly estimate, with reasonable accuracy, the amount of ΔV required to stay within a specific lobe?

The following chapters detail a solution method and analyze results in order to answer those questions. Chapter II presents an overview of proximity operation and relative motion research currently in the literature. Chapter III introduces the elements needed to solve the problem including the equations of motion, development of cost and constraint functions, and analysis of symmetries in the problem that reduce the number of cases needed to confirm the conclusions. Chapter IV describes how the optimal trajectory is found, along with definitions of the initial and final conditions. This chapter ends with an overview of the research cases found in the results. Chapter V presents and discusses optimal trajectories for four different lobes. Finally, conclusions and suggestions for future research are found in Chapter VI. The appendices are ordered such that they build from mathematical preliminaries to derivation of the foundation equations to application of those equations. Therefore, they will not be referenced in alphabetical order in the main document.

II. Literature Review

2.1 Background

It was G.W. Hill who developed the restricted three-body problem of the Sun-Earth-Moon system in terms of a relative rotating reference frame [16]. The advent of artificial satellites and the potential for constructing larger structures in space and/or docking with those structures necessitated a method of rendezvous. This need led to W.H. Clohessy and R.S. Wiltshire's adoption of Hill's methodology and the production of their famed Clohessy-Wiltshire relative equations of motion in the early 1960's [8]. These equations allow for not only docking and rendezvous but also close-proximity operations in which a deputy satellite is placed in a closed relative orbit about the chief. Although the Clohessy-Wiltshire equations (abbreviated CW henceforth) are valid only for chief satellites in a circular orbit, they have proven quite useful in solving a wide variety of satellite dynamics problems. In addition, by assuming the chief and deputy are *close* in comparison to the orbital radius of the chief, the CW equations very nicely linearize to a form that is suitable for linear analysis and control techniques. These restrictions can be removed with more complex sets of equations and have been studied extensively in recent years [5, 20, 25].

Research into relative orbit dynamics (see references in Section 2.2 to Section 2.6) has exploded over the last two decades as the potential payoff for coordinated satellite formations has been brought into sharp focus. Government interest, specifically from the USAF and DARPA, is clear by the numerous programs dedicated to formation flying and its associated technology development. The TechSat 21 program [31], although now defunct, investigated technologies critical to satellite formations such as micro-satellite bus and micro-propulsion. TechSat 21 had planned to be a proof of concept for distributed mission architecture, sparse aperture sensing, and collaborative behavior [6, 49]. In an effort to demonstrate proximity operations, the AFRL Space Vehicles directorate has executed the XSS-10 and XSS-11 missions [52]. The XSS-11, launched in April 2005, successfully performed a variety of rendezvous and proximity missions of several US-owned, dead, or inactive space

objects. DARPA's Orbital Express Space Operations Architecture similarly sought to validate a host of proximity operations, including autonomous on-orbit refueling and reconfiguration of satellites [40]. It successfully launched on 8 March 2007 and completed its technology demonstration mission on 29 June 2007. Finally, NASA's Demonstration of Autonomous Rendezvous Technology (DART) program launched in April 2005 and successfully completed the location and rendezvous phases of its operations but was unable to complete all of its close-proximity and circumnavigation operations due to lack of fuel [1, 39].

The technical papers have been collected in five categories:

1. Dynamic Analysis
2. Formation Establishment, Maintenance, and Reconfiguration
3. Effect of Perturbations
4. Extension to Elliptical Chief Orbits
5. Constrained Formation Geometries

2.2 Dynamic Analysis

The first group consists of papers that investigated either alternate means of expressing the relative equations of motion or higher order expansions of the CW equations. Many researchers have abandoned the relative Cartesian coordinates of the CW equations for those based on classical orbital elements of the chief or differences between the chief and deputy elements [45, 46]. This has been used to derive minimum, maximum, and mean distance between the two spacecraft [15]. An approximate second-order solution to the relative orbit equations was derived by Karlgaard and Lutze [22] that shows a two-orders-of-magnitude improvement over the linear solution over one period of the reference orbit. A third-order analytical solution was developed by Richardson and Mitchell [43]. In an effort to compare the various relative orbit models head to head, Alfriend and Yan [2] have created a useful tool for

evaluating and comparing the accuracy of different models through the use of a modeling error index. Finally, Amico and Montenbruck [9] have adapted the concept of eccentricity/inclination-vector separation (originally used for geostationary satellites) to low Earth orbit formations and show its utility for proximity analysis as well as orbit control.

2.3 Formation Establishment, Maintenance, and Reconfiguration

Armed with the right set of equations, researchers have looked at numerous techniques for placing satellites in specific formations and keeping them there. Of course, one of the main advantages of a satellite formation is its ability to adapt to new missions, upgrade with new satellites, and gracefully handle the loss of a damaged or dead member, resulting in investigation of methods of time- and fuel-optimal formation reconfigurations. Vaddi et al. [58] derived an analytical, two-impulse solution using orbital element differences to establish and reconfigure a circular satellite formation. Yeh et al. [68] used sliding mode control with the nonlinear Hill's equations to maintain the formation in the presence of drag, third-body effects, and an oblate Earth. A similar approach was used by Massey and Shtessel [32]. Lovell and Tragesser [30] proposed a multiple-impulsive maneuver for reconfiguration based on an alternative parameterization of the CW equations which allowed mission planners to search for optimal solutions. Paiewonsky and Woodrow [41] tackled the problem of finding time-optimal solutions to rendezvous with constraints on the thrust magnitude and fuel availability. Guibout and Scheeres [14] used a Hamiltonian approach to solve the two-point boundary value problem of formation reconfiguration. Palmer [42] found analytic solutions for minimum-fuel transfer paths between two relative orbits with a fixed time of flight and boundary conditions. Although much of the recent literature has focused on nonlinear control techniques, the original work and some current authors utilize linear control methods [21, 60]. Other similar works on this topic are found in [11, 34].

2.4 *Effect of Perturbations*

The majority of the research community has focused on oblate Earth and atmospheric drag perturbations as the primary influences on relative satellite orbits. Humi and Carter [19] investigated relative motion in the presence of linear drag. This work is later expanded to allow for quadratic drag [7]. Schweighart and Sedwick [47] developed a set of linearized constant coefficient differential equations that describe satellite relative motion in the presence of the J_2 potential. They later updated and simplified the cross-track equations in reference [48]. Wiesel [64] employs Floquet theory to include all zonal harmonics of the Earth's gravitational field, which produces accuracies over two orders of magnitude better than CW, and then finds an optimal impulsive control law for stationkeeping [65]. Leonard et al. [27] found methods of using differential drag to control relative positions. Vadali et al. [55] determined initial conditions to match mean J_2 -induced drift rates, thereby requiring less fuel to maintain the formation. A second method imposed periodic boundary conditions on the relative position and velocity in a rotating coordinate system. Finally, Williams and Wang [66] looked at the effects of solar radiation pressure on formations in highly elliptical orbits. Other similar works on dealing with perturbations are found in [35,56].

2.5 *Extension to Elliptical Chief Orbits*

More recent research has investigated control of the nonlinear equations of motion either through higher order approximations or attempts to handle the full nonlinear equations. This is motivated by the rather restrictive assumption of the original CW equations that the chief exists on a circular inertial orbit. Inalhan et al [20] reintroduced the community to previous extensions of the CW equations to eccentric chief orbits. They also developed an algorithm to find initial conditions that produced stable periodic solutions. Yamanaka and Ankersen [67] found a set of linear differential equations with time-dependent coefficients that describe relative motion of satellites in elliptical orbits. Alfriend et al. [3] found a second-order theory for relative motion that allows for any eccentricity and contains first-order J_2 effects that

can be easily modified for higher order geopotential terms. Gim and Alfriend [13] continue this exploration by finding a closed-form state transition matrix using both osculating and mean elements that allows for elliptical orbits and J_2 . Mitchell and Richardson [36] have developed a method to control a deputy satellite using a first-order approximation of the nonlinear CW equations by forcing the nonlinear system onto an invariant manifold of the linear system. Along-track position drift was reduced by a factor of 12 with only a slight control increase in the radial and cross-track drift. Gurfil and Kasdin [23] present a method to obtain higher-order approximations of the relative motion in which the coefficients of the time series are functions of the orbital elements. Broucke [5] is the first to present results with time as the independent variable, leading to a set of linearized equations for deputy motion close to a target in an elliptic orbit. Lane and Axelrad [25] have developed a set of geometric relationships that approximate relative motion for satellites in eccentric orbits. Vaddi et al. [57] established corrections to the initial conditions of the linearized equations of motion that produce periodic solutions for the nonlinear CW equations.

2.6 Constrained Formation Geometries

The final area of research reviewed is an emerging class of problems and is the basis of this dissertation. The work discussed above was almost exclusively concerned with relative orbits that followed closed elliptical paths about the chief satellite and how to maintain or reconfigure those orbits. As discussed in the introduction, there may be cases in which we desire the deputy not to orbit around the chief but to stay in a specific constrained volume relative to the chief. Since the natural dynamics of the system indicate zero-energy closed-path relative orbits exist only in a restricted case, staying within an arbitrary constrained volume will require additional energy (i.e., thrusting). The first foray into finding “hovering” orbits considered finding closed orbits in the inertial plane of the chief satellite. Hope and Trask [17] found that utilizing the natural drift of the relative orbit led to a trajectory in the inertial plane that intersected itself, providing a point at which to perform a single impulsive

thrust to keep the deputy in a constrained area. This work was expanded by Lovell and Tollefson [29] who developed a simpler closed-form solution for designing the size and shape of the hovering orbit. Finally, there has been work in optimal control of hovering satellites within weak gravitational fields such as missions near an asteroid [4,12,18,44]. While interesting, the low gravity field assumption has little applicability to this research.

2.7 Summary

The literature is replete with relative satellite motion research but is mostly concerned with higher fidelity modeling of the equations of motion or creating and maintaining fixed geometry formations. Initial research has been done on constrained relative orbits but has approached the problem by analyzing trajectory geometry to find feasible orbits without addressing the fuel-optimality of those orbits. This heretofore unexplored area of relative satellite motion research provides ample opportunity to contribute to the community.

III. Methodology

This chapter provides the mathematical underpinnings of the problem and proposed solution. Starting with the equations of motion, suitable cost and constraint functions are derived. Also provided is a lengthy discussion on symmetries within the problem that greatly reduce the number of examples needed to confirm the results and make conclusions.

Previous work on “hovering” orbits has considered closed orbits in the inertial plane of the chief satellite [17]. The teardrop orbit is designed by finding a drifting relative orbit in the inertial plane that intersects itself, providing a point at which to perform a single impulsive thrust to keep the deputy in a constrained area. This research adds fuel-optimality as a condition while finding constrained relative orbits and extends the problem to three dimensions. In short, the problem statement, as introduced in Chapter I, is to

develop a control strategy to place a deputy satellite inside a specific lobe defined in the chief body-fixed frame and keep it there in a fuel-optimal manner.

The control strategy proposed is to execute impulsive thrusts such that the location, magnitude, and direction of thrust are results of an optimization algorithm developed herein. The simplest realizable case is the one in which two satellites share the same circular orbit but have different angular positions in their inertial orbits about the Earth. In the absence of perturbations, the two would stay in a fixed relative position with each other. We desire more flexibility in the relative placement, however, and seek to define a general closed lobe (region) of arbitrary size, location, and orientation near the chief satellite and fixed in the relative frame that bounds the relative motion of the deputy (see Figure 1). This is the essence of “hovering” and is formally defined as

Hovering: Remaining inside a specified volume defined in a chief-centered reference frame.

We especially want hovering trajectories that are fuel-optimal which we define as

Fuel-Optimal Hovering Trajectory: A trajectory that minimizes the total amount of fuel spent per unit time of hovering.

We also want to evaluate closed and non-closed trajectories where

Closed Trajectory: A trajectory in which the final relative position and velocity are equal to the initial, thus allowing a repeatable relative orbit.

Figure 1 illustrates a general lobe with a center that is defined by the angles α and β and a distance γ from the chief satellite. The reference frame centered on the chief satellite is defined as follows. The \hat{X} is oriented along a line from the center of the Earth to the chief, \hat{Z} is perpendicular to the orbit plane of the chief and \hat{Y} completes the frame as the cross product $\hat{Z} \times \hat{X}$. The in-track direction is aligned with the velocity vector of the chief when in a circular orbit. This frame is commonly referred to as the Local-Vertical/Local-Horizon (LVLH) frame.

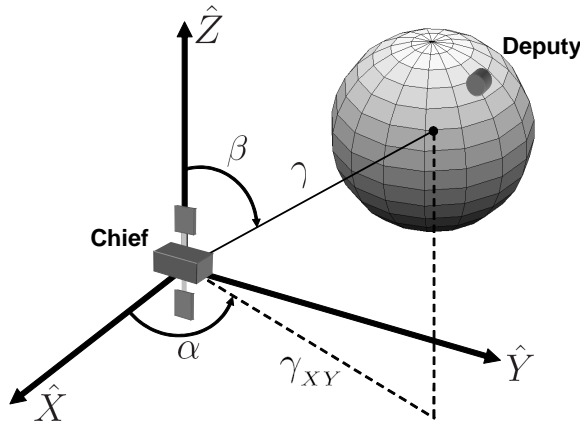


Figure 1: General Problem Formulation

3.1 Notation

The following notation is used in this research. The positions, x_i , y_i , and z_i are the coordinates of the i th point defined in the LVLH frame and indicate where an impulsive thrust may occur. An ellipse (see Figure 2(a)) is used to define the lobe boundary in the chief's orbit plane ($\hat{X}\hat{Y}$). This provides significant flexibility for designing hover regions without overly complicating the mathematics. As we will see

in later sections, motion in the \hat{Z} direction is decoupled from motion in the $\hat{X}\hat{Y}$ plane, thus an elliptical cylinder (see Figure 2(b)) is selected in order to prevent recoupling of those equations. The lobe center is located at

$$\begin{aligned}x_L &= \gamma_{XY} \cos \alpha = \gamma \cos \alpha \sin \beta \\y_L &= \gamma_{XY} \sin \alpha = \gamma \sin \alpha \sin \beta \\z_L &= \gamma \cos \beta\end{aligned}$$

where α is the angular position of the lobe center in the $\hat{X}\hat{Y}$ plane measured counter-clockwise from the \hat{X} axis, β is the angular position of the lobe center measured from the \hat{Z} axis, γ is the distance from the chief to the lobe center, γ_{XY} is the projection of γ in the $\hat{X}\hat{Y}$ plane, η is the angular orientation of the ellipse measured counter-clockwise from the \hat{X} axis, and τ_x and τ_y are the ellipse axes. For lobes that exist in three dimensions we must also define h , the half height of the elliptical cylinder.

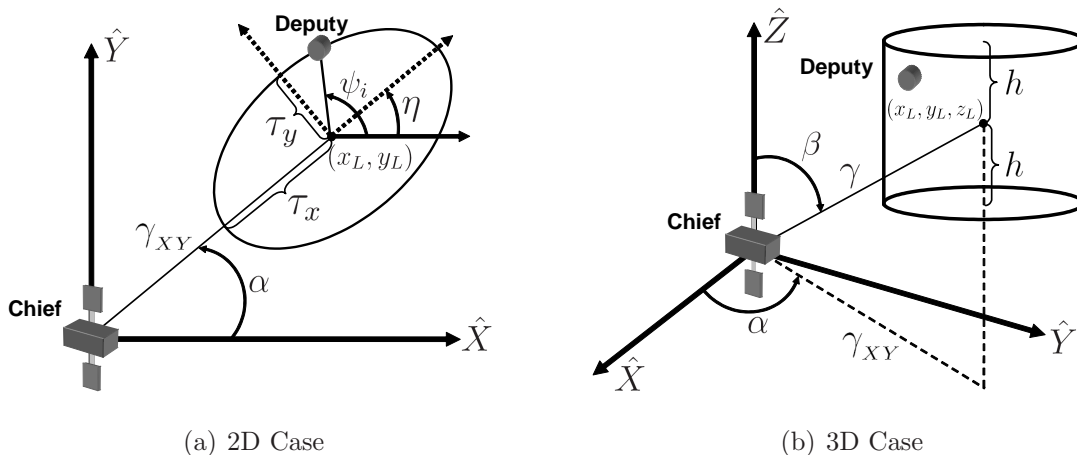


Figure 2: Lobe Parameters

Polar coordinates prove useful for defining impulsive thrust locations on the ellipse, thus the angle and radius of the i th point are designated by ψ_i and r_i where (derivation in Appendix B)

$$\begin{aligned}\psi_i &= \tan^{-1} \left[\frac{y_i - \gamma \sin \alpha \sin \beta}{x_i - \gamma \cos \alpha \sin \beta} \right] \\r_i &= \sqrt{(x_i - \gamma \cos \alpha \sin \beta)^2 + (y_i - \gamma \sin \alpha \sin \beta)^2}\end{aligned}$$

Conversion back to cartesian coordinates yields

$$\begin{aligned}
 x_i &= \gamma \cos \alpha \sin \beta + \frac{\tau_x \tau_y \cos \psi_i}{\sqrt{\tau_y^2 \cos^2(\psi_i - \eta) + \tau_x^2 \sin^2(\psi_i - \eta)}} \\
 y_i &= \gamma \sin \alpha \sin \beta + \frac{\tau_x \tau_y \sin \psi_i}{\sqrt{\tau_y^2 \cos^2(\psi_i - \eta) + \tau_x^2 \sin^2(\psi_i - \eta)}}
 \end{aligned}$$

The time-of-flight between the i th and $[i + 1]$ th points is denoted by

$$T_{i,i+1}$$

Note that, unless otherwise specified, the deputy starts at the initial position at $t = 0$. Time-of-flight is easily scaled by converting it to fractions of the chief's orbital period (P) defined as [62]

$$P = 2\pi \sqrt{\frac{a_{\text{SMA}}^3}{\mu}} = \frac{2\pi}{n} \quad (1)$$

where a_{SMA} is the semi-major axis of the chief orbit, μ is the gravitational parameter (constant for a specific two-body system), and n is the mean motion of the chief

$$\begin{aligned}
 \mu &= G(m_1 + m_2) \\
 n &= \sqrt{\frac{\mu}{a_{\text{SMA}}^3}}
 \end{aligned}$$

where G is the fundamental gravitational constant and equal to $6.6695 \times 10^{-11} \frac{\text{N}\cdot\text{m}^2}{\text{kg}^2}$ and m is mass. Time-of-flight as a fraction of chief orbit period (\tilde{T}) is

$$\tilde{T}_{i,i+1} = \frac{T_{i,i+1}}{P} = \frac{nT_{i,i+1}}{2\pi} \quad (2)$$

Two velocities are associated with each impulsive thrust point, an arriving velocity which is a function of the previous position, the current position, and the time-of-flight between them:

$$\begin{aligned}
 \dot{x}_i^- &= f_1(\psi_{i-1}, r_{i-1}, \psi_i, r_i, T_{i-1,i}) \\
 \dot{y}_i^- &= f_2(\psi_{i-1}, r_{i-1}, \psi_i, r_i, T_{i-1,i})
 \end{aligned}$$

$$\dot{z}_i^- = f_3(z_{i-1}, z_i, T_{i-1,i})$$

and a departing velocity which is a function of current position, next position, and the time-of-flight between them

$$\dot{x}_i^+ = f_4(\psi_i, r_i, \psi_{i+1}, r_{i+1}, T_{i,i+1})$$

$$\dot{y}_i^+ = f_5(\psi_i, r_i, \psi_{i+1}, r_{i+1}, T_{i,i+1})$$

$$\dot{z}_i^+ = f_6(z_i, z_{i+1}, T_{i,i+1})$$

The particular form of these equations and method of evaluation will depend on whether the chief is in a circular or elliptical orbit.

3.2 *The Equations of Motion*

The relative equations of motion (EOM) form the basis of the optimization algorithm presented in later sections. Specifically, calculation of relative velocity will be crucial to evaluating the cost, which will be a function of ΔV (since fuel-optimality is of great concern). Relative velocity will also be key in evaluating our trajectory constraint (i.e., staying within the lobe) since its initial value along with a given initial relative position will completely define a trajectory. We start with the general equations of relative motion.

Assume the chief satellite is in a closed Keplerian orbit and gravity of the central body is the only force of significance. The equations of relative motion between a chief and deputy satellite are (derivation in Appendix E)

$$\ddot{x} - 2\dot{\nu}\dot{y} - \ddot{\nu}y - \dot{\nu}^2 \left[x + \frac{r_o}{1 + e \cos \nu} - \frac{r_o^3(r_o + x)}{(1 + e \cos \nu) [(r_o + x)^2 + y^2 + z^2]^{\frac{3}{2}}} \right] = 0 \quad (3a)$$

$$\ddot{y} + 2\dot{\nu}\dot{x} + \ddot{\nu}x - \dot{\nu}^2 y \left[1 - \frac{r_o^3}{(1 + e \cos \nu) [(r_o + x)^2 + y^2 + z^2]^{\frac{3}{2}}} \right] = 0 \quad (3b)$$

$$\ddot{z} + \dot{\nu}^2 z \left[\frac{r_o^3}{(1 + e \cos \nu) [(r_o + x)^2 + y^2 + z^2]^{\frac{3}{2}}} \right] = 0 \quad (3c)$$

where e is the eccentricity of the chief orbit and r_o is the instantaneous orbital radius, a function of time (or true anomaly):

$$r_o = \frac{a_{\text{SMA}}(1 - e^2)}{1 + e \cos \nu} \quad (4)$$

The derivatives of true anomaly (ν) are (derivations in Appendix D)

$$\begin{aligned} \dot{\nu} &= \frac{n(1 + e \cos \nu)^2}{(1 - e^2)^{\frac{3}{2}}} \\ \ddot{\nu} &= \frac{-2e\dot{\nu}^2 \sin \nu}{1 + e \cos \nu} \end{aligned}$$

If we assume that the deputy is close to the chief satellite in comparison to the chief's instantaneous orbital radius

$$\sqrt{x^2 + y^2 + z^2} \ll r_o$$

then the relative equations reduce to (derivation in Appendix E)

$$\ddot{x} - 2\dot{\nu}\dot{y} - \ddot{\nu}y - \dot{\nu}^2x \left[\frac{3 + e \cos \nu}{1 + e \cos \nu} \right] = 0 \quad (5a)$$

$$\ddot{y} + 2\dot{\nu}\dot{x} + \ddot{\nu}x - \dot{\nu}^2y \left[\frac{e \cos \nu}{1 + e \cos \nu} \right] = 0 \quad (5b)$$

$$\ddot{z} + \dot{\nu}^2z \left[\frac{1}{1 + e \cos \nu} \right] = 0 \quad (5c)$$

It is possible, and highly desirable for this application, to express time as a fraction of the chief orbit period as opposed to an absolute time. This allows us to separate the relative equations from a particular semi-major axis and μ . Referencing Equation (2)

$$t = \frac{2\pi}{n} \tilde{t}$$

where \tilde{t} is time expressed in fractions of a chief orbit. The following conversions are made between the positions, velocities, and accelerations (see Appendix F):

$$\begin{aligned} \tilde{(\cdot)} &= (\cdot) & \dot{\tilde{(\cdot)}} &= \dot{(\cdot)} \frac{2\pi}{n} & \ddot{\tilde{(\cdot)}} &= \ddot{(\cdot)} \frac{4\pi^2}{n^2} \end{aligned}$$

where (\cdot) represents x , y , and z and tilde over \tilde{x} , \tilde{y} , and \tilde{z} indicate that they are functions of chief orbit period. It is important to emphasize that position does not scale, thus the trajectories produced by these equations are exactly the same regardless of the chief's semi-major axis or the value of μ . The relative equations of motion are now (note that $\tilde{\nu} = \nu$)

$$\ddot{\tilde{x}} - 2\dot{\tilde{\nu}}\dot{\tilde{y}} - \ddot{\tilde{\nu}}\tilde{y} - \dot{\tilde{\nu}}^2\tilde{x} \left[\frac{3 + e \cos \tilde{\nu}}{1 + e \cos \tilde{\nu}} \right] = 0 \quad (6a)$$

$$\ddot{\tilde{y}} + 2\dot{\tilde{\nu}}\dot{\tilde{x}} + \ddot{\tilde{\nu}}\tilde{x} - \dot{\tilde{\nu}}^2\tilde{y} \left[\frac{e \cos \tilde{\nu}}{1 + e \cos \tilde{\nu}} \right] = 0 \quad (6b)$$

$$\ddot{\tilde{z}} + \dot{\tilde{\nu}}^2\tilde{z} \left[\frac{1}{1 + e \cos \tilde{\nu}} \right] = 0 \quad (6c)$$

where the derivatives of the now scaled true anomaly are defined as

$$\begin{aligned} \dot{\tilde{\nu}} &= \frac{2\pi}{n} \dot{\nu} = \frac{2\pi(1 + e \cos \nu)^2}{(1 - e^2)^{\frac{3}{2}}} \\ \ddot{\tilde{\nu}} &= \frac{4\pi^2}{n^2} \ddot{\nu} = \frac{-8\pi^2 e(1 + e \cos \nu)^3 \sin \nu}{(1 - e^2)^3} \end{aligned}$$

If the chief is in a circular orbit ($e = 0$), these equations simplify even further

$$\dot{\tilde{\nu}} = 2\pi$$

$$\ddot{\tilde{\nu}} = 0$$

thus

$$\ddot{\tilde{x}} - 4\pi\dot{\tilde{y}} - 12\pi^2\tilde{x} = 0 \quad (7a)$$

$$\ddot{\tilde{y}} + 4\pi\dot{\tilde{x}} = 0 \quad (7b)$$

$$\ddot{\tilde{z}} + 4\pi^2\tilde{z} = 0 \quad (7c)$$

These linear time-invariant, constant coefficient, differential equations are the classical CW equations [8], albeit in a less conventional form. In this special case, the \hat{Y} axis of the LVLH frame is parallel to the inertial velocity vector of the chief. The CW equations describe two types of relative orbits shown in Figure 3. The closed relative orbit is constrained to be a 2x1 ellipse that is centered somewhere along the \hat{Y} axis. The term “2x1” is a reference to the fixed ratio of the semi-major to semi-minor axes of the closed relative orbit. The drifting relative orbit occurs when the \hat{X} offset parameter, a , (Equation (10a) below) is nonzero, a result of a difference between the deputy and chief’s semi-major axis leading to a difference in periods. The “teardrop” feature size and shape as well as average distance from the chief can be specified [29]. These differential equations can be solved closed-form (derivation in Appendix G).

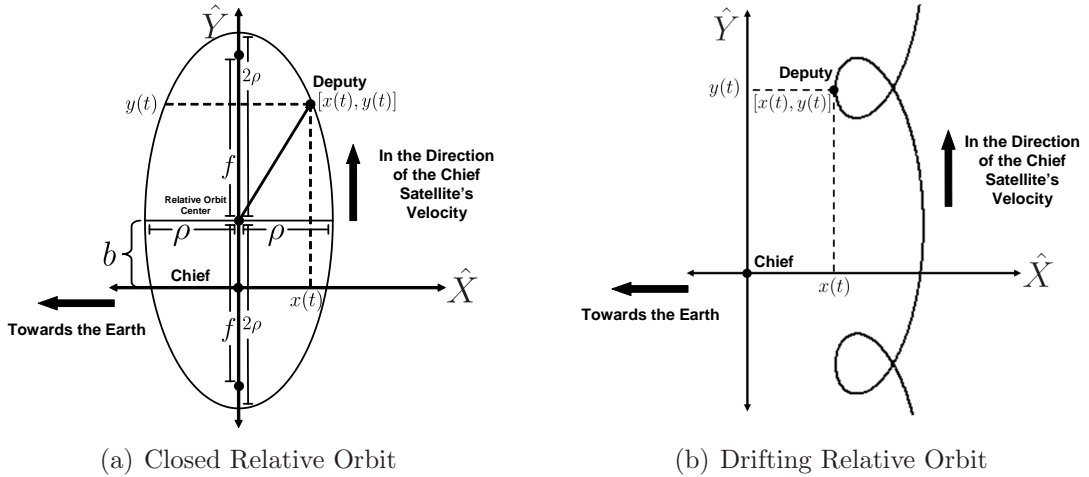


Figure 3: Types of Relative Trajectories

$$\tilde{x}(\tilde{t}) = \rho \sin(2\pi\tilde{t} + \theta) + a \quad (8a)$$

$$\tilde{y}(\tilde{t}) = 2\rho \cos(2\pi\tilde{t} + \theta) - 3\pi a\tilde{t} + b \quad (8b)$$

$$\tilde{z}(\tilde{t}) = l\rho \sin(2\pi\tilde{t} + \theta) + 2q\rho \cos(2\pi\tilde{t} + \theta) \quad (8c)$$

A useful variant of the \hat{Z} motion is (Equation (97) from Appendix G)

$$\tilde{z}(\tilde{t}) = \tilde{z}_{\max} \cos(2\pi\tilde{t} + \phi) \quad (9)$$

where the relative orbital elements (ρ , a , b , θ , l , q , \tilde{z}_{\max} , and ϕ) are all functions of both the initial relative position and velocity. In this form, the relative orbit parameters are given by

$$a = \frac{1}{\pi} \dot{y}_o + 4\tilde{x}_o \quad (10a)$$

$$b = \tilde{y}_o - \frac{1}{\pi} \dot{x}_o \quad (10b)$$

$$\rho = \sqrt{(\tilde{x}_o - a)^2 + \left(\frac{1}{2\pi} \dot{x}_o\right)^2} \quad (10c)$$

$$l = \frac{\dot{z}_o \dot{x}_o - 4\pi^2 \tilde{z}_o (a - \tilde{x}_o)}{\dot{x}_o^2 + 4\pi^2 (a - \tilde{x}_o)^2} \quad (10d)$$

$$q = \frac{\pi \tilde{z}_o \dot{x}_o + \pi \dot{z}_o (a - \tilde{x}_o)}{\dot{x}_o^2 + 4\pi^2 (a - \tilde{x}_o)^2} \quad (10e)$$

$$\theta = \tan^{-1} \left[\frac{2\pi(\tilde{x}_o - a)}{\dot{x}_o} \right] \quad (10f)$$

$$\tilde{z}_{\max} = \sqrt{\left(\frac{\dot{z}_o}{2\pi}\right)^2 + \tilde{z}_o^2} \quad (10g)$$

$$\phi = \tan^{-1} \left(\frac{-\dot{z}_o}{2\pi \tilde{z}_o} \right) \quad (10h)$$

For the approach presented, the derivatives of these equations will also be necessary, and are

$$\dot{\tilde{x}}(\tilde{t}) = 2\pi\rho \cos(2\pi\tilde{t} + \theta) \quad (11a)$$

$$\dot{\tilde{y}}(\tilde{t}) = -4\pi\rho \sin(2\pi\tilde{t} + \theta) - 3\pi a \quad (11b)$$

$$\dot{\tilde{z}}(\tilde{t}) = 2\pi l\rho \cos(2\pi\tilde{t} + \theta) - 4\pi q\rho \sin(2\pi\tilde{t} + \theta) \quad (11c)$$

or

$$\dot{\tilde{z}}(\tilde{t}) = -2\pi\tilde{z}_{\max} \sin(2\pi\tilde{t} + \phi) \quad (12)$$

The equations above form the basis of the controllers developed in later sections. Note that a continuous-thrust controller that keeps the deputy in a fixed position relative to the chief is easily synthesized (a linear quadratic regulator for example). The research hypothesis, however, is that a discrete impulsive-thrust controller is more fuel-optimal. To explore this, these equations will be used piecewise, with continuous position but discontinuous velocities.

3.2.1 Initial & Final Relative Velocities. Perhaps the most important information to extract from the above equations of motion are the initial and final relative velocities. They are key to calculating ΔV as well as initializing trajectory propagation to check for breaches of the lobe boundary. The initial relative velocity under the circular chief orbit assumption is (derivation in Appendix I.1)

$$\begin{bmatrix} \dot{\tilde{x}}_o \\ \dot{\tilde{y}}_o \\ \dot{\tilde{z}}_o \end{bmatrix} = 2\pi \underbrace{\begin{bmatrix} \frac{-4\tilde{S}+6\pi\tilde{T}\tilde{C}}{8-6\pi\tilde{T}\tilde{S}-8\tilde{C}} & \frac{2-2\tilde{C}}{8-6\pi\tilde{T}\tilde{S}-8\tilde{C}} & 0 & \frac{4\tilde{S}-6\pi\tilde{T}}{8-6\pi\tilde{T}\tilde{S}-8\tilde{C}} & \frac{-2+2\tilde{C}}{8-6\pi\tilde{T}\tilde{S}-8\tilde{C}} & 0 \\ \frac{-14+12\pi\tilde{T}\tilde{S}+14\tilde{C}}{8-6\pi\tilde{T}\tilde{S}-8\tilde{C}} & \frac{-\tilde{S}}{8-6\pi\tilde{T}\tilde{S}-8\tilde{C}} & 0 & \frac{2-2\tilde{C}}{8-6\pi\tilde{T}\tilde{S}-8\tilde{C}} & \frac{\tilde{S}}{8-6\pi\tilde{T}\tilde{S}-8\tilde{C}} & 0 \\ 0 & 0 & -\frac{\tilde{C}}{\tilde{S}} & 0 & 0 & \frac{1}{\tilde{S}} \end{bmatrix}}_{\tilde{M}_o} \begin{bmatrix} \tilde{x}_o \\ \tilde{y}_o \\ \tilde{z}_o \\ \tilde{x}_f \\ \tilde{y}_f \\ \tilde{z}_f \end{bmatrix} \quad (13)$$

where

$$\tilde{T} = \frac{T}{P} \quad \tilde{S} = \sin(2\pi\tilde{T}) \quad \tilde{C} = \cos(2\pi\tilde{T})$$

and \tilde{M}_o is the transformation matrix that maps the initial and final positions into initial relative velocity. The final relative velocity is (derivation in Appendix I.2)

$$\begin{bmatrix} \dot{\tilde{x}}_f \\ \dot{\tilde{y}}_f \\ \dot{\tilde{z}}_f \end{bmatrix} = 2\pi \underbrace{\begin{bmatrix} \frac{-4\tilde{S}+6\pi\tilde{T}}{8-6\pi\tilde{T}\tilde{S}-8\tilde{C}} & \frac{-2+2\tilde{C}}{8-6\pi\tilde{T}\tilde{S}-8\tilde{C}} & 0 & \frac{4\tilde{S}-6\pi\tilde{T}\tilde{C}}{8-6\pi\tilde{T}\tilde{S}-8\tilde{C}} & \frac{2-2\tilde{C}}{8-6\pi\tilde{T}\tilde{S}-8\tilde{C}} & 0 \\ \frac{2-2\tilde{C}}{8-6\pi\tilde{T}\tilde{S}-8\tilde{C}} & \frac{-\tilde{S}}{8-6\pi\tilde{T}\tilde{S}-8\tilde{C}} & 0 & \frac{-14+12\pi\tilde{T}\tilde{S}+14\tilde{C}}{8-6\pi\tilde{T}\tilde{S}-8\tilde{C}} & \frac{\tilde{S}}{8-6\pi\tilde{T}\tilde{S}-8\tilde{C}} & 0 \\ 0 & 0 & -\frac{1}{\tilde{S}} & 0 & 0 & \frac{\tilde{C}}{\tilde{S}} \end{bmatrix}}_{\tilde{M}_f} \begin{bmatrix} \tilde{x}_o \\ \tilde{y}_o \\ \tilde{z}_o \\ \tilde{x}_f \\ \tilde{y}_f \\ \tilde{z}_f \end{bmatrix} \quad (14)$$

where \tilde{M}_f maps initial and final positions into final relative velocity. Note that there are two singularities in \tilde{M}_o and \tilde{M}_f at

$$\begin{aligned} \sin(2\pi\tilde{T}) &= 0 \\ 8 - 6\pi\tilde{T} \sin(2\pi\tilde{T}) - 8 \cos(2\pi\tilde{T}) &= 0 \end{aligned}$$

The first, $\sin(2\pi\tilde{T})$, is easily solved for time-of-flight: $\tilde{T} = 0, \frac{1}{2}, 1, \frac{3}{2}, \dots, \frac{i}{2}$ and is only active if there is \hat{Z} motion. Physically the deputy is passing through the relative orbit's axis of rotation. This is the intersection of an infinite number of orbits and thus the linear system is indeterminate.

The second singularity (see Figure 4) is not as easy to find except for the first two zeros: $\tilde{T} = 0$ and $\tilde{T} = 1$. If not for the secular term, a closed-form expression could be found. Unfortunately we must find further zeros numerically. Figure 5 illustrates the change in the interval between zero crossings, an interval that is clearly converging to 0.5 chief orbits. Note that the zero crossing number is an integer value, however, the graph points are connected for clarity. There appears to be two exponential decay patterns: one for even and one for odd crossings. It may not be difficult to express

these decays closed-form, however, we are normally only interested in times-of-flight between 0 and 1, therefore finding the zero crossing pattern is not germane to this research.

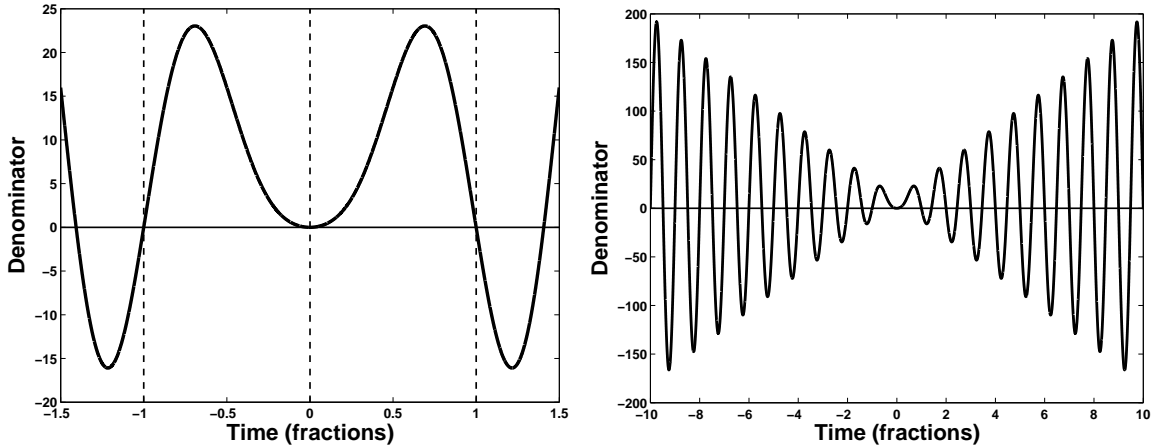


Figure 4: Plot of $f(\tilde{T}) = 8 - 6\pi\tilde{T}\tilde{S} - 8\tilde{C}$

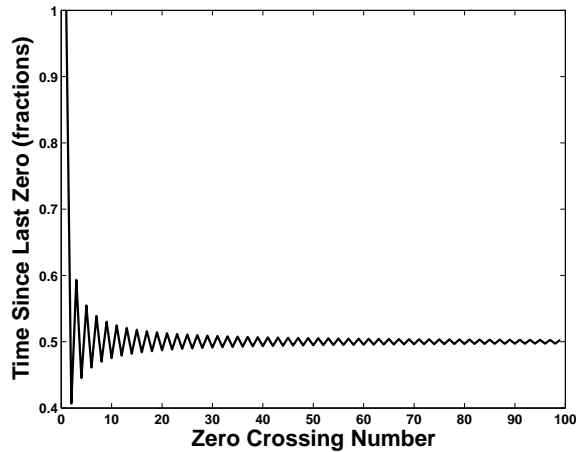


Figure 5: Time Between the Zeros of $f(\tilde{T}) = 8 - 6\pi\tilde{T}\tilde{S} - 8\tilde{C}$

3.2.2 Equilibrium Points of the EOM. It is always prudent to find the equilibrium points of any set of differential equations. This is especially important for this analysis since equilibrium represents zero-fuel solutions and may be the ideal place to put the deputy satellite. While in equilibrium, fuel is used only to reject disturbances and linearization errors in order to stay at the equilibrium point. Starting

with the CW equations of motion (Equation (7)), let

$$\ddot{\tilde{x}} = \ddot{\tilde{y}} = \ddot{\tilde{z}} = \dot{\tilde{x}} = \dot{\tilde{y}} = \dot{\tilde{z}} = 0$$

then

$$\ddot{\tilde{x}} - 4\pi\dot{\tilde{y}} - 12\pi^2\tilde{x} \rightarrow (0) - 4\pi(0) - 12\pi^2\tilde{x} = -12\pi^2\tilde{x} = 0$$

$$\ddot{\tilde{y}} + 4\pi\dot{\tilde{x}} \rightarrow (0) + 4\pi(0) = 0$$

$$\ddot{\tilde{z}} + 4\pi^2\tilde{z} \rightarrow (0) + 4\pi^2\tilde{z} = 0$$

Thus $\tilde{x} = 0$ and $\tilde{z} = 0$ without any restriction on \tilde{y} , meaning the entire \hat{Y} axis is an equilibrium point (under linear assumptions). Similarly, the equilibrium condition for the non-linearized equations of motion can also be found. Applying the zero derivative conditions to Equation (74), Appendix E.

$$(0) - (0) - n^2(r_o + x) \left[1 - \frac{r_o^3}{[(r_o+x)^2+y^2+z^2]^{\frac{3}{2}}} \right] = 0$$

$$(0) + (0) - n^2y \left[1 - \frac{r_o^3}{[(r_o+x)^2+y^2+z^2]^{\frac{3}{2}}} \right] = 0$$

$$(0) + n^2z \left[\frac{r_o^3}{[(r_o+x)^2+y^2+z^2]^{\frac{3}{2}}} \right] = 0$$

Note there is no longer any advantage to using the scaled tilde versions of the relative position and velocity since r_o appears in these equations. Since r_o and n are always positive and $(r_o + x)^2 + y^2 + z^2$ non-zero, it is clear that $z = 0$. In the other two directions, the term

$$1 - \frac{r_o^3}{[(r_o + x)^2 + y^2 + z^2]^{\frac{3}{2}}}$$

going to zero will satisfy the equilibrium conditions (so will $x = y = 0$, the trivial solution). Solving yields

$$\begin{aligned} [r_o + x]^2 + y^2 + z^2]^{\frac{3}{2}} - r_o^3 &= 0 \\ [(r_o + x)^2 + y^2 + z^2]^{\frac{3}{2}} &= r_o^3 \\ [(r_o + x)^2 + y^2 + z^2] &= r_o^2 \end{aligned}$$

Note that the left hand side is the square of the magnitude of the deputy's inertial position (\vec{M}) written in relative coordinates. Thus

$$\|\vec{M}\|_2^2 = r_o^2 \quad \Rightarrow \quad \|\vec{M}\|_2 = r_o$$

Therefore the deputy must be in same size circular orbit as the chief. Also, since $z = 0$, the deputy's orbit must be co-planar with the chief satellite. All together, this means the chief and deputy share the same orbit but may have different arguments of latitude.

3.2.3 Symmetries of the Circular Chief Relative EOM. The circular chief equations of motion contain symmetries that allow us to generalize results from lobes in one quadrant of the relative frame to results in any of the other four quadrants, thereby significantly reducing the number of results we need to produce and examine. First recall that a function is odd if [24]

$$f(-x) = -f(x)$$

The equation for initial velocity and final velocity are obviously odd since they are linear in the states:

$$\begin{bmatrix} -\dot{\tilde{x}}_o \\ -\dot{\tilde{y}}_o \\ -\dot{\tilde{z}}_o \end{bmatrix} = 2\pi \tilde{M}_o(\tilde{T}) \begin{bmatrix} -\tilde{x}_o \\ -\tilde{y}_o \\ -\tilde{z}_o \\ -\tilde{x}_f \\ -\tilde{y}_f \\ -\tilde{z}_f \end{bmatrix} \quad \begin{bmatrix} -\dot{\tilde{x}}_f \\ -\dot{\tilde{y}}_f \\ -\dot{\tilde{z}}_f \end{bmatrix} = 2\pi \tilde{M}_f(\tilde{T}) \begin{bmatrix} -\tilde{x}_o \\ -\tilde{y}_o \\ -\tilde{z}_o \\ -\tilde{x}_f \\ -\tilde{y}_f \\ -\tilde{z}_f \end{bmatrix}$$

Converting Equation (108), Appendix I to time units of chief orbit period:

$$\begin{bmatrix} \tilde{x}(\tilde{t}) \\ \tilde{y}(\tilde{t}) \\ \tilde{z}(\tilde{t}) \end{bmatrix} = \frac{1}{2\pi} \begin{bmatrix} S & 2[1-C] & 0 \\ 2[-1+C] & [4S-6\pi\tilde{t}] & 0 \\ 0 & 0 & S \end{bmatrix} \begin{bmatrix} \dot{\tilde{x}}_o \\ \dot{\tilde{y}}_o \\ \dot{\tilde{z}}_o \end{bmatrix} + \begin{bmatrix} [4-3C]\tilde{x}_o \\ [6S-12\pi\tilde{t}]\tilde{x}_o + \tilde{y}_o \\ C\tilde{z}_o \end{bmatrix}$$

where $S = \sin(2\pi\tilde{t})$ and $C = \cos(2\pi\tilde{t})$. As a function solely of starting and ending relative positions and time-of-flight:

$$\begin{bmatrix} \tilde{x}(\tilde{t}) \\ \tilde{y}(\tilde{t}) \\ \tilde{z}(\tilde{t}) \end{bmatrix} = \begin{bmatrix} S & 2[1-C] & 0 \\ 2[-1+C] & [4S-6\pi\tilde{t}] & 0 \\ 0 & 0 & S \end{bmatrix} \tilde{M}_o(\tilde{T}) \begin{bmatrix} \tilde{x}_o \\ \tilde{y}_o \\ \tilde{z}_o \\ \tilde{x}_f \\ \tilde{y}_f \\ \tilde{z}_f \end{bmatrix} + \begin{bmatrix} [4-3C] & 0 & 0 & 0 & 0 & 0 \\ [6S-12\pi\tilde{t}] & 1 & 0 & 0 & 0 & 0 \\ 0 & 0 & C & 0 & 0 & 0 \end{bmatrix} \begin{bmatrix} \tilde{x}_o \\ \tilde{y}_o \\ \tilde{z}_o \\ \tilde{x}_f \\ \tilde{y}_f \\ \tilde{z}_f \end{bmatrix}$$

$$= \left(\begin{bmatrix} S & 2[1-C] & 0 \\ 2[-1+C] & [4S-6\pi\tilde{t}] & 0 \\ 0 & 0 & S \end{bmatrix} \tilde{M}_o(\tilde{T}) + \begin{bmatrix} [4-3C] & 0 & 0 & 0 & 0 & 0 \\ [6S-12\pi\tilde{t}] & 1 & 0 & 0 & 0 & 0 \\ 0 & 0 & C & 0 & 0 & 0 \end{bmatrix} \right) \begin{bmatrix} \tilde{x}_o \\ \tilde{y}_o \\ \tilde{z}_o \\ \tilde{x}_f \\ \tilde{y}_f \\ \tilde{z}_f \end{bmatrix}$$

Once again we have a function that is linear in the states and thus an odd function. An example is provided in Figure 6; the deputy starts at (2 km, 1 km) and (-2 km, -1 km) and ends at (1 km, 0.25 km) and (-1 km, -0.25 km) both with a time-of-flight of 0.35 chief orbits. Each point on one trajectory can be rotated about the origin π radians while maintaining equidistance from the origin to get the corresponding point on the other trajectory. These two points occur at the same \tilde{t} in their respective trajectories.

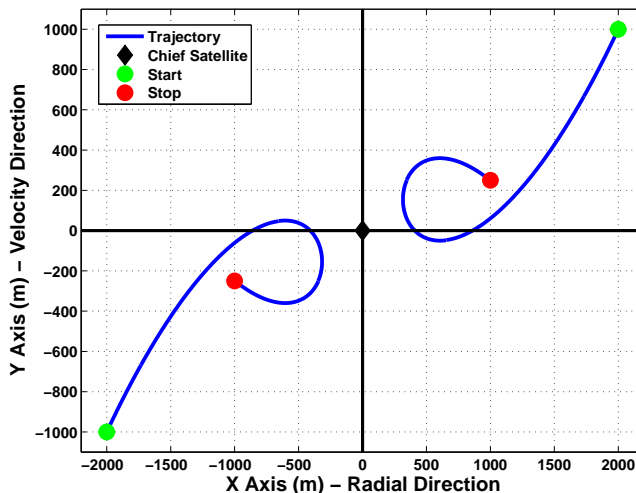


Figure 6: Symmetry of the Circular Chief Equations of Motion

3.2.4 Error Analysis. Several different forms of the equations of motion have been presented. Some have linearizing assumptions and all do not model perturbations and other error sources. Before posing and solving the optimization method, the validity and accuracy of these equations must be verified.

As with most engineering problems, the optimization algorithm is based on a reduced-order model for which mathematically tractable solutions are available. As we will see, the short total time-of-flight associated with this problem keep total errors within a reasonable range. There are four main sources of error:

1. Integration errors

2. Numerical errors during the conversion between inertial and relative reference frames
3. Linearization error from the closeness approximation
4. Unmodeled perturbations

Integration errors during trajectory propagation are a standard problem with orbital research and can be mitigated with the proper choice of a maximum propagation timestep. Figure 7 displays the final position error for trajectories produced with Equation (7) (CW solutions as functions of chief orbit period) for various maximum timesteps. The error is calculated by comparing the final position of each integration run over one chief period versus an extremely small timestep run (1×10^{-4}). In order to achieve integration errors less than 1×10^{-8} meters, 0.003 has been chosen as the largest acceptable timestep.

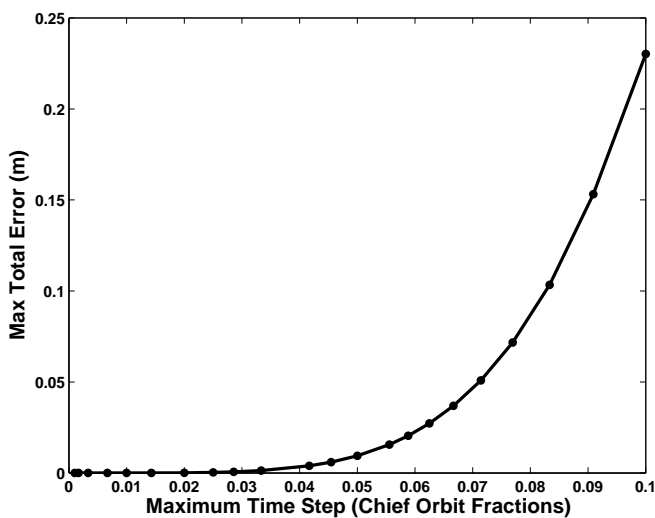


Figure 7: Trajectory Integration Errors Over One Chief Period

Additional numerical errors are encountered when using the inertially propagated truth model which requires the rotation of inertial relative position and velocity vectors into the LVLH frame (Appendix H). These results are differenced from trajectory propagations of Equation (3) with $e = 0$ (which yields $\dot{\nu} = n$ and $\ddot{\nu} = 0$). Since there are no linearization assumptions, errors between the trajectories are numeri-

cal in nature caused by an additional mathematical operation within the algorithm during which roundoff and truncation errors occur. There is little that can be done to mitigate this error besides proper maximum time step choice as discussed above. Figure 8 shows the magnitude and trends of the transformation errors. Although it

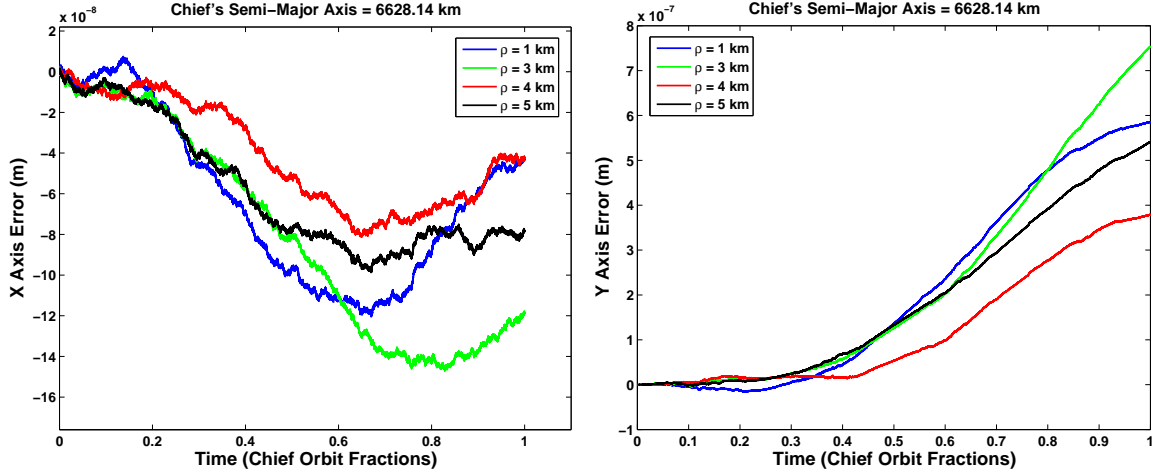


Figure 8: Numerical Error Due to Inertial to Relative Frame Rotations

is clear that the numerical imprecision builds with time, at least in the \hat{Y} direction, the errors are well within acceptable limits even after one chief orbit. Although errors are not scaled to a ρ to r_o ratio, Figure 8 shows the results of four separate runs with different values of ρ . To summarize, the first two error sources are standard assumptions for orbital mechanics problems. Most missions to which this technique will be applied are of short duration and close proximity, both of which work in our favor to reduce errors.

The third source of error occurs when we make the following linearization assumption for model simplification (see Appendix E):

$$\frac{x^2}{r_o^2} \approx \frac{y^2}{r_o^2} \approx \frac{z^2}{r_o^2} \approx 0 \quad \text{and} \quad r_o + 3x \approx r_o$$

where r_o is the instantaneous orbital radius of the chief. We naturally expect to see errors increase as average chief to deputy distance increases and/or as the orbital radius decreases. The relative orbit element ρ is a good parameter with which to

measure average distance from the chief. Figure 9 shows errors for a deputy in a closed relative orbit about the chief (i.e. the \hat{X} offset, a , is zero). Errors for closed

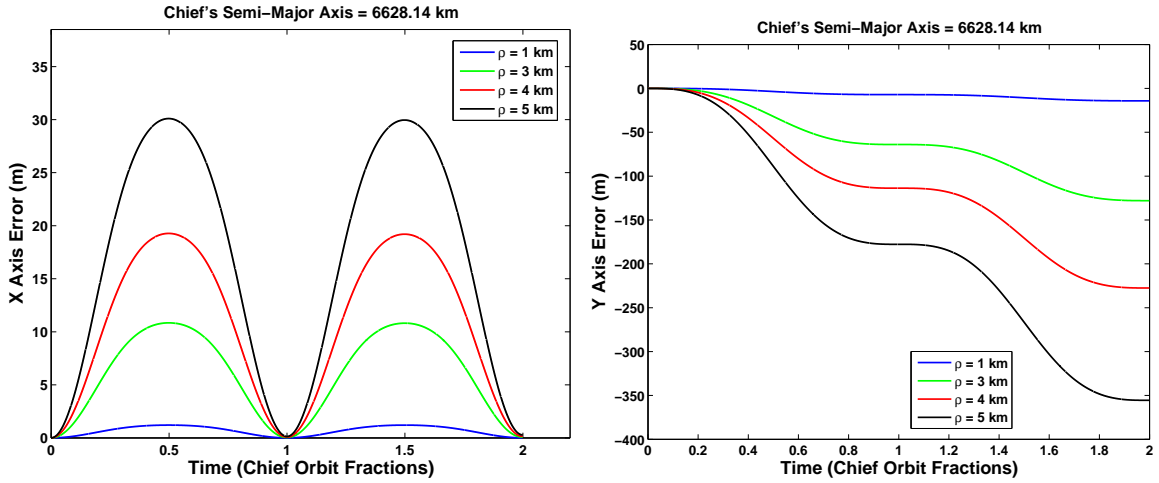


Figure 9: Linearization Error in a Closed Relative Orbit ($a = 0$ km)

relative orbits are nearly periodic in the \hat{X} axis but have a strong secular drift in the \hat{Y} axis. Although setting $a = 0$ cancels the first-order secular term, it leaves higher-order secular terms that build in error with time. Eventually, the deputy will drift far enough away from the chief to invalidate the linearized equations of motion. This happens even more quickly in the drifting relative orbit case (Figure 10) in which the substantial first-order drift term adds to the growth in distance between chief and deputy. It is clear that a short time-of-flight for each trajectory leg is key to the validity of the reduced-order model upon which the optimization routine is built. Figure 11 shows the maximum error of the deputy after one period of the chief orbit due to linearization errors.

The final source of error is due to unmodeled perturbations. The two largest perturbations are due to the oblate Earth (J_2) and atmospheric drag [59]. Both are inversely proportional to semi-major axis and are thus stronger at lower altitudes. At these lower altitudes, the Earth is better modeled as non-spherical and with non-uniform density, leading to a infinite series of correction terms to the two body problem. The first and most significant of these terms is J_2 (derivation and

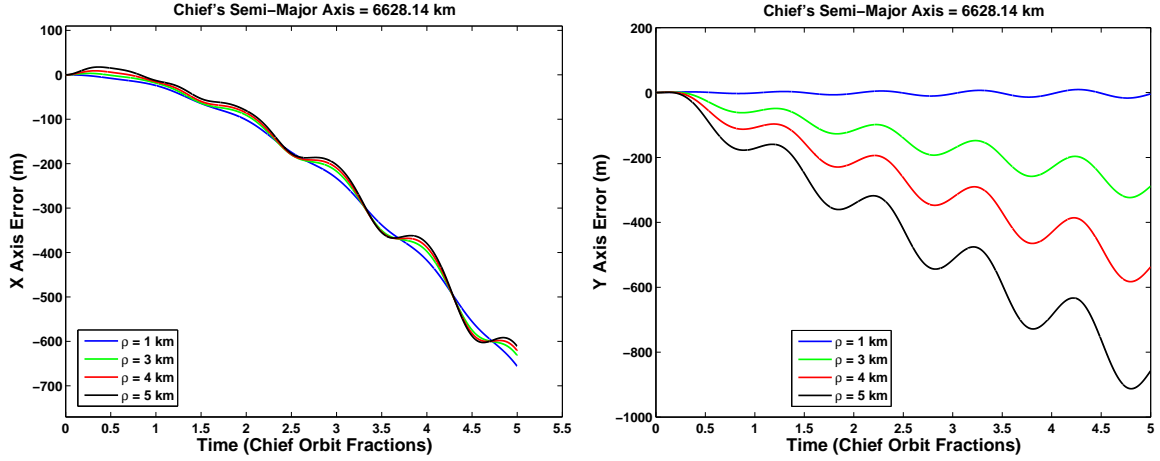


Figure 10: Linearization Error in a Drifting Relative Orbit ($a = 2$ km)

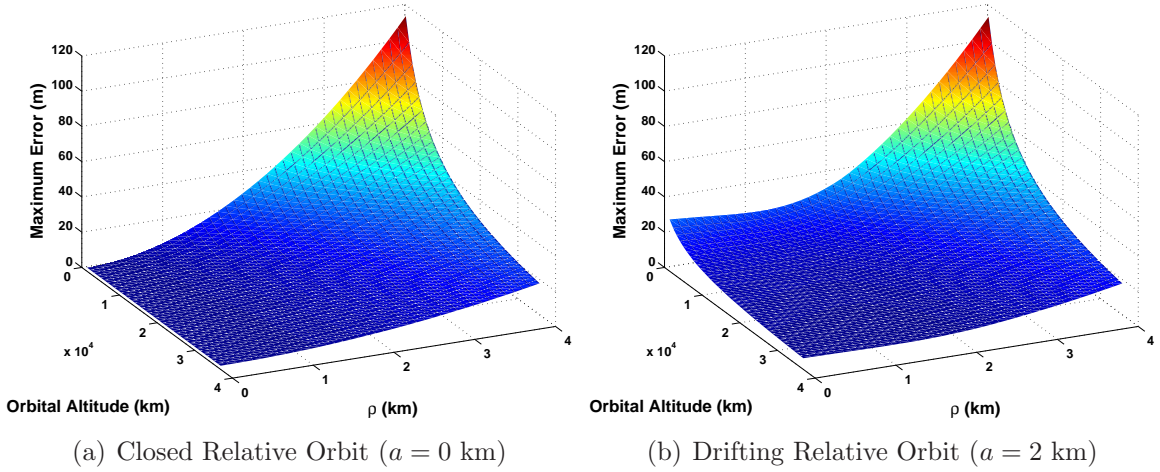


Figure 11: Maximum Linearization Errors Over One Chief Period

discussion in Appendix O.2):

$$\vec{a}_{J_2} = \frac{\mu J_2 R_e^2}{2} \begin{bmatrix} \frac{15Z^2 X}{d^7} - \frac{3X}{d^5} \\ \frac{15Z^2 Y}{d^7} - \frac{3Y}{d^5} \\ \frac{15Z^3}{d^7} - \frac{9Z}{d^5} \end{bmatrix} \quad (15)$$

where R_e is the radius of the Earth, X , Y , and Z are the inertial coordinates the satellite and

$$d = \sqrt{X^2 + Y^2 + Z^2}$$

Measurements of the zonal, tesseral, and sectorial coefficients reveal that J_2 is at least 400 times larger than the next most significant term and is thus the only harmonic considered here. Figure 12 shows the error between the full nonlinear CW model and a truth model including J_2 effects at an orbital altitude of 250 km.

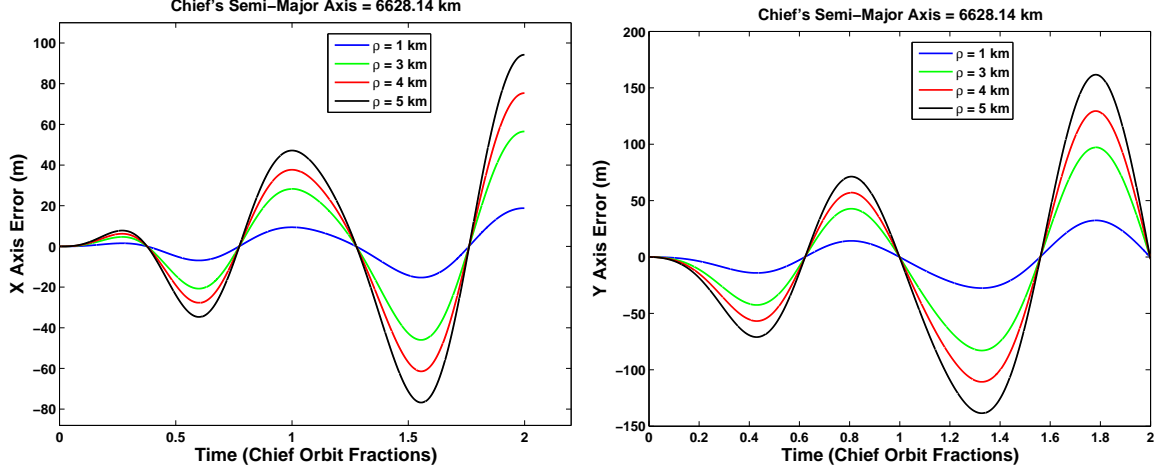


Figure 12: Perturbations Due to J_2 (Orbital Altitude = 250 km)

The second source of error considered is atmospheric drag, modeled as a force opposing the relative wind of the satellite and based on an exponential model of atmospheric density (derivation and discussion in Appendix O.3).

$$\vec{a}_{\text{drag}} = -\frac{V_{\text{rel}}}{2B_C} \rho_o e^{\frac{h_o - h_d}{H}} \vec{V}_{\text{rel}} \quad (16)$$

where V_{rel} is the satellite's velocity relative to the atmosphere, B_C is the ballistic coefficient, ρ_o is the nominal density, h_o is the reference altitude, h_d is the satellite's altitude, and H is the scale height. The error charts presented in Figure 13 are a worse case scenario of low altitude (250 km) and disparate ballistic coefficients between chief and deputy. Representative values of the ballistic coefficient are chosen from historical satellites, a micro satellite for the deputy and a larger scientific class satellite for the chief.

$$\text{Chief } B_C = 25 \frac{\text{kg}}{\text{m}^2} \quad \text{Deputy } B_C = 128 \frac{\text{kg}}{\text{m}^2}$$

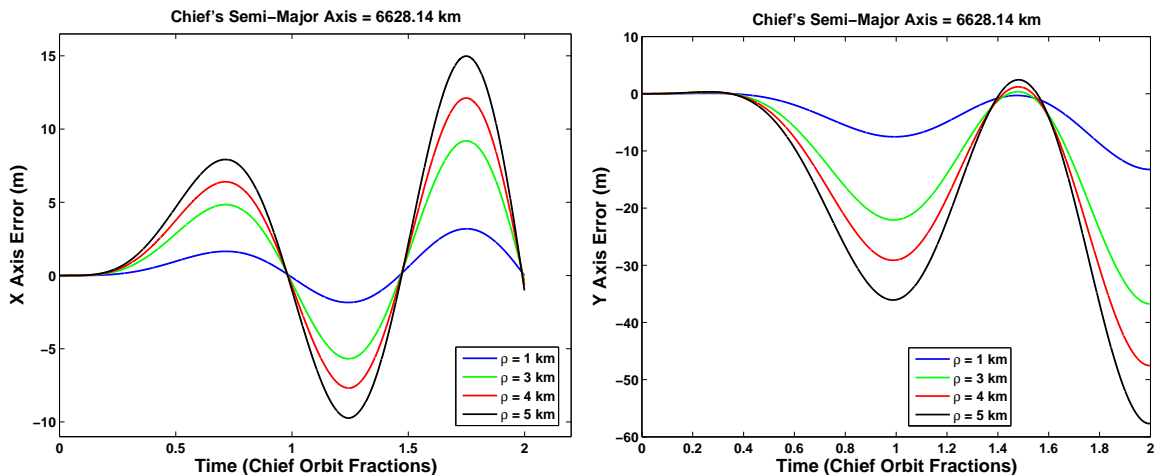


Figure 13: Perturbations Due to Atmospheric Drag (Orbital Altitude = 250 km)

Assuming proper choice of time step, the largest sources of error by far are linearization and J_2 . All of the results presented in this research are for lobes that are less than 3 km from the chief; therefore, over one chief orbit period the total error should be less than 100 meters. Of course, most hovering trajectories will have a time-of-flight well under a chief orbit period, therefore only minor changes to the path will be noticeable.

3.3 The Cost Function

The problem statement motivates an optimization problem that requires the formulation of a cost function. Ideally, we want to maximize the time spent inside the lobe per unit of fuel expended, or equivalently we can minimize the cost function J :

$$J = \frac{\text{Fuel Spent}}{\text{Time-of-Flight}} = \frac{\Delta V_F + \sum_{i=1}^k \Delta V_i}{T_F + \sum_{i=1}^k T_{i,i+1}}$$

where ΔV_i is the instantaneous change of velocity required at the i th point of impulsive thrust, k is the number of legs (a leg being defined as the trajectory between two impulsive thrusts), and the subscript F (for final) represents a possible exit burn and time-of-flight. ΔV is calculated by taking the Euclidean norm of the difference

between pre- and post-thrust relative velocities (derivation in Appendix K).

$$\Delta V_i = \|\Delta \vec{v}_i\|_2 = \|\vec{v}_i^+ - \vec{v}_i^-\|_2 = \sqrt{(\dot{x}_i^+ - \dot{x}_i^-)^2 + (\dot{y}_i^+ - \dot{y}_i^-)^2}$$

Using ΔV^2 yields a more mathematically compact solution for impulsive thrust and allows for closed-form solutions of the cost functions's gradient. This gradient yielded only minimal performance gains during calculation of the optimal trajectory and therefore was not implemented in the final results; however, the derivation of the gradient is provided to future researchers in Appendix P. Since ΔV is always positive, minimizing the square will minimize the value itself, thus our cost function is

$$J = \frac{\Delta V_1^2 + \Delta V_2^2 + \Delta V_3^2 + \dots + \Delta V_k^2 + \Delta V_F^2}{T_{1,2} + T_{2,3} + T_{3,4} + \dots + T_{k,k+1} + T_F}$$

Impulsive maneuvers and the time-of-flight can be expressed in a wide range of units. Initial investigations into the problem found unacceptably flat cost functions, thus encouraging the proper use of scaling. Experimentation with this cost function showed that it was generally desirable to keep both the sum of the ΔV 's and the total time-of-flight somewhere in the range of 0 to 1. For the numerator, an appropriate scaling term is the continuous ΔV (ΔV_C) required to keep the deputy at the x_{\min} position, which is the optimal place to stay for a continuous thrust scenario. As will be shown in Section 4.6, the minimum continuous thrust ΔV is

$$\Delta V_C = 6x_{\min}n\pi\tilde{T}_T$$

where \tilde{T}_T is the total time-of-flight. Likewise, time-of-flight is conveniently scaled by the chief's orbit period (P):

$$\frac{1}{P} [T_{1,2} + T_{2,3} + T_{3,4} + \dots + T_{k,k+1} + T_F] = \tilde{T}_{1,2} + \tilde{T}_{2,3} + \tilde{T}_{3,4} + \dots + \tilde{T}_{k,k+1} + \tilde{T}_F$$

Combining the scaling of ΔV and time-of-flight, the cost function is now

$$J = \frac{1}{\Delta V_C^2} \frac{[\Delta V_1^2 + \Delta V_2^2 + \Delta V_3^2 + \dots + \Delta V_k^2 + \Delta V_F^2]}{\tilde{T}_{1,2} + \tilde{T}_{2,3} + \tilde{T}_{3,4} + \dots + \tilde{T}_{k,k+1} + \tilde{T}_F}$$

As discussed in Section 3.2, it is desirable to have equations that are not a function of the chief's semi-major axis or μ . To that end, define *specific* delta V, $\Delta\check{V}$ as (see Appendix K.2)

$$\Delta\check{V} = \frac{\Delta V}{n} = \frac{\Delta\check{V}}{2\pi} \quad (17)$$

where $\Delta\check{V}$ is the Euclidean norm of the difference of the relative velocities expressed with time in units of chief orbit period. The equation for the square of $\Delta\check{V}$ is (derivation in Appendix K)

$$\Delta\check{V}_i^2 = \begin{bmatrix} \tilde{x}_{i-1} & \tilde{y}_{i-1} & \tilde{x}_i & \tilde{y}_i & \tilde{x}_{i+1} & \tilde{y}_{i+1} \end{bmatrix} \tilde{R}\tilde{R}' \begin{bmatrix} \tilde{x}_{i-1} \\ \tilde{y}_{i-1} \\ \tilde{x}_i \\ \tilde{y}_i \\ \tilde{x}_{i+1} \\ \tilde{y}_{i+1} \end{bmatrix} \quad (18)$$

with \tilde{R} defined as

$$\tilde{R} = \begin{bmatrix} \frac{4\tilde{S}^- - 6\pi\tilde{T}^-}{8 - 6\pi\tilde{T}^- \tilde{S}^- - 8\tilde{C}^-} & \frac{-2 + 2\tilde{C}^-}{8 - 6\pi\tilde{T}^- \tilde{S}^- - 8\tilde{C}^-} \\ \frac{2 - 2\tilde{C}^-}{8 - 6\pi\tilde{T}^- \tilde{S}^- - 8\tilde{C}^-} & \frac{\tilde{S}^-}{8 - 6\pi\tilde{T}^- \tilde{S}^- - 8\tilde{C}^-} \\ \frac{-4\tilde{S}^+ + 6\pi\tilde{T}^+ \tilde{C}^+}{8 - 6\pi\tilde{T}^+ \tilde{S}^+ - 8\tilde{C}^+} - \frac{4\tilde{S}^- - 6\pi\tilde{T}^- \tilde{C}^-}{8 - 6\pi\tilde{T}^- \tilde{S}^- - 8\tilde{C}^-} & \frac{-14 + 12\pi\tilde{T}^+ \tilde{S}^+ + 14\tilde{C}^+}{8 - 6\pi\tilde{T}^+ \tilde{S}^+ - 8\tilde{C}^+} - \frac{-14 + 12\pi\tilde{T}^- \tilde{S}^- + 14\tilde{C}^-}{8 - 6\pi\tilde{T}^- \tilde{S}^- - 8\tilde{C}^-} \\ \frac{2 - 2\tilde{C}^+}{8 - 6\pi\tilde{T}^+ \tilde{S}^+ - 8\tilde{C}^+} - \frac{2 - 2\tilde{C}^-}{8 - 6\pi\tilde{T}^- \tilde{S}^- - 8\tilde{C}^-} & \frac{-\tilde{S}^+}{8 - 6\pi\tilde{T}^+ \tilde{S}^+ - 8\tilde{C}^+} - \frac{\tilde{S}^-}{8 - 6\pi\tilde{T}^- \tilde{S}^- - 8\tilde{C}^-} \\ \frac{4\tilde{S}^+ - 6\pi\tilde{T}^+}{8 - 6\pi\tilde{T}^+ \tilde{S}^+ - 8\tilde{C}^+} & \frac{2 - 2\tilde{C}^+}{8 - 6\pi\tilde{T}^+ \tilde{S}^+ - 8\tilde{C}^+} \\ \frac{-2 + 2\tilde{C}^+}{8 - 6\pi\tilde{T}^+ \tilde{S}^+ - 8\tilde{C}^+} & \frac{\tilde{S}^+}{8 - 6\pi\tilde{T}^+ \tilde{S}^+ - 8\tilde{C}^+} \end{bmatrix} \quad (19)$$

where

$$\begin{aligned}
\tilde{T}^- &= \tilde{T}_{i-1,i} & \tilde{T}^+ &= \tilde{T}_{i,i+1} \\
\tilde{S}^- &= \sin(2\pi\tilde{T}_{i-1,i}) & \tilde{S}^+ &= \sin(2\pi\tilde{T}_{i,i+1}) \\
\tilde{C}^- &= \cos(2\pi\tilde{T}_{i-1,i}) & \tilde{C}^+ &= \cos(2\pi\tilde{T}_{i,i+1})
\end{aligned}$$

and the positions are (derivation in Appendix B)

$$\begin{aligned}
x_i &= \gamma \cos \alpha \sin \beta + \frac{\tau_x \tau_y \cos \psi_i}{\sqrt{\tau_y^2 \cos^2(\psi_i - \eta) + \tau_x^2 \sin^2(\psi_i - \eta)}} \\
y_i &= \gamma \sin \alpha \sin \beta + \frac{\tau_x \tau_y \sin \psi_i}{\sqrt{\tau_y^2 \cos^2(\psi_i - \eta) + \tau_x^2 \sin^2(\psi_i - \eta)}}
\end{aligned}$$

Noting that the continuous thrust scaling term as a specific ΔV is

$$\Delta \check{V}_C^2 = \frac{\Delta V_C^2}{n^2} = 36x_{\min}^2 \pi^2 \tilde{T}_T^2$$

This results in a cost function for the problem posed herein of

$$J = \frac{1}{36x_{\min}^2 \pi^2 \tilde{T}_T^2} \frac{[\Delta \check{V}_1^2 + \Delta \check{V}_2^2 + \Delta \check{V}_3^2 + \dots + \Delta \check{V}_k^2 + \Delta \check{V}_F^2]}{\tilde{T}_{1,2} + \tilde{T}_{2,3} + \tilde{T}_{3,4} + \dots + \tilde{T}_{k,k+1} + \tilde{T}_F} \quad (20)$$

3.4 Interior Thrust Points

As a simplifying assumption, all thrusting is required to occur on the lobe boundary. This removes a degree of freedom from the problem and thus only a single coordinate (ψ) is required to specify a thrust point. In addition to being a natural assumption to start with, it turns out that the cost function is ill-posed to handle interior points. Let's assume a minimum-cost single leg trajectory is found. Without additional constraints on the lower bound of the time-of-flight for each leg or a minimum $\Delta \check{V}$ magnitude, there is nothing to prevent the algorithm from simply parsing that single leg solution into as many "legs" as are requested. Application of those additional constraints or a reposed cost function that is more favorable to interior points is left to future researchers.

3.5 Units

The non-dimensional time, \tilde{T} , is of course unitless and more importantly, not tied to a particular orbital radius. A similar disentanglement between ΔV and orbital radius is made possible with specific ΔV and has the following units

$$\Delta\check{V} = \frac{\Delta V}{n} = \frac{\frac{\text{length}}{\text{time}}}{\frac{1}{\text{time}}} = \mathbf{length}$$

Likewise the units of relative velocity when time is expressed in units of chief orbital period are

$$\dot{(\cdot)} = \frac{2\pi}{n}(\dot{\cdot}) = \frac{\frac{\text{length}}{\text{time}}}{\frac{1}{\text{time}}} = \mathbf{length}$$

and the relative accelerations

$$\ddot{(\cdot)} = \frac{4\pi^2}{n^2}(\ddot{\cdot}) = \frac{\frac{\text{length}}{\text{time}^2}}{\frac{1}{\text{time}^2}} = \mathbf{length}$$

Since $\sum \Delta\check{V}^2$ are scaled by $\Delta\check{V}_C^2$, the numerator of J is unitless. Dividing by the unitless total time-of-flight we note that

$$J = \mathbf{unitless}$$

as desired.

3.6 The Constraint

From a mission planner's standpoint, the only constraint on the deputy satellite's motion is that it stay within the prescribed lobe. While there are several methods to pose this constraint, one relatively simple way is to force the time-of-flight to be smaller than or equal to some maximum time-of-flight. This maximum time-of-flight is naturally defined as as the largest time-of-flight for which the deputy's entire trajectory remains inside the lobe. If two positions are chosen in the relative frame along

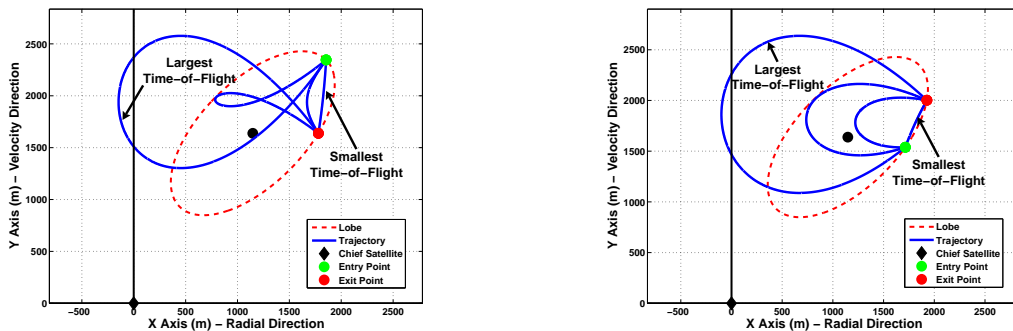


Figure 14: Notional Time-of-Flight Comparisons

with a time-of-flight between them, the relative velocities can be found via Equations (13) and (14). An appropriately small time-of-flight produces a trajectory that closely approximates a straight line between the two points and has a large magnitude relative velocity. As the time-of-flight is increased, the trajectory exhibits larger and larger loops that may or may not cross back over themselves (teardrop maneuvers). As demonstrated in Figure 14, there is a maximum time-of-flight after which any larger time-of-flight creates a trajectory that partially leaves the constraint lobe. Any time-of-flight smaller than this maximum will satisfy the mission planner’s constraint. Thus the constraint is formulated as

$$\tilde{T}_{i,i+1} \leq \tilde{T}_{\max_{i,i+1}}(\psi_1, \psi_2) \quad (21)$$

The maximum time-of-flight between any two points is precomputable, and a surface is easily generated for a specific lobe size and shape (example Figure 15). Interpolating between points is a very effective way to calculate the constraint during optimization searches. Note that unless otherwise stated, all constraint surfaces in this document use the same normalized colorbar. Thus green in one figure is the same value of \tilde{T}_{\max} as green in another figure.

All constraint surfaces have a valley of $\tilde{T}_{\max} = 0$, the set of ψ ’s from which the deputy cannot start and end without leaving the lobe no matter how small the

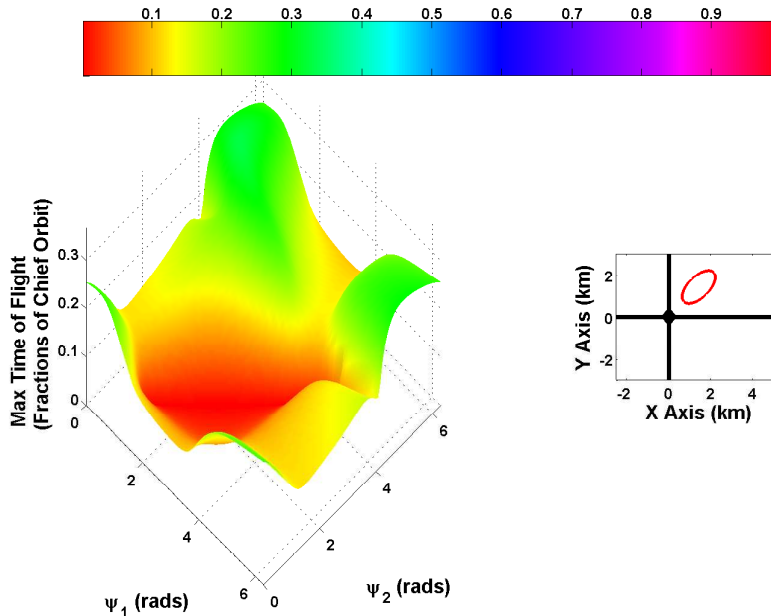


Figure 15: Maximum Time-of-Flight ($\alpha = 45^\circ, \gamma = 2 \text{ km}, \tau_x = 1 \text{ km}, \tau_y = 0.5 \text{ km}$)

time-of-flight. These points are located on the side of the lobe closest to the \hat{Y} axis (see Figure 16). Since our lobe is a closed concave shape, we can always draw a straight line between any two points that stays completely within the lobe (and as noted previously, as $\tilde{T}_{\max} \rightarrow 0$ the trajectory becomes a straight line), therefore this valley will always be along the line $\psi_1 = \psi_2$. Lobes that do not intersect the \hat{Y} axis will also have a peak formation. Note that this surface repeats in both the ψ_1 and ψ_2 directions since the angle is modulo 2π and thus the four peaks in Figure 15 are in fact a single peak.

3.6.1 Calculation of \tilde{T}_{\max} . Unfortunately, no closed-form solution for \tilde{T}_{\max} is available, prompting a numerical solution. Two methods of calculation were explored for this research. The most robust and most computationally expensive method is to increment time-of-flight and check the resulting trajectory, converging on a solution when the time-of-flight produces a trajectory that leaves the lobe. In practice, the midpoint of an upper and lower bound is used for the trajectory check. If the trajectory stays within the lobe, the midpoint is now the new lower bound while it becomes

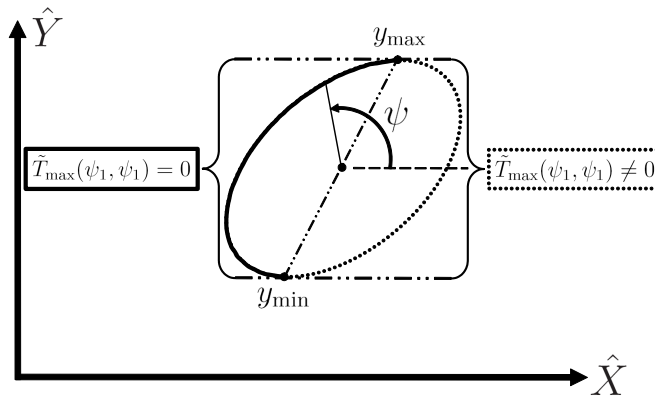


Figure 16: Points of Zero Maximum Time-of-Flight

the new upper bound if it violates the boundary. The flowchart of this process is found in Figure 17.

The second numerical technique involves identifying two conditions of a trajectory which has a single point of tangency with the lobe. The first is that the point of tangency (ψ_T) occurs on the lobe boundary:

$$r(\psi_T) - \frac{\tau_x \tau_y}{\sqrt{\tau_y^2 \cos^2(\psi_T - \eta) + \tau_x^2 \sin^2(\psi_T - \eta)}} = 0$$

and the second that the relative velocity of trajectory at ψ_T is tangent to the lobe:

$$\dot{x}_T \cos \psi_T + \dot{y}_T \sin \psi_T = 0$$

These two nonlinear equations must be solved numerically, but algorithms such as FSOLVE in MATLAB[®] do the job quickly and efficiently. This method was found to be less robust, however, when the point of tangency occurred at or near the beginning or end point of the trajectory. Because accuracy was valued over speed for this particular application, the first method was chosen to produce the constraint surface.

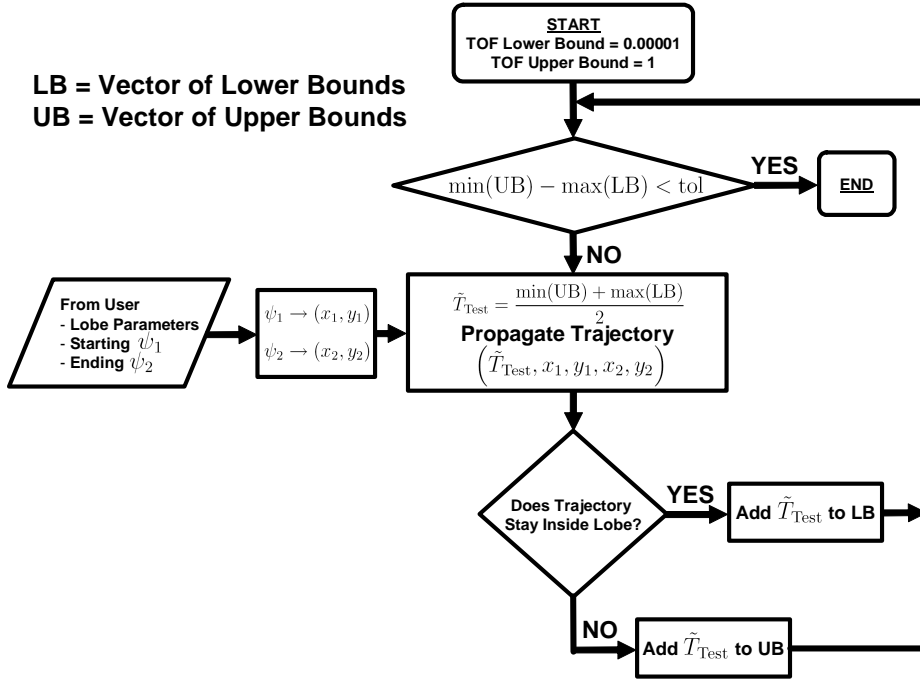


Figure 17: Flowchart for Finding \tilde{T}_{\max}

Definition and calculation method in hand, we turn next to several properties of the constraint surface that will narrow the relevant lobe parameter space and yield more efficient calculations of the constraint surface.

3.6.2 Invariance of the Constraint Surface to y_L . Under the CW assumptions, it can be shown that the constraint surface is invariant to the y coordinate of the lobe center (y_L). The first indication of this is found in the original differential equations (Equation (7)), none of which are functions of the y coordinate. However, clearer proof is found by examining the initial and final relative velocity equations

(Equations (13) and (14)). Let $D = 8 - 6\pi\tilde{T} \sin(2\pi\tilde{T}) - 8 \cos(2\pi\tilde{T})$, then:

$$\begin{aligned}\dot{\tilde{x}}_o &= f_o(\tilde{x}_o, \tilde{x}_f) + \frac{2 - 2 \cos(2\pi\tilde{T})}{D} \tilde{y}_o + \frac{-2 + 2 \cos(2\pi\tilde{T})}{D} \tilde{y}_f \\ &= f_o(\tilde{x}_o, \tilde{x}_f) - \frac{2 - 2 \cos(2\pi\tilde{T})}{D} (\tilde{y}_f - \tilde{y}_o) \\ \dot{\tilde{y}}_o &= g_o(\tilde{x}_o, \tilde{x}_f) - \frac{\sin(2\pi\tilde{T})}{D} \tilde{y}_o + \frac{\sin(2\pi\tilde{T})}{D} \tilde{y}_f \\ &= g_o(\tilde{x}_o, \tilde{x}_f) - \frac{-\sin(2\pi\tilde{T})}{D} (\tilde{y}_f - \tilde{y}_o)\end{aligned}$$

Likewise,

$$\begin{aligned}\dot{\tilde{x}}_f &= f_f(\tilde{x}_o, \tilde{x}_f) - \frac{2 \cos(2\pi\tilde{T})}{D} (\tilde{y}_f - \tilde{y}_o) \\ \dot{\tilde{y}}_f &= g_f(\tilde{x}_o, \tilde{x}_f) + \frac{\sin(2\pi\tilde{T})}{D} (\tilde{y}_f - \tilde{y}_o)\end{aligned}$$

We see that the relative velocities are functions of $\Delta\tilde{y}$ only and not the absolute positions causing the constraint surface to remain unchanged as it slides up or down a line parallel to the \hat{Y} axis (see Figure 18). This is convenient for users desiring to precompute the constraint.

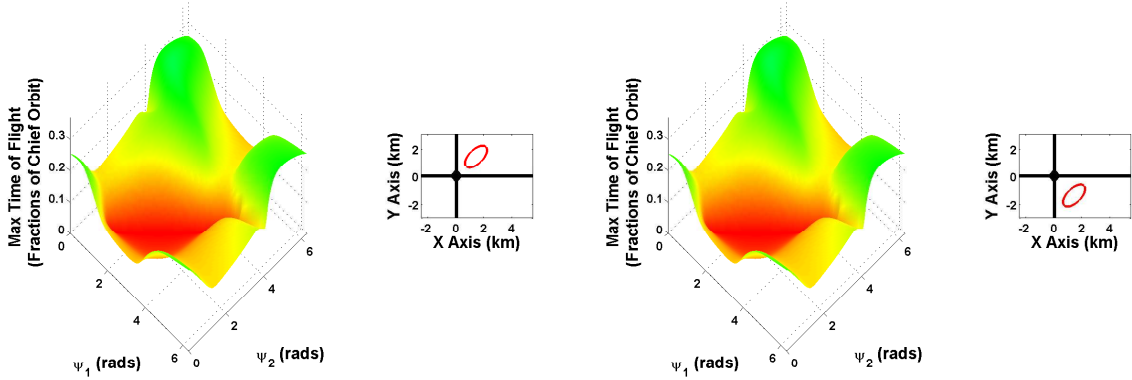


Figure 18: Invariance of the Constraint Surface to y_L

3.6.3 Symmetries Between Constraint Surfaces in the Right and Left Hand Planes. In Section 3.2.3, the equations of motion were shown to be odd functions

meaning that every trajectory has a twin trajectory in the opposite quadrant that is rotated by π (as, for example, Figure 19). Taking this concept a step further, if we project our lobe into the opposite quadrant as well, we find that the maximum time-of-flight (\tilde{T}_{\max}) of a trajectory between ψ_1 and ψ_2 in the 1st quadrant is also the maximum time-of-flight between $\psi_1 + \pi$ and $\psi_2 + \pi$ in the 3rd quadrant.

$$\underbrace{\tilde{T}_{\max}(\psi_1, \psi_2)}_{\text{Lobe 1}} = \underbrace{\tilde{T}_{\max}(\psi_1 + \pi, \psi_2 + \pi)}_{\text{Lobe 2}}$$

It is the symmetry of the lobe that allows this transformation to occur (i.e., our

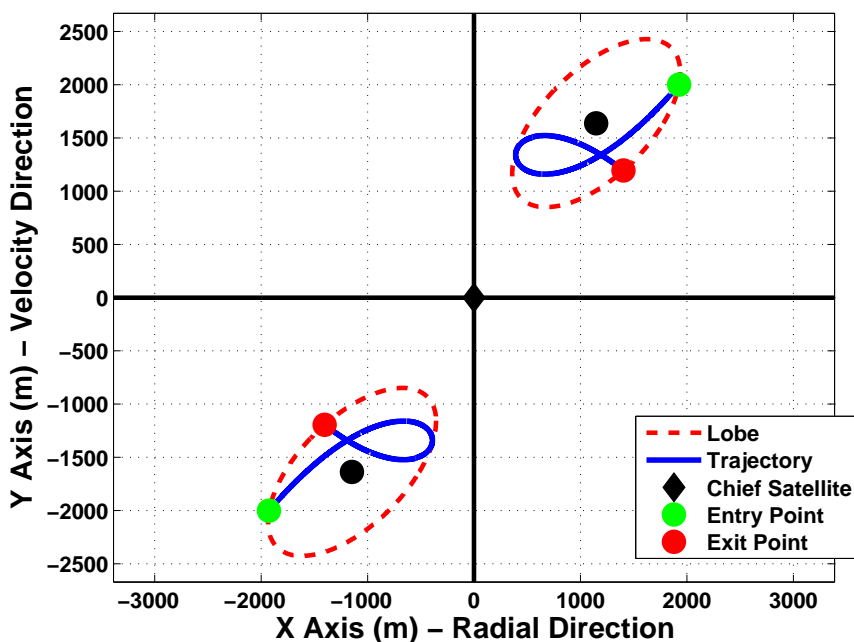


Figure 19: Symmetric Lobes and Reflective Trajectories

mirror ellipse orientation is $\eta^- = \eta + \pi$). The two trajectories are negatives of each other:

$$\begin{aligned}\tilde{x}(\tilde{t})^- &= -\tilde{x}(\tilde{t}) \\ \tilde{y}(\tilde{t})^- &= -\tilde{y}(\tilde{t}) \\ \text{for } 0 < \tilde{t} < \tilde{T}_{\max}\end{aligned}$$

To prove this, observe that the second lobe is located at $\alpha^- = \alpha + \pi$. Then

$$\begin{aligned}\tilde{x}^- &= \gamma \cos(\alpha + \pi) \sin \beta + \frac{\tau_x \tau_y \cos(\psi_i + \pi)}{\sqrt{\tau_y^2 \cos^2(\psi_i - [\eta + \pi]) + \tau_x^2 \sin^2(\psi_i - [\eta + \pi])}} \\ \tilde{y}^- &= \gamma \sin(\alpha + \pi) \sin \beta + \frac{\tau_x \tau_y \sin(\psi_i + \pi)}{\sqrt{\tau_y^2 \cos^2(\psi_i - [\eta + \pi]) + \tau_x^2 \sin^2(\psi_i - [\eta + \pi])}}\end{aligned}$$

Noting that

$$\begin{aligned}\sin(\psi_i + \pi) &= -\sin \psi_i \\ \cos(\psi_i + \pi) &= -\cos \psi_i \\ \sin^2(\psi_i - [\eta + \pi]) &= \sin^2(\psi_i - \eta) \\ \cos^2(\psi_i - [\eta + \pi]) &= \cos^2(\psi_i - \eta)\end{aligned}$$

then

$$\begin{aligned}\tilde{x}^- &= -\gamma \cos \alpha \sin \beta - \frac{\tau_x \tau_y \cos \psi_i}{\sqrt{\tau_y^2 \cos^2(\psi_i - \eta) + \tau_x^2 \sin^2(\psi_i - \eta)}} = -\tilde{x} \\ \tilde{y}^- &= -\gamma \sin \alpha \sin \beta - \frac{\tau_x \tau_y \sin \psi_i}{\sqrt{\tau_y^2 \cos^2(\psi_i - \eta) + \tau_x^2 \sin^2(\psi_i - \eta)}} = -\tilde{y}\end{aligned}$$

Thus we see that transforming the constraint surface from the 1st to the 3rd quadrant involves a shift of the starting and ending ψ by π radians. Applying the invariance to the y_L discussed in Section 3.6.2, we can translate the negative lobe into the 2nd quadrant (illustrated in Figure 20). So, for the computational price of one lobe we get a family of lobes along lines parallel to the \hat{Y} axis in both the right and left hand planes (Figure 21). Lobes are therefore functions only of the x coordinate of their centers (x_L), size (τ_x, τ_y) , and orientation (η). The ΔV calculations are also functions of Δy as they are derived directly from the relative velocity equations. Thus, with the constraint surfaces and ΔV calculations being invariant to being placed in either the right or left hand planes (same distance from the \hat{Y} axis) and identical in the

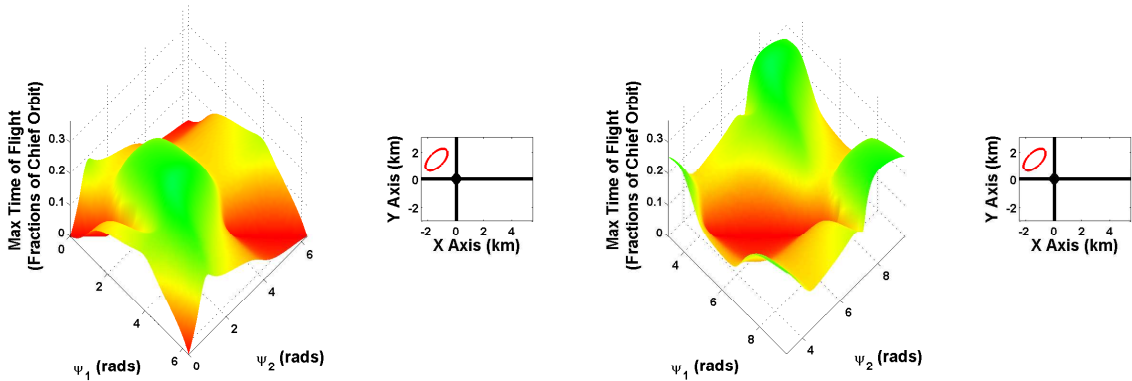


Figure 20: Equivalent Constraint Surfaces ($\alpha = 135^\circ, \gamma = 2 \text{ km}, \tau_x = 1 \text{ km}, \tau_y = 0.5 \text{ km}$)

upper and lower half planes, we can conclude that optimal trajectories found in lobes in the 1st quadrant are indicative of lobes in any other quadrant. We will therefore concentrate solely on 1st quadrant lobes in the results chapter, as these results can easily be mapped to any quadrant.

3.6.4 Lobes Symmetric About Their Horizontal Axis. Lobes that are symmetric about their horizontal axes have an additional symmetry in their constraint surface that can halve the needed computation time. For these lobes,

$$\tilde{T}_{\max}(\psi_1, 2\pi - \psi_2) = \tilde{T}_{\max}(\psi_2, 2\pi - \psi_1)$$

An example is provided in Figure 22.

3.6.5 Lobes that Intersect the \hat{Y} Axis. Section 3.2.2 demonstrated that the \hat{Y} axis is the set of equilibrium points for the linearized equations of motion (chief in a circular orbit). We expect that lobes containing the \hat{Y} axis will have unique properties. An infinite number of 2x1 closed relative orbit ellipses can be placed within lobes that have two points of intersection with the \hat{Y} , and certain combinations of η and x_L allow a single closed relative orbit to be tangent to both points of intersection. This provides an opportunity to start and end at either the upper or lower \hat{Y} axis

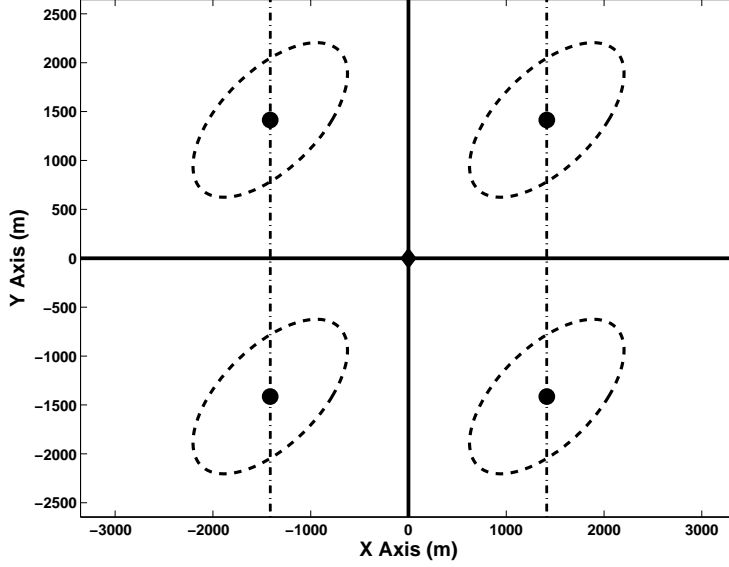


Figure 21: Equivalent Lobes

intersection point and come back to the same point in one full chief orbit. It also provides a trajectory that in the absence of perturbations and ignoring linearization error can be maintained with zero fuel. Note that the relative velocity (Equations (13) and (14)) is undefined at $\tilde{T} = 1$, a singularity of which we must be cognizant when evaluating these orbits. If the upper lobe intersection point is ψ_U and the lower intersection ψ_L , then there are four regions about which there is an opportunity for a trajectory that is or nearly is one full chief orbit; they are:

$$(1) \ \psi_U, \psi_U \tag{22a}$$

$$(2) \ \psi_U, \psi_L \tag{22b}$$

$$(3) \ \psi_L, \psi_U \tag{22c}$$

$$(4) \ \psi_L, \psi_L \tag{22d}$$

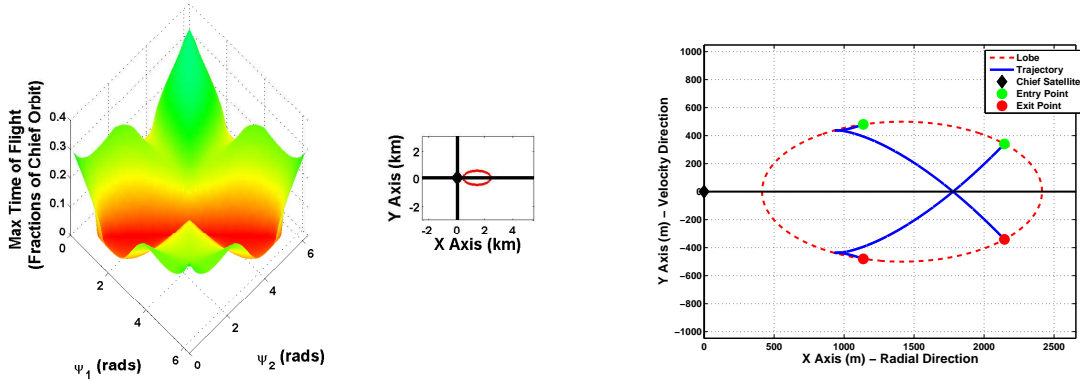


Figure 22: Lobe Symmetric About Horizontal Axis ($\alpha = 0^\circ, \gamma = 1.414 \text{ km}, \tau_x = 1 \text{ km}, \tau_y = 0.5 \text{ km}, \eta = 0^\circ$)

Pairs (1) and (4) yield 2x1 closed relative orbit ellipses (Figure 23(a)) that have a maximum possible semi-major axis of (derivation in Appendix M.1)

$$\rho < \frac{r(\psi_U) \sin \psi_U - r(\psi_L) \sin \psi_L}{4} \quad (23)$$

Pairs (2) and (3) represent drifting relative orbits with small ρ and a values that are nearly contained within the lobe over one chief orbit period (see Figure 23(b)). The constraint surface for lobes that do not intersect the \hat{Y} axis have a single peak

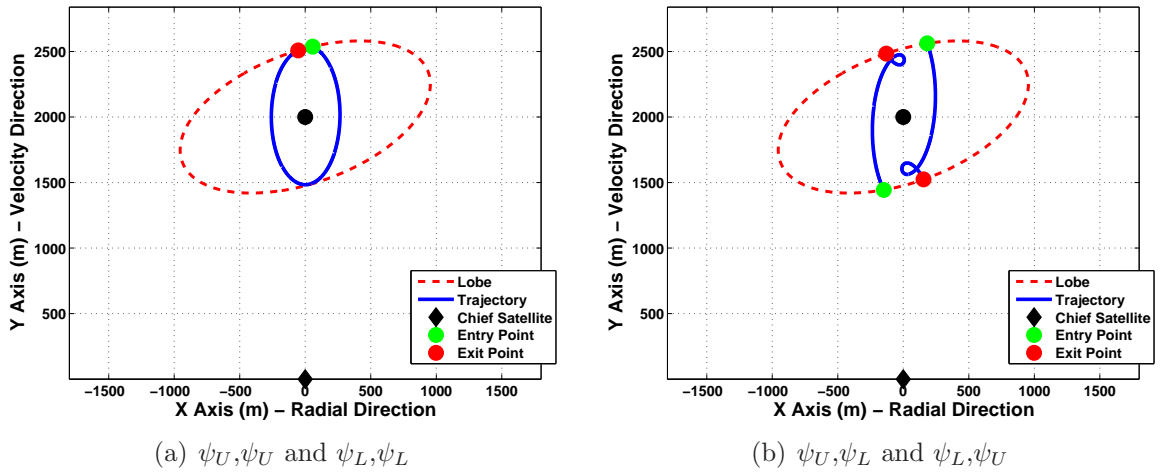


Figure 23: Trajectories of Nearly One Chief Orbit Period

formation. As the lobe passes through the \hat{Y} axis, this single peak splits into four

peaks attached to the four conditions in Equation (22). Peaks surrounding angle pairs (1) and (4) will slide along the line $\psi_1 = \psi_2$ while (2) and (3) will slide along $2\pi - \psi_1 = \psi_2$, all corresponding to the ψ 's of lobe's intersection with the \hat{Y} axis. To illustrate this, Figure 24 displays the constraint surface and peak location for the following lobe:

$$\alpha = 90^\circ \quad \gamma_{XY} = 2 \text{ km} \quad \tau_x = 1 \text{ km} \quad \tau_y = 0.5 \text{ km} \quad \eta = 20^\circ \quad (24)$$

thus the center is located at $x_L = 0$ and the intersection points are in the neighborhood of

$$\psi_U \approx \frac{\pi}{2} \quad \psi_L \approx \frac{3\pi}{2}$$

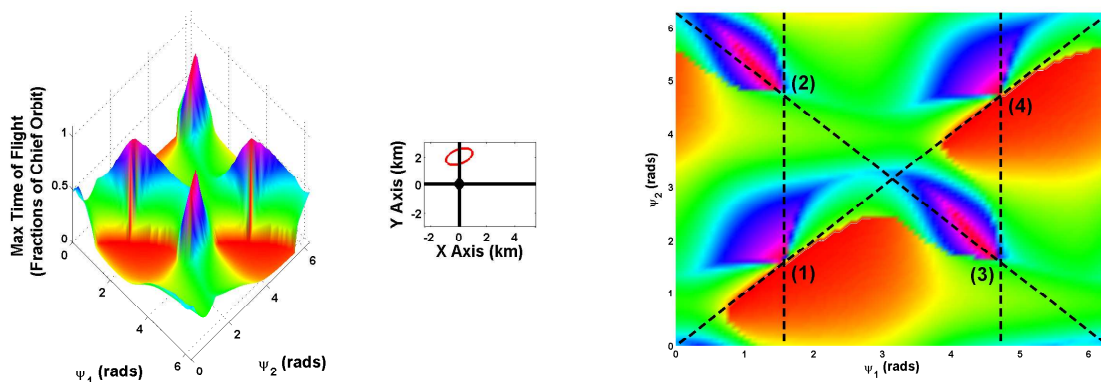


Figure 24: Lobe Intersection of the \hat{Y} Axis ($\alpha = 90^\circ, \gamma = 2 \text{ km}, \tau_x = 1 \text{ km}, \tau_y = 0.5 \text{ km}, \eta = 20^\circ$)

3.6.6 Sensitivity of the Constraint Surface to Lobe Size. Larger lobes provide more drifting room for deputy satellite trajectories and not surprisingly result in valid trajectories that have a larger time-of-flight. The overall shape of the lobe changes little while the peak rises rather substantially with larger τ_x and τ_y (Figure 25). Note that the peak time-of-flight does not increase linearly with lobe size. In our example we see a 50% increase by doubling τ_x, τ_y and a 200% increase by tripling them. Since

the lobe shapes do not change appreciably, we expect that the optimal trajectories will be similar albeit with a larger total time-of-flight. This is shown in Section 5.6.

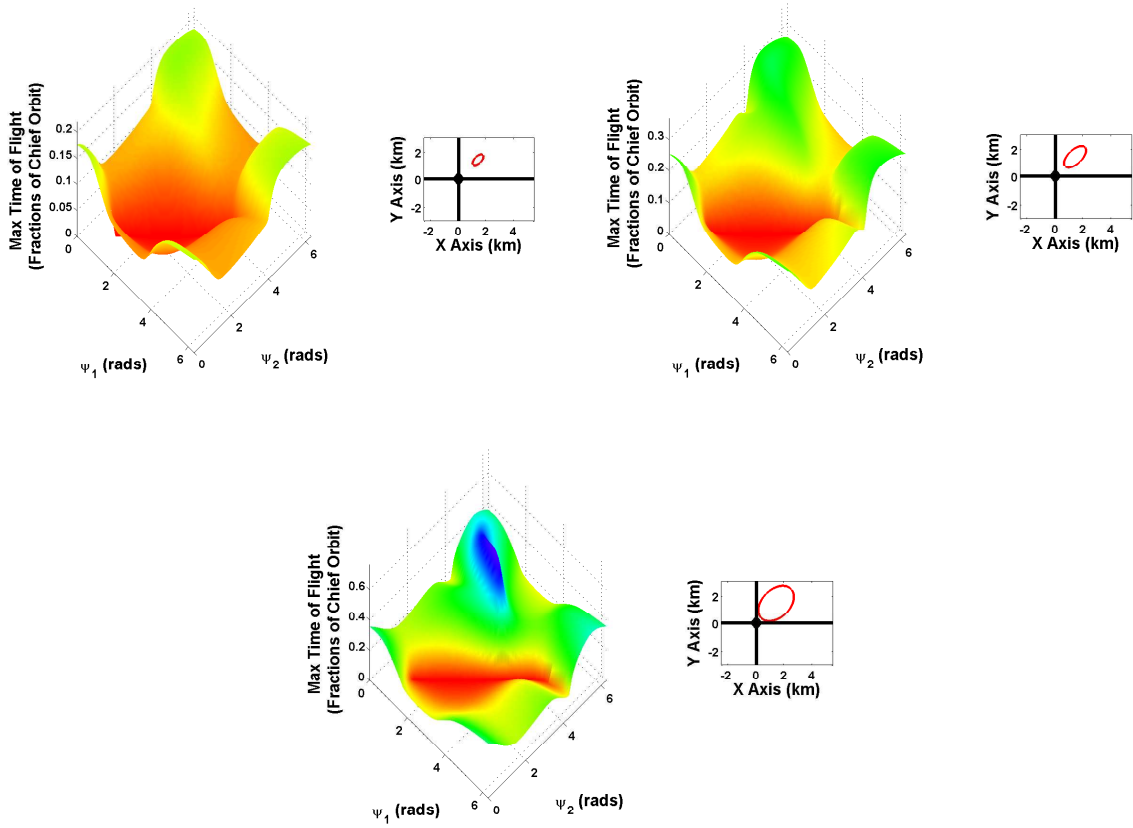


Figure 25: Constraint Surfaces for Varying Size Lobes ($\alpha = 45^\circ, \gamma = 2 \text{ km}, \eta = 45^\circ$)

3.6.7 Sensitivity of the Constraint Surface to x_L . Increasing the \hat{X} coordinate of the lobe center (x_L) also has an effect on the constraint surface. Recall that a nonzero a value represents a difference in the chief and deputy's semi-major axis, resulting in drifting orbits. The larger this difference, the greater the difference in orbital period and the bigger the relative velocities. Thus, even though trajectories themselves appear similar, the relative velocities are larger in lobes further from the \hat{Y} axis, causing a decrease in the maximum time-of-flight peak (Figure 26). Of particular note, it appears that doubling x_L has the same reducing effect on the constraint

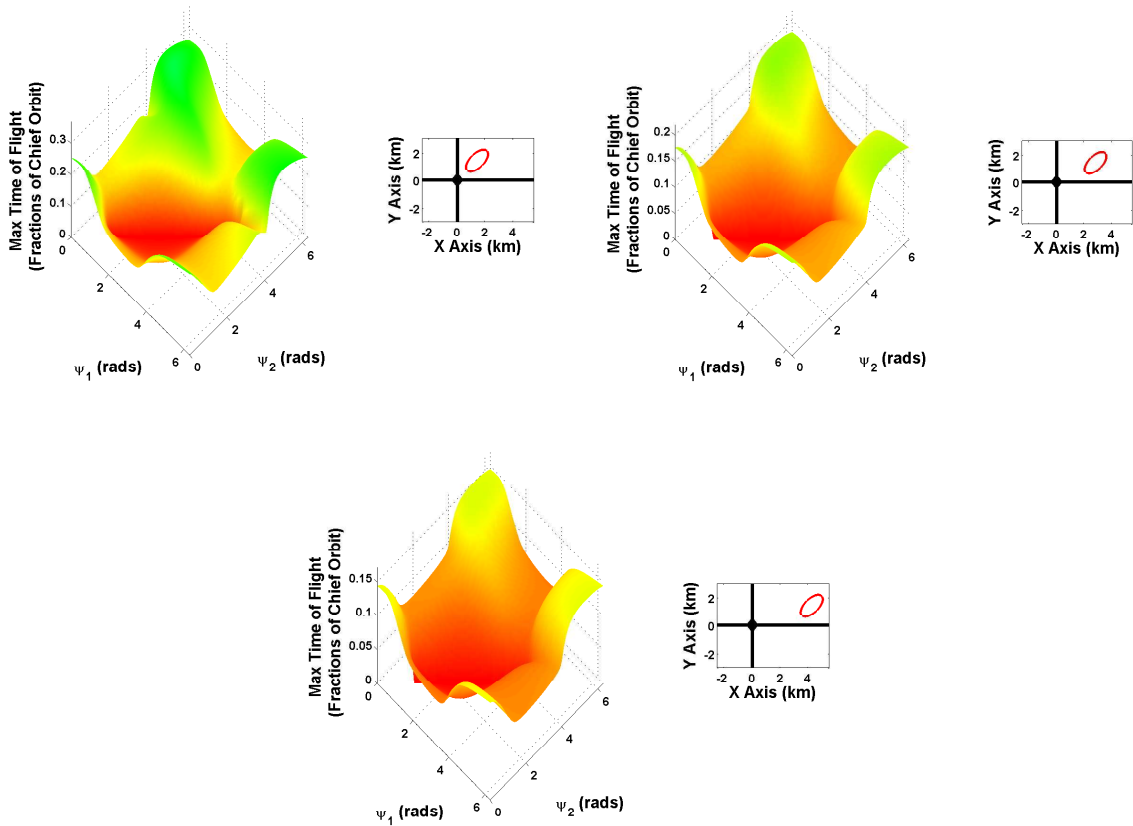


Figure 26: Constraint Surfaces for Varying Distances from the \hat{Y} Axis ($\tau_x = 1$ km, $\tau_y = 0.5$ km, $\eta = 45^\circ$)

surface as halving the size of the lobe. Further study is warranted and will be left to future researchers.

3.6.8 The Constraint Surface for Elliptical Chief Orbits. Precomputing the constraint surface for elliptical chief orbits is similar to the circular case with two notable exceptions. First, the elliptical relative equations of motion (Equation (6)) are functions of true anomaly (ν) and thus constraint surfaces are only valid for a specific initial ν_o . This means that, at the end of a leg, a new constraint surface with a new ν_o must be used to find \tilde{T}_{\max} for the next leg. For a given lobe and eccentricity, the chief's orbit must be discretized with appropriate resolution and a library of constraint surfaces stored in order to find multiple leg trajectories. If only a single leg is needed, a single constraint surface can be used.

Second, unlike the circular chief case, there is no closed-form solution for the relative velocities. Several researchers (see Section 2.5 of the literature review) have proposed high fidelity models for finding relative velocities for elliptical chiefs, however, a very simple and robust method was used to calculate relative velocities in this research. Using final position error as the cost function, MATLAB's[®] FSOLVE algorithm can find the relative velocity given an initial/final position and a time-of-flight with acceptable accuracy and speed.

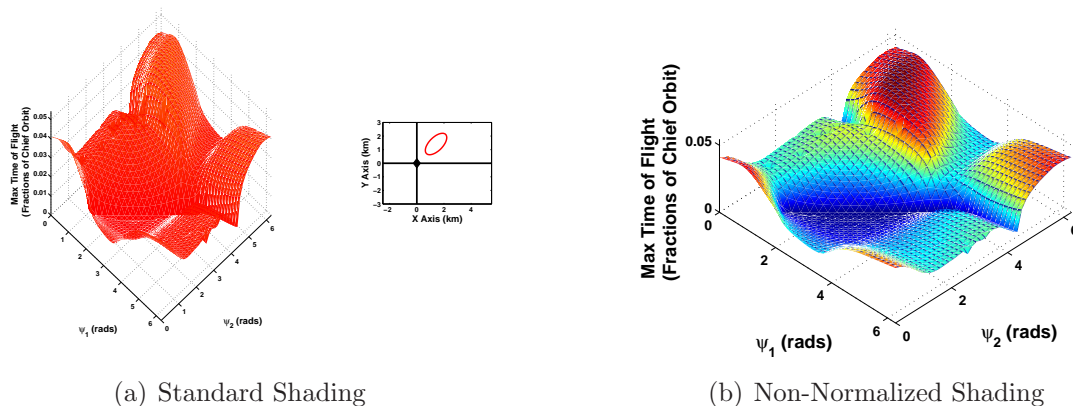


Figure 27: Elliptical Chief Constraint Surface $e = 0.7, \nu_o = 0$ rad

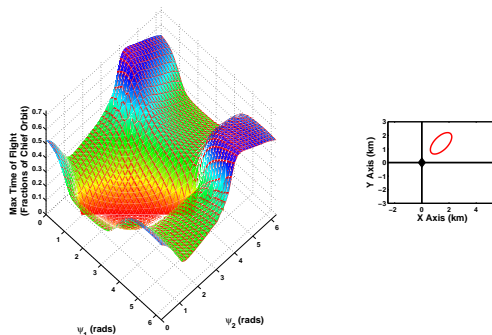


Figure 28: Elliptical Chief Constraint Surface $e = 0.7, \nu_o = \pi$ rad

Notice the striking difference between the constraint surface magnitudes at perigee (Figure 27) and apogee (Figure 28). This is due to the corresponding difference in relative velocity magnitudes at apogee and perigee. At apogee, the inertial and relative velocities have a smaller magnitude than at perigee and therefore pass

between any two points considerably more slowly, resulting in a larger \tilde{T}_{\max} . This phenomena must factor into the overall hovering strategy since more burns with higher ΔV 's will be required for hovering at perigee as opposed to apogee.

3.6.9 Other Constraints. Certainly there are other attractive constraints that could be applied to the cost function in order to coax even more desirable trajectories. Perhaps the first that comes to mind is an equality constraint or minimum constraint on total time-of-flight in order to satisfy a mission objective, such additions should be avoided. Any constraint added to an optimal control problem risks obscuring a candidate extremal point. Mission planners can specify the number of legs and can control if the trajectory closes back on itself (repeating hover orbit condition), both of which have the potential to increase time-of-flight without imposing additional constraints. The repeating hover orbit in particular has the potential to satisfy any desired hover time by traversing the same trajectory over and over again until the minimum time-of-flight is met.

3.6.10 Summary. Examination of the constraint surface provides key insight into the behavior of the solution as lobe parameters change. Some are intuitive such as larger lobes yield larger maximum time-of-flight and thus have the potential to lower the cost function. Others are less intuitive such as how changes in orientation angle which shift the peak location will affect the solution. These will be explored in Chapter V. Now that we have derived the equations of motion, developed a cost function, and bounded the problem with a constraint, we can start formulating a trajectory planner to meet our stated objectives. The ultimate goal is to produce an algorithm that outputs a set of impulsive thrust locations and the time-of-flight between them. This is done in the next chapter.

IV. The Optimal Trajectory

The optimal trajectory will be the output of a nonlinear programming algorithm that searches for the lowest value of the cost function while staying within the maximum time-of-flight constraint. We seek a method in which the user provides the number of legs (k), entry/exit conditions, and lobe position, orientation, and shape, after which the algorithm provides the angular positions of the impulsive thrust locations and the time-of-flight between them:

Given	Output
k (Number of legs)	$\psi_1, \psi_2, \dots, \psi_{k+1}$
Entry Condition	$\tilde{T}_{1,2}, \tilde{T}_{2,3}, \dots, \tilde{T}_{k,k+1}$
Exit Condition	
α, β, γ	
τ_x, τ_y, η, h	

These outputs can easily be transformed into impulsive thrust vectors and thrust times. The propagated trajectories shown in the results chapter are calculated by taking the final velocity of the previous leg (or the entry conditions for the first leg), adding the impulsive thrust vector and then propagating until the next thrust time. In this manner, we can ascertain the error incurred by using a reduced order model for the optimization and then applying it to a higher fidelity truth model.

Since motion in the $\hat{X}\hat{Y}$ plane and \hat{Z} direction decouple, the optimal trajectories for both will be found separately. Optimization in the $\hat{X}\hat{Y}$ plane produces a trajectory and total time-of-flight (\tilde{T}_T). This total time-of-flight is then used to find a closed-form optimal trajectory for motion in the \hat{Z} direction. The two motions can then be combined for a final trajectory. We start with optimization in the $\hat{X}\hat{Y}$ plane.

4.1 The Optimal Trajectory in the $\hat{X}\hat{Y}$ Plane

The cost function is Equation (20) from Section 3.3:

$$J = \frac{1}{36x_{\min}^2\pi^2\tilde{T}_T^2} \left[\Delta\check{V}_1^2 + \Delta\check{V}_2^2 + \Delta\check{V}_3^2 + \dots + \Delta\check{V}_k^2 + \Delta\check{V}_F^2 \right] \\ \tilde{T}_{1,2} + \tilde{T}_{2,3} + \tilde{T}_{3,4} + \dots + \tilde{T}_{k,k+1} + \tilde{T}_F$$

where $\Delta\check{V}$ is specific ΔV and has no dependence on the chief's semi-major axis or μ . In an effort to keep the numerator close to unity, the $\Delta\check{V}$'s are scaled by the amount of specific ΔV required to remain at the minimum x coordinate of the lobe boundary (x_{\min}). If the lobe intersects the \hat{Y} axis ($x_{\min} = 0$), an alternative optimal trajectory is employed and is discussed in Section 5.1. The constraint on each time-of-flight is (from Section 3.6)

$$\tilde{T}_{i,i+1} \leq \tilde{T}_{\max_{i,i+1}}(\psi_1, \psi_2)$$

where \tilde{T}_{\max} is the maximum time-of-flight that keeps the entire trajectory within the lobe. There are no constraints on the angular positions (ψ) unless specified by the entry/exit conditions which are discussed later in this chapter. The cost function is minimized via the FMINCON nonlinear programming routine in MATLAB[®] which is specifically designed for nonlinear cost functions that have nonlinear constraints. The pseudocode for this routine is found in Appendix Q.

4.2 The Optimal Trajectory in the \hat{Z} Direction

Recall that motion in the \hat{Z} direction is a harmonic oscillator with a closed-form solution of (Equation (9), Section 3.2)

$$\tilde{z}(\tilde{t}) = \tilde{z}_{\max} \cos(2\pi\tilde{t} + \phi) \quad (25)$$

where

$$\tilde{z}_{\max} = \sqrt{\left(\frac{\dot{\tilde{z}}_o}{2\pi}\right)^2 + \tilde{z}_o^2} \quad \phi = \tan^{-1}\left(-\frac{\dot{\tilde{z}}_o}{2\pi\tilde{z}_o}\right)$$

It can be shown (derivation in Appendix J) that the maximum time-of-flight in which the deputy stays between a minimum (\tilde{z}_{\min}) and maximum (\tilde{z}_{\max}) \hat{Z} coordinate is

$$\tilde{T}_{\max} = \frac{1}{\pi} \cos^{-1} \left(\frac{\tilde{z}_{\min}}{\tilde{z}_{\max}} \right) \quad (26)$$

The \cos^{-1} function has a domain of $0 < \frac{\tilde{z}_{\min}}{\tilde{z}_{\max}} < 1$ and this fits well with our definition of the elliptical cylinder. Motion in the \hat{Z} direction is caused by differences in the chief and deputy's inclinations and/or longitude of the ascending node. As intuition and Equation (25) show us, the period of the \hat{Z} oscillation is 2π and is centered about the chief's orbit plane. Half of the chief's period is spent above the orbit plane and half below. Thus, any \hat{Z} period greater than 0.5 would indicate that the deputy has passed through the chief's orbit plane. Lobes that include the chief's orbit plane will have $\tilde{z}_{\min}/\tilde{z}_{\max}$ ratios that are less than zero (change in sign between \tilde{z}_{\min} and \tilde{z}_{\max}) and ill-defined lobes are greater than 1 ($|\tilde{z}_{\min}|$ is larger than $|\tilde{z}_{\max}|$). Therefore, either the lobe intersects the orbit plane, in which case the optimal solution is to stay in the orbit plane with no \hat{Z} motion, or the lobe is improperly defined. We can expect only ratios between 0 and 1 and \tilde{T}_{\max} 's between 0 and 0.5 chief orbits.

A harmonic oscillator affords a single degree-of-freedom to optimize the problem. The period of the \hat{Z} oscillation (\tilde{P}_z) is chosen as the optimization parameter based on the following argument. Assume the $\hat{X}\hat{Y}$ plane optimization has yielded a total time-of-flight (\tilde{T}_T). We desire the deputy to stay between \tilde{z}_{\min} and \tilde{z}_{\max} for the same amount of time. The minimum number of burns required is

$$\# \text{ Burns} = \left\lfloor \frac{\tilde{T}_T}{\tilde{P}_z} \right\rfloor$$

where $\lfloor \cdot \rfloor$ represents the floor function. It can be shown that the ΔV required for each of these burns is (derivation in Appendix K.3)

$$\Delta \check{V}_i = \frac{\Delta V_i}{n} = 2\tilde{z}_{\min} \tan \left(\pi \tilde{P}_z \right)$$

Thus the total ΔV required is

$$\begin{aligned}\Delta\check{V}_Z &= 2 \left[\frac{\tilde{T}_T}{\tilde{P}_z} \right] \tilde{z}_{\min} \tan \left(\pi \tilde{P}_z \right) \\ &= 2\tilde{z}_{\min} (k_z - 1) \tan \left(\frac{\pi \tilde{T}_T}{k_z} \right)\end{aligned}\tag{27}$$

where k_z is the number of legs in the \hat{Z} direction. Note that $\Delta\check{V}_Z$ is inversely proportional to \tilde{P}_z ; thus we desire the largest possible period (or fewest number of bounces, k_z) without exceeding the maximum period defined by Equation (26). An example problem is found in Figure 29. Assume that the $\hat{X}\hat{Y}$ optimization has yielded a total time-of-flight of $\tilde{T}_T = 0.45$, that $\tilde{z}_{\min} = 1$, and $\tilde{z}_{\max} = 1.25$. The period of the \hat{Z} motion is therefore constrained to be less than

$$\tilde{T}_{\max} = \frac{1}{\pi} \cos^{-1}(0.8) \approx 0.2$$

Referencing Figure 29, the smallest possible total $\Delta\check{V}_Z$ occurs at

$$\tilde{P}_z = \frac{\tilde{T}_T}{3} = 0.15$$

The green line is the $\Delta\check{V}$ required for a continuous thrust hover at \tilde{z}_{\min} and is equal to (Equation (137) in Appendix L)

$$\Delta\check{V}_C = 2\tilde{z}_{\min}\pi\tilde{T}_T$$

Note how the discrete solution converges to the continuous-thrust line as $\tilde{P}_z \rightarrow 0$, that is, as the number of bounces (k_z) goes to infinity (see Appendix K.3 for the full proof).

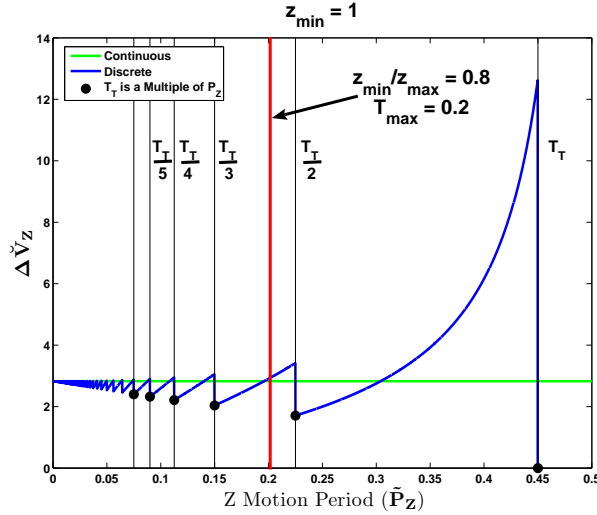


Figure 29: Notional $\Delta\check{V}_z$ vs Z Period

4.3 Entry Condition Definitions

In addition to lobe size and orientation, the mission planner has flexibility in choosing entry and exit conditions to and from the lobe. Combinations of these conditions are used to define the cases presented later. There are three types of lobe entry conditions used in this research. They are:

1. Defined Entry Condition
2. Open Entry Condition
3. Entry from a Closed Relative Orbit

and are explained in the following subsections.

4.3.1 Defined Entry Condition. The first entry condition, Defined Entry Condition (DEnC), enables the user to specify the deputy's relative entry position and velocity. Thus, in addition to the standard inputs listed at the beginning of this chapter, the user must specify:

$$\psi_1, (\dot{x}_1^-, \dot{y}_1^-)$$

This will affect the calculation of $\Delta\check{V}_1^2$ (Equation (124) in Appendix K):

$$\Delta\check{V}_1^2 = \begin{bmatrix} \dot{\tilde{x}}_1^+ - \dot{\tilde{x}}_1^- & \dot{\tilde{y}}_1^+ - \dot{\tilde{y}}_1^- \end{bmatrix} \begin{bmatrix} \dot{\tilde{x}}_1^+ - \dot{\tilde{x}}_1^- \\ \dot{\tilde{y}}_1^+ - \dot{\tilde{y}}_1^- \end{bmatrix}$$

where

$$\begin{bmatrix} \dot{\tilde{x}}_1^+ - \dot{\tilde{x}}_1^- \\ \dot{\tilde{y}}_1^+ - \dot{\tilde{y}}_1^- \end{bmatrix} = \begin{bmatrix} \frac{-4\tilde{S}^+ + 6\pi\tilde{T}_{1,2}\tilde{C}^+}{8 - 6\pi\tilde{T}_{1,2}\tilde{S}^+ - 8\tilde{C}^+} & \frac{4\tilde{S}^+ - 6\pi\tilde{T}_{1,2}}{8 - 6\pi\tilde{T}_{1,2}\tilde{S}^+ - 8\tilde{C}^+} & \frac{-2 + 2\tilde{C}^+}{8 - 6\pi\tilde{T}_{1,2}\tilde{S}^+ - 8\tilde{C}^+} \\ \frac{-14 + 12\pi\tilde{T}_{1,2}\tilde{S}^+ + 14\tilde{C}^+}{8 - 6\pi\tilde{T}_{1,2}\tilde{S}^+ - 8\tilde{C}^+} & \frac{2 - 2\tilde{C}^+}{8 - 6\pi\tilde{T}_{1,2}\tilde{S}^+ - 8\tilde{C}^+} & \frac{\tilde{S}^+}{8 - 6\pi\tilde{T}_{1,2}\tilde{S}^+ - 8\tilde{C}^+} \end{bmatrix} \begin{bmatrix} \tilde{x}_1 \\ \tilde{x}_2 \\ \Delta\tilde{y} \end{bmatrix} - \begin{bmatrix} \dot{\tilde{x}}_1^- \\ \dot{\tilde{y}}_1^- \end{bmatrix}$$

$$\Delta\tilde{y} = \tilde{y}_2 - \tilde{y}_1$$

4.3.2 Open Entry Condition. The second variant, Open Entry Condition (OEnC), puts no restrictions on the relative start position and velocity; thus the algorithm is free to choose these in whatever manner is most optimal. Since the deputy is entering the lobe at the desired position and velocity, there is no thrust at the first point:

$$\Delta\check{V}_1^2 = 0$$

4.3.3 Entry from a Closed-Relative Orbit. The Entry from a Closed-Relative Orbit (EnCRO), enables the algorithm to search for an optimal start position but constrains the velocity at that point to match a closed-relative orbit that is centered on the chief and intersects the lobe at that point. While closed-relative orbits can be centered about any point along the \hat{Y} axis, the choice was made to center on the chief. Setting the relative orbit parameters a and b (Equations (10a) and (10b) in Section 3.2) to zero,

$$\begin{aligned} \dot{\tilde{x}}_1^- &= \pi\tilde{y}_1 \\ \dot{\tilde{y}}_1^- &= -4\pi\tilde{x}_1 \end{aligned}$$

This will effect the calculation of $\Delta\check{V}_1^2$:

$$\Delta\check{V}_1^2 = \begin{bmatrix} \dot{\tilde{x}}_1^+ - \dot{\tilde{x}}_1^- & \dot{\tilde{y}}_1^+ - \dot{\tilde{y}}_1^- \\ \dot{\tilde{y}}_1^+ - \dot{\tilde{y}}_1^- \end{bmatrix}$$

where

$$\begin{bmatrix} \dot{\tilde{x}}_1^+ - \dot{\tilde{x}}_1^- \\ \dot{\tilde{y}}_1^+ - \dot{\tilde{y}}_1^- \end{bmatrix} = \begin{bmatrix} \frac{-4\tilde{S}^+ + 6\pi\tilde{T}_{1,2}\tilde{C}^+}{8 - 6\pi\tilde{T}_{1,2}\tilde{S}^+ - 8\tilde{C}^+} & \frac{4\tilde{S}^+ - 6\pi\tilde{T}_{1,2}}{8 - 6\pi\tilde{T}_{1,2}\tilde{S}^+ - 8\tilde{C}^+} & \frac{-2 + 2\tilde{C}^+}{8 - 6\pi\tilde{T}_{1,2}\tilde{S}^+ - 8\tilde{C}^+} \\ \frac{-14 + 12\pi\tilde{T}_{1,2}\tilde{S}^+ + 14\tilde{C}^+}{8 - 6\pi\tilde{T}_{1,2}\tilde{S}^+ - 8\tilde{C}^+} & \frac{2 - 2\tilde{C}^+}{8 - 6\pi\tilde{T}_{1,2}\tilde{S}^+ - 8\tilde{C}^+} & \frac{\tilde{S}^+}{8 - 6\pi\tilde{T}_{1,2}\tilde{S}^+ - 8\tilde{C}^+} \end{bmatrix} \begin{bmatrix} \tilde{x}_1 \\ \tilde{x}_2 \\ \Delta\tilde{y} \end{bmatrix} - \begin{bmatrix} \pi\tilde{y}_1 \\ -4\pi\tilde{x}_1 \end{bmatrix}$$

$$\Delta\tilde{y} = \tilde{y}_2 - \tilde{y}_1$$

4.4 *Exit Condition Definitions*

The lobe exit conditions used in this research are

1. Defined Exit Condition
2. Open Exit Condition
3. Exit to a Closed Relative Orbit
4. Repeating Hover Orbit

and are explained in the following subsections.

4.4.1 Defined Exit Condition. The first exit condition, Defined Exit Condition (DExC), enables the user to specify the deputy's relative exit position and velocity. Thus, in addition to the standard inputs listed at the beginning of this chapter, the user must specify:

$$\psi_{k+1}, (\dot{\tilde{x}}_{k+1}^+, \dot{\tilde{y}}_{k+1}^+)$$

This will effect the calculation of $\Delta\check{V}_F^2$ (Equation (124) in Appendix K):

$$\Delta\check{V}_F^2 = \begin{bmatrix} \dot{\tilde{x}}_1^+ - \dot{\tilde{x}}_1^- & \dot{\tilde{y}}_1^+ - \dot{\tilde{y}}_1^- \end{bmatrix} \begin{bmatrix} \dot{\tilde{x}}_1^+ - \dot{\tilde{x}}_1^- \\ \dot{\tilde{y}}_1^+ - \dot{\tilde{y}}_1^- \end{bmatrix}$$

where

$$\begin{bmatrix} \dot{\tilde{x}}_1^+ - \dot{\tilde{x}}_1^- \\ \dot{\tilde{y}}_1^+ - \dot{\tilde{y}}_1^- \end{bmatrix} = \begin{bmatrix} \dot{\tilde{x}}_1^+ \\ \dot{\tilde{y}}_1^+ \end{bmatrix} - \begin{bmatrix} \frac{-4\tilde{S}^+ + 6\pi\tilde{T}_{1,2}\tilde{C}^+}{8 - 6\pi\tilde{T}_{1,2}\tilde{S}^+ - 8\tilde{C}^+} & \frac{4\tilde{S}^+ - 6\pi\tilde{T}_{1,2}}{8 - 6\pi\tilde{T}_{1,2}\tilde{S}^+ - 8\tilde{C}^+} & \frac{-2 + 2\tilde{C}^+}{8 - 6\pi\tilde{T}_{1,2}\tilde{S}^+ - 8\tilde{C}^+} \\ \frac{-14 + 12\pi\tilde{T}_{1,2}\tilde{S}^+ + 14\tilde{C}^+}{8 - 6\pi\tilde{T}_{1,2}\tilde{S}^+ - 8\tilde{C}^+} & \frac{2 - 2\tilde{C}^+}{8 - 6\pi\tilde{T}_{1,2}\tilde{S}^+ - 8\tilde{C}^+} & \frac{\tilde{S}^+}{8 - 6\pi\tilde{T}_{1,2}\tilde{S}^+ - 8\tilde{C}^+} \end{bmatrix} \begin{bmatrix} \tilde{x}_1 \\ \tilde{x}_2 \\ \Delta\tilde{y} \end{bmatrix}$$

$$\Delta\tilde{y} = \tilde{y}_2 - \tilde{y}_1$$

4.4.2 Open Exit Condition. The second variant, Open Exit Condition (OExC), puts no restrictions on the relative exit position and velocity. Thus the deputy will leave the lobe on the trajectory resulting from the $\Delta\check{V}_k$ burn. There is no burn at the final point:

$$\Delta\check{V}_F^2 = 0$$

4.4.3 Exit to a Closed-Relative Orbit. The Exit to a Closed-Relative Orbit (ExCRO), enables the algorithm to search for an optimal exit position but constrains the velocity at that point to match a closed-relative orbit that is centered on the chief and intersects the lobe at that point. While closed-relative orbits can be centered about any point along the \hat{Y} axis, the choice was made to center on the chief. Setting the relative orbit parameters a and b (Equations (10a) and (10b) in Section 3.2) to zero,

$$\begin{aligned} \dot{\tilde{x}}_{k+1}^+ &= \pi\tilde{y}_{k+1} \\ \dot{\tilde{y}}_{k+1}^+ &= -4\pi\tilde{x}_{k+1} \end{aligned}$$

$\Delta\check{V}_F^2$ is:

$$\Delta\check{V}_F^2 = \begin{bmatrix} \dot{\tilde{x}}_{k+1}^+ - \dot{\tilde{x}}_{k+1}^- & \dot{\tilde{y}}_{k+1}^+ - \dot{\tilde{y}}_{k+1}^- \end{bmatrix} \begin{bmatrix} \dot{\tilde{x}}_{k+1}^+ - \dot{\tilde{x}}_{k+1}^- \\ \dot{\tilde{y}}_{k+1}^+ - \dot{\tilde{y}}_{k+1}^- \end{bmatrix}$$

where

$$\begin{bmatrix} \dot{\tilde{x}}_{k+1}^+ - \dot{\tilde{x}}_{k+1}^- \\ \dot{\tilde{y}}_{k+1}^+ - \dot{\tilde{y}}_{k+1}^- \end{bmatrix} = \begin{bmatrix} \pi\tilde{y}_{k+1} \\ -4\pi\tilde{x}_{k+1} \end{bmatrix} - \begin{bmatrix} \frac{-4\tilde{S}^- + 6\pi\tilde{T}}{8-6\pi\tilde{T}\tilde{S}^- - 8\tilde{C}^-} & \frac{4\tilde{S}^- - 6\pi\tilde{T}\tilde{C}^-}{8-6\pi\tilde{T}\tilde{S}^- - 8\tilde{C}^-} & \frac{2-2\tilde{C}^-}{8-6\pi\tilde{T}\tilde{S}^- - 8\tilde{C}^-} \\ \frac{2-2\tilde{C}^-}{8-6\pi\tilde{T}\tilde{S}^- - 8\tilde{C}^-} & \frac{-14+12\pi\tilde{T}\tilde{S}^- + 14\tilde{C}}{8-6\pi\tilde{T}\tilde{S}^- - 8\tilde{C}^-} & \frac{\tilde{S}^-}{8-6\pi\tilde{T}\tilde{S}^- - 8\tilde{C}^-} \end{bmatrix} \begin{bmatrix} \tilde{x}_k \\ \tilde{x}_{k+1} \\ \Delta\tilde{y} \end{bmatrix}$$

$$\Delta\tilde{y} = \tilde{y}_{k+1} - \tilde{y}_k$$

4.4.4 Repeating Hover Orbit. The repeating hover orbit is not an exit condition per se. Instead, we seek a closed relative orbit contained within the lobe in which the starting relative position and velocity are identical to the ending conditions. This produces a trajectory that can be traversed for as many periods as desired or as long as fuel is available. In order to enforce a closed orbit, the following constraints are applied to the cost function:

$$\tilde{x}_{k+1} = \tilde{x}_1$$

$$\tilde{y}_{k+1} = \tilde{y}_1$$

$$\tilde{T}_{k+1,k} = 0$$

$$\tilde{T}_F = \tilde{T}_{k,1}$$

$$\Delta\check{V}_F^2 = \begin{bmatrix} \tilde{x}_k & \tilde{y}_k & \tilde{x}_1 & \tilde{y}_1 & \tilde{x}_2 & \tilde{y}_2 \end{bmatrix} \tilde{R}(\tilde{T}_F, \tilde{T}_{1,2}) \tilde{R}'(\tilde{T}_F, \tilde{T}_{1,2}) \begin{bmatrix} \tilde{x}_k \\ \tilde{y}_k \\ \tilde{x}_1 \\ \tilde{y}_1 \\ \tilde{x}_2 \\ \tilde{y}_2 \end{bmatrix}$$

4.5 *Research Cases*

The availability of three entry and four exit conditions provides us with twelve possible entry/exit combinations. In the interest of brevity and given that only a handful of combinations are of true interest to mission planners, only three cases are presented herein. They are:

1. Defined Entry Condition/Open Exit Condition
2. Entry From a Closed Relative Orbit/Exit to a Closed Relative Orbit
3. Open Entry Condition/Repeating Hover Orbit

4.6 *The Continuous-Thrust Solution*

As a benchmark to which to compare our discrete-thrust trajectories, a continuous-thrust solution is derived. We can quickly find the closed-form solution for a continuous-thrust controller that keeps the deputy at a specified point in the relative frame. A shortened version of the derivation in Appendix L is provided below. The velocities at this hover point must be zero:

$$\dot{\tilde{x}} = 0 \quad \dot{\tilde{y}} = 0 \quad \dot{\tilde{z}} = 0$$

which reduces Equation (7) to:

$$\begin{aligned}\ddot{\tilde{x}} &= 4\pi(0) + 12\pi^2\tilde{x} = 12\pi^2\tilde{x} \\ \ddot{\tilde{y}} &= -4\pi(0) = 0 \\ \ddot{\tilde{z}} &= -4\pi^2\tilde{z}\end{aligned}$$

Since the $\ddot{\tilde{y}}$ equation is now zero, we need only worry about the accelerations along the \hat{X} and \hat{Z} axes. Integrating from zero to the total time-of-flight (\tilde{T}_T) yields the ΔV as a function of chief orbit period ($\Delta\tilde{V}_C$) required to keep the deputy hovering at

a given $(\tilde{x}_o, \tilde{y}_o, \tilde{z}_o)$:

$$\begin{aligned}\Delta\tilde{V}_C &= \int_0^{\tilde{T}_T} |\ddot{\tilde{x}}|d\tilde{t} + \int_0^{\tilde{T}_T} |\ddot{\tilde{z}}|d\tilde{t} = \int_0^{\tilde{T}_T} 12\pi^2|\tilde{x}_o|d\tilde{t} + \int_0^{\tilde{T}_T} 4\pi^2|\tilde{z}_o|d\tilde{t} \\ &= \pi^2(12|\tilde{x}_o| + 4|\tilde{z}_o|) \int_0^{\tilde{T}_T} d\tilde{t} = \pi^2(12|\tilde{x}_o| + 4|\tilde{z}_o|) \tilde{T}_T\end{aligned}$$

where the C subscript indicates “continuous”. The location of \tilde{x}_o and \tilde{z}_o is arbitrary but the smallest continuous $\Delta\tilde{V}$ is attained when \tilde{x}_o and \tilde{z}_o are at their minimum, thus \tilde{x}_{\min} and \tilde{z}_{\min} represent the absolute value of the coordinate on the lobe that is closest to the \hat{Y} axis and $\hat{X}\hat{Y}$ plane respectively, and

$$\Delta\tilde{V}_C = (12\tilde{x}_{\min} + 4\tilde{z}_{\min}) \pi^2\tilde{T}_T \quad (28)$$

If the lobe happens to intersect the \hat{Y} axis, then the optimal solution (for the linear CW case) is to stay on that \hat{Y} axis (the loci of equilibrium points) or on a closed 2x1 ellipse about it (see Section 5.1). We can also express the continuous ΔV as a specific $\Delta\check{V}$ by applying the conversion in Equation (17), Appendix 3.3

$$\Delta\check{V}_C = \frac{\Delta\tilde{V}_C}{2\pi} = \left[\frac{1}{2\pi} \right] (12\tilde{x}_{\min} + 4\tilde{z}_{\min}) \pi^2\tilde{T}_T = (6\tilde{x}_{\min} + 2\tilde{z}_{\min}) \pi\tilde{T}_T \quad (29)$$

The above equation works well if we assume the deputy starts at the minimum x and z values, however, in order to use this as a fair comparison, the ΔV needed to get into and out of that position must also be included. This motivates finding minimum-fuel entry and exit legs as shown in Figure 30.

4.6.1 Entry Leg. Assume that the continuous burn solution starts at the same entry position $(\tilde{x}_1, \tilde{y}_1)$ and velocity $(\dot{\tilde{x}}_1^-, \dot{\tilde{y}}_1^-)$ as the discrete-thrust solution. The ΔV required to get to the \tilde{x}_{\min} position is (from Equation (124) in Appendix K):

$$\Delta\check{V}_1^2 = \frac{1}{4\pi^2} \begin{bmatrix} \dot{\tilde{x}}_1^+ - \dot{\tilde{x}}_1^- & \dot{\tilde{y}}_1^+ - \dot{\tilde{y}}_1^- \end{bmatrix} \begin{bmatrix} \dot{\tilde{x}}_1^+ - \dot{\tilde{x}}_1^- \\ \dot{\tilde{y}}_1^+ - \dot{\tilde{y}}_1^- \end{bmatrix}$$

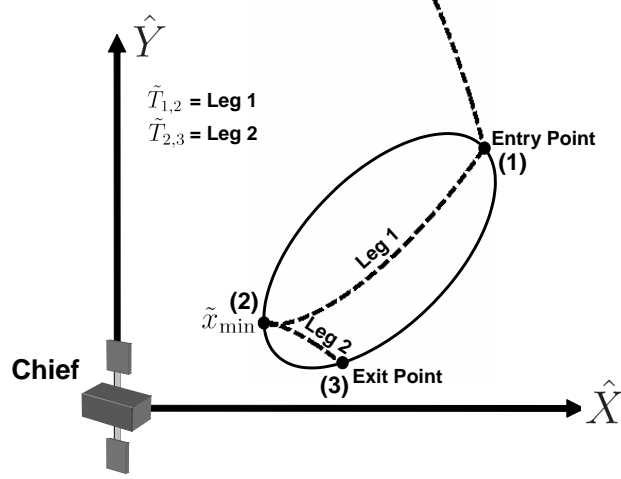


Figure 30: The Continuous-Thrust Trajectory

where

$$\begin{bmatrix} \dot{\tilde{x}}_1^+ - \dot{\tilde{x}}_1^- \\ \dot{\tilde{y}}_1^+ - \dot{\tilde{y}}_1^- \end{bmatrix} = \begin{bmatrix} \frac{-4\tilde{S}+6\pi\tilde{T}\tilde{C}}{8-6\pi\tilde{T}\tilde{S}-8\tilde{C}} & \frac{4\tilde{S}-6\pi\tilde{T}}{8-6\pi\tilde{T}\tilde{S}-8\tilde{C}} & \frac{-2+2\tilde{C}}{8-6\pi\tilde{T}\tilde{S}-8\tilde{C}} \\ \frac{-14+12\pi\tilde{T}\tilde{S}+14\tilde{C}}{8-6\pi\tilde{T}\tilde{S}-8\tilde{C}} & \frac{2-2\tilde{C}}{8-6\pi\tilde{T}\tilde{S}-8\tilde{C}} & \frac{\tilde{S}}{8-6\pi\tilde{T}\tilde{S}-8\tilde{C}} \end{bmatrix} \begin{bmatrix} \tilde{x}_1 \\ \tilde{x}_{\min} \\ \Delta\tilde{y}_{\text{Leg 1}} \end{bmatrix} - \begin{bmatrix} \dot{\tilde{x}}_1^- \\ \dot{\tilde{y}}_1^- \end{bmatrix}$$

$$\Delta\tilde{y}_{\text{Leg 1}} = \tilde{y}_2 - \tilde{y}_1 \quad \tilde{S} = \sin(2\pi\tilde{T}_{1,2}) \quad \tilde{C} = \cos(2\pi\tilde{T}_{1,2})$$

Once at the \tilde{x}_{\min} position, the deputy must make a burn to cancel its relative velocity that is equal in magnitude but opposite in direction to the final velocity of the previous leg

$$\Delta\check{V}_2 = \frac{1}{2\pi} \|\dot{\tilde{x}}_2^- \hat{X} + \dot{\tilde{y}}_2^- \hat{Y}\|_2$$

where

$$\begin{bmatrix} \dot{\tilde{x}}_2^- \\ \dot{\tilde{y}}_2^- \end{bmatrix} = \begin{bmatrix} \frac{-4\tilde{S}+6\pi\tilde{T}}{8-6\pi\tilde{T}\tilde{S}-8\tilde{C}} & \frac{4\tilde{S}-6\pi\tilde{T}\tilde{C}}{8-6\pi\tilde{T}\tilde{S}-8\tilde{C}} & \frac{2-2\tilde{C}}{8-6\pi\tilde{T}\tilde{S}-8\tilde{C}} \\ \frac{2-2\tilde{C}}{8-6\pi\tilde{T}\tilde{S}-8\tilde{C}} & \frac{-14+12\pi\tilde{T}\tilde{S}+14\tilde{C}}{8-6\pi\tilde{T}\tilde{S}-8\tilde{C}} & \frac{\tilde{S}}{8-6\pi\tilde{T}\tilde{S}-8\tilde{C}} \end{bmatrix} \begin{bmatrix} \tilde{x}_1 \\ \tilde{x}_{\min} \\ \Delta\tilde{y}_{\text{Leg 1}} \end{bmatrix}$$

We can use either a minimization routine or a global search over the range of time-of-flight:

$$0 < \tilde{T}_{1,2} < \tilde{T}_{\max_{1,2}}$$

to find the smallest total ΔV required to arrive and stop at \tilde{x}_{\min} :

$$\Delta\check{V}_{\text{Entry}} = \min \left[\Delta\check{V}_1 + \Delta\check{V}_2 \right]$$

4.6.2 Exit Leg. The exit leg will depend on the user-specified exit condition. If the exit condition is open, the deputy is allowed to drift out of the lobe and requires no additional ΔV :

$$\Delta\check{V}_{\text{Exit}} = 0$$

If a repeating hover orbit is requested, the deputy never leaves the \tilde{x}_{\min} position and $\Delta\check{V}_{\text{Exit}}$ is again zero. If the exit condition is an exit to a closed-relative orbit or if the exit position and relative velocity are specified, then the deputy will need to perform two burns to leave \tilde{x}_{\min} to arrive at the exit position and then to leave the lobe at ψ_3 . The ΔV required to get from the \tilde{x}_{\min} position to the exit point is (from Equation (124) in Appendix K)

$$\Delta\check{V}_3 = \frac{1}{2\pi} \|\dot{\tilde{x}}_2^+ \hat{X} + \dot{\tilde{y}}_2^+ \hat{Y}\|_2$$

where

$$\begin{bmatrix} \dot{\tilde{x}}_2^+ \\ \dot{\tilde{y}}_2^+ \end{bmatrix} = 2\pi \begin{bmatrix} \frac{-4\tilde{S}+6\pi\tilde{T}\tilde{C}}{8-6\pi\tilde{T}\tilde{S}-8\tilde{C}} & \frac{4\tilde{S}-6\pi\tilde{T}}{8-6\pi\tilde{T}\tilde{S}-8\tilde{C}} & \frac{-2+2\tilde{C}}{8-6\pi\tilde{T}\tilde{S}-8\tilde{C}} \\ \frac{-14+12\pi\tilde{T}\tilde{S}+14\tilde{C}}{8-6\pi\tilde{T}\tilde{S}-8\tilde{C}} & \frac{2-2\tilde{C}}{8-6\pi\tilde{T}\tilde{S}-8\tilde{C}} & \frac{\tilde{S}}{8-6\pi\tilde{T}\tilde{S}-8\tilde{C}} \end{bmatrix} \begin{bmatrix} \tilde{x}_{\min} \\ \tilde{x}_3 \\ \Delta\check{y}_{\text{Leg } 2} \end{bmatrix}$$

The ΔV required to exit the lobe,

$$\Delta\check{V}_4^2 = \frac{1}{4\pi^2} \begin{bmatrix} \dot{\tilde{x}}_3^+ - \dot{\tilde{x}}_3^- & \dot{\tilde{y}}_3^+ - \dot{\tilde{y}}_3^- \end{bmatrix} \begin{bmatrix} \dot{\tilde{x}}_3^+ - \dot{\tilde{x}}_3^- \\ \dot{\tilde{y}}_3^+ - \dot{\tilde{y}}_3^- \end{bmatrix}$$

where for the defined exit condition

$$\begin{bmatrix} \dot{x}_3^+ - \dot{x}_3^- \\ \dot{y}_3^+ - \dot{y}_3^- \end{bmatrix} = \begin{bmatrix} \dot{x}_3^+ \\ \dot{y}_3^+ \end{bmatrix} - 2\pi \begin{bmatrix} \frac{-4\tilde{S}+6\pi\tilde{T}}{8-6\pi\tilde{T}\tilde{S}-8\tilde{C}} & \frac{4\tilde{S}-6\pi\tilde{T}\tilde{C}}{8-6\pi\tilde{T}\tilde{S}-8\tilde{C}} & \frac{2-2\tilde{C}}{8-6\pi\tilde{T}\tilde{S}-8\tilde{C}} \\ \frac{2-2\tilde{C}}{8-6\pi\tilde{T}\tilde{S}-8\tilde{C}} & \frac{-14+12\pi\tilde{T}\tilde{S}+14\tilde{C}}{8-6\pi\tilde{T}\tilde{S}-8\tilde{C}} & \frac{\tilde{S}}{8-6\pi\tilde{T}\tilde{S}-8\tilde{C}} \end{bmatrix} \begin{bmatrix} \tilde{x}_{\min} \\ \tilde{x}_3 \\ \Delta\tilde{y}_{\text{Leg 2}} \end{bmatrix}$$

For the exit to a closed-relative orbit, the relative velocity at ψ_3 must be the same as a closed-relative orbit centered on the chief that passes through ψ_3 . Setting $a = b = 0$ (Equations (10a) and (10b)),

$$\dot{y}_3^+ = -4\pi\tilde{x}_3 \quad \dot{x}_3^+ = \pi\tilde{y}_3$$

and

$$\begin{bmatrix} \dot{x}_3^+ - \dot{x}_3^- \\ \dot{y}_3^+ - \dot{y}_3^- \end{bmatrix} = \begin{bmatrix} \pi\tilde{y}_3 \\ -4\pi\tilde{x}_3 \end{bmatrix} - 2\pi \begin{bmatrix} \frac{-4\tilde{S}+6\pi\tilde{T}}{8-6\pi\tilde{T}\tilde{S}-8\tilde{C}} & \frac{4\tilde{S}-6\pi\tilde{T}\tilde{C}}{8-6\pi\tilde{T}\tilde{S}-8\tilde{C}} & \frac{2-2\tilde{C}}{8-6\pi\tilde{T}\tilde{S}-8\tilde{C}} \\ \frac{2-2\tilde{C}}{8-6\pi\tilde{T}\tilde{S}-8\tilde{C}} & \frac{-14+12\pi\tilde{T}\tilde{S}+14\tilde{C}}{8-6\pi\tilde{T}\tilde{S}-8\tilde{C}} & \frac{\tilde{S}}{8-6\pi\tilde{T}\tilde{S}-8\tilde{C}} \end{bmatrix} \begin{bmatrix} \tilde{x}_{\min} \\ \tilde{x}_3 \\ \Delta\tilde{y}_{\text{Leg 2}} \end{bmatrix}$$

We can use either a minimization routine or a global search over the range of time-of-flight:

$$0 < \tilde{T}_{2,3} < \tilde{T}_{\max_{2,3}}$$

to find the smallest total ΔV required to leave x_{\min} and exit the lobe:

$$\Delta\check{V}_{\text{Exit}} = \min \left[\Delta\check{V}_3 + \Delta\check{V}_4 \right]$$

4.6.3 Hover Time. The time-of-flight for each leg is obviously independent of the total time-of-flight produced by the discrete-thrust algorithm. Whatever time remains after getting to \tilde{x}_{\min} and exiting the lobe will be spent hovering at \tilde{x}_{\min} with continuous-thrust; thus:

$$\tilde{T}_{\text{Hover}} = \tilde{T}_T - \tilde{T}_{1,2} - \tilde{T}_{2,3}$$

There are cases in which the discrete-thrust solution total time-of-flight is less than the sum of the two continuous-thrust legs, this must be taken account when comparing the two results.

4.6.4 Summary. This chapter has derived all the necessary components to generate fuel-optimal discrete-thrust trajectories as well as a benchmark continuous method with which to compare those results. We are finally ready to present and analyze those final results.

V. Results and Analysis

With an understanding of the dynamics and solution method in hand, we turn next to analyzing the results and drawing conclusions. The symmetries of the constraint and cost function assure us that optimal trajectories for lobes in the upper right quadrant are representative of lobes in any other quadrant (see Section 3.6). This is very convenient, as it allows us to use a small number of results to make general conclusions about optimal trajectories. Further, these results are applicable to any sized circular chief orbit and about any celestial body, assuming two body dynamics are the dominant force.

First, results are presented for the a special class of hovering orbits that take advantage of the equilibrium condition of the equations of motion. Next are optimal trajectories for each of the three cases defined in Section 4.5 as applied to lobes 2, 3, and 4 (shown in Figure 31 with parameters in Table 1). Lobe 1 is a special case in which the lobe intersects the \hat{Y} axis and will only be examined in the persistent hover orbit section (Section 5.1). Trajectories are propagated with the unperturbed, linearized equations of motion.

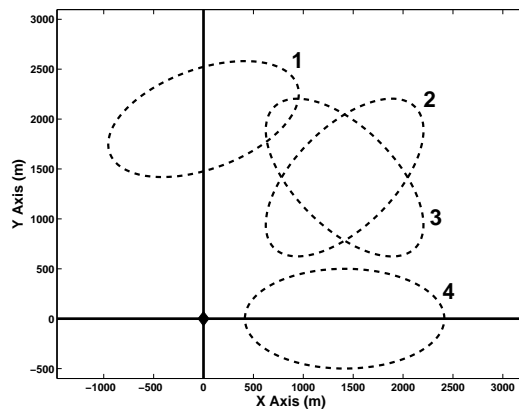


Figure 31: Lobes of the Results Section

Table 1: Lobe Parameters

Lobe #	α (degs)	β (degs)	γ (km)	τ_x (km)	τ_y (km)	η (degs)
1	90	90	2	1	0.5	20
2	45	90	2	1	0.5	45
3	45	90	2	0.5	1	45
4	0	90	1.414	1	0.5	0

5.1 The Persistent Hover Orbit

As mentioned earlier and discussed in detail in Section 3.2.2 and Appendix M, the \hat{Y} axis is the locus of equilibrium points for the linearized equations of motion about a chief in a circular orbit (Equation (7)). Lobes that contain some portion of the \hat{Y} axis deserve special consideration. First, let us examine the output of the optimization algorithm when given a lobe that intersects the \hat{Y} axis. Figure 32 is the result of an optimization run for a defined entry ($\psi_1 = \frac{\pi}{2}$) and open exit on Lobe 1. The entry relative velocity is chosen such that the deputy enters from a closed relative orbit centered on the chief at ψ_1 . The result is, not surprisingly, to place the deputy on

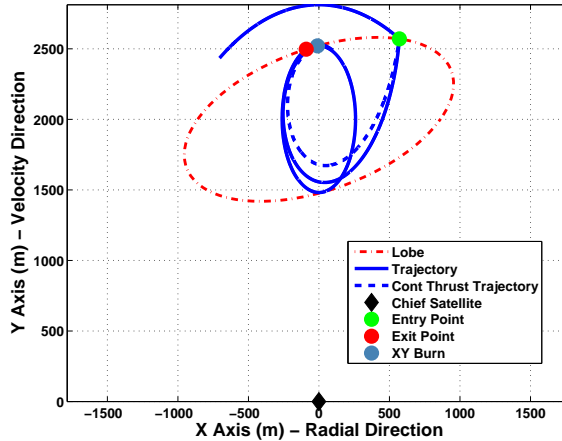


Figure 32: Optimization Algorithm Results for Lobe 1

a 2x1 ellipse. This special case relative orbit is called a persistent hover orbit (PHO), defined as any natural closed orbit that fits entirely within the lobe (see Figure 33). The PHO is a type of repeating hover orbit that does not require any impulsive thrusting to maintain, other than what is required to correct for perturbations and

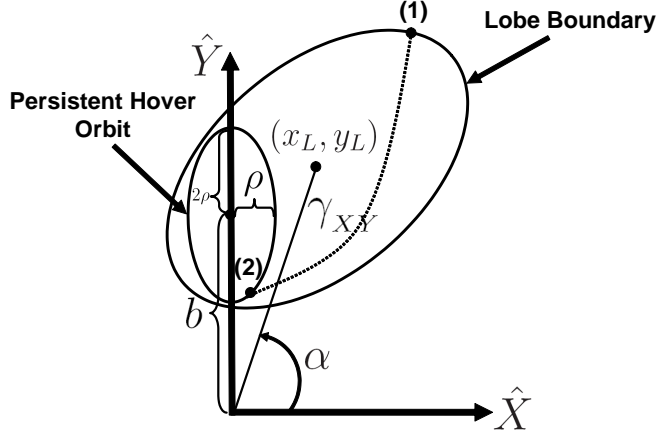
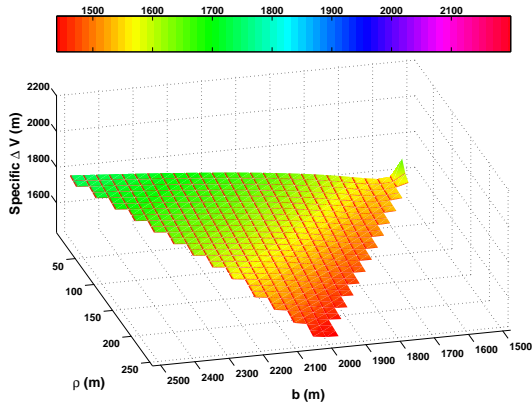


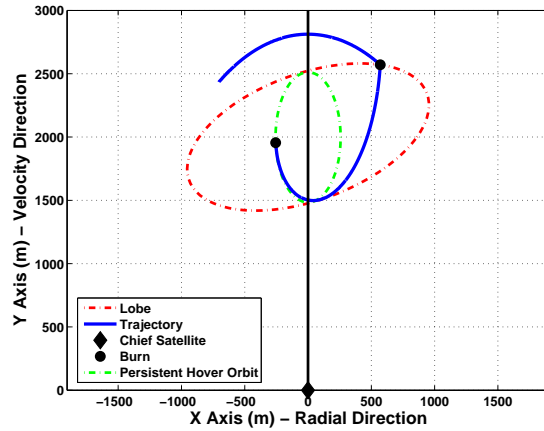
Figure 33: The Persistent Hover Orbit

linearization errors, making it ideal for long-term proximity operations. The PHO is specified by two parameters: the semi-minor axis (ρ) and the center coordinate along the \hat{Y} axis (b). In the limit as $\rho \rightarrow 0$, the PHO becomes a point on the \hat{Y} axis. Finding acceptable PHOs for a given lobe is the subject of Appendix M. The PHO problem is as follows. Assume the deputy's trajectory intersects the lobe at some entry position with a given relative velocity. Positioning the deputy onto the PHO requires two impulsive thrusts, the first at lobe entry to place the deputy on a trajectory towards the PHO and another to enter it. This greatly simplifies our optimization routine since we can globally search for the minimum-fuel solution of these two burns. The only remaining question, is what are the best values of the PHO semi-minor axis (ρ) and center position (b).

Although an exhaustive proof will not be made here, indications are that the minimum-fuel answer is to choose ρ and b such that ρ is as large as possible. Figures 34 and 35 present the result of evaluating all values of ρ and b that yield PHOs that are completely contained inside Lobe 1. The left-hand side figures are the $\Delta\check{V}$ surface over ρ and b while the right-hand figure shows the resultant minimum-fuel trajectory. Note that only combinations of ρ and b that fit completely inside the lobe are evaluated and the staircase feature is due to discretization of the search

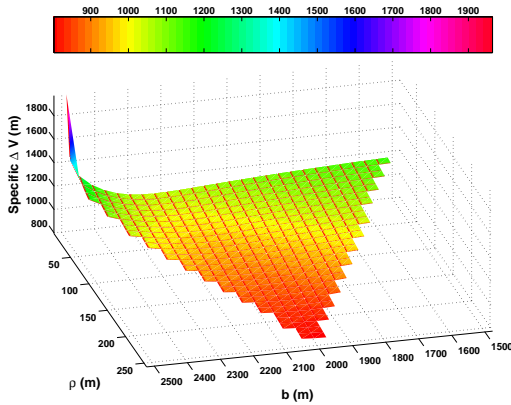


(a) $\Delta\check{V}$ as a Function of ρ and b

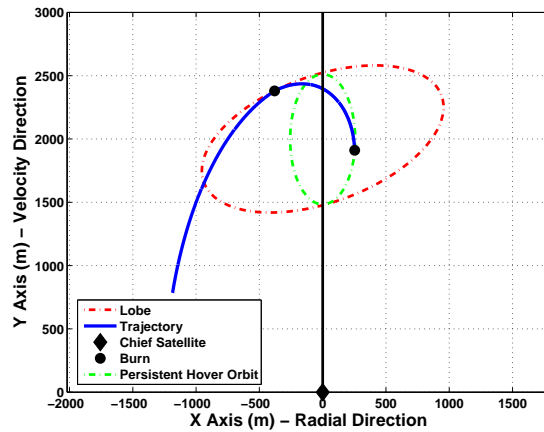


(b) The Minimum $\Delta\check{V}$ Trajectory

Figure 34: Persistent Hover Orbit Test: $\psi_1 = \frac{\pi}{4}$



(a) $\Delta\check{V}$ as a Function of ρ and b



(b) The Minimum $\Delta\check{V}$ Trajectory

Figure 35: Persistent Hover Orbit Test: $\psi_1 = \frac{3\pi}{4}$

space. In both cases, the minimum $\Delta\check{V}$ occurred when the largest possible ρ value was chosen. Note that if mission requirements dictate a fairly small time-of-flight, then optimizing the cost function over one or two legs may still yield the lowest total fuel solution; however, if a longer total time-of-flight is required, searching for the minimum two-thrust solution to place the deputy onto a PHO is optimal.

5.2 Case 1: Defined Entry Condition/Open Exit Condition

Case 1 investigates trajectories for which the entry condition is defined and the exit condition is left open. Recall that the defined entry condition requires the user to provide an incoming relative velocity at a specified lobe entry point. For convenience, and because choice of this initial condition is arbitrary, the following results will use the relative velocity of the closed relative orbit that intersects the lobe at the specified point and is assumed to be centered on the chief. Setting the relative orbit parameters a and b (Equations (10a) and (10b), Section 3.2) to zero yields

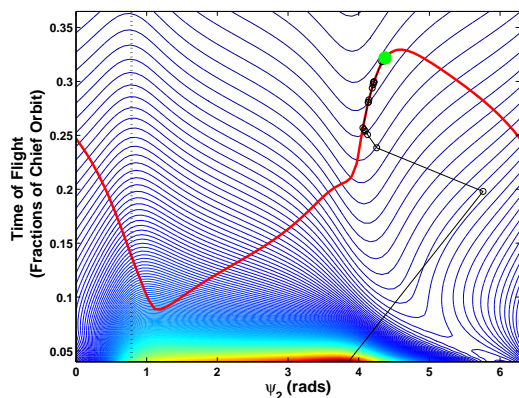
$$\dot{\tilde{y}}_1^- = -4\pi\tilde{x}_1 \quad \dot{\tilde{x}}_1^- = \pi\tilde{y}_1$$

Case 1 is of particular interest because, for the single-leg case, there are only two optimization parameters (ψ_2 and $\tilde{T}_{1,2}$); thus we can plot the cost surface and watch the iteration path of the nonlinear programming algorithm. Let

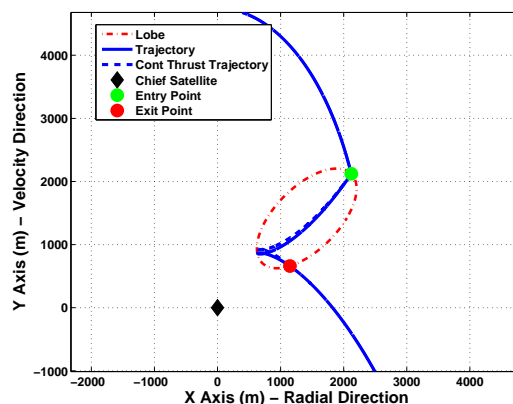
$$\psi_1 = \frac{\pi}{4}$$

The results of the optimization algorithm for each of the three lobes under the conditions specified above are shown in Figures 36, 37, and 38 where the red line on the cost contour plot is the line of maximum time-of-flight.

In all three examples, we can visually confirm that the optimization routine has converged on a minimum solution. We can also confirm that these are not in fact the global minima for this particular entry/exit condition. In each lobe, the closed relative orbit on which the deputy arrives can pass through the lobe and intersect a second point on the lobe. Since the exit condition is open, the zero-fuel solution is to stay on the original closed relative orbit and exit the lobe at the second intersection point. This is most clearly demonstrated in Lobe 3 (Figure 37) for which the true global minimum is $\psi_2 = 5.31$ rad, $\tilde{T}_{1,2} = 0.048$. Figure 39 is a repeated run of the optimization algorithm with different initial conditions that converges to the global

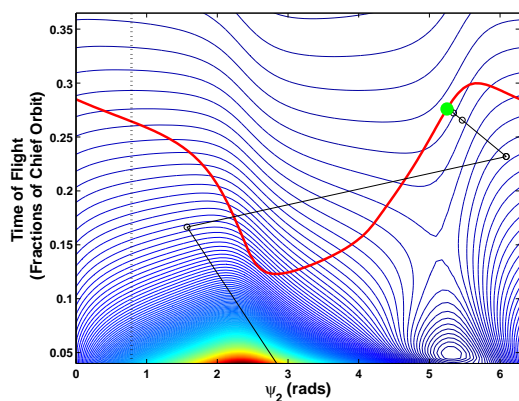


(a) Cost Function and Optimization Iterations

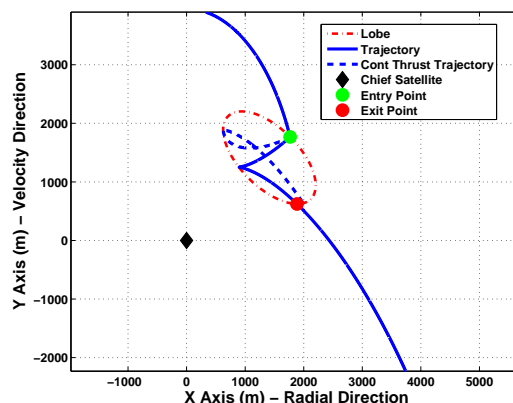


(b) Optimal Discrete Trajectory

Figure 36: Case 1, Lobe 2, Single Leg



(a) Cost Function and Optimization Iterations

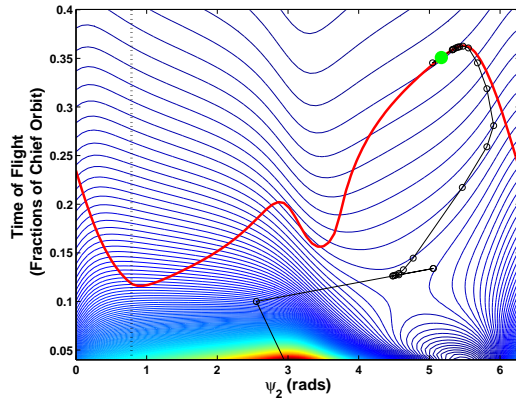


(b) Optimal Discrete Trajectory

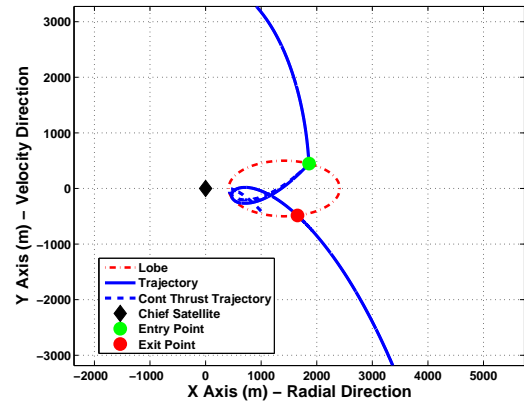
Figure 37: Case 1, Lobe 3, Single Leg

minimum above. This is the trivial solution and is not, in general, the solution of interest for the mission planner.

The example above highlights the sensitivity of the optimization algorithm to initial condition choice. As with most nonlinear optimization problems, we must be cognizant of the possibility of multiple local minima. Two are apparent in our simple example above and more should be expected as the dimensionality increases (by increasing the number of legs, k). Unfortunately, we do not have the luxury of visually verifying convergence to the correct solution when going to higher dimensional search spaces. In order to increase confidence in finding the desired minimum point,

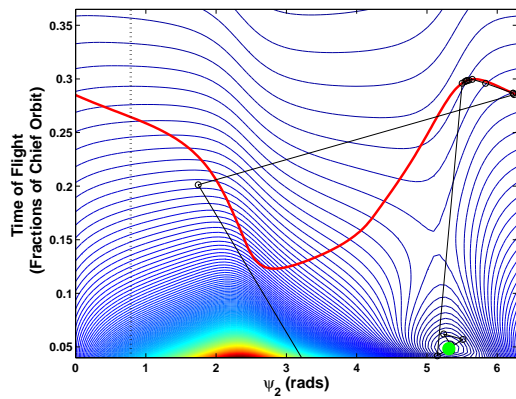


(a) Cost Function and Optimization Iterations

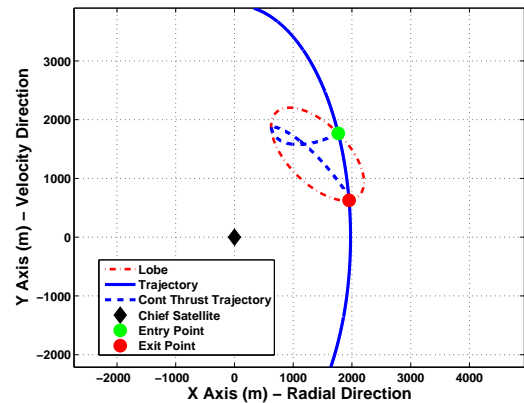


(b) Optimal Discrete Trajectory

Figure 38: Case 1, Lobe 4, Single Leg



(a) Cost Function and Optimization Iterations



(b) Optimal Discrete Trajectory

Figure 39: Case 1, Lobe 3, The Trivial Solution

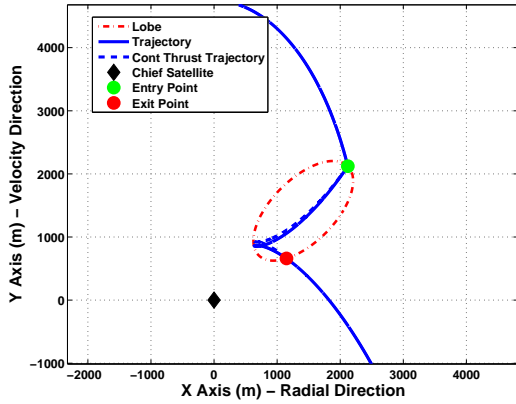
all simulations were executed with multiple initial guesses with the lowest cost result presented. Currently the initial choice of ψ is accomplished by the user; however, there is no reason the process could not be automated in order to look over a wide range of initial conditions.

The next set of graphs show the evolution of trajectories for each of the three lobes as the number of legs increases. The left-hand plots show the lowest cost discrete trajectory found after multiple initial condition choices. The right-hand plots are the time history of the discrete- and continuous-thrust trajectories. The continuous-thrust solution is described in Section 4.6 and is a function only of the lobe shape,

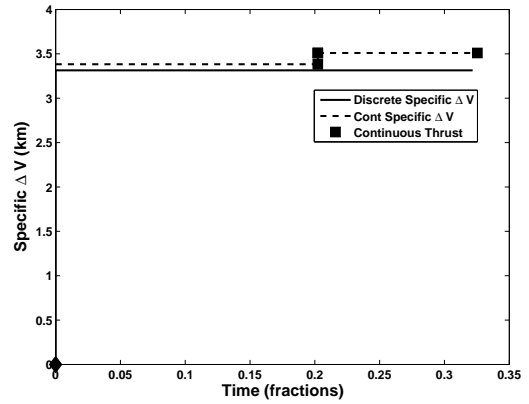
position, orientation, and entry position and velocity. In general, it consists of an entry leg to the \tilde{x}_{\min} coordinate, possible hovering at \tilde{x}_{\min} , and exiting the lobe either at a designated point, drifting out of the lobe, exiting onto another closed relative orbit, or remaining at \tilde{x}_{\min} . These thrusts are based on minimum ΔV solutions. The continuous solution entry and exit legs will both have a fixed time-of-flight, again based on the minimum ΔV solution. The difference between the sum of these two legs and the total time-of-flight of the discrete thrust solution is made up by hovering with continuous-thrust at \tilde{x}_{\min} . Since there is no minimum total time-of-flight constraint applied to the cost function, it is possible that the sum of the entry and exit legs is greater than the time-of-flight found in the optimization routine. In this case, no hovering is required and the continuous thrust time-of-flight will be longer than the discrete solution. Care must be taken when comparing the discrete and continuous solutions in these cases.

Figures 40-44 show the evolution of trajectories for Lobe 2 as the number of legs increases from one to five. There are minor changes in the trajectory and performance as additional legs are requested, but there is a definite pattern of convergence towards a final trajectory. In all but the single-leg case, the continuous solution outperforms the discrete case. Also, all but the five-leg simulation runs into the problem discussed above with the time-of-flight of the entry and exit legs of the continuous solution being larger than the entire discrete time-of-flight. It is clear that, for Lobe 1, a continuous-thrust strategy is more efficient.

Figures 45-49 are trajectories within Lobe 3. Again there is clear convergence to a final trajectory, but unlike in the previous case, there are slight fuel savings by using discrete solution in all but the final ($k = 5$) simulation. This set of runs is also a good example of how additional legs are accommodated by clustering several smaller thrusts to take the place of one larger thrust. In most cases, this is significantly less efficient, a fact notably displayed in Figure 49. In the $k \leq 4$ trajectories, the first leg from the entry point to near the top of the lobe is the result of a single thrust. When $k = 5$, this single thrust is split into three thrusts. Although the time-of-flight and

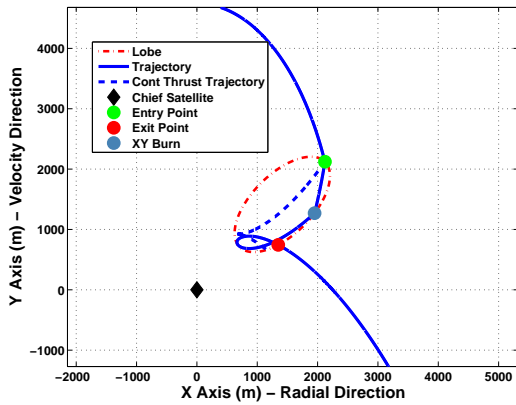


(a) $\hat{X}\hat{Y}$ Plane Trajectory

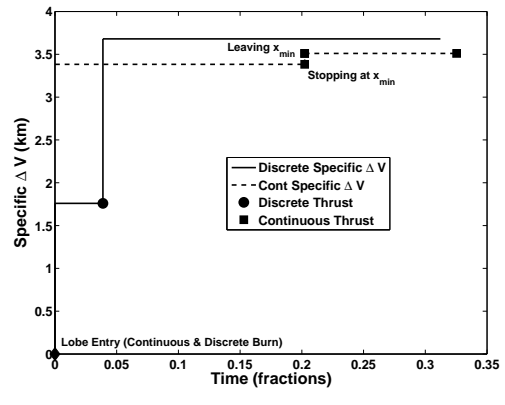


(b) Growth of $\Delta\check{V}$

Figure 40: Case 1, Lobe 2, Legs = 1



(a) $\hat{X}\hat{Y}$ Plane Trajectory

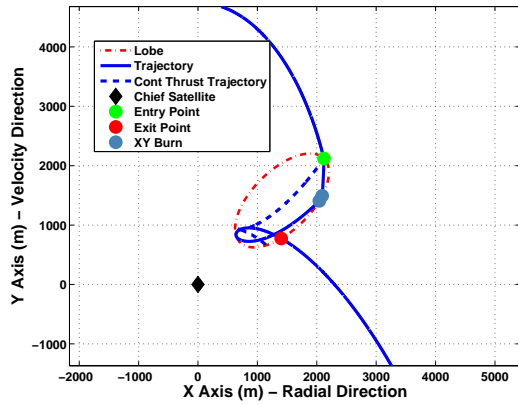


(b) Growth of $\Delta\check{V}$

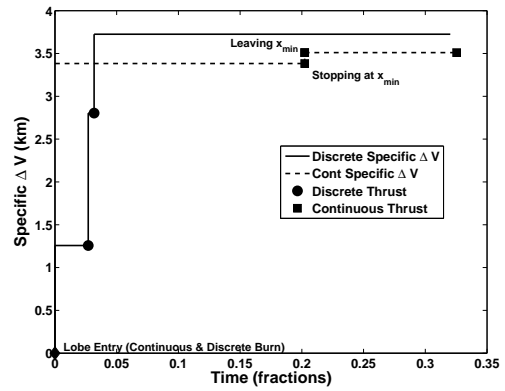
Figure 41: Case 1, Lobe 2, Legs = 2

trajectory of this leg remain nearly identical, the fuel spent is nearly 70% greater in the latter case. This splitting phenomena is due to the unrestricted bounds on each leg's time-of-flight and $\Delta\check{V}$. With no minimum time-of-flight, optimal trajectories are split into smaller pieces in order to satisfy the requirement for more legs. This is a shortcoming of the cost function as posed and should be addressed in future work. The splitting effect makes it clear that, although there are some increases to time-of-flight, there is a distinct k after which there is no improvement.

The final set of plots is for Lobe 4. The results are similar to those above, with the single leg requiring no hover from the continuous solution and some gains in

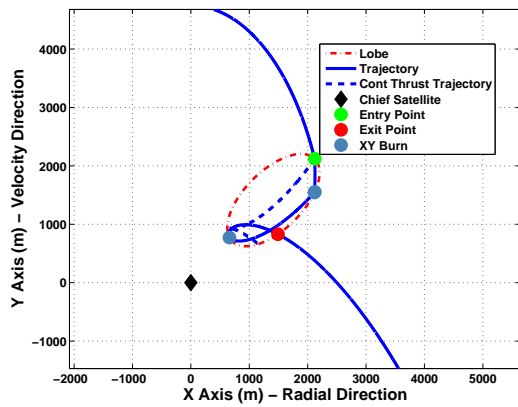


(a) $\hat{X}\hat{Y}$ Plane Trajectory

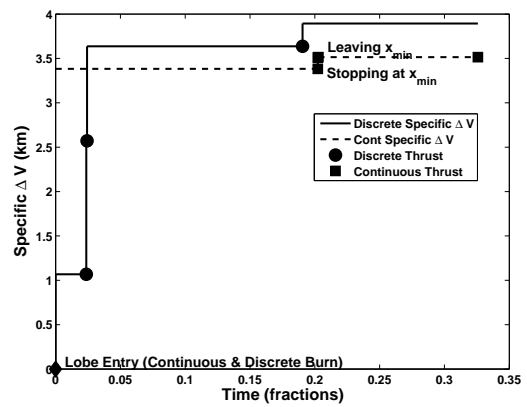


(b) Growth of $\Delta\check{V}$

Figure 42: Case 1, Lobe 2, Legs = 3



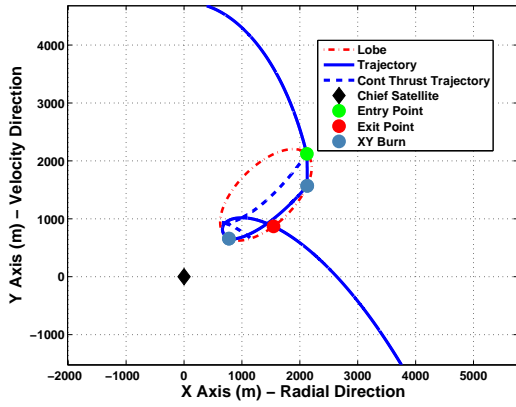
(a) $\hat{X}\hat{Y}$ Plane Trajectory



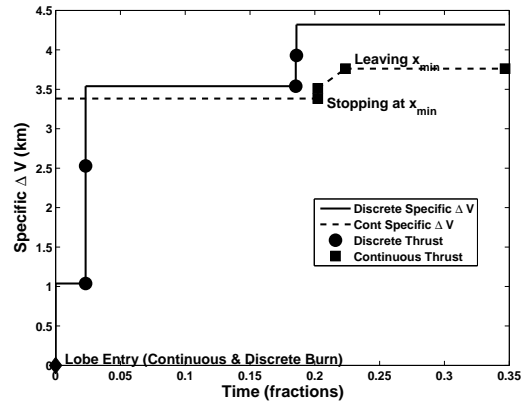
(b) Growth of $\Delta\check{V}$

Figure 43: Case 1, Lobe 2, Legs = 4

time-of-flight for higher numbers of legs. This scenario seems to split the difference between the first two as far as performance comparisons between the continuous and discrete solutions. Whereas the continuous solution provided lower fuel costs in Lobe 2 and the discrete solution marginally lower fuel costs in Lobe 3, there are examples of both in Lobe 4. For $k \leq 3$, the discrete thrust solution requires slightly less fuel while anything larger should use a continuous solution. The results of Case 1 over the three lobe shapes indicate that the orientation angle (η) strongly influences correct method choice (discrete or continuous).

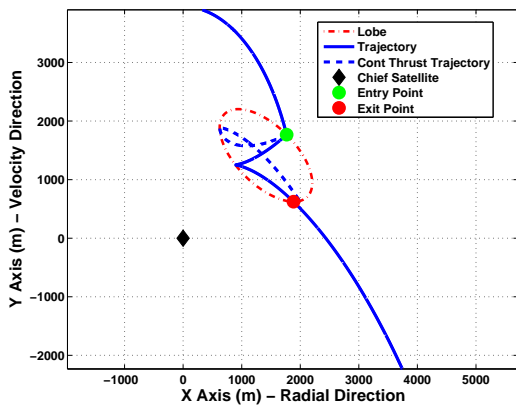


(a) $\hat{X}\hat{Y}$ Plane Trajectory

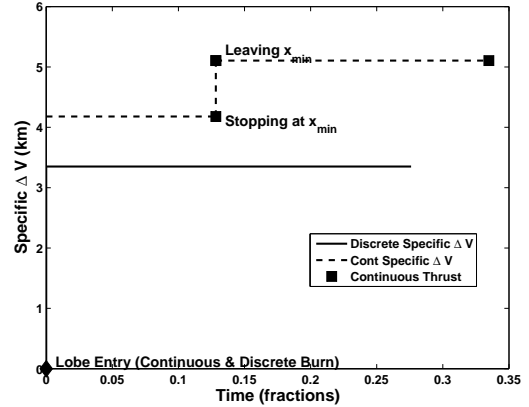


(b) Growth of $\Delta\check{V}$

Figure 44: Case 1, Lobe 2, Legs = 5

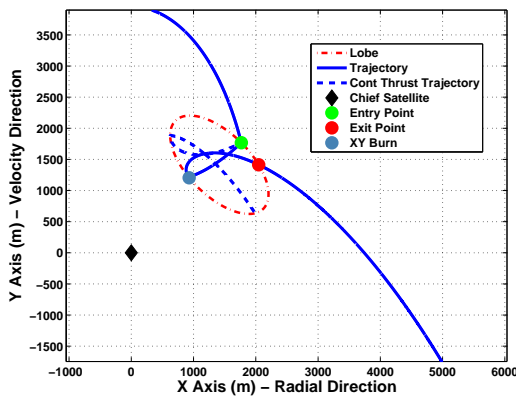


(a) $\hat{X}\hat{Y}$ Plane Trajectory

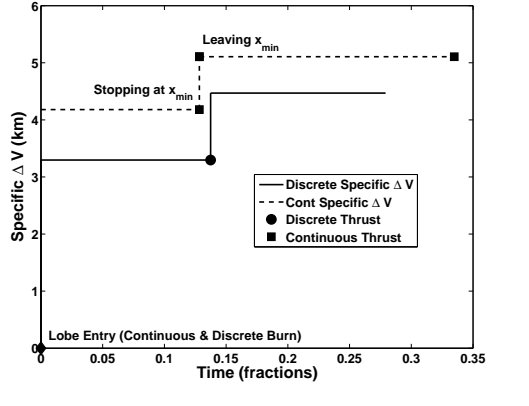


(b) Growth of $\Delta\check{V}$

Figure 45: Case 1, Lobe 3, Legs = 1

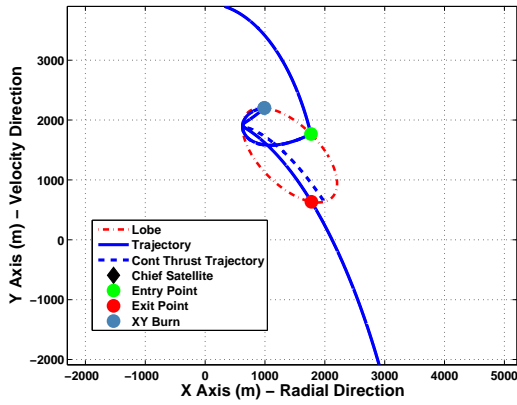


(a) $\hat{X}\hat{Y}$ Plane Trajectory

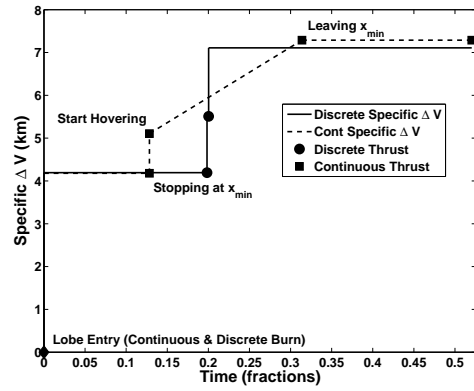


(b) Growth of $\Delta\check{V}$

Figure 46: Case 1, Lobe 3, Legs = 2

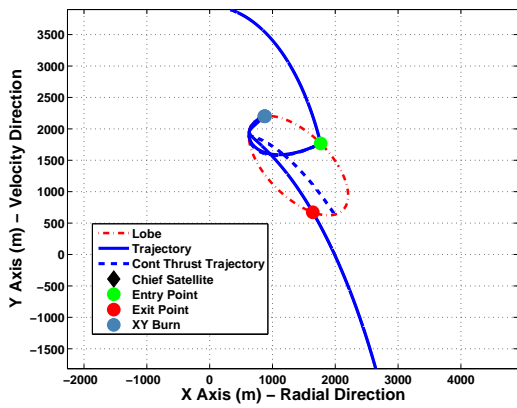


(a) $\hat{X}\hat{Y}$ Plane Trajectory

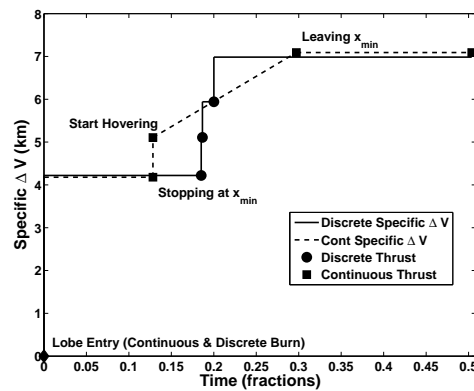


(b) Growth of $\Delta\check{V}$

Figure 47: Case 1, Lobe 3, Legs = 3

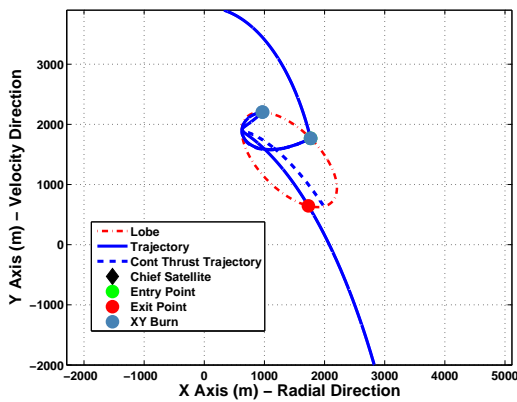


(a) $\hat{X}\hat{Y}$ Plane Trajectory

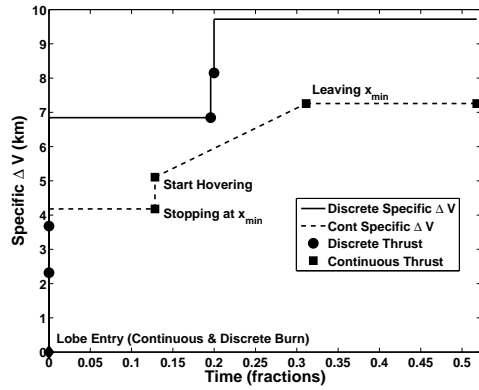


(b) Growth of $\Delta\check{V}$

Figure 48: Case 1, Lobe 3, Legs = 4

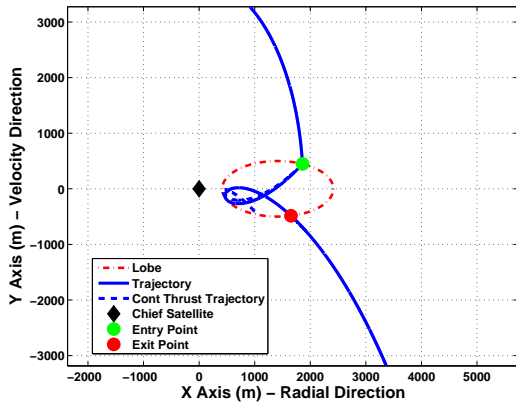


(a) $\hat{X}\hat{Y}$ Plane Trajectory

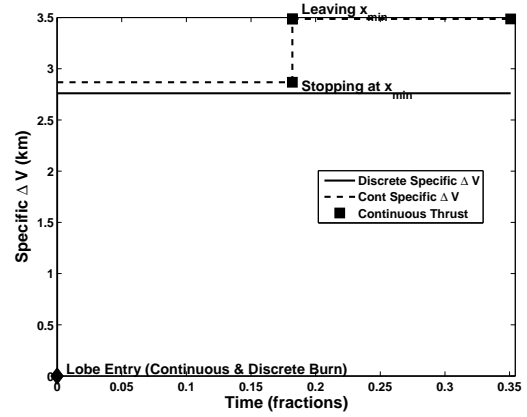


(b) Growth of $\Delta\check{V}$

Figure 49: Case 1, Lobe 3, Legs = 5

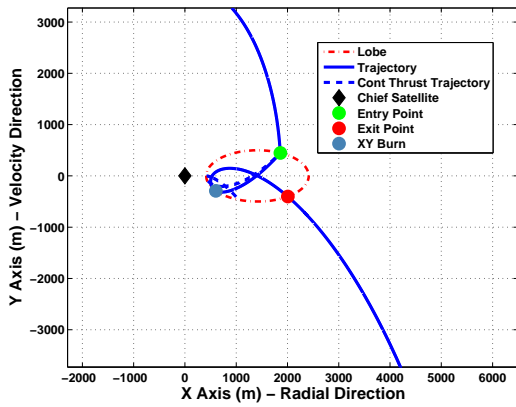


(a) $\hat{X}\hat{Y}$ Plane Trajectory

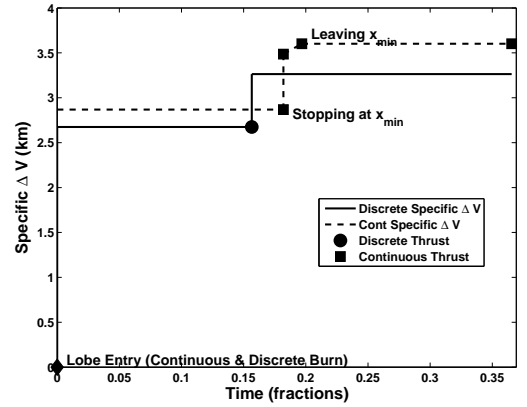


(b) Growth of $\Delta\check{V}$

Figure 50: Case 1, Lobe 4, Legs = 1

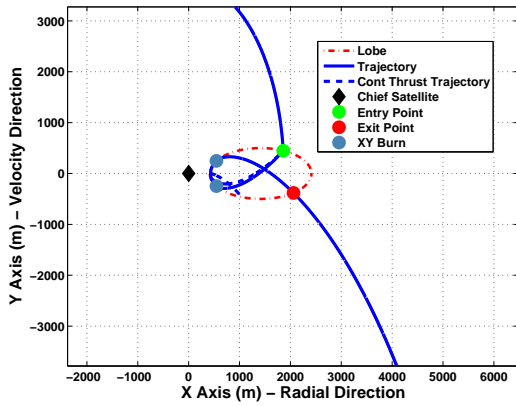


(a) $\hat{X}\hat{Y}$ Plane Trajectory

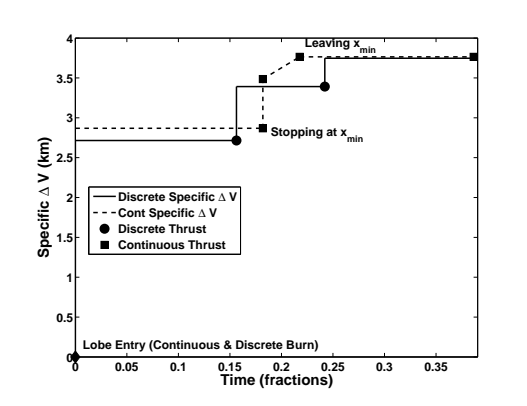


(b) Growth of $\Delta\check{V}$

Figure 51: Case 1, Lobe 4, Legs = 2

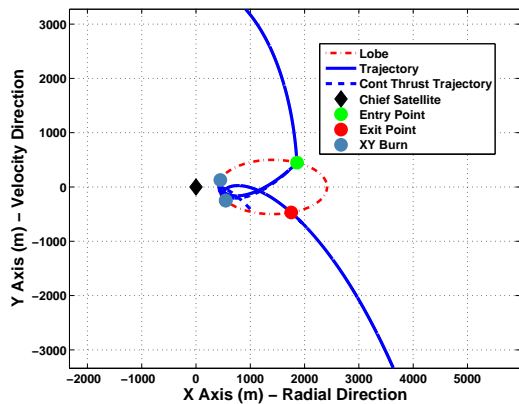


(a) $\hat{X}\hat{Y}$ Plane Trajectory

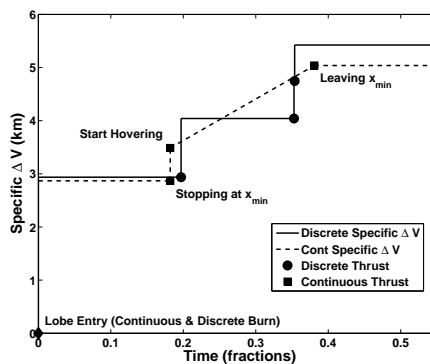


(b) Growth of $\Delta\check{V}$

Figure 52: Case 1, Lobe 4, Legs = 3

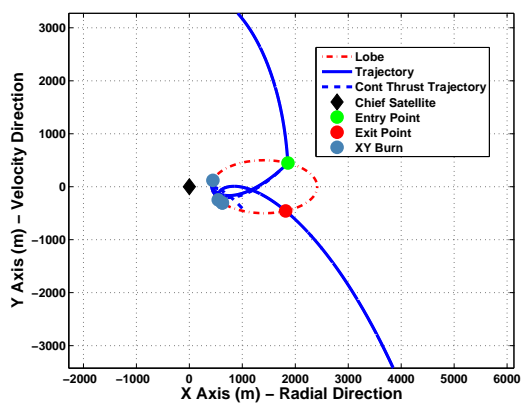


(a) $\hat{X}\hat{Y}$ Plane Trajectory

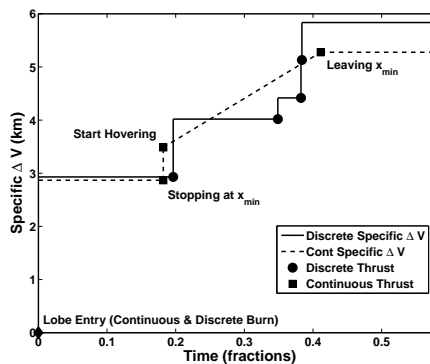


(b) Growth of $\Delta\check{V}$

Figure 53: Case 1, Lobe 4, Legs = 4



(a) $\hat{X}\hat{Y}$ Plane Trajectory



(b) Growth of $\Delta\check{V}$

Figure 54: Case 1, Lobe 4, Legs = 5

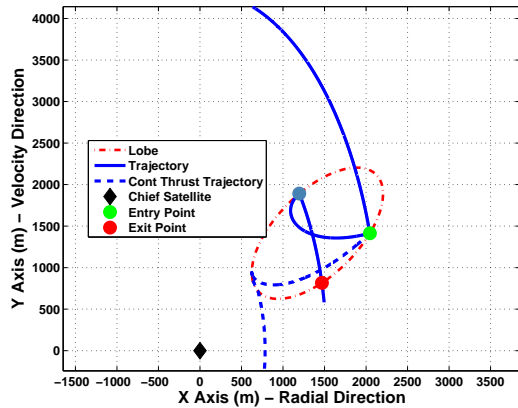
5.3 Case 2: Entry From a Closed-Relative Orbit/Exit to a Closed-Relative Orbit

The entry from and exit to a closed-relative orbit add additional constraints to the relative velocities at the entry and exit points, even though the entry/exit ψ are free parameters. The mission scenario might be for an observation or sentry satellite that is already in a near orbit with its period matched to the chief but needs to “pause” in a certain quadrant of the chief in order to perform a task and then continue on in a non-drifting closed-relative orbit that may or may not be the same as the one at entry. Like Case 1, convergence to a final trajectory happens after about two or three legs, therefore, in the interest of brevity, only $k \leq 3$ results are shown.

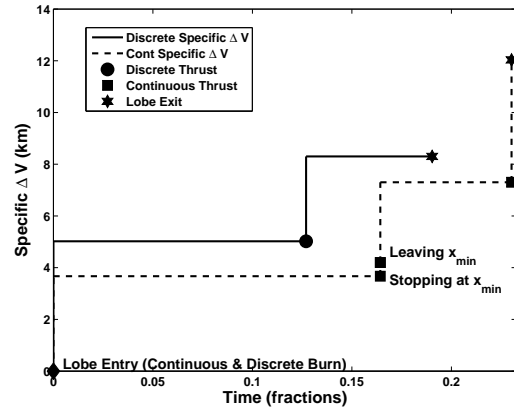
This particular exit condition presents a harsher scenario for the continuous-thrust solution. At the start of the exit leg, the deputy is at the \tilde{x}_{\min} position with zero relative velocity. The algorithm searches for a minimum-fuel ψ from which to leave the lobe under the condition that at that point, the deputy must thrust in order to match the relative velocity of a closed relative orbit. In other words, the deputy has to accelerate from zero to a fairly large relative velocity that may occur in one or two separate burns (one to leave \tilde{x}_{\min} and one to exit the lobe). On the other hand, the discrete solution does not slow to a zero relative velocity during its trajectory and therefore the final exiting ΔV is smaller. This results in discrete-thrust solutions that have significant fuel savings over the continuous solution for all three lobes.

There is one other feature of note. In the single leg of Lobe 2 and all three examples in Lobe 3, the trajectory seems to have an extra leg. This is a result of the algorithm finding an exiting closed relative orbit on which to leave that continues to pass through the lobe after the burn. The algorithm detects that the exit leg remains inside the lobe and adds the additional time-of-flight to the discrete thrust solution. For example in Figure 55, we have requested a single leg trajectory. The algorithm finds $\psi_2 = 115^\circ$ as the optimal exit point that corresponds to a closed relative orbit originating on the upper side of the lobe and finally exiting on the lower

side. The calculated time-of-flight is 0.127 fractions of a chief period; however, the algorithm determines that the final leg remains in the lobe resulting in 0.06 fractions of additional hover time.

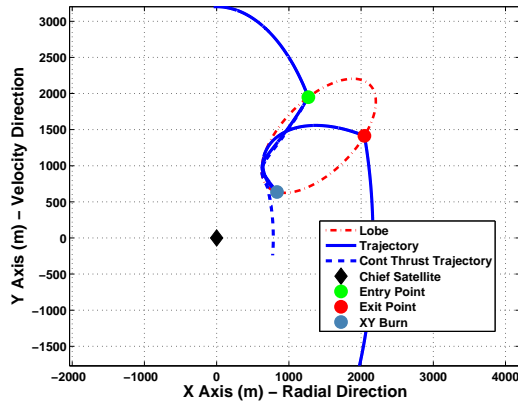


(a) $\hat{X}\hat{Y}$ Plane Trajectory

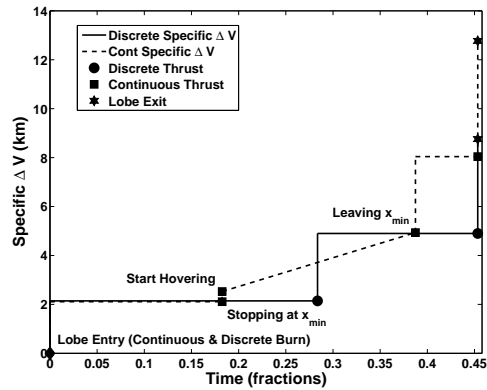


(b) Growth of $\Delta\check{V}$

Figure 55: Case 2, Lobe 2, Legs = 1

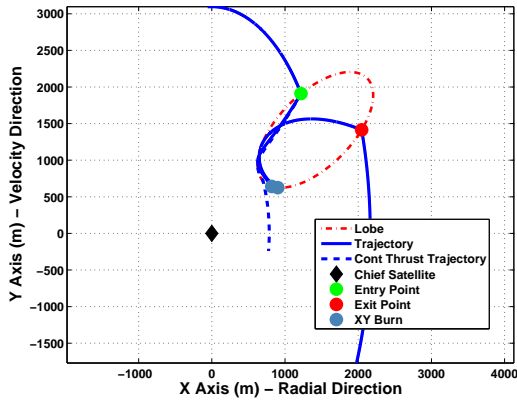


(a) $\hat{X}\hat{Y}$ Plane Trajectory

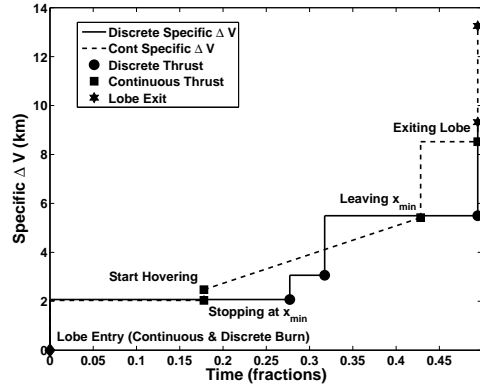


(b) Growth of $\Delta\check{V}$

Figure 56: Case 2, Lobe 2, Legs = 2

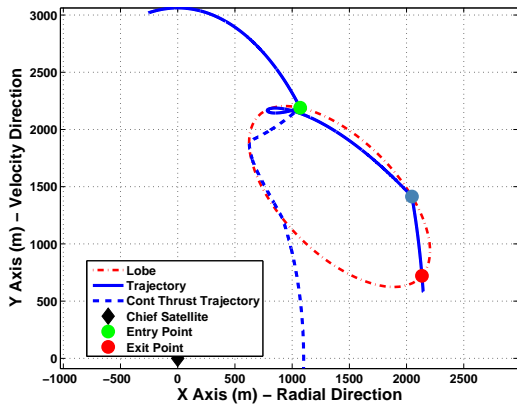


(a) $\hat{X}\hat{Y}$ Plane Trajectory

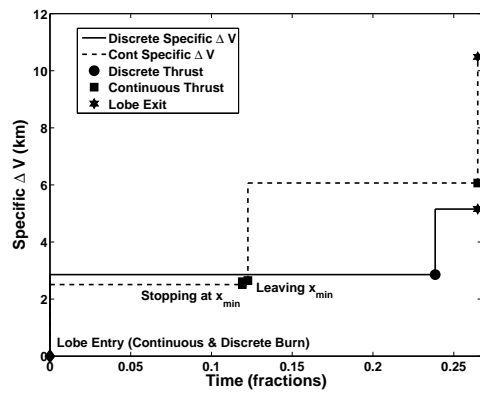


(b) Growth of $\Delta\check{V}$

Figure 57: Case 2, Lobe 2, Legs = 3

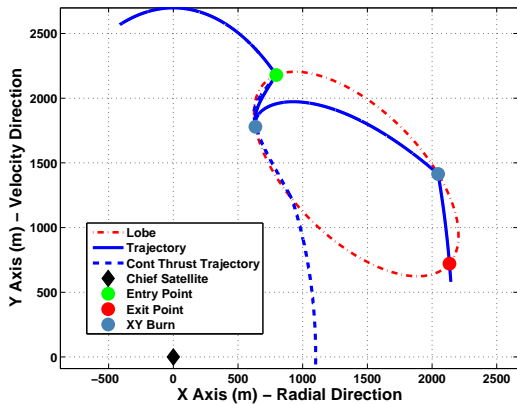


(a) $\hat{X}\hat{Y}$ Plane Trajectory

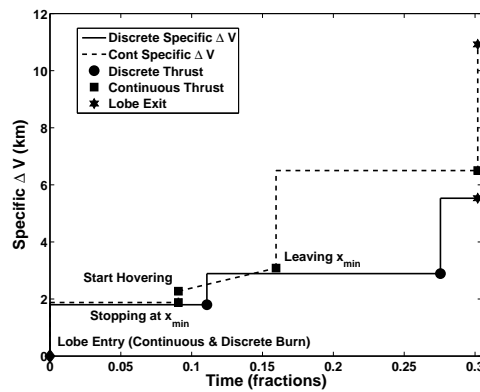


(b) Growth of $\Delta\check{V}$

Figure 58: Case 2, Lobe 3, Legs = 1

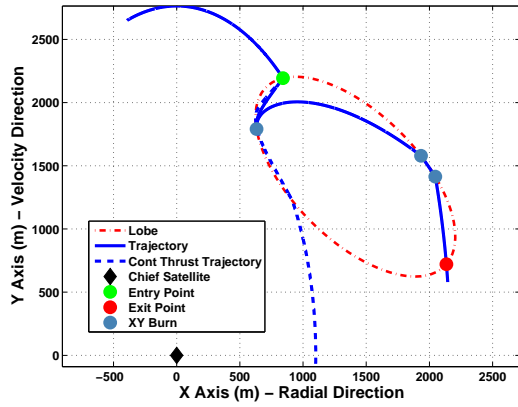


(a) $\hat{X}\hat{Y}$ Plane Trajectory

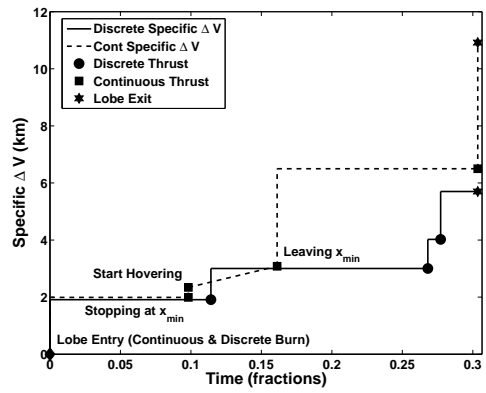


(b) Growth of $\Delta\check{V}$

Figure 59: Case 2, Lobe 3, Legs = 2

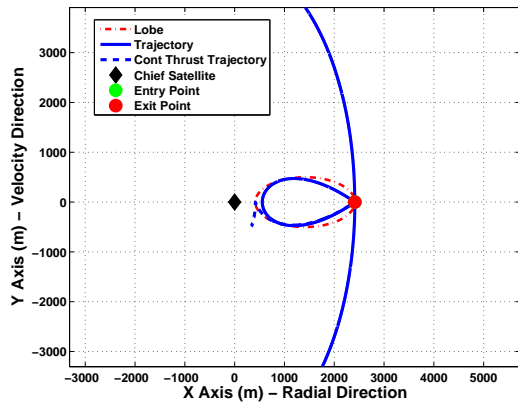


(a) $\hat{X}\hat{Y}$ Plane Trajectory

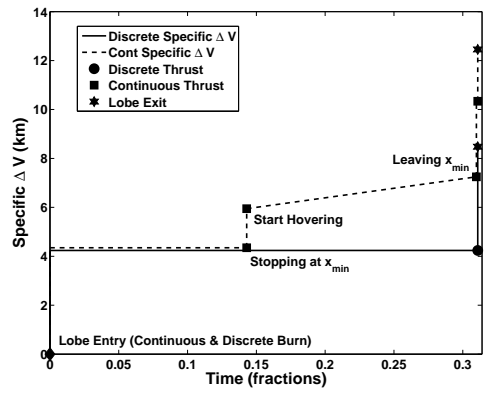


(b) Growth of $\Delta\check{V}$

Figure 60: Case 2, Lobe 3, Legs = 3

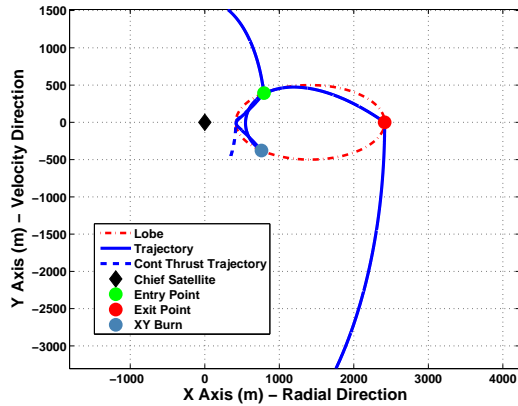


(a) $\hat{X}\hat{Y}$ Plane Trajectory

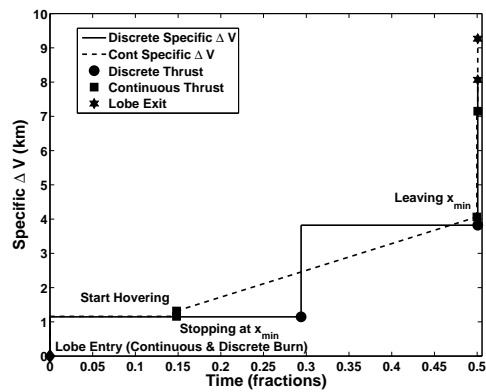


(b) Growth of $\Delta\check{V}$

Figure 61: Case 2, Lobe 4, Legs = 1

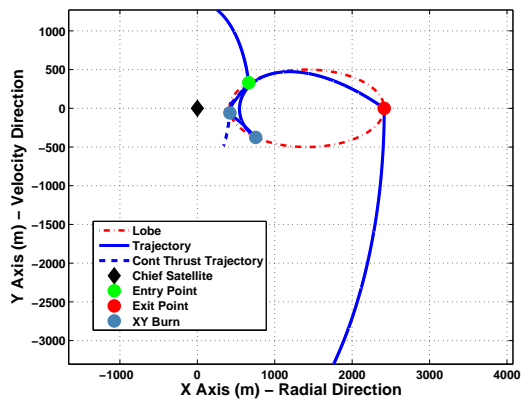


(a) $\hat{X}\hat{Y}$ Plane Trajectory

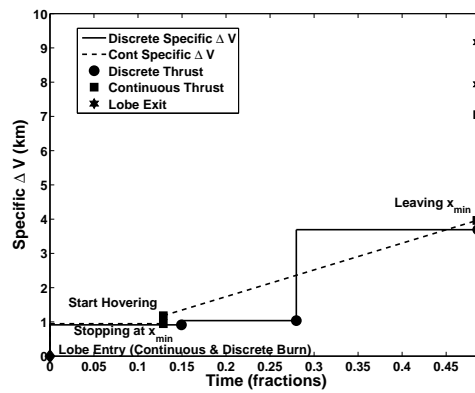


(b) Growth of $\Delta\check{V}$

Figure 62: Case 2, Lobe 4, Legs = 2



(a) $\hat{X}\hat{Y}$ Plane Trajectory



(b) Growth of $\Delta \check{V}$

Figure 63: Case 2, Lobe 4, Legs = 3

5.4 Case 3: Open Entry Condition/Repeating Hover Orbit

By specifying open entry/repeating hover, we seek to find closed trajectories that can be sustained for as long as the mission planner desires and the deputy's fuel stores last. This is done by constraining the relative position and velocity at the final point (post thrust) to be the same as the initial relative position and velocity. These closed trajectories are recommended when simply increasing the number of legs does not yield the needed total time-of-flight. Two types of closed-relative orbits are obtained by the algorithm. The first is the classic teardrop in which the trajectory intersects itself at a single point, providing an opportunity to perform an impulsive thrust and repeat the teardrop. The second is called the bounce trajectory (Figure 65) and occurs when the deputy bounces back and forth between two points. The teardrop trajectory outperforms the bounce and is the focus of further discussion.

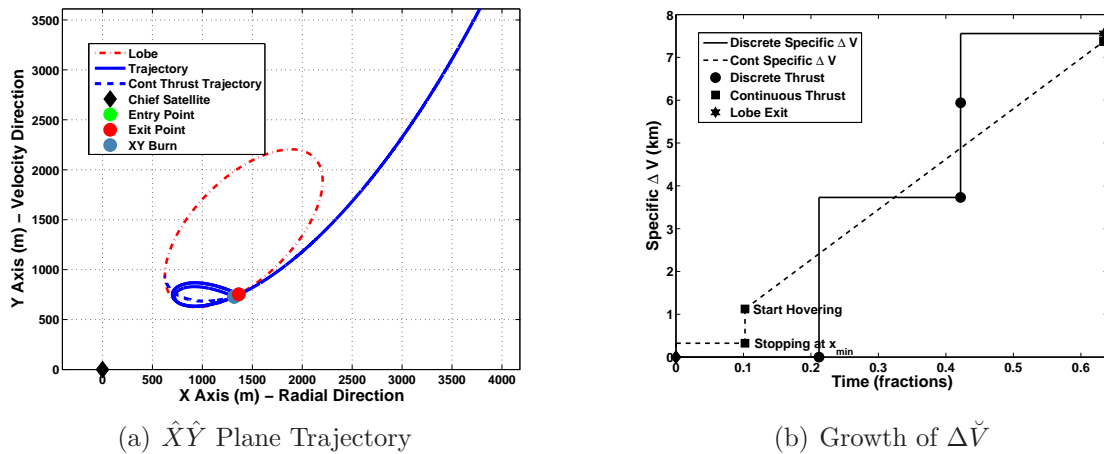
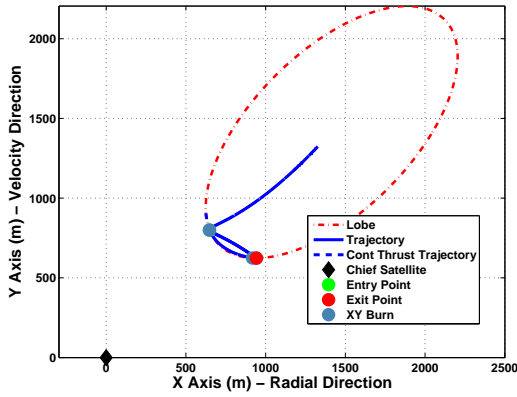
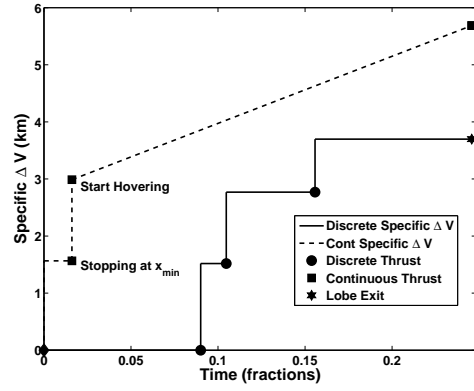


Figure 64: Case 3, Lobe 2, Legs = 3, Teardrop

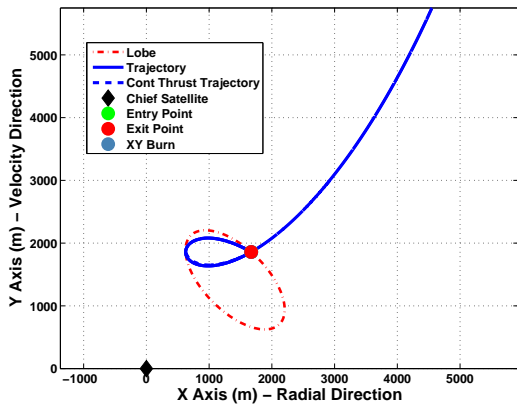


(a) $\hat{X}\hat{Y}$ Plane Trajectory

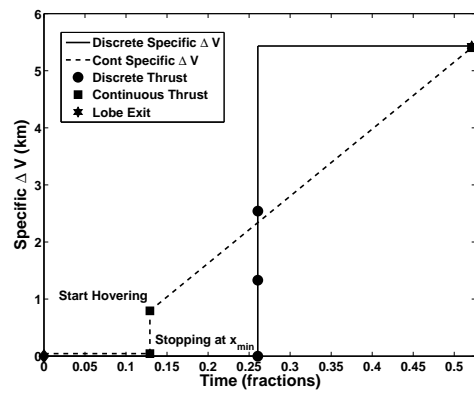


(b) Growth of $\Delta\check{V}$

Figure 65: Case 3, Lobe 2, Legs = 2, Bounce

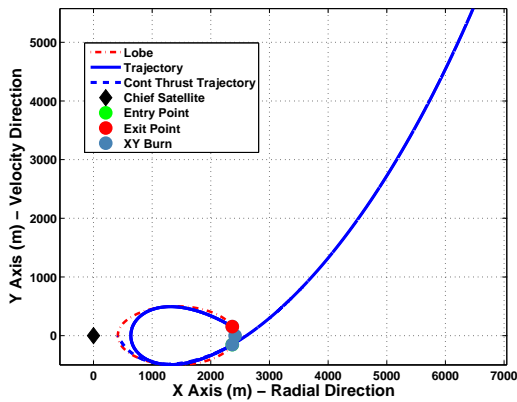


(a) $\hat{X}\hat{Y}$ Plane Trajectory

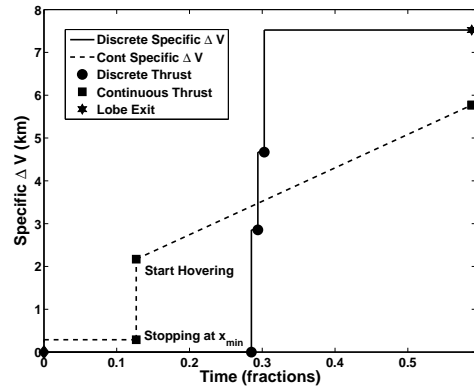


(b) Growth of $\Delta\check{V}$

Figure 66: Case 3, Lobe 3, Legs = 3, Teardrop

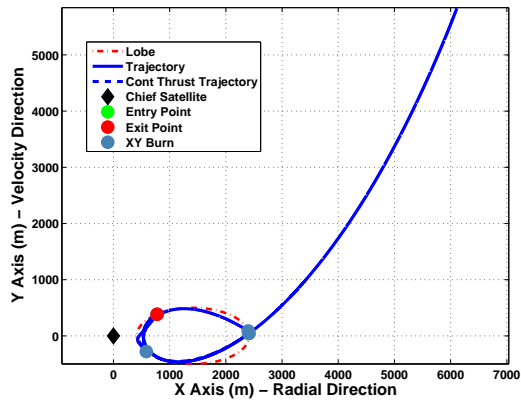


(a) $\hat{X}\hat{Y}$ Plane Trajectory

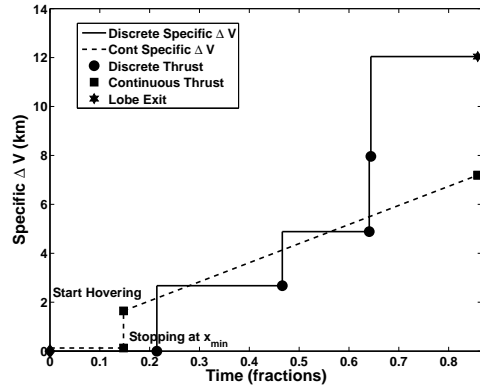


(b) Growth of $\Delta\check{V}$

Figure 67: Case 3, Lobe 4, Legs = 3, Teardrop



(a) $\hat{X}\hat{Y}$ Plane Trajectory



(b) Growth of $\Delta \check{V}$

Figure 68: Case 3, Lobe 4, Legs = 4, Teardrop

Just as the PHO analysis in Section 5.1 provided insight into a more efficient and accurate calculation of orbits about the equilibrium condition, so too does examination of the Case 3 trajectories (Figures 64-68). In all simulations, the lowest cost solution is a teardrop with expected numerical imprecisions producing orbits that are not perfect teardrops returning to a single point but close approximations. This encourages analysis of all possible teardrops and their cycle cost (ΔV per cycle). Figures 69-71 present the results of that analysis. In each example, only ψ 's that have $\tilde{T}_{\max}(\psi_1, \psi_1) > 0$ are evaluated (see Figure 16, Section 3.6 and accompanying discussion) and only for $\tilde{T} < \tilde{T}_{\max}(\psi_1, \psi_1)$, thus producing regions of no data in the cost surface. That cost surface, as seen in sub-figures (a), show that although there is a single global minimum, a family of nearly identical cost teardrops are available to a mission planner. Thus, if cycle period is an important mission parameter, a wide range of values can be selected with only small changes to cycle cost. Sub-figures (b) display a representative of this family of choices chosen for its larger time-of-flight. Sub-figures (c) demonstrate the repeating pattern of the relative specific velocities.

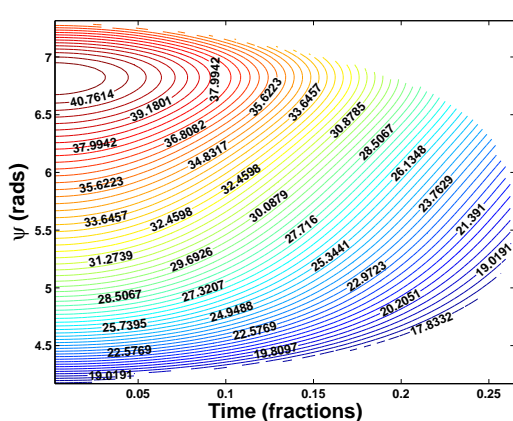
It can be shown (Appendix N) that thrusting at the apex of a teardrop in order to remain on that relative orbit is equivalent to thrusting continuously at the time-averaged x coordinate (centroid) of the teardrop (Equation (144)).

$$\bar{x}_{TD} = \frac{1}{\tilde{T}_{TD}} \int_0^{\tilde{T}_{TD}} \tilde{x}(\tilde{t}) d\tilde{t} = \frac{2(1 - \tilde{C})\tilde{x}_o}{8 - 6\pi\tilde{T}_{TD}\tilde{S} - 8\tilde{C}} \quad (30)$$

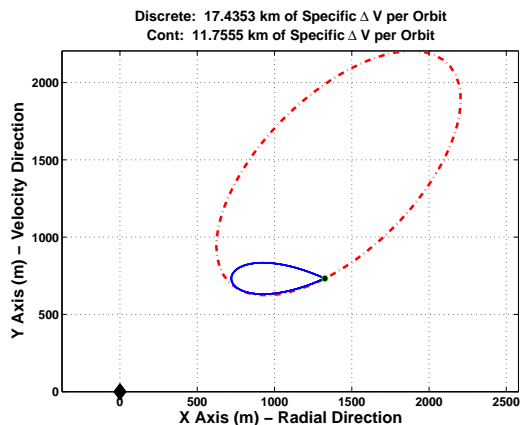
The total $\Delta\check{V}$ per cycle can be found closed form (Equation (145)):

$$\Delta\check{V}_{TD} = \frac{12\pi\tilde{T}_{TD}(1 - \tilde{C})\tilde{x}_o}{8 - 6\pi\tilde{T}_{TD}\tilde{S} - 8\tilde{C}} \quad (31)$$

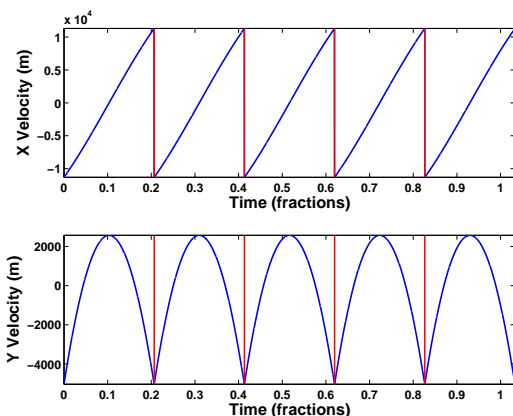
This is plotted in sub-figures (d) and track exactly with the stairstep of the discrete-thrust solution. Sub-figures (d) can be used to make decisions between the discrete and continuous solutions. Note that these solutions assume that the deputy started in the desired position (start of the teardrop for discrete and at \tilde{x}_{\min} for the continuous)



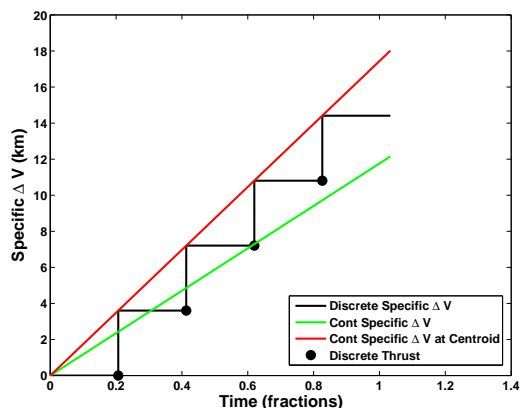
(a) ΔV Cost Per Cycle



(b) Teardrop Trajectory



(c) Relative Specific Velocity Profile



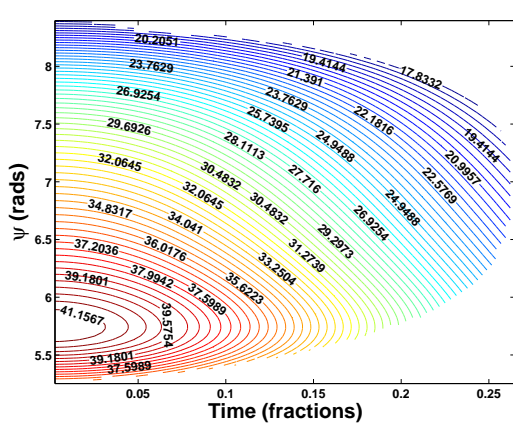
(d) Growth of $\Delta \check{V}$

Figure 69: Lobe 2 Teardrop Analysis

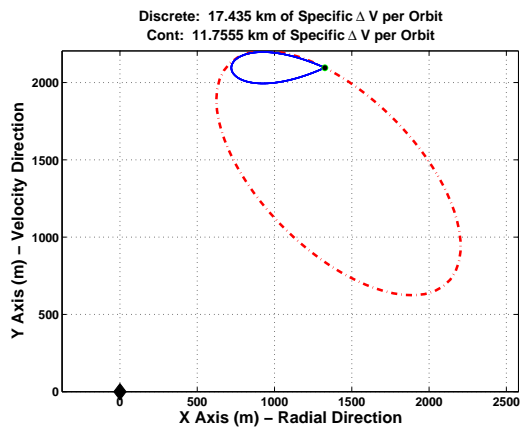
with the desired relative velocity. Fuel usage to get to those initial conditions, however, must be taken into account. That minimum-fuel solution is treated here as a simple constant added to a linear function that will shift the $\Delta \check{V}$ growth profiles up. They will not, in general, be the same for the continuous and discrete solutions. The total fuel used in the discrete solution will be

$$\Delta \check{V}_{\text{Discrete}} = \Delta \check{V}_D \left[\frac{\tilde{T}_T}{P_D} \right] + \Delta \check{V}_{D_{IC}}$$

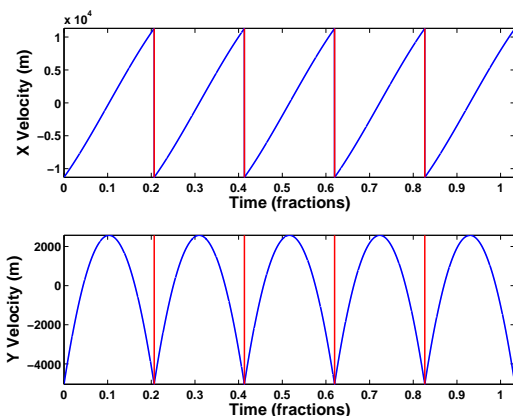
where $\Delta \check{V}_D$ is the specific ΔV required at each teardrop burn, \tilde{T}_T is the total time-of-flight required, P_D is the period of the teardrop, and $\Delta \check{V}_{D_{IC}}$ is the ΔV required to



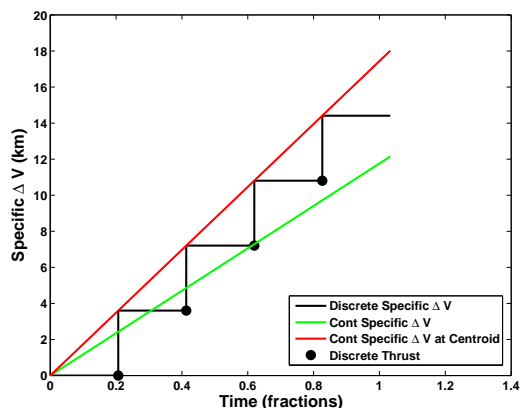
(a) ΔV Cost Per Cycle



(b) Teardrop Trajectory



(c) Relative Specific Velocity Profile



(d) Growth of $\Delta \check{V}$

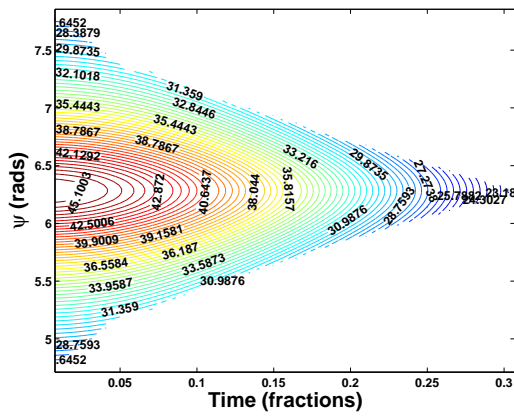
Figure 70: Lobe 3 Teardrop Analysis

get into position for the first teardrop. The continuous solution is

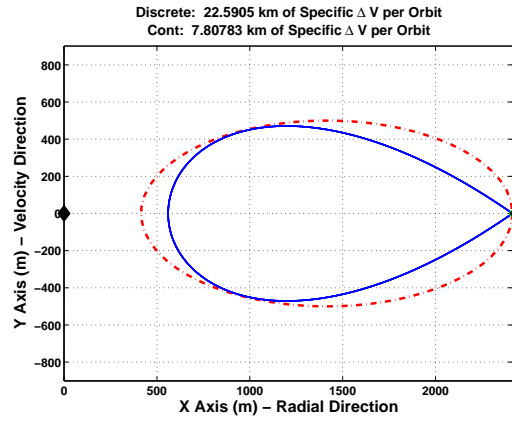
$$\Delta \check{V}_C = 6\tilde{x}_{\min}\pi\tilde{T}_T + \Delta \check{V}_{CIC}$$

In order for the discrete-thrust solution to be the fuel-optimal choice we need

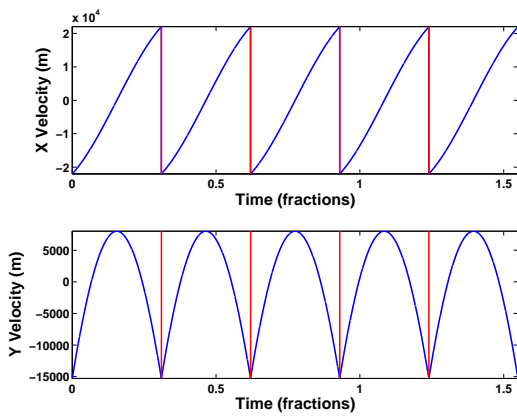
$$\begin{aligned} \Delta \check{V}_{\text{Discrete}} &< \Delta \check{V}_C \\ \Delta \check{V}_D \left[\frac{\tilde{T}_T}{P_D} \right] + \Delta \check{V}_{DIC} &< 6\tilde{x}_{\min}\pi\tilde{T}_T + \Delta \check{V}_{CIC} \\ \left[\frac{\tilde{T}_T}{P_D} \right] &< \frac{6\tilde{x}_{\min}\pi\tilde{T}_T + \Delta \check{V}_{CIC} - \Delta \check{V}_{DIC}}{\Delta \check{V}_D} \end{aligned}$$



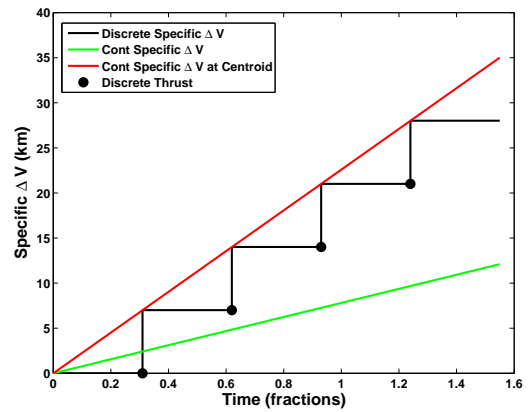
(a) ΔV Cost Per Cycle



(b) Teardrop Trajectory



(c) Relative Specific Velocity Profile



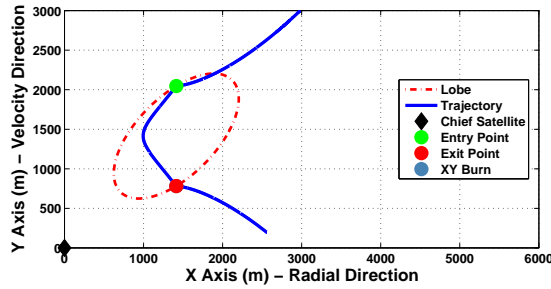
(d) Growth of $\Delta \check{V}$

Figure 71: Lobe 4 Teardrop Analysis

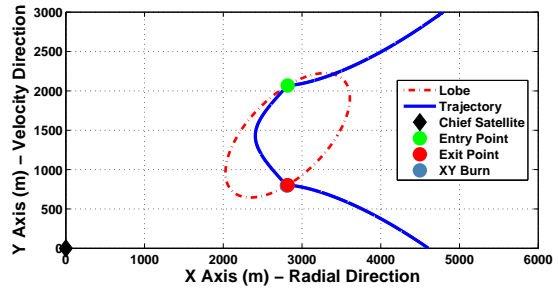
This is our criterion for choosing between a discrete and continuous solution. In all cases, the continuous solution will eventually outperform the discrete, but for a shorter total time-of-flight, it makes sense to use a discrete strategy.

5.5 Trajectory Changes Due to Increased x_L

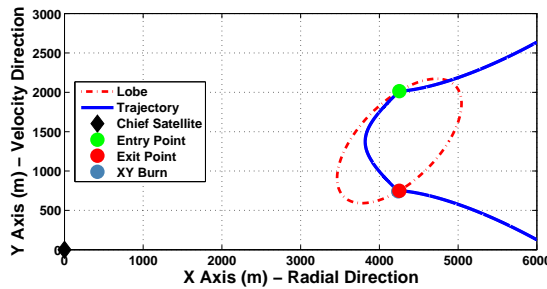
As noted in Section 3.6.7, the maximum time-of-flight between any two ψ 's decreases as the lobe is pushed farther from the \hat{Y} axis (increase in the lobe center x coordinate, x_L). This is due to larger relative velocities that are a result of larger differences in the inertial orbit period between the chief and deputy. Figure 72 shows a series of lobes with increasing x_L . In effort to compare like entry and exit conditions, this is a defined entry/defined exit, both of which have relative velocities of $(0,0,0)$. Had the entry velocity been chosen based on a closed relative orbit (as in earlier examples), the velocity would have changed dramatically as x_L increased. Defining the entry velocity as $(0,0,0)$ provides a more consistent comparison of the three simulations. Two legs were specified, but in each simulation, the second burn occurs nearly simultaneously with the exit burn. There are slight changes to the trajectory (both discrete and continuous) with increasing x_L , however, more importantly is the significant change in time-of-flight. Again, this is to be expected after examining the effect of x_L on the constraint surface and is verified here.



(a) $x_L = 1.41$ km, TOF = 0.225 fractions



(b) $x_L = 2.82$ km, TOF = 0.139 fractions

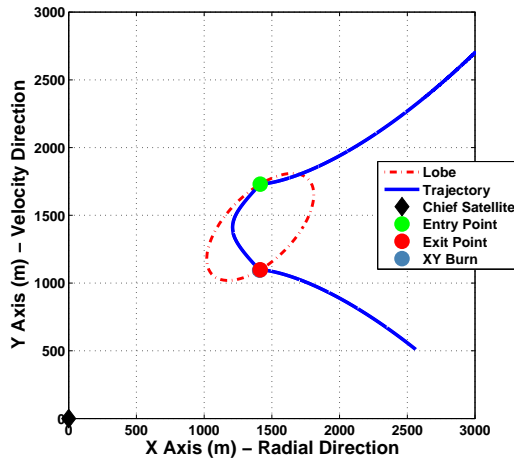


(c) $x_L = 4.25$ km, TOF = 0.109 fractions

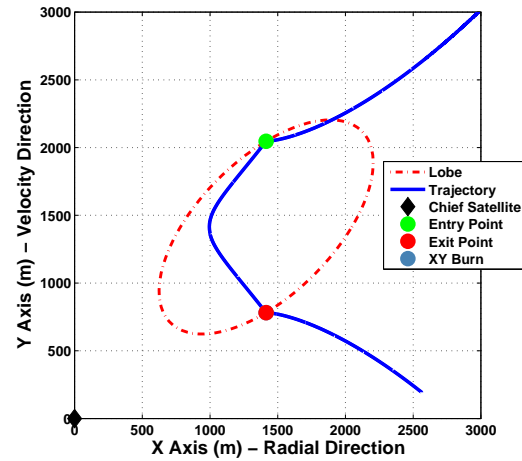
Figure 72: Defined Entry/Defined Exit, Legs = 2

5.6 Trajectory Changes Due to Increased Lobe Size

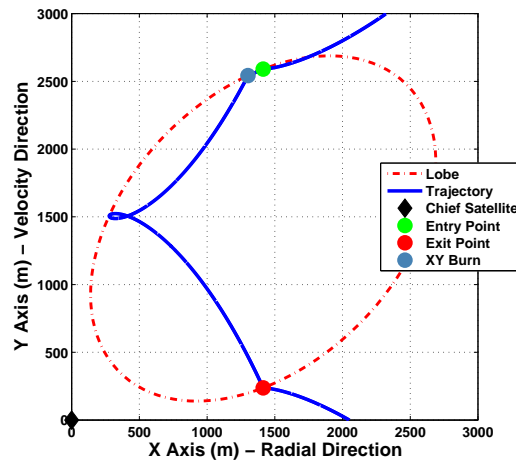
Changing the size of the lobe also has an effect on trajectory and time-of-flight. Again, from our discussion in Section 3.6.6, we know that increasing the overall size of the lobe increases the maximum time-of-flight. Figure 73 illustrates the sensitivity to lobe size. The changes in trajectory are more pronounced than they are in Section 5.5 and as expected a larger time-of-flight is produced with larger lobe size.



(a) $\tau_x = 0.5$ km, $\tau_y = 0.25$ km, TOF = 0.139 fractions



(b) $\tau_x = 1$ km, $\tau_y = 0.5$ km, TOF = 0.225 fractions



(c) $\tau_x = 1.5$ km, $\tau_y = 1$ km, TOF = 0.543 fractions

Figure 73: Defined Entry/Defined Exit, Legs = 2

5.7 Trajectory Check in Other Quadrants

As an illustration of our claim that lobes in the first quadrant are representative of lobes in each of the other quadrants (see Section 3.6), the optimization for Case 1 (Defined Entry/Open Exit) with two legs is found for the mirror of Lobe 2 (that is, $\alpha = 225^\circ$). Figure 74 compares the two trajectories and we can see that they are, as expected, identical once the rotations discussed in Section 3.2.3 are applied.

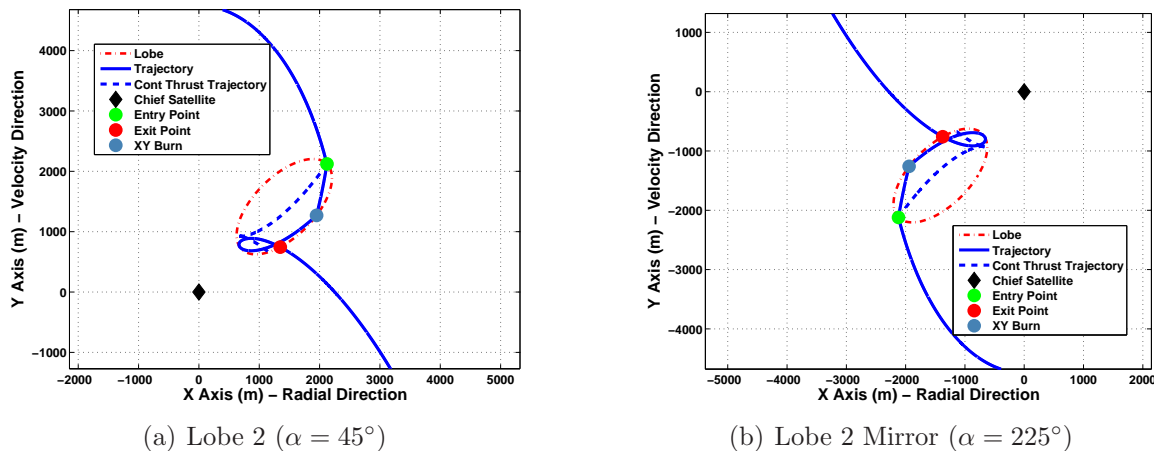
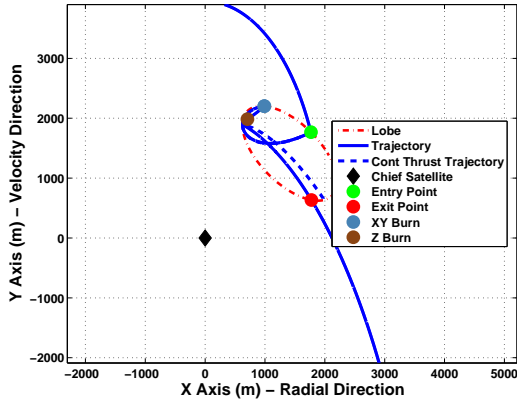


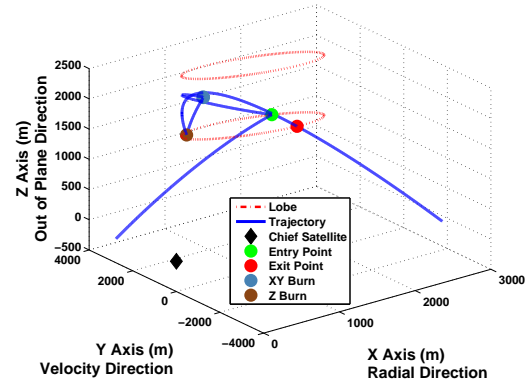
Figure 74: Comparison of Lobe 2 Results to its Mirror Lobe

5.8 Addition of \hat{Z} Axis Motion

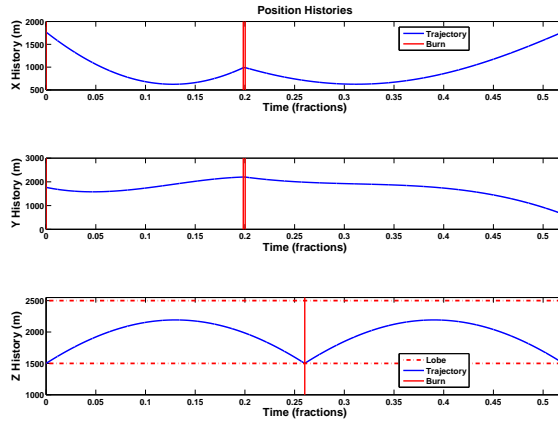
As discussed in Section 4.2, motion in the \hat{Z} direction is completely decoupled from the $\hat{X}\hat{Y}$ plane and can be calculated and appended to the $\hat{X}\hat{Y}$ solution independently. A few examples of this, based on previous results, are provided below.



(a) $\hat{X}\hat{Y}$ Plane

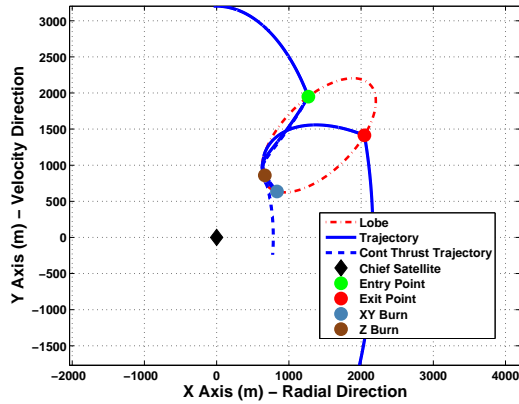


(b) 3D Trajectory

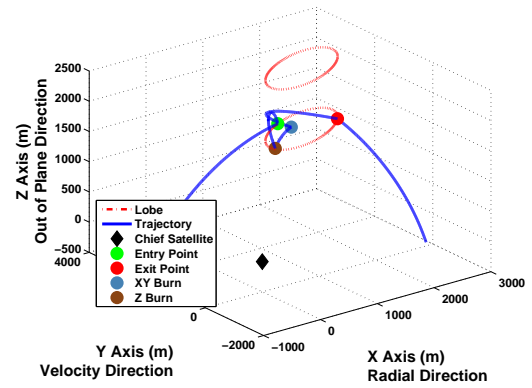


(c) Position History

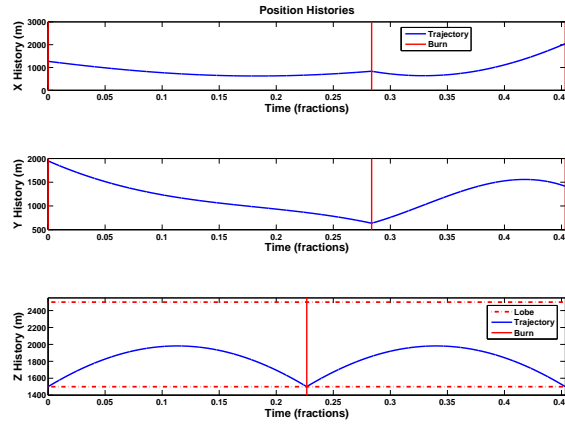
Figure 75: Case 1, Lobe 3, Legs = 3, $\beta = 45^\circ$, $h = 0.5$ km



(a) $\hat{X}\hat{Y}$ Plane

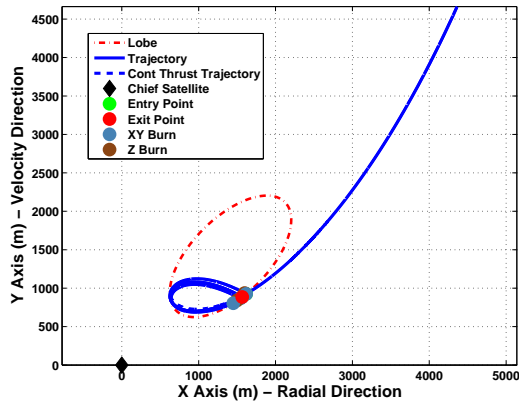


(b) 3D Trajectory

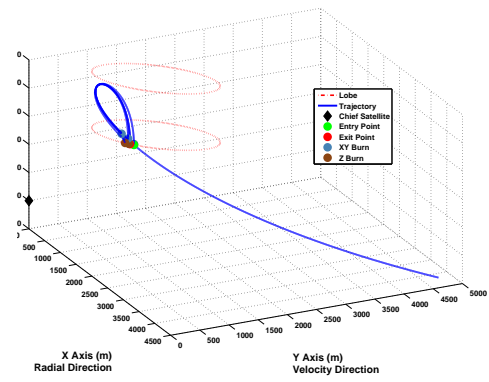


(c) Position History

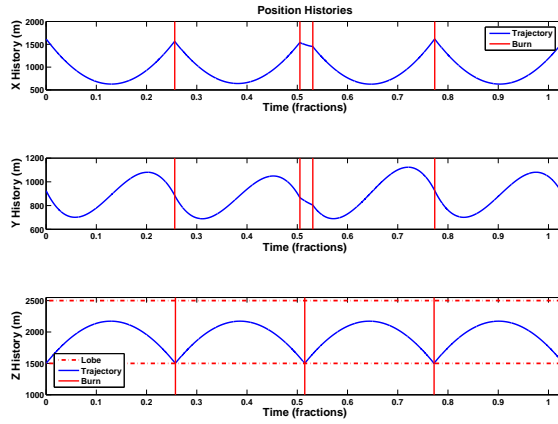
Figure 76: Case 2, Lobe 2, Legs = 2, $\beta = 45^\circ$, $h = 0.5$ km



(a) $\hat{X}\hat{Y}$ Plane



(b) 3D Trajectory



(c) Position History

Figure 77: Case 3, Lobe 2, Legs = 4, $\beta = 45^\circ$, $h = 0.5$ km

5.9 Results from Elliptical Chief Orbit

The elliptical chief results are not much different from what has been presented in the circular case. Recall that, unlike the circular case that can use a single constraint surface, the elliptical maximum time-of-flight is a function of initial true anomaly. This means that practical calculation of an optimal trajectory using precomputed constraint surfaces requires a library of those surfaces discretized over true anomaly. The following result is for a single leg on Lobe 2, with defined entry ($\psi_1 = 45^\circ$) and open exit with an entry velocity of $(0,0,0)$. It demonstrates that results from the elliptical case can be found with no change to the cost function and are similar to the circular case (compare to Figure 40).

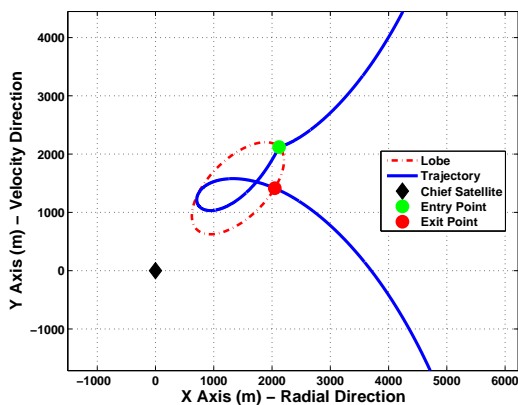


Figure 78: Case 1, Lobe 2, Legs = 1, Elliptical Chief Orbit

5.10 Summary

The results produced above show that there are a wide variety of practical lobes available to mission planners. There are also simple tests to indicate the most fuel-optimal method (continuous or discrete) to use for a specified lobe, entry/exit conditions, and required total time-of-flight. It is also important to note that there are mission scenarios for which a discrete-thrust method is preferable even if it is less fuel-optimal than the continuous. Issues such as stealth, plume impingement on the chief, and sensor vibrations may lead a mission planner to the discrete strategy.

VI. Conclusions and Recommendations

The goal of this research was to answer two questions. The first, “Can a discrete trajectory be found that outperforms the benchmark continuous-thrust solution for a fuel criterion of optimality?” The second is, “Can we quickly and robustly estimate, with reasonable accuracy, the amount of ΔV required to stay in a specific lobe?”

The answer to the first question is a qualified yes. The qualification is that it can be accomplished only in certain combinations of entry/exit conditions and then only for a relatively short total time-of-flight. In fact, entry/exit conditions appear to have the greatest effect on which strategy is fuel-optimal. For a mission planner attempting to decide between a discrete- and continuous-thrust solution for a given lobe and entry/exit conditions, he or she should start with a single leg and find optimal trajectories for about $k < 5$. If any of these meet the total time-of-flight required, then a simple check of the ΔV growth charts will indicate the fuel-optimal method. If the total time-of-flight cannot be satisfied by increasing the number of legs, an evaluation of repeating hover orbits is needed, as discussed in Section 5.4, in which a simple test can determine the best choice of longer-term hovering orbits. As mentioned in Section 5.10, there may be other concerns besides fuel-optimality that may lead a mission planner to the discrete solution.

The answer to the second question is a definite yes. The continuous-thrust solution is robustly and rapidly calculated without any pre-computing of the constraint surface. It is also a very reasonable estimate of the total ΔV required to hover in a specific lobe. That estimate can be scaled by the inverse of the chief’s mean motion (n) to get the actual ΔV cost for a given sized orbit. The ability to compare all possible size chief orbits is a very important aspect of this research.

A first step was made towards applying this technique to relative motion about chiefs in elliptical orbits. Although it is much more computationally expensive to calculate the relative velocities and to pre-compute a family of constraint surfaces with different true anomalies, the core method of using a minimum-fuel per time-of-flight cost function and a maximum time-of-flight constraint surface is sound.

Proximity operations and hovering specifically are fuel-expensive operations to perform and will only be undertaken when mission needs are great. These tasks are not however out of the ΔV capability range of current micro-satellites.

6.1 Contributions

Although work in the realm of relative satellite motion and proximity operations has been extensive, this research has added several contributions to the field. Most significantly, this research enables mission planners to search for and compare continuous and discrete fuel-optimal trajectories that are constrained to remain within a lobe of the user's choosing and are not tied to a particular chief semi-major axis or μ . In completing that task, several minor contributions were also made:

1. Created a set of mission-realistic lobe entry and lobe exit conditions for use in initializing trajectories
2. Provided an analysis of maximum time-of-flight surfaces and their sensitivity to various factors
3. Developed a simplified optimization routine for finding persistent hover orbits that intersect the \hat{Y} axis
4. Derived a closed-form solution for optimal hovering along the \hat{Z} axis that is independent of the trajectory in the $\hat{X}\hat{Y}$ plane
5. Applied this method to an elliptical chief orbit scenario
6. Provided a full derivation of the partial derivatives of the cost function

Mission Impact: This research enhances USAF proficiency in satellite proximity operations and space situational awareness by enabling a practical method of finding relative motion trajectories that allow hovering near a chief satellite.

6.2 Topics for Future Research

This research provides only the first step into hovering orbits. A wide array of topics are available to future researchers

1. Expand the work on hovering about chiefs in elliptical orbits to include newer research on more efficient relative velocity calculations.
2. Re-pose the cost function or add constraints to allow the possibility of thrust points interior to the lobe. Compare those results to those trajectories produced when thrusting is allowed only on the lobe boundary.
3. Apply additional constraints such as total time-of-flight or minimum ΔV per burn to the cost function. This may prevent the thrust splitting phenomena documented in Chapter V and would allow inclusion of hardware related constraints.
4. Include attitude control in addition to trajectory planning for completeness of the total mission requirements. What if we wanted the deputy pointing towards the chief while it is hovering?
5. Develop a strategy to include additional thrusts that correct the trajectory for perturbations and equations of motion linearization errors. This is especially important for repeating hover orbits that may drift out of the lobe over time.

Appendix A. Math Preliminaries

This appendix contains mathematical theorems and proofs that are used in subsequent derivations. None of these derivations are original to this work nor particularly hard to find in mathematical or engineering texts. They are, however, key to later derivations and included here for completeness and to put them into dissertation notation.

A.1 Theorem: Radius of an Ellipse

The radius of an ellipse measured from the origin is

$$r = \frac{ab}{\sqrt{a^2 \sin^2 \theta + b^2 \cos^2 \theta}}$$

with all variables as defined in Figure 79.

Proof:

Referencing Figure 79, choose an arbitrary point (x, y) on an ellipse that is centered

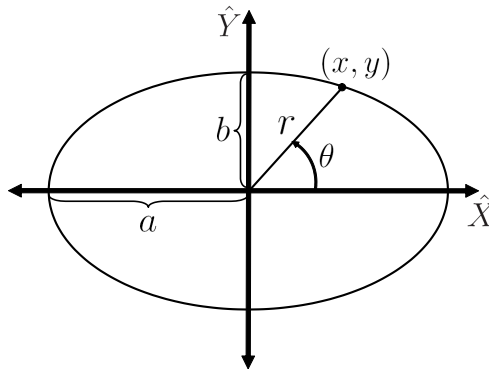


Figure 79: Ellipse Centered on the Origin

at the origin. In polar form:

$$x = r \cos \theta$$

$$y = r \sin \theta$$

Substituting these equations into the standard form of an ellipse,

$$\frac{x^2}{a^2} + \frac{y^2}{b^2} = 1$$

$$\frac{r^2 \cos^2 \theta}{a^2} + \frac{r^2 \sin^2 \theta}{b^2} = 1$$

solving for r ,

$$r^2 \left[\frac{\cos^2 \theta}{a^2} + \frac{\sin^2 \theta}{b^2} \right] = 1$$

$$r^2 [b^2 \cos^2 \theta + a^2 \sin^2 \theta] = a^2 b^2$$

$$r^2 = \frac{a^2 b^2}{b^2 \cos^2 \theta + a^2 \sin^2 \theta}$$

we find that,

$$r = \frac{ab}{\sqrt{b^2 \cos^2 \theta + a^2 \sin^2 \theta}} \quad (32)$$

A.2 *Theorem: The Inertial Derivative*

The derivative of a vector defined in a rotating reference frame is

$$\hat{i}\hat{j}\hat{k}\frac{d(\vec{V})}{dt} = \hat{x}\hat{y}\hat{z}\frac{d(\vec{V})}{dt} + \omega \times \vec{V}$$

where ω is the angular velocity of the $\hat{X}\hat{Y}\hat{Z}$ frame with respect to the $\hat{I}\hat{J}\hat{K}$ frame and the notation $\hat{i}\hat{j}\hat{k}\frac{d(\vec{V})}{dt}$ indicates a derivative taken in the $\hat{I}\hat{J}\hat{K}$ frame.

Proof:

The following is a modification of the derivation given in Wiesel [63]. Let $\hat{I}\hat{J}\hat{K}$ be the inertial frame and $\hat{X}\hat{Y}\hat{Z}$ a rotating local reference frame and let the vector \vec{V} be defined in the $\hat{X}\hat{Y}\hat{Z}$ frame, then

$$\vec{V} = V_x \hat{X} + V_y \hat{Y} + V_z \hat{Z}$$

Taking the derivative using the chain rule

$$\hat{i}\hat{j}\hat{k}\frac{d\vec{V}}{dt} = V_x\hat{i}\hat{j}\hat{k}\frac{d\hat{X}}{dt} + \dot{V}_x\hat{X} + V_y\hat{i}\hat{j}\hat{k}\frac{d\hat{Y}}{dt} + \dot{V}_y\hat{Y} + V_z\hat{i}\hat{j}\hat{k}\frac{d\hat{Z}}{dt} + \dot{V}_z\hat{Z} \quad (33)$$

Noting that

$$\hat{x}\hat{y}\hat{z}\frac{d\vec{V}}{dt} = \dot{V}_x\hat{X} + \dot{V}_y\hat{Y} + \dot{V}_z\hat{Z}$$

The changes in the $\hat{X}\hat{Y}\hat{Z}$ frame unit vectors can be found by referencing Figure 80. Assume the local frame has rotated during the period Δt . This rotation is formed by inspection of Figure 80.

$$\begin{aligned} \hat{X}' &= \cos(\omega\Delta t)\hat{X} + \sin(\omega\Delta t)\hat{Y} \\ \hat{Y}' &= -\sin(\omega\Delta t)\hat{X} + \cos(\omega\Delta t)\hat{Y} \\ \hat{Z}' &= \hat{Z} \end{aligned}$$

Thus

$$\begin{aligned} \Delta\hat{X} &= \hat{X}' - \hat{X} = \cos(\omega\Delta t)\hat{X} + \sin(\omega\Delta t)\hat{Y} - \hat{X} = [\cos(\omega\Delta t) - 1]\hat{X} + \sin(\omega\Delta t)\hat{Y} \\ \Delta\hat{Y} &= \hat{Y}' - \hat{Y} = -\sin(\omega\Delta t)\hat{X} + \cos(\omega\Delta t)\hat{Y} - \hat{Y} = -\sin(\omega\Delta t)\hat{X} + [\cos(\omega\Delta t) - 1]\hat{Y} \\ \Delta\hat{Z} &= \hat{Z}' - \hat{Z} = 0 \end{aligned}$$

As Δt goes to 0

$$\begin{aligned} \omega\Delta t &\rightarrow \omega dt \\ \Delta\hat{X} &\rightarrow d\hat{X} \\ \Delta\hat{Y} &\rightarrow d\hat{Y} \\ \cos(\omega\Delta t) &\rightarrow 1 \\ \sin(\omega\Delta t) &\rightarrow \omega dt \end{aligned}$$

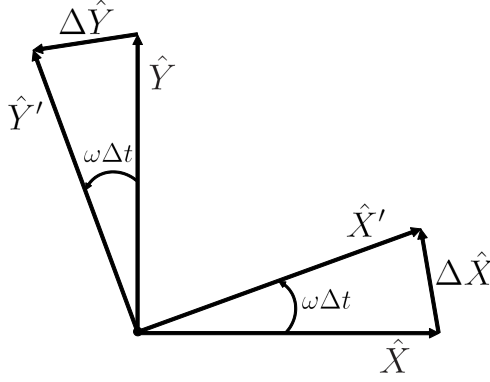


Figure 80: Derivatives of the $\hat{X}\hat{Y}\hat{Z}$ Frame Unit Vectors

then

$$\begin{aligned} d\hat{X} &= \Delta\hat{X} = \omega dt \hat{Y} \\ d\hat{Y} &= \Delta\hat{Y} = -\omega dt \hat{X} \end{aligned}$$

Dividing through by dt

$$\begin{aligned} \hat{i}\hat{j}\hat{k} \frac{d\hat{X}}{dt} &= \omega \hat{Y} \\ \hat{i}\hat{j}\hat{k} \frac{d\hat{Y}}{dt} &= -\omega \hat{X} \\ \hat{i}\hat{j}\hat{k} \frac{d\hat{Z}}{dt} &= 0 \end{aligned}$$

Equation (33) becomes

$$\begin{aligned} \hat{i}\hat{j}\hat{k} \frac{d\vec{V}}{dt} &= \hat{x}\hat{y}\hat{z} \frac{d\vec{V}}{dt} + V_x \omega \hat{Y} - V_y \omega \hat{X} + 0\hat{Z} \\ &= \hat{x}\hat{y}\hat{z} \frac{d\vec{V}}{dt} + \begin{vmatrix} \hat{X} & \hat{Y} & \hat{Z} \\ 0 & 0 & \omega \\ V_x & V_y & V_z \end{vmatrix} \end{aligned}$$

Therefore the inertial derivative is

$${}_{iJK}\frac{d\vec{V}}{dt} = {}_{\hat{x}\hat{y}\hat{z}}\frac{d\vec{V}}{dt} + \omega \times \vec{V} \quad (34)$$

A.3 Theorem: The Harmonic Addition Theorem

The following derivation is taken from Reference [61]. The sum of two sinusoids is equal to:

$$\begin{aligned} a \cos \theta + b \sin \theta &= \sqrt{a^2 + b^2} \cos \left[\theta - \tan^{-1} \left(\frac{b}{a} \right) \right] \\ a \cos \theta + b \sin \theta &= \sqrt{a^2 + b^2} \sin \left[\theta + \tan^{-1} \left(\frac{a}{b} \right) \right] \end{aligned}$$

Proof:

Let

$$f(\theta) = a \cos \theta + b \sin \theta$$

Assume we want to express this as a function of a single sinusoid

$$f(\theta) = c \cos(\theta + \omega)$$

Expanding the above equation [53]

$$f(\theta) = c \cos \theta \cos \omega - c \sin \theta \sin \omega$$

which means

$$a = c \cos \omega$$

$$b = -c \sin \omega$$

Finding c

$$a^2 + b^2 = c^2 \cos^2 \omega + c^2 \sin^2 \omega = c^2$$

and ω

$$\frac{b}{a} = \frac{-c \sin \omega}{c \cos \omega} = -\tan \omega$$

thus

$$\begin{aligned} c &= \sqrt{a^2 + b^2} \\ \omega &= \tan^{-1} \left(-\frac{b}{a} \right) = -\tan^{-1} \left(\frac{b}{a} \right) \end{aligned}$$

Therefore

$$a \cos \theta + b \sin \theta = \sqrt{a^2 + b^2} \cos \left[\theta - \tan^{-1} \left(\frac{b}{a} \right) \right] \quad (35)$$

We can also express this in terms of a sine function. Let

$$f(\theta) = c \sin(\theta + \omega)$$

Expanding [53]

$$f(\theta) = c \sin \theta \cos \omega + c \cos \theta \sin \omega$$

which means

$$a = c \sin \omega$$

$$b = c \cos \omega$$

Finding c

$$a^2 + b^2 = c^2 \sin^2 \omega + c^2 \cos^2 \omega = c^2$$

and ω

$$\frac{a}{b} = \frac{c \sin \omega}{c \cos \omega} = \tan \omega$$

thus

$$\begin{aligned} c &= \sqrt{a^2 + b^2} \\ \omega &= \tan^{-1} \left(\frac{a}{b} \right) \end{aligned}$$

Therefore

$$a \cos \theta + b \sin \theta = \sqrt{a^2 + b^2} \sin \left[\theta + \tan^{-1} \left(\frac{a}{b} \right) \right] \quad (36)$$

A.4 Theorem: Partial Derivative of $u'RR'u$ with Respect to a Scalar (u is a Function of the Scalar)

The following derivation is introduced in [33]. Let R be an $i \times j$ matrix and let the components of u be functions of the scalar v ; then

$$\frac{\partial (u'RR'u)}{\partial v} = 2u'RR' \frac{\partial u}{\partial v}$$

Proof:

Let

$$\begin{aligned} A &= u'RR'u = \begin{bmatrix} u_1 & u_2 & \dots & u_i \end{bmatrix} \begin{bmatrix} r_{11} & r_{12} & \dots & r_{1j} \\ r_{21} & r_{22} & \dots & r_{2j} \\ \vdots & \vdots & \ddots & \vdots \\ r_{i1} & r_{i2} & \dots & r_{ij} \end{bmatrix} \begin{bmatrix} r_{11} & r_{21} & \dots & r_{i1} \\ r_{12} & r_{22} & \dots & r_{i2} \\ \vdots & \vdots & \ddots & \vdots \\ r_{1j} & r_{2j} & \dots & r_{ij} \end{bmatrix} \begin{bmatrix} u_1 \\ u_2 \\ \vdots \\ u_i \end{bmatrix} \\ &= \begin{bmatrix} (u_1r_{11} + \dots + u_i r_{i1}) & (u_1r_{12} + \dots + u_i r_{i2}) & \dots & (u_1r_{1j} + \dots + u_i r_{ij}) \end{bmatrix} \begin{bmatrix} (u_1r_{11} + \dots + u_i r_{i1}) \\ (u_1r_{12} + \dots + u_i r_{i2}) \\ \vdots \\ (u_1r_{1j} + \dots + u_i r_{ij}) \end{bmatrix} \\ &= (u_1r_{11} + \dots + u_i r_{i1})^2 + (u_1r_{12} + \dots + u_i r_{i2})^2 + \dots + (u_1r_{1j} + \dots + u_i r_{ij})^2 \end{aligned}$$

Taking the partial derivative:

$$\begin{aligned}
\frac{\partial A}{\partial v} &= 2(u_1 r_{11} + u_2 r_{21} + \dots + u_i r_{i1}) \left(r_{11} \frac{\partial u_1}{\partial v} + r_{21} \frac{\partial u_2}{\partial v} + \dots + r_{i1} \frac{\partial u_i}{\partial v} \right) \\
&\quad + 2(u_1 r_{12} + u_2 r_{22} + \dots + u_i r_{i2}) \left(r_{12} \frac{\partial u_1}{\partial v} + r_{22} \frac{\partial u_2}{\partial v} + \dots + r_{i2} \frac{\partial u_i}{\partial v} \right) \\
&\quad \vdots \\
&\quad + 2(u_1 r_{1j} + u_2 r_{2j} + \dots + u_i r_{ij}) \left(r_{1j} \frac{\partial u_1}{\partial v} + r_{2j} \frac{\partial u_2}{\partial v} + \dots + r_{ij} \frac{\partial u_i}{\partial v} \right)
\end{aligned}$$

Separating into matrix form:

$$= 2 \left[(u_1 r_{11} + \dots + u_i r_{i1}) \quad (u_1 r_{12} + \dots + u_i r_{i2}) \quad \dots \quad (u_1 r_{1j} + \dots + u_i r_{ij}) \right] * \begin{bmatrix} (r_{11} \frac{\partial u_1}{\partial v} + \dots + r_{i1} \frac{\partial u_i}{\partial v}) \\ (r_{12} \frac{\partial u_1}{\partial v} + \dots + r_{i2} \frac{\partial u_i}{\partial v}) \\ \vdots \\ (r_{1j} \frac{\partial u_1}{\partial v} + \dots + r_{ij} \frac{\partial u_i}{\partial v}) \end{bmatrix}$$

and separating again

$$= 2 \begin{bmatrix} u_1 & u_2 & \dots & u_i \end{bmatrix} \begin{bmatrix} r_{11} & r_{12} & \dots & r_{1j} \\ r_{21} & r_{22} & \dots & r_{2j} \\ \vdots & \vdots & \ddots & \vdots \\ r_{i1} & r_{i2} & \dots & r_{ij} \end{bmatrix} \begin{bmatrix} r_{11} & r_{21} & \dots & r_{i1} \\ r_{12} & r_{22} & \dots & r_{i2} \\ \vdots & \vdots & \ddots & \vdots \\ r_{1j} & r_{2j} & \dots & r_{ij} \end{bmatrix} \begin{bmatrix} \frac{\partial u_1}{\partial v} \\ \frac{\partial u_2}{\partial v} \\ \vdots \\ \frac{\partial u_i}{\partial v} \end{bmatrix}$$

thus

$$\frac{\partial (u' R R' u)}{\partial v} = \frac{\partial A}{\partial v} = 2u' R R' \frac{\partial u}{\partial v} \tag{37}$$

A.5 Theorem: Partial Derivative of $u'RR'u$ with Respect to a Scalar
(R is a Function of the Scalar)

The following derivation is introduced in [33]. Let R be an $i \times j$ matrix and its components be functions of the scalar v , then

$$\frac{\partial (u'RR'u)}{\partial v} = 2u'R \frac{\partial R'}{\partial v} u$$

Proof:

Let

$$\begin{aligned} A &= u'RR'u = \begin{bmatrix} u_1 & u_2 & \dots & u_i \end{bmatrix} \begin{bmatrix} r_{11} & r_{12} & \dots & r_{1j} \\ r_{21} & r_{22} & \dots & r_{2j} \\ \vdots & \vdots & \ddots & \vdots \\ r_{i1} & r_{i2} & \dots & r_{ij} \end{bmatrix} \begin{bmatrix} r_{11} & r_{21} & \dots & r_{i1} \\ r_{12} & r_{22} & \dots & r_{i2} \\ \vdots & \vdots & \ddots & \vdots \\ r_{1j} & r_{2j} & \dots & r_{ij} \end{bmatrix} \begin{bmatrix} u_1 \\ u_2 \\ \vdots \\ u_i \end{bmatrix} \\ &= \begin{bmatrix} (u_1 r_{11} + \dots + u_i r_{i1}) & (u_1 r_{12} + \dots + u_i r_{i2}) & \dots & (u_1 r_{1j} + \dots + u_i r_{ij}) \end{bmatrix} \begin{bmatrix} (u_1 r_{11} + \dots + u_i r_{i1}) \\ (u_1 r_{12} + \dots + u_i r_{i2}) \\ \vdots \\ (u_1 r_{1j} + \dots + u_i r_{ij}) \end{bmatrix} \\ &= (u_1 r_{11} + \dots + u_i r_{i1})^2 + (u_1 r_{12} + \dots + u_i r_{i2})^2 + \dots + (u_1 r_{1j} + \dots + u_i r_{ij})^2 \end{aligned}$$

Taking the partial derivative:

$$\begin{aligned} \frac{\partial A}{\partial v} &= 2(u_1 r_{11} + u_2 r_{21} + \dots + u_i r_{i1}) \left(u_1 \frac{\partial r_{11}}{\partial v} + u_2 \frac{\partial r_{21}}{\partial v} + \dots + u_i \frac{\partial r_{i1}}{\partial v} \right) \\ &\quad + 2(u_1 r_{12} + u_2 r_{22} + \dots + u_i r_{i2}) \left(u_1 \frac{\partial r_{12}}{\partial v} + u_2 \frac{\partial r_{22}}{\partial v} + \dots + u_i \frac{\partial r_{i2}}{\partial v} \right) \\ &\quad \vdots \\ &\quad + 2(u_1 r_{1j} + u_2 r_{2j} + \dots + u_i r_{ij}) \left(u_1 \frac{\partial r_{1j}}{\partial v} + u_2 \frac{\partial r_{2j}}{\partial v} + \dots + u_i \frac{\partial r_{ij}}{\partial v} \right) \end{aligned}$$

Separating into matrix form:

$$= 2 \left[(u_1 r_{11} + \dots + u_i r_{i1}) \quad (u_1 r_{12} + \dots + u_i r_{i2}) \quad \dots \quad (u_1 r_{1j} + \dots + u_i r_{ij}) \right] * \begin{bmatrix} \left(u_1 \frac{\partial r_{11}}{\partial v} + \dots + u_i \frac{\partial r_{i1}}{\partial v} \right) \\ \left(u_1 \frac{\partial r_{12}}{\partial v} + \dots + u_i \frac{\partial r_{i2}}{\partial v} \right) \\ \vdots \\ \left(u_1 \frac{\partial r_{1j}}{\partial v} + \dots + u_i \frac{\partial r_{ij}}{\partial v} \right) \end{bmatrix}$$

and separating again

$$= 2 \begin{bmatrix} u_1 & u_2 & \dots & u_i \end{bmatrix} \begin{bmatrix} r_{11} & r_{12} & \dots & r_{1j} \\ r_{21} & r_{22} & \dots & r_{2j} \\ \vdots & \vdots & \ddots & \vdots \\ r_{i1} & r_{i2} & \dots & r_{ij} \end{bmatrix} \begin{bmatrix} \frac{\partial r_{11}}{\partial v} & \frac{\partial r_{21}}{\partial v} & \dots & \frac{\partial r_{i1}}{\partial v} \\ \frac{\partial r_{12}}{\partial v} & \frac{\partial r_{22}}{\partial v} & \dots & \frac{\partial r_{i2}}{\partial v} \\ \vdots & \vdots & \ddots & \vdots \\ \frac{\partial r_{1j}}{\partial v} & \frac{\partial r_{2j}}{\partial v} & \dots & \frac{\partial r_{ij}}{\partial v} \end{bmatrix} \begin{bmatrix} u_1 \\ u_2 \\ \vdots \\ u_i \end{bmatrix}$$

thus

$$\frac{\partial (u' R R' u)}{\partial v} = \frac{\partial A}{\partial v} = 2u' R \frac{\partial R'}{\partial v} u \quad (38)$$

Appendix B. The User-Defined Lobe

Ideally the user should have maximum flexibility in specifying the lobe in which the deputy will hover. For chiefs in circular orbits, the out-of-plane and in-plane motion decouple, therefore the lobe shapes will be independently constructed.

B.1 In the Orbit Plane

In the orbit plane of the chief, an ellipse is a convenient closed shape that provides the utility we seek without overly complicating the mathematics. The following is a derivation of the polar coordinates for an arbitrarily placed and oriented ellipse. Reference Figure 81 for variable definitions. The Cartesian coordinates of the deputy

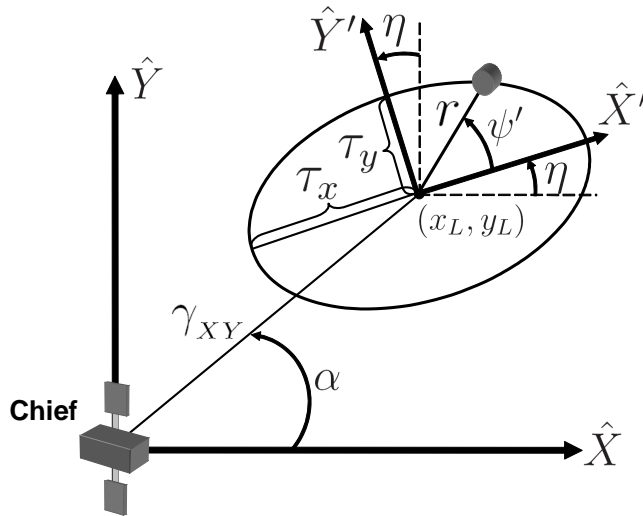


Figure 81: The Lobe in Two Dimensions

in the $\hat{X}'\hat{Y}'$ frame are

$$\begin{aligned} x' &= r \cos \psi' \\ y' &= r \sin \psi' \end{aligned}$$

where, from the proof in Appendix A.1,

$$r = \frac{\tau_x \tau_y}{\sqrt{\tau_y^2 \cos^2 \psi' + \tau_x^2 \sin^2 \psi'}} \quad (39)$$

We can rotate these coordinates into the chief centered frame via

$$\begin{bmatrix} \hat{X} \\ \hat{Y} \end{bmatrix} = \begin{bmatrix} \cos \eta & -\sin \eta \\ \sin \eta & \cos \eta \end{bmatrix} \begin{bmatrix} \hat{X}' \\ \hat{Y}' \end{bmatrix}$$

thus

$$\begin{bmatrix} x_i \\ y_i \end{bmatrix} = \begin{bmatrix} \cos \eta & -\sin \eta \\ \sin \eta & \cos \eta \end{bmatrix} \begin{bmatrix} r_i \cos \psi'_i \\ r_i \sin \psi'_i \end{bmatrix} = \begin{bmatrix} r_i \cos \eta \cos \psi'_i - r_i \sin \eta \sin \psi'_i \\ r_i \sin \eta \cos \psi'_i + r_i \cos \eta \sin \psi'_i \end{bmatrix}$$

Simplifying,

$$\begin{aligned} x_i &= r_i \cos (\eta + \psi'_i) \\ y_i &= r_i \sin (\eta + \psi'_i) \end{aligned}$$

Let the angular position (ψ_i) be measured with respect to a line parallel to the \hat{X} axis

$$\psi_i = \eta + \psi'_i \quad (40)$$

Substituting

$$\begin{aligned} r(\psi_i) &= \frac{\tau_x \tau_y}{\sqrt{\tau_y^2 \cos^2 (\psi_i - \eta) + \tau_x^2 \sin^2 (\psi_i - \eta)}} \\ x_i &= \frac{\tau_x \tau_y \cos \psi_i}{\sqrt{\tau_y^2 \cos^2 (\psi_i - \eta) + \tau_x^2 \sin^2 (\psi_i - \eta)}} \\ y_i &= \frac{\tau_x \tau_y \sin \psi_i}{\sqrt{\tau_y^2 \cos^2 (\psi_i - \eta) + \tau_x^2 \sin^2 (\psi_i - \eta)}} \end{aligned} \quad (41)$$

Translating the ellipse so that it is centered at (x_L, y_L) , where

$$\begin{aligned} x_L &= \gamma_{XY} \cos \alpha = \gamma \cos \alpha \sin \beta \\ y_L &= \gamma_{XY} \sin \alpha = \gamma \sin \alpha \sin \beta \end{aligned}$$

yields

$$x_i = \gamma \cos \alpha \sin \beta + \frac{\tau_x \tau_y \cos \psi_i}{\sqrt{\tau_y^2 \cos^2 (\psi_i - \eta) + \tau_x^2 \sin^2 (\psi_i - \eta)}} \quad (42)$$

$$y_i = \gamma \sin \alpha \sin \beta + \frac{\tau_x \tau_y \sin \psi_i}{\sqrt{\tau_y^2 \cos^2 (\psi_i - \eta) + \tau_x^2 \sin^2 (\psi_i - \eta)}} \quad (43)$$

if $\tau_x = \tau_y$, the ellipse becomes a circle with radius τ and the equations above reduce to

$$x_i = \gamma \cos \alpha \sin \beta + \tau \cos \psi_i \quad (44)$$

$$y_i = \gamma \sin \alpha \sin \beta + \tau \sin \psi_i \quad (45)$$

Next we need the partial derivatives of Equations (42) and (43) with respect to ψ_i .

First the partial derivative of the denominator

$$\begin{aligned} \frac{\partial \text{denom}}{\partial \psi_i} &= \frac{\frac{1}{2} [-2\tau_y^2 \cos(\psi_i - \eta) \sin(\psi_i - \eta) + 2\tau_x^2 \sin(\psi_i - \eta) \cos(\psi_i - \eta)]}{\sqrt{\tau_y^2 \cos^2 (\psi_i - \eta) + \tau_x^2 \sin^2 (\psi_i - \eta)}} \\ &= \frac{(\tau_x^2 - \tau_y^2) \cos(\psi_i - \eta) \sin(\psi_i - \eta)}{\sqrt{\tau_y^2 \cos^2 (\psi_i - \eta) + \tau_x^2 \sin^2 (\psi_i - \eta)}} = \frac{r_i (\tau_x^2 - \tau_y^2) \cos(\psi_i - \eta) \sin(\psi_i - \eta)}{\tau_x \tau_y} \quad (46) \end{aligned}$$

Then

$$\begin{aligned} \frac{\partial x_i}{\partial \psi_i} &= \frac{\sqrt{\tau_y^2 \cos^2 (\psi_i - \eta) + \tau_x^2 \sin^2 (\psi_i - \eta)} \tau_x \tau_y (-\sin \psi_i) - \tau_x \tau_y \cos \psi_i \frac{\partial \text{denom}}{\partial \psi_i}}{\tau_y^2 \cos^2 (\psi_i - \eta) + \tau_x^2 \sin^2 (\psi_i - \eta)} \\ \frac{\partial y_i}{\partial \psi_i} &= \frac{\sqrt{\tau_y^2 \cos^2 (\psi_i - \eta) + \tau_x^2 \sin^2 (\psi_i - \eta)} \tau_x \tau_y (\cos \psi_i) - \tau_x \tau_y \sin \psi_i \frac{\partial \text{denom}}{\partial \psi_i}}{\tau_y^2 \cos^2 (\psi_i - \eta) + \tau_x^2 \sin^2 (\psi_i - \eta)} \end{aligned}$$

Substituting Equation (41)

$$\begin{aligned}
 \frac{\partial x_i}{\partial \psi_i} &= \frac{-\frac{\tau_x^2 \tau_y^2}{r_i} \sin \psi_i - r_i (\tau_x^2 - \tau_y^2) \cos(\psi_i - \eta) \sin(\psi_i - \eta) \cos \psi_i}{\frac{\tau_x^2 \tau_y^2}{r_i^2}} \\
 &= -r_i \sin \psi_i - r_i^3 \frac{\tau_x^2 - \tau_y^2}{2\tau_x^2 \tau_y^2} \sin(2\psi_i - 2\eta) \cos \psi_i
 \end{aligned} \tag{47}$$

$$\begin{aligned}
 \frac{\partial y_i}{\partial \psi_i} &= \frac{\frac{\tau_x^2 \tau_y^2}{r_i} \cos \psi_i - r_i (\tau_x^2 - \tau_y^2) \cos(\psi_i - \eta) \sin(\psi_i - \eta) \sin \psi_i}{\frac{\tau_x^2 \tau_y^2}{r_i^2}} \\
 &= r_i \cos \psi_i - r_i^3 \frac{\tau_x^2 - \tau_y^2}{2\tau_x^2 \tau_y^2} \sin(2\psi_i - 2\eta) \sin \psi_i
 \end{aligned} \tag{48}$$

and, for a circular lobe ($r_i = \tau_x = \tau_y = \tau$),

$$\begin{aligned}
 \frac{\partial x_i}{\partial \psi_i} &= -\tau \sin \psi_i \\
 \frac{\partial y_i}{\partial \psi_i} &= \tau \cos \psi_i
 \end{aligned}$$

Conversion back to polar coordinates from Cartesian is setup in Figure 82. Note that,

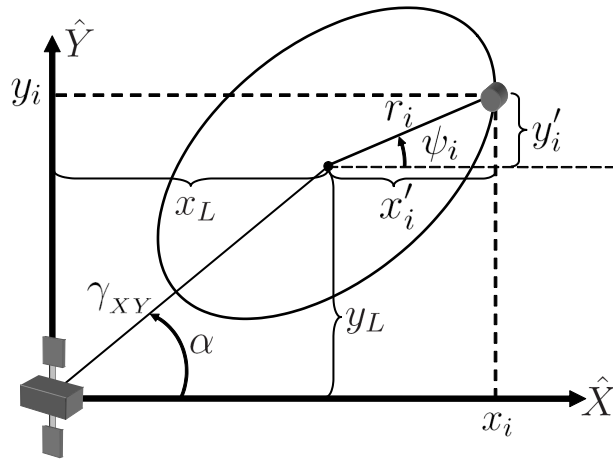


Figure 82: Conversion from Cartesian to Polar Coordinates

$$\gamma_{XY} = \gamma \sin \beta$$

The relationship of x' and y' to ψ is

$$\tan \psi_i = \frac{y'_i}{x'_i}$$

Thus

$$\psi_i = \tan^{-1} \left[\frac{y'_i}{x'_i} \right] = \tan^{-1} \left[\frac{y_i - \gamma \sin \alpha \sin \beta}{x_i - \gamma \cos \alpha \sin \beta} \right] \quad (49)$$

and the radius (r_i) is given by

$$r_i = \sqrt{(x'_i)^2 + (y'_i)^2} = \sqrt{(x_i - \gamma \cos \alpha \sin \beta)^2 + (y_i - \gamma \sin \alpha \sin \beta)^2} \quad (50)$$

B.2 Out of the Orbit Plane

In three dimensions, the lobe is constrained to be an elliptical cylinder. Employing a one dimensional lobe shape in the out-of-plane direction, allows us to take advantage of the decoupling of the equations of motion. Thus a single parameter, (h) the half height of the lobe, is required to define the lobe in three dimensions.

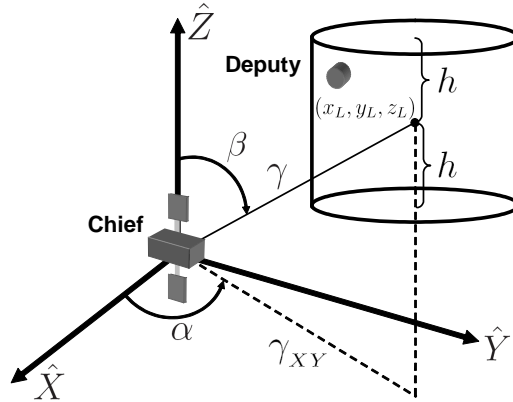


Figure 83: The Lobe in Three Dimensions

Appendix C. The Two Body Problem

The classical two body orbit problem is derived below for completeness. To find the acceleration of a satellite about a much larger primary body due to the force of gravity, consider Figure 84, in which \vec{d} are position vectors in inertial space:

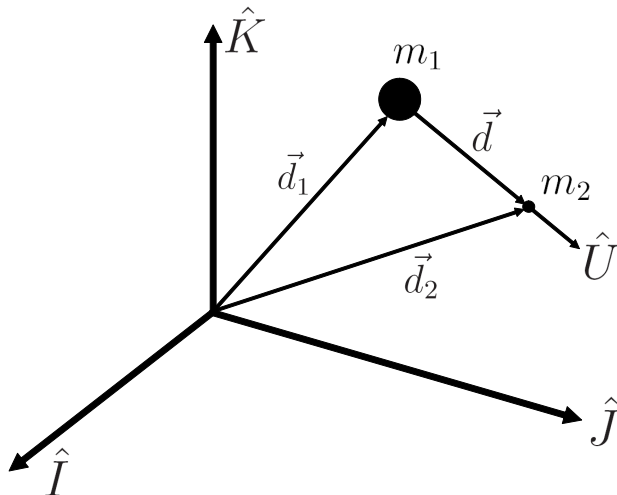


Figure 84: Two Body Problem

By Newton's second law [38],

$$\sum \vec{F} = \text{Mass} * \text{Acceleration} = ma \quad (51)$$

In the presence of perturbations

$$\vec{F}_g + \vec{f}_c + \vec{f}_p = ma \quad (52)$$

where \vec{F}_g is the force due to gravity, \vec{f}_c is a vector of control forces, and \vec{f}_p is a vector of perturbative forces. Gravity obeys an inverse square law

$$|\vec{F}_g| \propto \frac{m_1 m_2}{\|\vec{d}\|_2^2}$$

where $\|\vec{d}\|_2$ is the Euclidean norm of the relative position. To make this proportionality equation an equality, the gravitational constant is used $\left(G = 6.672 \times 10^{-11} \frac{\text{N} \cdot \text{m}^2}{\text{kg}^2}\right)$

$$|\vec{F}_g| = \frac{Gm_1m_2}{\|\vec{d}\|_2^2}$$

In order to apply Newton's law, we need to move the inertial reference frame so that it is centered on the larger mass (m_1). This means we are assuming the larger mass is not accelerating in the true inertial frame and thus is an inertial frame itself. As long as the masses are sufficiently disparate and there are no other forces of consequence operating on m_1 , this is a reasonable approximation. Substituting into Equation (52) for both masses

$$\begin{aligned} \left[\frac{Gm_1m_2}{\|\vec{d}\|_2^2} \right] \hat{U} + \vec{f}_{c1} + \vec{f}_{p1} &= m_1 \ddot{\vec{d}}_1 \\ \left[\frac{Gm_1m_2}{\|\vec{d}\|_2^2} \right] (-\hat{U}) + \vec{f}_{c2} + \vec{f}_{p2} &= m_2 \ddot{\vec{d}}_2 \end{aligned}$$

where \hat{U} is a unit vector parallel to \vec{d} and gives the scalar force of gravity a direction. Making the following substitution

$$\hat{U} = \frac{\vec{d}}{\|\vec{d}\|_2}$$

yields

$$\begin{aligned} \left[\frac{Gm_1m_2}{\|\vec{d}\|_2^2} \right] \frac{\vec{d}}{\|\vec{d}\|_2} + \vec{f}_{c1} + \vec{f}_{p1} &= m_1 \ddot{\vec{d}}_1 \\ - \left[\frac{Gm_1m_2}{\|\vec{d}\|_2^2} \right] \frac{\vec{d}}{\|\vec{d}\|_2} + \vec{f}_{c2} + \vec{f}_{p2} &= m_2 \ddot{\vec{d}}_2 \end{aligned}$$

Combining terms and dividing through by the masses to isolate the acceleration,

$$\ddot{\vec{d}}_1 = \left[\frac{Gm_2}{\|\vec{d}\|_2^3} \right] \vec{d} + \frac{\vec{f}_{c1}}{m_1} + \frac{\vec{f}_{p1}}{m_1} \quad (53)$$

$$\ddot{\vec{d}}_2 = \left[\frac{-Gm_1}{\|\vec{d}\|_2^3} \right] \vec{d} + \frac{\vec{f}_{c2}}{m_2} + \frac{\vec{f}_{p2}}{m_2} \quad (54)$$

$\vec{d} = \vec{d}_2 - \vec{d}_1$; taking the derivative twice yields

$$\ddot{\vec{d}} = \ddot{\vec{d}}_2 - \ddot{\vec{d}}_1$$

Substituting Equations (53) and (54) into the above equation

$$\ddot{\vec{d}} = \left[\frac{-Gm_1}{\|\vec{d}\|_2^3} \right] \vec{d} + \frac{\vec{f}_{c2}}{m_2} + \frac{\vec{f}_{p2}}{m_2} - \left[\frac{Gm_2}{\|\vec{d}\|_2^3} \right] \vec{d} - \frac{\vec{f}_{c1}}{m_1} - \frac{\vec{f}_{p1}}{m_1}$$

Combining terms

$$\ddot{\vec{d}} = \frac{-G(m_1 + m_2)\vec{d}}{\|\vec{d}\|_2^3} - \frac{\vec{f}_{c1}}{m_1} - \frac{\vec{f}_{p1}}{m_1} + \frac{\vec{f}_{c2}}{m_2} + \frac{\vec{f}_{p2}}{m_2}$$

If the first body is the Earth and the second body a satellite orbiting the Earth, then $m_1 = m_{\text{earth}}$, $m_2 = m_{\text{sat}}$, $f_{c1} = f_{\text{earth-control}}$, $f_{c2} = f_{\text{sat-control}}$, $f_{p1} = f_{\text{earth-pert}}$, and $f_{p2} = f_{\text{sat-pert}}$

$$\begin{aligned} \ddot{\vec{d}} &= \frac{-G(m_{\text{earth}} + m_{\text{sat}})\vec{d}}{\|\vec{d}\|_2^3} - \frac{\vec{f}_{\text{earth-control}}}{m_{\text{earth}}} - \frac{\vec{f}_{\text{earth-pert}}}{m_{\text{earth}}} \\ &+ \frac{\vec{f}_{\text{sat-control}}}{m_{\text{sat}}} + \frac{\vec{f}_{\text{sat-pert}}}{m_{\text{sat}}} \end{aligned}$$

Since $m_{\text{earth}} \gg m_{\text{sat}}$ we can assume that $m_{\text{earth}} + m_{\text{sat}} \approx m_{\text{earth}}$, further, if the Earth is being used as the inertial reference frame for the satellite then $\vec{f}_{\text{earth-control}} = \vec{f}_{\text{earth-pert}} = 0$:

$$\ddot{\vec{d}} = \frac{-Gm_{\text{earth}}\vec{d}}{\|\vec{d}\|_2^3} + \frac{\vec{f}_{\text{sat-control}}}{m_{\text{sat}}} + \frac{\vec{f}_{\text{sat-pert}}}{m_{\text{sat}}}$$

Defining the constant μ such that

$$\begin{aligned}\mu &= Gm_{\text{earth}} = 6.672 \times 10^{-11} \frac{\text{N} \cdot \text{m}^2}{\text{kg}^2} \times 5.974236 \times 10^{24} \text{ kg} \\ &= 3.98601 \times 10^{14} \frac{\text{m}^3}{\text{s}^2} = 398601 \frac{\text{km}^3}{\text{s}^2}\end{aligned}$$

and defining the specific forces (accelerations)

$$\begin{aligned}\vec{a}_c &= \frac{\vec{f}_{\text{sat-control}}}{m_{\text{sat}}} \\ \vec{a}_p &= \frac{\vec{f}_{\text{sat-pert}}}{m_{\text{sat}}}\end{aligned}$$

Then the equation of motion for a satellite about the Earth with control input of \vec{a}_c and a perturbative acceleration of \vec{a}_p is

$$\ddot{\vec{d}} = \frac{-\mu\vec{d}}{\|\vec{d}\|_2^3} + \vec{a}_c + \vec{a}_p \quad (55)$$

Appendix D. Orbital Mechanics

Several orbital mechanics quantities are needed in subsequent derivations. This entire appendix originates from equations and discussion found in [63].

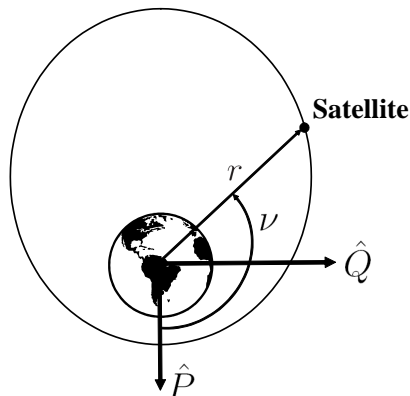


Figure 85: The General Elliptical Orbit

D.1 True Anomaly (ν)

Referencing Figure 85, the $\hat{P}\hat{Q}\hat{W}$ is an inertial frame oriented such that \hat{P} points towards perigee, \hat{Q} is along the semi-latus rectum, and \hat{W} is $\hat{P} \times \hat{Q}$ along the angular momentum vector. The position vector by inspection is

$$\vec{r} = r \cos \nu \hat{P} + r \sin \nu \hat{Q}$$

Taking the derivative

$$\vec{v} = [\dot{r} \cos \nu - r \dot{\nu} \sin \nu] \hat{P} + [\dot{r} \sin \nu + r \dot{\nu} \cos \nu] \hat{Q}$$

The angular momentum vector is

$$\begin{aligned}\vec{H} = \vec{r} \times \vec{v} &= \begin{vmatrix} \hat{P} & \hat{Q} & \hat{W} \\ r \cos \nu & r \sin \nu & 0 \\ \dot{r} \cos \nu - r\dot{\nu} \sin \nu & \dot{r} \sin \nu + r\dot{\nu} \cos \nu & 0 \end{vmatrix} \\ &= \begin{bmatrix} 0\hat{P} \\ 0\hat{Q} \\ (r\dot{r} \cos \nu \sin \nu + r^2\dot{\nu} \cos^2 \nu) \\ -(r\dot{r} \cos \nu \sin \nu - r^2\dot{\nu} \sin^2 \nu)\hat{W} \end{bmatrix} = r^2\dot{\nu}\hat{W}\end{aligned}$$

The angular momentum is also equal to [63]

$$H = \sqrt{\mu p}$$

Substituting r from the next section (Equation (64))

$$r\dot{\nu} = \frac{\sqrt{\mu p}}{r} = \sqrt{\mu p} \frac{1 + e \cos \nu}{p} = \sqrt{\frac{\mu}{p}} (1 + e \cos \nu) \quad (56)$$

Note that [63]

$$\sqrt{\frac{\mu}{p}} = \frac{r\dot{\nu}}{1 + e \cos \nu} \quad (57)$$

$$p = a_{\text{SMA}}(1 - e^2) \quad (58)$$

$$n = \sqrt{\frac{\mu}{a_{\text{SMA}}^3}} \quad (59)$$

Solving for $\dot{\nu}$ with another substitution of r ,

$$\begin{aligned}\dot{\nu} &= \sqrt{\frac{\mu}{p}} (1 + e \cos \nu) \frac{1 + e \cos \nu}{p} = \sqrt{\frac{\mu}{p^3}} (1 + e \cos \nu)^2 \\ &= \sqrt{\frac{\mu}{a_{\text{SMA}}^3}} \frac{(1 + e \cos \nu)^2}{(1 - e^2)^{\frac{3}{2}}} \\ &= \frac{n(1 + e \cos \nu)^2}{(1 - e^2)^{\frac{3}{2}}}\end{aligned} \quad (60)$$

The angular rate can also be expressed as

$$\begin{aligned} r^2 \dot{\nu} &= \sqrt{\mu p} \\ \dot{\nu}^2 &= \frac{\mu p}{r^4} = \frac{\mu r(1 + e \cos \nu)}{r^4} = \frac{\mu(1 + e \cos \nu)}{r^3} \end{aligned} \quad (61)$$

Taking the derivative of Equation (60)

$$\begin{aligned} \ddot{\nu} &= \frac{n}{(1 - e^2)^{\frac{3}{2}}} 2(1 + e \cos \nu) e (-\sin \nu) \dot{\nu} \\ &= \frac{-2ne\dot{\nu}(1 + e \cos \nu) \sin \nu}{(1 - e^2)^{\frac{3}{2}}} = \frac{-2e\dot{\nu}^2 \sin \nu}{1 + e \cos \nu} \end{aligned} \quad (62)$$

or, in terms of only ν ,

$$\begin{aligned} \ddot{\nu} &= \frac{-2e \sin \nu}{1 + e \cos \nu} \left[\frac{n(1 + e \cos \nu)^2}{(1 - e^2)^{\frac{3}{2}}} \right]^2 \\ &= \frac{-2n^2 e (1 + e \cos \nu)^3 \sin \nu}{(1 - e^2)^3} \end{aligned} \quad (63)$$

D.2 Ellipse Radius (r)

The radius of an orbit is a function of true anomaly (ν) and comes from the equation of a conic section [63]

$$r = \frac{a_{\text{SMA}}(1 - e^2)}{1 + e \cos \nu} = \frac{p}{1 + e \cos \nu} \quad (64)$$

where p is the semi-latus rectum. The derivative is

$$\dot{r} = p [-(1 + e \cos \nu)^{-2} (-\dot{\nu} e \sin \nu)] = \frac{pe\dot{\nu} \sin \nu}{(1 + e \cos \nu)^2} = r\dot{\nu} \frac{e \sin \nu}{1 + e \cos \nu} \quad (65)$$

Substituting Equation (56)

$$\dot{r} = \sqrt{\frac{\mu}{p}} e \sin \nu \quad (66)$$

and finally the second derivative of r

$$\ddot{r} = \sqrt{\frac{\mu}{p}} e \dot{\nu} \cos \nu$$

and substituting Equation (57)

$$\ddot{r} = \left(\frac{r \dot{\nu}}{1 + e \cos \nu} \right) e \dot{\nu} \cos \nu = \frac{r e \dot{\nu}^2 \cos \nu}{1 + e \cos \nu} \quad (67)$$

Appendix E. General Relative Motion Derivation

Assume the chief satellite is in a closed Keplerian orbit and define the following chief centered reference frame: the \hat{X} is oriented along a line from the center of the Earth to the chief, \hat{Z} is perpendicular to the orbit plane of the chief and \hat{Y} completes the frame as the cross product $\hat{Z} \times \hat{X}$. The in-track direction is aligned with the velocity vector of the chief when in a circular orbit. This frame is commonly referred to as the Local-Vertical/Local-Horizon (LVLH) frame. By inspection of Figure 86, the position vectors in the LVLH frame are:

$$\begin{aligned}\vec{L} &= r_o \hat{X} + 0 \hat{Y} + 0 \hat{Z} \\ \vec{P} &= x \hat{X} + y \hat{Y} + z \hat{Z} \\ \vec{M} &= \vec{L} + \vec{P} = (r_o + x) \hat{X} + y \hat{Y} + z \hat{Z}\end{aligned}\tag{68}$$

where r_o is the instantaneous orbit radius of the chief satellite and is a function of time.

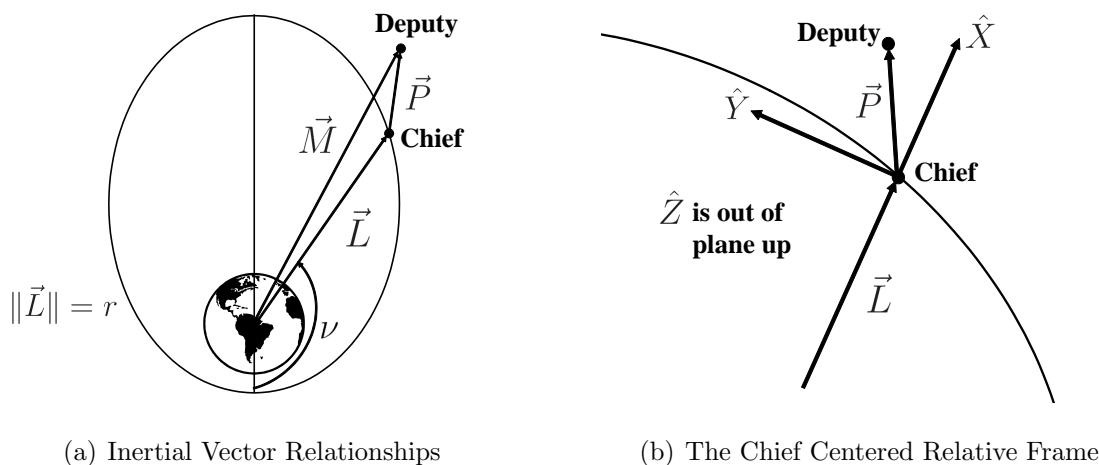


Figure 86: General Relative Motion Setup

The inertial derivative of a vector written in a rotating frame is derived in Appendix A.2 as

$$\dot{\vec{V}} = \hat{x}\hat{y}\hat{z}\frac{d(\vec{V})}{dt} + \omega \times \vec{V}$$

where ω is the angular velocity of the $\hat{X}\hat{Y}\hat{Z}$ frame with respect to the inertial frame. For the orbit problem, $\omega = 0\hat{X} + 0\hat{Y} + \dot{\nu}\hat{Z}$ where $\dot{\nu}$ is the time rate of change of the chief's true anomaly. Taking the inertial derivative of Equation (68) yields the relative velocity:

$$\dot{\vec{M}} = {}^{\hat{X}\hat{Y}\hat{Z}}\dot{\vec{M}} + (\dot{\nu}\hat{Z}) \times \vec{M}$$

where ${}^{\hat{X}\hat{Y}\hat{Z}}\dot{\vec{M}}$ is the derivative of \vec{M} in the $\hat{X}\hat{Y}\hat{Z}$ frame.

$${}^{\hat{X}\hat{Y}\hat{Z}}\dot{\vec{M}} = (\dot{r}_o + \dot{x})\hat{X} + \dot{y}\hat{Y} + \dot{z}\hat{Z}$$

$$(\dot{\nu}\hat{Z}) \times \vec{M} = \begin{vmatrix} \hat{X} & \hat{Y} & \hat{Z} \\ 0 & 0 & \dot{\nu} \\ r_o + x & y & z \end{vmatrix} = \begin{bmatrix} -\dot{\nu}y\hat{X} \\ \dot{\nu}(r_o + x)\hat{Y} \\ 0\hat{Z} \end{bmatrix}$$

Adding these together yields:

$$\dot{\vec{M}} = (\dot{r}_o + \dot{x} - \dot{\nu}y)\hat{X} + [\dot{y} + \dot{\nu}(r_o + x)]\hat{Y} + \dot{z}\hat{Z} \quad (69)$$

Taking the inertial derivative of Equation (69) yields the acceleration:

$$\ddot{\vec{M}} = {}^{\hat{X}\hat{Y}\hat{Z}}\ddot{\vec{M}} + (\dot{\nu}\hat{Z}) \times \dot{\vec{M}}$$

where ${}^{\hat{X}\hat{Y}\hat{Z}}\ddot{\vec{M}}$ is the derivative of $\dot{\vec{M}}$ in the $\hat{X}\hat{Y}\hat{Z}$ frame.

$${}^{\hat{X}\hat{Y}\hat{Z}}\ddot{\vec{M}} = [\ddot{r}_o + \ddot{x} - (\ddot{\nu}y + \dot{\nu}\dot{y})]\hat{X} + [\ddot{y} + \ddot{\nu}(r_o + x) + \dot{\nu}(\dot{r}_o + \dot{x})]\hat{Y} + \ddot{z}\hat{Z}$$

$$(\dot{\nu}\hat{Z}) \times \dot{\vec{M}} = \begin{vmatrix} \hat{X} & \hat{Y} & \hat{Z} \\ 0 & 0 & \dot{\nu} \\ \dot{r}_o + \dot{x} - \dot{\nu}y & \dot{y} + \dot{\nu}(r_o + x) & \dot{z} \end{vmatrix} = \begin{bmatrix} -[\dot{\nu}\dot{y} + \dot{\nu}^2(r_o + x)]\hat{X} \\ [\dot{\nu}\dot{r}_o + \dot{\nu}\dot{x} - \dot{\nu}^2y]\hat{Y} \\ 0\hat{Z} \end{bmatrix}$$

Adding these together yields:

$$\ddot{\vec{M}} = [\ddot{r}_o + \ddot{x} - 2\dot{\nu}\dot{y} - \ddot{\nu}y - \dot{\nu}^2(r_o + x)]\hat{X} + [\ddot{y} + 2\dot{\nu}(\dot{r}_o + \dot{x}) - \dot{\nu}^2y + \ddot{\nu}(r_o + x)]\hat{Y} + \ddot{z}\hat{Z}$$

Note that (via substitution of Equations (62) and (65))

$$2\dot{\nu}\dot{r}_o + \ddot{\nu}r_o = 2\dot{\nu} \left[\frac{r_o\dot{\nu}e \sin \nu}{1 + e \cos \nu} \right] - \frac{2e\dot{\nu}^2 \sin \nu}{1 + e \cos \nu} r_o = 0$$

and also (via substitution of Equations (61) and (67))

$$\begin{aligned} \ddot{r}_o - \dot{\nu}^2 r_o &= \frac{r_o e \dot{\nu}^2 \cos \nu}{1 + e \cos \nu} - \dot{\nu}^2 r_o = \dot{\nu}^2 r_o \left[\frac{e \cos \nu}{1 + e \cos \nu} - 1 \right] = \frac{-\dot{\nu}^2 r_o}{1 + e \cos \nu} \\ &= - \left[\frac{\mu(1 + e \cos \nu)}{r_o^3} \right] \frac{r_o}{1 + e \cos \nu} = \frac{-\mu}{r_o^2} \end{aligned}$$

Thus

$$\ddot{\vec{M}} = \left[\ddot{x} - 2\dot{\nu}\dot{y} - \ddot{\nu}y - \dot{\nu}^2 x - \frac{\mu}{r_o^2} \right] \hat{X} + [\ddot{y} + 2\dot{\nu}\dot{x} - \dot{\nu}^2 y + \ddot{\nu}x] \hat{Y} + \ddot{z} \hat{Z} \quad (70)$$

We know from Appendix C that acceleration due to gravity and control forces is:

$$\ddot{\vec{M}} = \frac{-\mu \vec{M}}{\|\vec{M}\|_2^3} + \vec{a}_c + \vec{a}_p$$

where μ is the gravitational constant, \vec{a}_c is the control acceleration, and \vec{a}_p is the perturbative acceleration. Expanding the magnitude of the position vector yields

$$\|\vec{M}\|_2^3 = \left[\sqrt{(r_o + x)^2 + y^2 + z^2} \right]^3 = [(r_o + x)^2 + y^2 + z^2]^{\frac{3}{2}}$$

Thus

$$\ddot{\vec{M}} = \frac{-\mu[(r_o + x)\hat{X} + y\hat{Y} + z\hat{Z}]}{[(r_o + x)^2 + y^2 + z^2]^{\frac{3}{2}}} + \vec{a}_c + \vec{a}_p \quad (71)$$

Setting Equations (70) and (71) equal to each other,

$$\begin{bmatrix} \left[\ddot{x} - 2\dot{\nu}\dot{y} - \ddot{\nu}y - \dot{\nu}^2 x - \frac{\mu}{r_o^2} \right] \hat{X} \\ [\ddot{y} + 2\dot{\nu}\dot{x} - \dot{\nu}^2 y + \ddot{\nu}x] \hat{Y} \\ \ddot{z} \hat{Z} \end{bmatrix} = \frac{-\mu}{[(r_o + x)^2 + y^2 + z^2]^{\frac{3}{2}}} \begin{bmatrix} (r_o + x)\hat{X} \\ y\hat{Y} \\ z\hat{Z} \end{bmatrix} + \begin{bmatrix} (a_{c_x} + a_{p_x})\hat{X} \\ (a_{c_y} + a_{p_y})\hat{Y} \\ (a_{c_z} + a_{p_z})\hat{Z} \end{bmatrix}$$

In scalar form and simplifying

$$\begin{aligned}\ddot{x} - 2\dot{\nu}\dot{y} - \ddot{y} - \dot{\nu}^2x - \mu \left[\frac{1}{r_o^2} - \frac{r_o + x}{[(r_o + x)^2 + y^2 + z^2]^{\frac{3}{2}}} \right] - a_{c_x} - a_{p_x} &= 0 \\ \ddot{y} + 2\dot{\nu}\dot{x} + \ddot{x} - \dot{\nu}^2y + \frac{\mu y}{[(r_o + x)^2 + y^2 + z^2]^{\frac{3}{2}}} - a_{c_y} - a_{p_y} &= 0 \\ \ddot{z} + \frac{\mu z}{[(r_o + x)^2 + y^2 + z^2]^{\frac{3}{2}}} - a_{c_z} - a_{p_z} &= 0\end{aligned}$$

From Equation (61) we can set μ equal to

$$\mu = \frac{r_o^3 \dot{\nu}^2}{1 + e \cos \nu}$$

Substituting

$$\begin{aligned}\ddot{x} - 2\dot{\nu}\dot{y} - \ddot{y} - \dot{\nu}^2x - \left(\frac{r_o^3 \dot{\nu}^2}{1 + e \cos \nu} \right) \left[\frac{1}{r_o^2} - \frac{r_o + x}{[(r_o + x)^2 + y^2 + z^2]^{\frac{3}{2}}} \right] - a_{c_x} - a_{p_x} &= 0 \\ \ddot{y} + 2\dot{\nu}\dot{x} + \ddot{x} - \dot{\nu}^2y + \left(\frac{r_o^3 \dot{\nu}^2}{1 + e \cos \nu} \right) \frac{y}{[(r_o + x)^2 + y^2 + z^2]^{\frac{3}{2}}} - a_{c_y} - a_{p_y} &= 0 \\ \ddot{z} + \left(\frac{r_o^3 \dot{\nu}^2}{1 + e \cos \nu} \right) \frac{z}{[(r_o + x)^2 + y^2 + z^2]^{\frac{3}{2}}} - a_{c_z} - a_{p_z} &= 0\end{aligned}$$

Factoring out a $\dot{\nu}^2$ yields the general relative equations of motion

$$\ddot{x} - 2\dot{\nu}\dot{y} - \ddot{y} - \dot{\nu}^2 \left[x + \frac{r_o}{1 + e \cos \nu} - \frac{r_o^3(r_o + x)}{(1 + e \cos \nu)[(r_o + x)^2 + y^2 + z^2]^{\frac{3}{2}}} \right] - a_{c_x} - a_{p_x} = 0 \quad (72a)$$

$$\ddot{y} + 2\dot{\nu}\dot{x} + \ddot{x} - \dot{\nu}^2y \left[1 - \frac{r_o^3}{(1 + e \cos \nu)[(r_o + x)^2 + y^2 + z^2]^{\frac{3}{2}}} \right] - a_{c_y} - a_{p_y} = 0 \quad (72b)$$

$$\ddot{z} + \dot{\nu}^2z \left[\frac{r_o^3}{(1 + e \cos \nu)[(r_o + x)^2 + y^2 + z^2]^{\frac{3}{2}}} \right] - a_{c_z} - a_{p_z} = 0 \quad (72c)$$

We can further simplify these equations by assuming that the deputy is close to the chief compared to the instantaneous orbit radius (r_o). Define the nonlinear term (NL)

as

$$NL = [(r_o + x)^2 + y^2 + z^2]^{\frac{3}{2}}$$

Expanding and factoring out an r_o^2

$$NL = \left[r_o^2 \left(1 + \frac{2x}{r_o} + \frac{x^2}{r_o^2} + \frac{y^2}{r_o^2} + \frac{z^2}{r_o^2} \right) \right]^{\frac{3}{2}} = r_o^3 \left(1 + \frac{2x}{r_o} + \frac{x^2}{r_o^2} + \frac{y^2}{r_o^2} + \frac{z^2}{r_o^2} \right)^{\frac{3}{2}}$$

Using the binomial series expansion [24], this becomes

$$NL = r_o^3 \left[1 + \frac{3}{2} \left(\frac{2x}{r_o} + \frac{x^2}{r_o^2} + \frac{y^2}{r_o^2} + \frac{z^2}{r_o^2} \right) + \mathcal{O}(x, y, z) \right]$$

Neglecting terms of order larger than two, $\mathcal{O}(x, y, z)$, and assuming that x , y , and z are appropriately small compared to the instantaneous radius of the chief's orbit (our underlying assumption for linearization) such that

$$\frac{x^2}{r_o^2} \approx \frac{y^2}{r_o^2} \approx \frac{z^2}{r_o^2} \approx 0$$

the nonlinear term is now

$$NL = r_o^3 \left(1 + \frac{3x}{r_o} \right) = r_o^3 \left(\frac{r_o + 3x}{r_o} \right)$$

and the general relative equations of motion are

$$\begin{aligned} \ddot{x} - 2\dot{\nu}\dot{y} - \ddot{\nu}y - \dot{\nu}^2 \left[x + \frac{r_o}{1 + e \cos \nu} - \frac{r_o^3(r_o + x)}{(1 + e \cos \nu) r_o^3 \left(\frac{r_o + 3x}{r_o} \right)} \right] - a_{c_x} - a_{p_x} &= 0 \\ \ddot{y} + 2\dot{\nu}\dot{x} + \ddot{\nu}x - \dot{\nu}^2 y \left[1 - \frac{r_o^3}{(1 + e \cos \nu) r_o^3 \left(\frac{r_o + 3x}{r_o} \right)} \right] - a_{c_y} - a_{p_y} &= 0 \\ \ddot{z} + \dot{\nu}^2 z \left[\frac{r_o^3}{(1 + e \cos \nu) r_o^3 \left(\frac{r_o + 3x}{r_o} \right)} \right] - a_{c_z} - a_{p_z} &= 0 \end{aligned}$$

Canceling r_o^3

$$\begin{aligned}\ddot{x} - 2\dot{\nu}\dot{y} - \ddot{\nu}y - \dot{\nu}^2 \left[x + \frac{r_o}{1 + e \cos \nu} - \frac{r_o(r_o + x)}{(1 + e \cos \nu)(r_o + 3x)} \right] - a_{c_x} - a_{p_x} &= 0 \\ \ddot{y} + 2\dot{\nu}\dot{x} + \ddot{\nu}x - \dot{\nu}^2 y \left[1 - \frac{r_o}{(1 + e \cos \nu)(r_o + 3x)} \right] - a_{c_y} - a_{p_y} &= 0 \\ \ddot{z} + \dot{\nu}^2 z \left[\frac{r_o}{(1 + e \cos \nu)(r_o + 3x)} \right] - a_{c_z} - a_{p_z} &= 0\end{aligned}$$

Combining terms

$$\begin{aligned}\ddot{x} - 2\dot{\nu}\dot{y} - \ddot{\nu}y - \dot{\nu}^2 \left[x + \frac{2xr_o}{(1 + e \cos \nu)(r_o + 3x)} \right] - a_{c_x} - a_{p_x} &= 0 \\ \ddot{y} + 2\dot{\nu}\dot{x} + \ddot{\nu}x - \dot{\nu}^2 y \left[1 - \frac{r_o}{(1 + e \cos \nu)(r_o + 3x)} \right] - a_{c_y} - a_{p_y} &= 0 \\ \ddot{z} + \dot{\nu}^2 z \left[\frac{r_o}{(1 + e \cos \nu)(r_o + 3x)} \right] - a_{c_z} - a_{p_z} &= 0\end{aligned}$$

Assume that r_o is appropriately large compared to x such that

$$r_o + 3x \approx r_o$$

Then

$$\begin{aligned}\ddot{x} - 2\dot{\nu}\dot{y} - \ddot{\nu}y - \dot{\nu}^2 \left[x + \frac{2x}{1 + e \cos \nu} \right] - a_{c_x} - a_{p_x} &= 0 \\ \ddot{y} + 2\dot{\nu}\dot{x} + \ddot{\nu}x - \dot{\nu}^2 y \left[1 - \frac{1}{1 + e \cos \nu} \right] - a_{c_y} - a_{p_y} &= 0 \\ \ddot{z} + \dot{\nu}^2 z \left[\frac{1}{1 + e \cos \nu} \right] - a_{c_z} - a_{p_z} &= 0\end{aligned}$$

and finally, combining terms, the simplified general relative equations of motion are

$$\ddot{x} - 2\dot{\nu}\dot{y} - \ddot{\nu}y - \dot{\nu}^2x \left[\frac{3 + e \cos \nu}{1 + e \cos \nu} \right] - a_{c_x} - a_{p_x} = 0 \quad (73a)$$

$$\ddot{y} + 2\dot{\nu}\dot{x} + \ddot{\nu}x - \dot{\nu}^2y \left[\frac{e \cos \nu}{1 + e \cos \nu} \right] - a_{c_y} - a_{p_y} = 0 \quad (73b)$$

$$\ddot{z} + \dot{\nu}^2z \left[\frac{1}{1 + e \cos \nu} \right] - a_{c_z} - a_{p_z} = 0 \quad (73c)$$

where

$$\begin{aligned} \dot{\nu} &= \frac{n(1 + e \cos \nu)^2}{(1 - e^2)^{\frac{3}{2}}} \\ \ddot{\nu} &= \frac{-2e\dot{\nu}^2 \sin \nu}{1 + e \cos \nu} = \frac{-2n^2e(1 + e \cos \nu)^3 \sin \nu}{(1 - e^2)^3} \end{aligned}$$

If the chief satellite is in a circular orbit, then

$$e = 0$$

$$\dot{\nu} = n$$

$$\ddot{\nu} = 0$$

and the general relative equations of motion (Equation (72)) reduce to

$$\ddot{x} - 2n\dot{y} - n^2(x + r_o) \left[1 - \frac{r_o^3}{[(r_o + x)^2 + y^2 + z^2]^{\frac{3}{2}}} \right] - a_{c_x} - a_{p_x} = 0 \quad (74a)$$

$$\ddot{y} + 2n\dot{x} - n^2y \left[1 - \frac{r_o^3}{[(r_o + x)^2 + y^2 + z^2]^{\frac{3}{2}}} \right] - a_{c_y} - a_{p_y} = 0 \quad (74b)$$

$$\ddot{z} + n^2z \left[\frac{r_o^3}{[(r_o + x)^2 + y^2 + z^2]^{\frac{3}{2}}} \right] - a_{c_z} - a_{p_z} = 0 \quad (74c)$$

The linear form of Equation (73) reduce to the familiar Clohessy-Wiltshire equations

$$\ddot{x} - 2n\dot{y} - 3n^2x - a_{c_x} - a_{p_x} = 0 \quad (75a)$$

$$\ddot{y} + 2n\dot{x} - a_{c_y} - a_{p_y} = 0 \quad (75b)$$

$$\ddot{z} + n^2z - a_{c_z} - a_{p_z} = 0 \quad (75c)$$

Appendix F. Chief Orbit Fractions as the Independent Variable

There are advantages to using chief orbit fractions as the independent variable as opposed to absolute time, primarily the disentanglement of the relative trajectory to semi-major axis (or orbital radius for $e = 0$). The relationship between absolute time (t) and time as a fraction of orbit period (\tilde{t}) is

$$\tilde{t} = \frac{t}{P}$$

where the chief orbit period (P) is [63]

$$P = 2\pi \sqrt{\frac{a_{\text{SMA}}^3}{\mu}} = \frac{2\pi}{n}$$

therefore

$$t = \frac{2\pi}{n} \tilde{t}$$

and the derivative of t with respect to \tilde{t} is

$$\frac{dt}{d\tilde{t}} = \frac{2\pi}{n} \tag{76}$$

The relative positions remained unchanged in this conversion

$$\tilde{x} = x \tag{77a}$$

$$\tilde{y} = y \tag{77b}$$

$$\tilde{z} = z \tag{77c}$$

The relative velocities as functions of chief orbit fractions are

$$\dot{\tilde{x}} = \frac{d\tilde{x}}{d\tilde{t}} = \frac{dx}{d\tilde{t}} = \frac{dx}{dt} \frac{dt}{d\tilde{t}} = \dot{x} \frac{2\pi}{n} \tag{78a}$$

$$\dot{\tilde{y}} = \frac{d\tilde{y}}{d\tilde{t}} = \frac{dy}{d\tilde{t}} = \frac{dy}{dt} \frac{dt}{d\tilde{t}} = \dot{y} \frac{2\pi}{n} \tag{78b}$$

$$\dot{\tilde{z}} = \frac{d\tilde{z}}{d\tilde{t}} = \frac{dz}{d\tilde{t}} = \frac{dz}{dt} \frac{dt}{d\tilde{t}} = \dot{z} \frac{2\pi}{n} \tag{78c}$$

and the accelerations

$$\ddot{\tilde{x}} = \frac{d\dot{\tilde{x}}}{d\tilde{t}} = \frac{2\pi}{n} \frac{d\dot{x}}{d\tilde{t}} = \frac{2\pi}{n} \frac{d\dot{x}}{dt} \frac{dt}{d\tilde{t}} = \ddot{x} \frac{4\pi^2}{n^2} \quad (79a)$$

$$\ddot{\tilde{y}} = \frac{d\dot{\tilde{y}}}{d\tilde{t}} = \frac{2\pi}{n} \frac{d\dot{y}}{d\tilde{t}} = \frac{2\pi}{n} \frac{d\dot{y}}{dt} \frac{dt}{d\tilde{t}} = \ddot{y} \frac{4\pi^2}{n^2} \quad (79b)$$

$$\ddot{\tilde{z}} = \frac{d\dot{\tilde{z}}}{d\tilde{t}} = \frac{2\pi}{n} \frac{d\dot{z}}{d\tilde{t}} = \frac{2\pi}{n} \frac{d\dot{z}}{dt} \frac{dt}{d\tilde{t}} = \ddot{z} \frac{4\pi^2}{n^2} \quad (79c)$$

Also let

$$\begin{aligned} \tilde{\nu} &= \nu \\ \dot{\tilde{\nu}} &= \dot{\nu} \frac{2\pi}{n} = \frac{2\pi(1 + e \cos \nu)^2}{(1 - e^2)^{\frac{3}{2}}} \\ \ddot{\tilde{\nu}} &= \ddot{\nu} \frac{4\pi^2}{n^2} = \frac{-8\pi^2 e(1 + e \cos \nu)^3 \sin \nu}{(1 - e^2)^3} \end{aligned}$$

We are now ready to formulate the general relative equations of motion as functions of chief orbit fractions. Starting with the homogeneous form of Equation (73) from Appendix E and dividing through by n^2

$$\begin{aligned} \frac{\ddot{x}}{n^2} - 2\frac{\dot{\nu}\dot{y}}{n^2} - \frac{\ddot{\nu}}{n^2}y - \frac{\dot{\nu}^2}{n^2}x \left[\frac{3 + e \cos \nu}{1 + e \cos \nu} \right] &= 0 \\ \frac{\ddot{y}}{n^2} + 2\frac{\dot{\nu}\dot{x}}{n^2} + \frac{\ddot{\nu}}{n^2}x - \frac{\dot{\nu}^2}{n^2}y \left[\frac{e \cos \nu}{1 + e \cos \nu} \right] &= 0 \\ \frac{\ddot{z}}{n^2} + \frac{\dot{\nu}^2}{n^2}z \left[\frac{1}{1 + e \cos \nu} \right] &= 0 \end{aligned}$$

Substituting the new acceleration, velocities, positions, and derivatives of true anomaly

$$\begin{aligned} \frac{1}{n^2} \ddot{\tilde{x}} \frac{n^2}{4\pi^2} - \frac{2}{n^2} \dot{\tilde{\nu}} \frac{n}{2\pi} \dot{\tilde{y}} \frac{n}{2\pi} - \frac{1}{n^2} \ddot{\tilde{\nu}} \frac{n^2}{4\pi^2} \tilde{y} - \frac{1}{n^2} \left(\dot{\tilde{\nu}} \frac{n}{2\pi} \right)^2 \tilde{x} \left[\frac{3 + e \cos \nu}{1 + e \cos \nu} \right] &= 0 \\ \frac{1}{n^2} \ddot{\tilde{y}} \frac{n^2}{4\pi^2} + \frac{2}{n^2} \dot{\tilde{\nu}} \frac{n}{2\pi} \dot{\tilde{x}} \frac{n}{2\pi} + \frac{1}{n^2} \ddot{\tilde{\nu}} \frac{n^2}{4\pi^2} \tilde{x} - \frac{1}{n^2} \left(\dot{\tilde{\nu}} \frac{n}{2\pi} \right)^2 \tilde{y} \left[\frac{e \cos \nu}{1 + e \cos \nu} \right] &= 0 \\ \frac{1}{n^2} \ddot{\tilde{z}} \frac{n^2}{4\pi^2} + \frac{1}{n^2} \left(\dot{\tilde{\nu}} \frac{n}{2\pi} \right)^2 \tilde{z} \left[\frac{1}{1 + e \cos \nu} \right] &= 0 \end{aligned}$$

Simplifying and multiplying through by $4\pi^2$

$$\ddot{\tilde{x}} - 2\dot{\tilde{\nu}}\dot{\tilde{y}} - \ddot{\tilde{\nu}}\tilde{y} - \dot{\tilde{\nu}}^2\tilde{x} \left[\frac{3 + e \cos \tilde{\nu}}{1 + e \cos \tilde{\nu}} \right] = 0 \quad (80a)$$

$$\ddot{\tilde{y}} + 2\dot{\tilde{\nu}}\dot{\tilde{x}} + \ddot{\tilde{\nu}}\tilde{x} - \dot{\tilde{\nu}}^2\tilde{y} \left[\frac{e \cos \tilde{\nu}}{1 + e \cos \tilde{\nu}} \right] = 0 \quad (80b)$$

$$\ddot{\tilde{z}} + \dot{\tilde{\nu}}^2\tilde{z} \left[\frac{1}{1 + e \cos \tilde{\nu}} \right] = 0 \quad (80c)$$

When the chief is in a circular orbit

$$e = 0$$

$$\dot{\tilde{\nu}} = 2\pi$$

$$\ddot{\tilde{\nu}} = 0$$

thus the Clohessy-Wiltshire equations a functions of chief orbit fractions are

$$\ddot{\tilde{x}} - 4\pi\dot{\tilde{y}} - 12\pi^2\tilde{x} = 0 \quad (81a)$$

$$\ddot{\tilde{y}} + 4\pi\dot{\tilde{x}} = 0 \quad (81b)$$

$$\ddot{\tilde{z}} + 4\pi^2\tilde{z} = 0 \quad (81c)$$

*Appendix G. A Closed-Form Solution of the Linear
Clohessy-Wiltshire Equations*

Start with the homogeneous linear Clohessy-Wiltshire equations (Equation (75) from Appendix E)

$$\ddot{x} - 2n\dot{y} - 3n^2x = 0$$

$$\ddot{y} + 2n\dot{x} = 0$$

$$\ddot{z} + n^2z = 0$$

Taking the Laplace transform

$$[s^2X(s) - sx_o - \dot{x}_o] - 2n[sY(s) - y_o] - 3n^2X(s) = 0$$

$$[s^2Y(s) - sy_o - \dot{y}_o] + 2n[sX(s) - x_o] = 0$$

$$[s^2Z(s) - sz_o - \dot{z}_o] + n^2Z(s) = 0$$

where x_o and \dot{x}_o are initial conditions of the relative position and velocity in the \hat{X} (radial) direction, y_o and \dot{y}_o are in the \hat{Y} (velocity) direction, and z_o and \dot{z}_o are in the \hat{Z} (out-of-plane) direction. Collecting terms and placing the equations in matrix form

$$\begin{bmatrix} s^2 - 3n^2 & -2ns & 0 \\ 2ns & s^2 & 0 \\ 0 & 0 & s^2 + n^2 \end{bmatrix} \begin{bmatrix} X(s) \\ Y(s) \\ Z(s) \end{bmatrix} = \begin{bmatrix} sx_o + \dot{x}_o - 2ny_o \\ sy_o + \dot{y}_o - 2nx_o \\ sz_o + \dot{z}_o \end{bmatrix}$$

Finding the inverse and solving for $X(s)$, $Y(s)$, and $Z(s)$

$$\begin{bmatrix} X(s) \\ Y(s) \\ Z(s) \end{bmatrix} = \begin{bmatrix} \frac{1}{s^2 + n^2} & \frac{2n}{s(s^2 + n^2)} & 0 \\ \frac{-2n}{s(s^2 + n^2)} & \frac{s^2 - 3n^2}{s^2(s^2 + n^2)} & 0 \\ 0 & 0 & \frac{1}{s^2 + n^2} \end{bmatrix} \begin{bmatrix} sx_o + \dot{x}_o - 2ny_o \\ sy_o + \dot{y}_o - 2nx_o \\ sz_o + \dot{z}_o \end{bmatrix}$$

Multiplying this out

$$\begin{bmatrix} X(s) \\ Y(s) \\ Z(s) \end{bmatrix} = \begin{bmatrix} \frac{sx_o + \dot{x}_o - 2ny_o}{s^2 + n^2} + \frac{2n(sy_o + \dot{y}_o + 2nx_o)}{s(s^2 + n^2)} \\ \frac{-2n(sx_o + \dot{x}_o - 2ny_o)}{s(s^2 + n^2)} + \frac{(s^2 - 3n^2)(sy_o + \dot{y}_o + 2nx_o)}{s^2(s^2 + n^2)} \\ \frac{sz_o + \dot{z}_o}{s^2 + n^2} \end{bmatrix}$$

Performing partial fraction expansion

$$\begin{bmatrix} X(s) \\ Y(s) \\ Z(s) \end{bmatrix} = \begin{bmatrix} \frac{sx_o + \dot{x}_o - 2ny_o}{s^2 + n^2} + \frac{2n^2y_o - 2s\dot{y}_o - 4snx_o}{n(s^2 + n^2)} + \frac{2\dot{y}_o + 4nx_o}{n} \frac{1}{s} \\ \frac{4sy_o + 4\dot{y}_o + 8nx_o}{s^2 + n^2} + \frac{-2n^2x_o + 2s\dot{x}_o - 4sy_o n}{n(s^2 + n^2)} + \frac{-3\dot{y}_o - 6nx_o}{s^2} + \frac{ny_o - 2\dot{x}_o}{n} \frac{1}{s} \\ \frac{sz_o + \dot{z}_o}{s^2 + n^2} \end{bmatrix}$$

Collecting terms

$$\begin{bmatrix} X(s) \\ Y(s) \\ Z(s) \end{bmatrix} = \begin{bmatrix} \frac{(x_o - \frac{2\dot{y}_o + 4nx_o}{n})s}{s^2 + n^2} + \frac{(\frac{\dot{x}_o}{n})n}{s^2 + n^2} + \frac{2\dot{y}_o + 4nx_o}{n} \frac{1}{s} \\ \frac{2(\frac{\dot{x}_o}{n})s}{s^2 + n^2} + \frac{2(\frac{2\dot{y}_o + 4nx_o}{n} - x_o)n}{s^2 + n^2} - \frac{3n}{2} \frac{2\dot{y}_o + 4nx_o}{n} \frac{1}{s^2} + \frac{ny_o - 2\dot{x}_o}{n} \frac{1}{s} \\ \frac{sz_o}{s^2 + n^2} + \frac{(\frac{\dot{z}_o}{n})n}{s^2 + n^2} \end{bmatrix}$$

Taking the inverse Laplace transform

$$\begin{bmatrix} x(t) \\ y(t) \\ z(t) \end{bmatrix} = \begin{bmatrix} \left[x_o - \frac{2\dot{y}_o + 4nx_o}{n} \right] \cos(nt) + \frac{\dot{x}_o}{n} \sin(nt) + \frac{2\dot{y}_o + 4nx_o}{n} \\ 2 \left(\frac{\dot{x}_o}{n} \right) \cos(nt) + 2 \left[\frac{2\dot{y}_o + 4nx_o}{n} - x_o \right] \sin(nt) - \frac{3nt}{2} \left(\frac{2\dot{y}_o + 4nx_o}{n} \right) + \frac{ny_o - 2\dot{x}_o}{n} \\ z_o \cos(nt) + \frac{\dot{z}_o}{n} \sin(nt) \end{bmatrix} \quad (82)$$

Since the ICs and n do not vary with time, two constants can be defined

$$a = \frac{2\dot{y}_o + 4nx_o}{n} \quad (83)$$

$$b = \frac{ny_o - 2\dot{x}_o}{n} \quad (84)$$

which simplifies Equation (82) to

$$x(t) = (x_o - a) \cos(nt) + \frac{\dot{x}_o}{n} \sin(nt) + a \quad (85a)$$

$$y(t) = \frac{2\dot{x}_o}{n} \cos(nt) + 2(a - x_o) \sin(nt) - \frac{3na}{2}t + b \quad (85b)$$

$$z(t) = z_o \cos(nt) + \frac{\dot{z}_o}{n} \sin(nt) \quad (85c)$$

For simplicity, $x = x(t)$, $y = y(t)$, $z = z(t)$. Isolating the sinusoidal terms.

$$\begin{aligned} x - a &= (x_o - a) \cos(nt) + \frac{\dot{x}_o}{n} \sin(nt) \\ \frac{y + \frac{3na}{2}t - b}{2} &= \frac{\dot{x}_o}{n} \cos(nt) + (a - x_o) \sin(nt) \end{aligned}$$

Squaring both sides yields:

$$\begin{aligned} [x - a]^2 &= (x_o - a)^2 \cos^2(nt) + \left(\frac{\dot{x}_o}{n}\right)^2 \sin^2(nt) \\ &\quad + 2(x_o - a) \frac{\dot{x}_o}{n} \cos(nt) \sin(nt) \end{aligned}$$

$$\begin{aligned} \frac{[y + \frac{3na}{2}t - b]^2}{4} &= \left(\frac{\dot{x}_o}{n}\right)^2 \cos^2(nt) + (a - x_o)^2 \sin^2(nt) \\ &\quad - 2(x_o - a) \frac{\dot{x}_o}{n} \cos(nt) \sin(nt) \end{aligned}$$

Adding these equations together

$$\begin{aligned} [x - a]^2 + \frac{[y + \frac{3na}{2}t - b]^2}{4} &= \left[(x_o - a)^2 + \left(\frac{\dot{x}_o}{n}\right)^2 \right] \cos^2(nt) \\ &\quad + \left[\left(\frac{\dot{x}_o}{n}\right)^2 + (-1)^2 (x_o - a)^2 \right] \sin^2(nt) \end{aligned}$$

Pulling out the common coefficient and using the identity $\cos^2(\alpha) + \sin^2(\alpha) = 1$

$$[x - a]^2 + \frac{[y + \frac{3na}{2}t - b]^2}{4} = (x_o - a)^2 + \left(\frac{\dot{x}_o}{n}\right)^2$$

The right side of this equation has no time varying terms, thus define the constant ρ

$$\rho^2 = (x_o - a)^2 + \left(\frac{\dot{x}_o}{n}\right)^2 \quad (86)$$

Substituting and dividing by ρ^2 yields

$$\frac{[x - a]^2}{\rho^2} + \frac{[y + \frac{3na}{2}t - b]^2}{4\rho^2} = 1 \quad (87)$$

This is the standard equation for an ellipse, thus the deputy satellite will follow an elliptical path about the chief satellite in the $\hat{X}\hat{Y}$ plane (Figure 87). Note that for a stable orbit (i.e. one that does not drift over time) about a chief satellite a must equal zero.

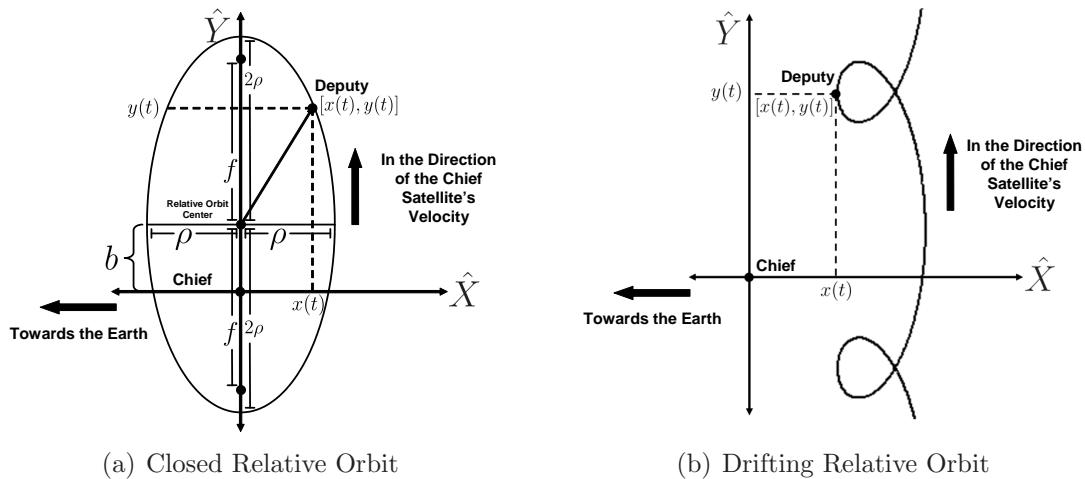


Figure 87: Relative Orbit Types

We can further simplify Equation (85) using harmonic addition theorem derived in Appendix A.3.

$$x(t) = \sqrt{(x_o - a)^2 + \left(\frac{\dot{x}_o}{n}\right)^2} \sin \left[nt + \tan^{-1} \left(\frac{n(x_o - a)}{\dot{x}_o} \right) \right] + a$$

$$y(t) = \sqrt{(2)^2 \left(\frac{\dot{x}_o}{n}\right)^2 + (-2)^2 (x_o - a)^2} \cos \left[nt + \tan^{-1} \left(\frac{-2n(a - x_o)}{2\dot{x}_o} \right) \right] - \frac{3na}{2}t + b$$

Substituting Equation (86) and defining a new constant θ

$$x(t) = \rho \sin (nt + \theta) + a \quad (88)$$

$$y(t) = 2\rho \cos (nt + \theta) - \frac{3na}{2}t + b \quad (89)$$

where

$$\theta = \tan^{-1} \left[\frac{n(x_o - a)}{\dot{x}_o} \right] \quad (90)$$

If we visualize the elliptical orbit from Figure 87(a) rotating about the major or minor axes, it is easy to see it will trace a line in $\hat{X}\hat{Z}$ plane, if rotated about the major axis, and the $\hat{Y}\hat{Z}$ plane, if rotated about the minor axis. Using the equation of a line and adding the effects of a rotation about both major and minor axes

$$z(t) = l[x(t) - a] + q \left[y(t) + \frac{3na}{2}t - b \right]$$

where l and q are the slopes of the lines formed by the rotation about the minor and major axes, respectively. Substituting Equations (88) and (89) into the above equation yields:

$$z(t) = l\rho \sin(nt + \theta) + 2q\rho \cos(nt + \theta) \quad (91)$$

This is the correct form expected from the inverse Laplace transform found in Equation (85c), an oscillatory function with a constant amplitude and a period of $\frac{2\pi}{n}$ or $2\pi\sqrt{\frac{r_o^3}{\mu}}$, which is the same as the orbital period of the chief satellite. To find expres-

sions of l and q in terms of initial conditions, we start with Equation (88) and its derivative (both at $t = 0$)

$$\begin{aligned}x_o - a &= \rho \sin(\theta) \\ \dot{x}_o &= \rho n \cos(\theta) \Leftrightarrow \frac{\dot{x}_o}{n} = \rho \cos(\theta)\end{aligned}$$

and inserting them into Equation (95) and its derivative (also at $t = 0$)

$$z_o = l\rho \sin(\theta) + 2q\rho \cos(\theta) = l(x_o - a) + q\left(2\frac{\dot{x}_o}{n}\right) \quad (92)$$

$$\dot{z}_o = l\rho n \cos(\theta) - 2q\rho n \sin(\theta) = l\dot{x}_o - q[2n(x_o - a)] \quad (93)$$

In matrix form

$$\begin{bmatrix} z_o \\ \dot{z}_o \end{bmatrix} = \begin{bmatrix} x_o - a & 2\frac{\dot{x}_o}{n} \\ \dot{x}_o & -2n(x_o - a) \end{bmatrix} \begin{bmatrix} l \\ q \end{bmatrix}$$

Solving for l and q by multiplying both sides by the matrix inverse

$$\begin{bmatrix} l \\ q \end{bmatrix} = \begin{bmatrix} \frac{-n^2(a-x_o)}{n^2x_o^2-2x_on^2a+n^2a^2+\dot{x}_o^2} & \frac{\dot{x}_o}{n^2x_o^2-2rn^2a+n^2a^2+\dot{x}_o^2} \\ \frac{\frac{1}{2}\dot{x}_on}{n^2x_o^2-2x_on^2a+n^2a^2+\dot{x}_o^2} & \frac{\frac{1}{2}(a-x_o)n}{n^2x_o^2-2x_on^2a+n^2a^2+\dot{x}_o^2} \end{bmatrix} \begin{bmatrix} z_o \\ \dot{z}_o \end{bmatrix}$$

Multiplying through and simplifying

$$\begin{aligned}l &= \frac{\dot{z}_o\dot{x}_o - z_on^2(a-x_o)}{\dot{x}_o^2 + n^2(a-x_o)^2} \\ q &= \frac{z_o\dot{x}_on + \dot{z}_on(a-x_o)}{2[\dot{x}_o^2 + n^2(a-x_o)^2]}\end{aligned}$$

The \hat{Z} motion can also be formulated in the alternative way. Starting with Equation (85c)

$$z(t) = z_o \cos(nt) + \frac{\dot{z}_o}{n} \sin(nt)$$

the sinusoidal terms can be combined via the harmonic addition theorem (Appendix A.3)

$$z(t) = \sqrt{\left(\frac{\dot{z}_o}{n}\right)^2 + z_o^2} \cos \left[nt + \tan^{-1} \left(\frac{-\dot{z}_o}{nz_o} \right) \right] \quad (94)$$

Define two new constants

$$\begin{aligned} z_{\max} &= \sqrt{\left(\frac{\dot{z}_o}{n}\right)^2 + z_o^2} \\ \phi &= \tan^{-1} \left(\frac{-\dot{z}_o}{nz_o} \right) \end{aligned}$$

Thus

$$z(t) = z_{\max} \cos(nt + \phi) \quad (95)$$

Using the conversions formulated in Appendix F, we can express these closed-form solutions as functions of chief orbit fractions as opposed to absolute time. Noting that $nt = 2\pi\tilde{t}$ (Equation (2) in Section 3.1)

$$\begin{aligned} \tilde{x}(\tilde{t}) = x(\tilde{t}) &= \rho \sin(2\pi\tilde{t} + \theta) + a \\ \tilde{y}(\tilde{t}) = y(\tilde{t}) &= 2\rho \cos(2\pi\tilde{t} + \theta) - 3\pi a\tilde{t} + b \\ \tilde{z}(\tilde{t}) = z(\tilde{t}) &= l\rho \sin(2\pi\tilde{t} + \theta) + 2q\rho \cos(2\pi\tilde{t} + \theta) \end{aligned}$$

or

$$\tilde{z}(\tilde{t}) = \tilde{z}_{\max} \cos(2\pi\tilde{t} + \phi) \quad (97)$$

where the values of the relative orbit elements do not change when calculated with the scaled versions of relative position and velocity

$$a = \frac{2\dot{y}_o + 4nx_o}{n} = \frac{1}{\pi}\dot{y}_o + 4\tilde{x}_o \quad (98a)$$

$$b = \frac{ny_o - 2\dot{x}_o}{n} = \tilde{y}_o - \frac{1}{\pi}\dot{x}_o \quad (98b)$$

$$\rho = \sqrt{(x_o - a)^2 + \left(\frac{\dot{x}_o}{n}\right)^2} = \sqrt{(\tilde{x}_o - a)^2 + \left(\frac{1}{2\pi}\dot{x}_o\right)^2} \quad (98c)$$

$$l = \frac{\dot{z}_o\dot{x}_o - z_on^2(a - x_o)}{\dot{x}_o^2 + n^2(a - x_o)^2} = \frac{\dot{z}_o\tilde{x}_o - 4\pi^2\tilde{z}_o(a - \tilde{x}_o)}{\dot{x}_o^2 + 4\pi^2(a - \tilde{x}_o)^2} \quad (98d)$$

$$q = \frac{z_o\dot{x}_on + \dot{z}_on(a - x_o)}{2[\dot{x}_o^2 + n^2(a - x_o)^2]} = \frac{\pi\tilde{z}_o\dot{x}_o + \pi\dot{z}_o(a - \tilde{x}_o)}{\dot{x}_o^2 + 4\pi^2(a - \tilde{x}_o)^2} \quad (98e)$$

$$\theta = \tan^{-1} \left[\frac{n(x_o - a)}{\dot{x}_o} \right] = \tan^{-1} \left[\frac{2\pi(\tilde{x}_o - a)}{\dot{x}_o} \right] \quad (98f)$$

$$\tilde{z}_{\max} = \sqrt{\left(\frac{\dot{z}_o}{n}\right)^2 + z_o^2} = \sqrt{\left(\frac{\dot{z}_o}{2\pi}\right)^2 + \tilde{z}_o^2} \quad (98g)$$

$$\phi = \tan^{-1} \left(\frac{-\dot{z}_o}{nz_o} \right) = \tan^{-1} \left(\frac{-\dot{z}_o}{2\pi\tilde{z}_o} \right) \quad (98h)$$

and the relative velocities

$$\begin{aligned} \dot{x}(\tilde{t}) &= \frac{2\pi}{n}\dot{x}(t) = 2\pi\rho \cos(2\pi\tilde{t} + \theta) \\ \dot{y}(\tilde{t}) &= \frac{2\pi}{n}\dot{y}(t) = -4\pi\rho \sin(2\pi\tilde{t} + \theta) - 3\pi a \\ \dot{z}(\tilde{t}) &= \frac{2\pi}{n}\dot{z}(t) = 2\pi l\rho \cos(2\pi\tilde{t} + \theta) - 4\pi q\rho \sin(2\pi\tilde{t} + \theta) \end{aligned}$$

or

$$\dot{z}(\tilde{t}) = \frac{2\pi}{n}\dot{z}(t) = -2\pi z_{\max} \sin(2\pi\tilde{t} + \phi)$$

G.1 Units Analysis

The variables x , y , and z are positions and defined in terms of a **length**. Likewise, \dot{x} , \dot{y} , and \dot{z} are velocities and are expressed as $\frac{\text{length}}{\text{time}}$. Finally, n is the angular frequency of the orbit and is expressed in units of $\frac{1}{\text{time}}$. These units will not change

if calculated using relative position and velocities as functions of chief orbit fractions.

$$a = \frac{\frac{\text{length}}{\text{time}} + \frac{1}{\text{time}} \text{length}}{\frac{1}{\text{time}}} = \frac{\frac{\text{length}}{\text{time}}}{\frac{1}{\text{time}}} = \text{length}$$

$$b = \frac{\frac{1}{\text{time}} \text{length} + \frac{\text{length}}{\text{time}}}{\frac{1}{\text{time}}} = \frac{\frac{\text{length}}{\text{time}}}{\frac{1}{\text{time}}} = \text{length}$$

$$\rho = \sqrt{(\text{length} - \text{length})^2 + \left(\frac{\frac{\text{length}}{\text{time}}}{\frac{1}{\text{time}}}\right)^2} = \sqrt{\text{length}^2 + \text{length}^2} = \text{length}$$

$$l = \frac{\frac{\text{length}}{\text{time}} \frac{\text{length}}{\text{time}} - \text{length} \left(\frac{1}{\text{time}}\right)^2 (\text{length} - \text{length})}{\left(\frac{\text{length}}{\text{time}}\right)^2 + \left(\frac{1}{\text{time}}\right)^2 (\text{length} - \text{length})^2} = \frac{\left(\frac{\text{length}}{\text{time}}\right)^2 - \frac{\text{length}^2}{\text{time}^2}}{\left(\frac{\text{length}}{\text{time}}\right)^2 + \frac{\text{length}^2}{\text{time}^2}} = \text{unitless}$$

$$q = \frac{\text{length} \frac{\text{length}}{\text{time}} \frac{1}{\text{time}} + \frac{\text{length}}{\text{time}} \frac{1}{\text{time}} (\text{length} - \text{length})}{\left(\frac{\text{length}}{\text{time}}\right)^2 + \left(\frac{1}{\text{time}}\right)^2 (\text{length} - \text{length})^2} = \frac{\frac{\text{length}^2}{\text{time}^2} + \frac{\text{length}^2}{\text{time}^2}}{\left(\frac{\text{length}}{\text{time}}\right)^2 + \frac{\text{length}^2}{\text{time}^2}} = \text{unitless}$$

$$\theta = \tan^{-1} \left(\frac{\frac{1}{\text{time}} (\text{length} - \text{length})}{\frac{\text{length}}{\text{time}}} \right) = \tan^{-1} \left(\frac{\frac{\text{length}}{\text{time}}}{\frac{\text{length}}{\text{time}}} \right) = \text{radians}$$

Appendix H. Transformations between the Inertial and Relative Reference Frames

In order to use an inertially propagated truth model, we need to be able to transform position and velocity vectors from the relative to inertial frames and vice versa.

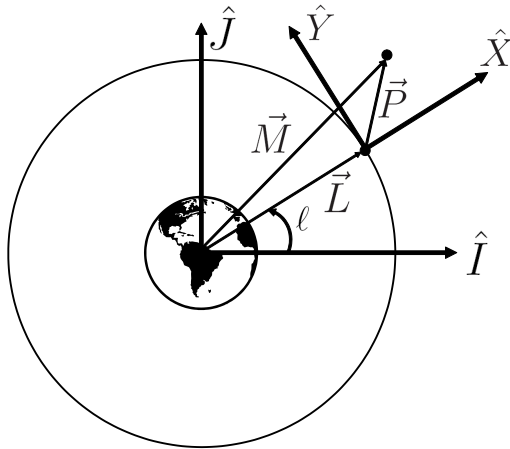


Figure 88: Relationship Between the $\hat{X}\hat{Y}\hat{Z}$ and $\hat{I}\hat{J}\hat{K}$ Frames

Referencing Figure 88, the position vector is

$${}^{i\hat{j}\hat{k}}\vec{M} = {}^{\hat{x}\hat{y}\hat{z}}\vec{P} + {}^{i\hat{j}\hat{k}}\vec{L}$$

The velocity is calculated via the inertial derivative (see Appendix A.2)

$${}^{i\hat{j}\hat{k}}\dot{\vec{M}} = {}^{\hat{x}\hat{y}\hat{z}}\dot{\vec{P}} + \begin{bmatrix} 0 \\ 0 \\ n \end{bmatrix} \times {}^{\hat{x}\hat{y}\hat{z}}\vec{P} + {}^{i\hat{j}\hat{k}}\dot{\vec{L}}$$

The vectors expressed in the relative frame need to be transformed to the inertial frame. If inertial position and velocity vectors of the chief satellite are available, the rotation matrices can be calculated as

$$C^{\text{R2I}} = \left[\hat{X} \mid \hat{Y} \mid \hat{Z} \right]$$

where \hat{X} , \hat{Y} , and \hat{Z} are unit vectors for each direction expressed in the $\hat{I}\hat{J}\hat{K}$ frame. The superscript $R2I$ indicates the rotation matrix from the relative to inertial frame and $I2R$ indicates the rotation matrix from the inertial to relative frame. The radial direction is simply the unit vector of the chief's position

$$\hat{X} = \frac{\hat{I}\hat{J}\hat{K}\vec{L}}{\|\hat{I}\hat{J}\hat{K}\vec{L}\|_2}$$

If the chief is in a circular orbit, then its velocity vector will always be perpendicular to the position vector

$$\hat{Y} = \frac{\hat{I}\hat{J}\hat{K}\dot{\vec{L}}}{\|\hat{I}\hat{J}\hat{K}\dot{\vec{L}}\|_2}$$

and the out-of-plane direction completes the right-handed coordinate system

$$\hat{Z} = \hat{X} \times \hat{Y} = \frac{\hat{I}\hat{J}\hat{K}\vec{L}}{\|\hat{I}\hat{J}\hat{K}\vec{L}\|_2} \times \frac{\hat{I}\hat{J}\hat{K}\dot{\vec{L}}}{\|\hat{I}\hat{J}\hat{K}\dot{\vec{L}}\|_2}$$

Thus, the position vector can be expressed as

$$\hat{I}\hat{J}\hat{K}\vec{M} = C^{R2I} \begin{bmatrix} x \\ y \\ z \end{bmatrix} + \hat{I}\hat{J}\hat{K}\vec{L} \quad (100)$$

and the velocity vector as

$$\begin{aligned} \hat{I}\hat{J}\hat{K}\dot{\vec{M}} &= C^{R2I} \left(\begin{bmatrix} \dot{x} \\ \dot{y} \\ \dot{z} \end{bmatrix} + \begin{bmatrix} 0 \\ 0 \\ n \end{bmatrix} \times \begin{bmatrix} x \\ y \\ z \end{bmatrix} \right) + \hat{I}\hat{J}\hat{K}\dot{\vec{L}} \\ &= C^{R2I} \begin{bmatrix} \dot{x} - ny \\ \dot{y} + nx \\ \dot{z} \end{bmatrix} + \hat{I}\hat{J}\hat{K}\dot{\vec{L}} \end{aligned} \quad (101)$$

Equations (100) and (101) can be solved for the relative vectors if we desire to go from the inertial to the relative frame.

$$C^{R2I} \begin{bmatrix} x \\ y \\ z \end{bmatrix} = i\hat{j}\hat{k}\vec{M} - i\hat{j}\hat{k}\vec{L} \quad (102)$$

$$C^{R2I} \begin{bmatrix} \dot{x} \\ \dot{y} \\ \dot{z} \end{bmatrix} = \left(i\hat{j}\hat{k}\dot{\vec{M}} - i\hat{j}\hat{k}\dot{\vec{L}} \right) - C^{R2I} \begin{bmatrix} -ny \\ nx \\ 0 \end{bmatrix}$$

Noting that for orthonormal rotation matrices [24]

$$C^{I2R} * C^{R2I} = C^{I2R} * (C^{I2R})' = C^{I2R} * (C^{I2R})^{-1} = I$$

we get

$$\hat{x}\hat{y}\hat{z}\vec{P} = \begin{bmatrix} x \\ y \\ z \end{bmatrix} = C^{I2R} \left(i\hat{j}\hat{k}\vec{M} - i\hat{j}\hat{k}\vec{L} \right) \quad (103)$$

$$\hat{x}\hat{y}\hat{z}\dot{\vec{P}} = \begin{bmatrix} \dot{x} \\ \dot{y} \\ \dot{z} \end{bmatrix} = C^{I2R} \left(i\hat{j}\hat{k}\dot{\vec{M}} - i\hat{j}\hat{k}\dot{\vec{L}} \right) + \begin{bmatrix} ny \\ -nx \\ 0 \end{bmatrix} \quad (104)$$

An alternative formulation of the rotation matrix is derived henceforth. By inspection, the rotation matrices are

$$\begin{bmatrix} \hat{X} \\ \hat{Y} \\ \hat{Z} \end{bmatrix} = \underbrace{\begin{bmatrix} \cos \ell & \sin \ell & 0 \\ -\sin \ell & \cos \ell & 0 \\ 0 & 0 & 1 \end{bmatrix}}_{C^{R2I}} \begin{bmatrix} \hat{I} \\ \hat{J} \\ \hat{K} \end{bmatrix} \quad (105)$$

$$\begin{bmatrix} \hat{I} \\ \hat{J} \\ \hat{K} \end{bmatrix} = \underbrace{\begin{bmatrix} \cos \ell & -\sin \ell & 0 \\ \sin \ell & \cos \ell & 0 \\ 0 & 0 & 1 \end{bmatrix}}_{C^{I2R}} \begin{bmatrix} \hat{X} \\ \hat{Y} \\ \hat{Z} \end{bmatrix} \quad (106)$$

where ℓ for the circular orbit is

$$\ell = nt_o$$

and t_o is the time since passage over \hat{I} . Equations (103) and (104) can be combined into a more compact form. Let

$$\hat{i}\hat{j}\hat{k}\vec{L} = \begin{bmatrix} X_C \\ Y_C \\ Z_C \end{bmatrix} \quad \hat{i}\hat{j}\hat{k}\vec{M} = \begin{bmatrix} X_D \\ Y_D \\ Z_D \end{bmatrix} \quad \hat{i}\hat{j}\hat{k}\dot{\vec{L}} = \begin{bmatrix} \dot{X}_C \\ \dot{Y}_C \\ \dot{Z}_C \end{bmatrix} \quad \hat{i}\hat{j}\hat{k}\dot{\vec{M}} = \begin{bmatrix} \dot{X}_D \\ \dot{Y}_D \\ \dot{Z}_D \end{bmatrix}$$

noting that

$$\begin{bmatrix} ny \\ -nx \\ 0 \end{bmatrix} = n \begin{bmatrix} 0 & 1 & 0 \\ -1 & 0 & 0 \\ 0 & 0 & 0 \end{bmatrix} \begin{bmatrix} x \\ y \\ z \end{bmatrix}$$

then

$$\begin{bmatrix} x \\ y \\ z \\ \dot{x} \\ \dot{y} \\ \dot{z} \end{bmatrix} = \begin{bmatrix} C^{I2R} \begin{bmatrix} X_D - X_C \\ Y_D - Y_C \\ Z_D - Z_C \end{bmatrix} \\ \dots \\ C^{I2R} \begin{bmatrix} \dot{X}_D - \dot{X}_C \\ \dot{Y}_D - \dot{Y}_C \\ \dot{Z}_D - \dot{Z}_C \end{bmatrix} + n \begin{bmatrix} 0 & 1 & 0 \\ -1 & 0 & 0 \\ 0 & 0 & 0 \end{bmatrix} C^{I2R} \begin{bmatrix} X_D - X_C \\ Y_D - Y_C \\ Z_D - Z_C \end{bmatrix} \end{bmatrix}$$

and substituting the rotation matrices, Equation (106), we get

$$\begin{bmatrix} x \\ y \\ z \\ \dot{x} \\ \dot{y} \\ \dot{z} \end{bmatrix} = \begin{bmatrix} \cos \ell & -\sin \ell & 0 & 0 & 0 & 0 \\ \sin \ell & \cos \ell & 0 & 0 & 0 & 0 \\ 0 & 0 & 1 & 0 & 0 & 0 \\ n \sin \ell & n \cos \ell & 0 & \cos \ell & -\sin \ell & 0 \\ -n \cos \ell & n \sin \ell & 0 & \sin \ell & \cos \ell & 0 \\ 0 & 0 & 0 & 0 & 0 & 1 \end{bmatrix} \begin{bmatrix} X_D - X_C \\ Y_D - Y_C \\ Z_D - Z_C \\ \dot{X}_D - \dot{X}_C \\ \dot{Y}_D - \dot{Y}_C \\ \dot{Z}_D - \dot{Z}_C \end{bmatrix} \quad (107)$$

Appendix I. Circular Chief Relative Velocities

Assuming we have found points of interest on or within the lobe between which we want the deputy to travel, a solution for the initial and final velocities is required.

I.1 Initial Relative Velocity

The following is a modification of the derivation presented by Mullins [37]. Assume that the deputy is at the initial point at $t_o = 0$ and at the final point at $t_f = T$. Let $x(T) = x_f$, $y(T) = y_f$, and $z(T) = z_f$. Start with a slightly modified form of Equation (82) from Appendix G

$$\begin{aligned} x_f &= x(T) = \frac{\dot{x}_o}{n} \sin(nT) - \left[\frac{2\dot{y}_o}{n} + 3x_o \right] \cos(nT) + \frac{2\dot{y}_o}{n} + 4x_o \\ y_f &= y(T) = 2 \left[\frac{2\dot{y}_o}{n} + 3x_o \right] \sin(nT) + \frac{2\dot{x}_o}{n} \cos(nT) - \frac{3}{2}n \left[\frac{2\dot{y}_o}{n} + 4x_o \right] T + y_o - \frac{2\dot{x}_o}{n} \\ z_f &= z(T) = \frac{\dot{z}_o}{n} \sin(nT) + z_o \cos(nT) \end{aligned}$$

Combining terms and preparing for matrix form

$$\begin{aligned} x_f &= \frac{1}{n} \sin(nT)\dot{x}_o + \frac{2}{n} [1 - \cos(nT)] \dot{y}_o + [4 - 3 \cos(nT)] x_o \\ y_f &= \frac{2}{n} [-1 + \cos(nT)] \dot{x}_o + \frac{1}{n} [4 \sin(nT) - 3nT] \dot{y}_o + [6 \sin(nT) - 6nT] x_o + y_o \\ z_f &= \frac{1}{n} \sin(nT)\dot{z}_o + \cos(nT)z_o \end{aligned}$$

yielding ($S = \sin(nT)$, $C = \cos(nT)$)

$$\begin{bmatrix} x_f \\ y_f \\ z_f \end{bmatrix} = \begin{bmatrix} \frac{1}{n}S & \frac{2}{n}[1-C] & 0 \\ \frac{2}{n}[-1+C] & \frac{1}{n}[4S-3nT] & 0 \\ 0 & 0 & \frac{1}{n}S \end{bmatrix} \begin{bmatrix} \dot{x}_o \\ \dot{y}_o \\ \dot{z}_o \end{bmatrix} + \begin{bmatrix} [4-3C]x_o \\ [6S-6nT]x_o + y_o \\ Cz_o \end{bmatrix} \quad (108)$$

Note that there is a sine term in the 3-by-3 element of the first matrix. When this sine function goes to zero, the matrix is singular. Physically the deputy satellite is passing through the \hat{Y} axis (or a line parallel to it), the intersect point for an infinite

number of relative orbits. Therefore the initial/final conditions and time-of-flight do not uniquely define an orbit-thus an indeterminate matrix. This restriction should not be a problem. Multiplying each side by n and rearranging terms:

$$\begin{bmatrix} nx_f - n[4 - 3C]x_o \\ ny_f - n[6S - 6nT]x_o - ny_o \\ nz_f - nCz_o \end{bmatrix} = \begin{bmatrix} S & 2 - 2C & 0 \\ -2 + 2C & 4S - 3nT & 0 \\ 0 & 0 & S \end{bmatrix} \begin{bmatrix} \dot{x}_o \\ \dot{y}_o \\ \dot{z}_o \end{bmatrix}$$

Finding the inverse via co-factors

$$\begin{aligned} A_{11} &= (4S - 3nT)S - 0 = 4S^2 - 3nTS \\ A_{12} &= -[(-2 + 2C)S - 0] = 2S - 2SC \\ A_{13} &= 0 - 0 = 0 \\ A_{21} &= -[(2 - 2C)S - 0] = -2S + 2SC \\ A_{22} &= S * S - 0 = S^2 \\ A_{23} &= -[0 - 0] = 0 \\ A_{31} &= 0 - 0 = 0 \\ A_{32} &= -[0 - 0] = 0 \\ A_{33} &= S(4S - 3nT) - (-2 + 2C)(2 - 2C) = 4S^2 - 3nTS + 4 - 8C + 4C^2 \\ &= 8 - 3nTS - 8C \end{aligned}$$

The determinant can be found from the first row

$$\begin{aligned} \|A\| &= a_{11}A_{11} + a_{12}A_{12} + a_{13}A_{13} \\ &= S(4S^2 - 3nTS) + (2 - 2C)(2S - 2SC) + 0 * 0 \\ &= S(8 - 3nTS - 8C) \end{aligned}$$

and finally the inverse [53]

$$A^{-1} = \frac{\text{adj } A}{\det A}$$

where the adjoint of A is the transpose of the co-factor matrix

$$\begin{aligned}
A^{-1} &= \frac{1}{S(8-3nTS-8C)} \begin{bmatrix} 4S^2-3nTS & 2S-2SC & 0 \\ -2S+2SC & S^2 & 0 \\ 0 & 0 & 8-3nTS-8C \end{bmatrix}' \\
&= \begin{bmatrix} \frac{4S^2-3nTS}{S(8-3nTS-8C)} & \frac{-2S+2SC}{S(8-3nTS-8C)} & 0 \\ \frac{2S-2SC}{S(8-3nTS-8C)} & \frac{S^2}{S(8-3nTS-8C)} & 0 \\ 0 & 0 & \frac{8-3nTS-8C}{S(8-3nTS-8C)} \end{bmatrix} \\
A^{-1} &= \begin{bmatrix} \frac{4 \sin(nT)-3nT}{8-3nT \sin(nT)-8 \cos(nT)} & \frac{-2+2 \cos(nT)}{8-3nT \sin(nT)-8 \cos(nT)} & 0 \\ \frac{2-2 \cos(nT)}{8-3nT \sin(nT)-8 \cos(nT)} & \frac{\sin(nT)}{8-3nT \sin(nT)-8 \cos(nT)} & 0 \\ 0 & 0 & \frac{1}{\sin(nT)} \end{bmatrix}
\end{aligned}$$

Therefore the solution to the initial relative velocities is

$$\begin{bmatrix} \dot{x}_o \\ \dot{y}_o \\ \dot{z}_o \end{bmatrix} = \begin{bmatrix} \frac{4 \sin(nT)-3nT}{8-3nT \sin(nT)-8 \cos(nT)} & \frac{-2+2 \cos(nT)}{8-3nT \sin(nT)-8 \cos(nT)} & 0 \\ \frac{2-2 \cos(nT)}{8-3nT \sin(nT)-8 \cos(nT)} & \frac{\sin(nT)}{8-3nT \sin(nT)-8 \cos(nT)} & 0 \\ 0 & 0 & \frac{1}{\sin(nT)} \end{bmatrix} \begin{bmatrix} nx_f - n[4-3 \cos(nT)]x_o \\ ny_f - n[6 \sin(nT) - 6nT]x_o - ny_o \\ nz_f - n \cos(nT)z_o \end{bmatrix}$$

We can further break down the second matrix into

$$n \begin{bmatrix} -4+3 \cos(nT) & 0 & 0 & 1 & 0 & 0 \\ -6 \sin(nT) + 6nT & -1 & 0 & 0 & 1 & 0 \\ 0 & 0 & -\cos(nT) & 0 & 0 & 1 \end{bmatrix} \begin{bmatrix} x_o \\ y_o \\ z_o \\ x_f \\ y_f \\ z_f \end{bmatrix}$$

Multiplying this out, the transformation matrix becomes

$$n \begin{bmatrix} \frac{[4S-3nT][-4+3C]+[-2+2C][-6S+6nT]}{8-3nTS-8C} & \frac{-[-2+2C]}{8-3nTS-8C} & 0 & \frac{4S-3nT}{8-3nTS-8C} & \frac{-2+2C}{8-3nTS-8C} & 0 \\ \frac{[2-2C][-4+3C]+S[-6S+6nT]}{8-3nTS-8C} & \frac{-S}{8-3nTS-8C} & 0 & \frac{2-2C}{8-3nTS-8C} & \frac{S}{8-3nTS-8C} & 0 \\ 0 & 0 & -\frac{C}{S} & 0 & 0 & \frac{1}{S} \end{bmatrix}$$

Simplifying

$$n \begin{bmatrix} \frac{-4S+3nTC}{8-3nTS-8C} & \frac{2-2C}{8-3nTS-8C} & 0 & \frac{4S-3nT}{8-3nTS-8C} & \frac{-2+2C}{8-3nTS-8C} & 0 \\ \frac{-14+6nTS+14C}{8-3nTS-8C} & \frac{-S}{8-3nTS-8C} & 0 & \frac{2-2C}{8-3nTS-8C} & \frac{S}{8-3nTS-8C} & 0 \\ 0 & 0 & -\frac{C}{S} & 0 & 0 & \frac{1}{S} \end{bmatrix}$$

Thus the transformation is

$$\begin{bmatrix} \dot{x}_o \\ \dot{y}_o \\ \dot{z}_o \end{bmatrix} = n \begin{bmatrix} \frac{-4S+3nTC}{8-3nTS-8C} & \frac{2-2C}{8-3nTS-8C} & 0 & \frac{4S-3nT}{8-3nTS-8C} & \frac{-2+2C}{8-3nTS-8C} & 0 \\ \frac{-14+6nTS+14C}{8-3nTS-8C} & \frac{-S}{8-3nTS-8C} & 0 & \frac{2-2C}{8-3nTS-8C} & \frac{S}{8-3nTS-8C} & 0 \\ 0 & 0 & -\frac{C}{S} & 0 & 0 & \frac{1}{S} \end{bmatrix} \begin{bmatrix} x_o \\ y_o \\ z_o \\ x_f \\ y_f \\ z_f \end{bmatrix} \quad (109)$$

We can also express this in terms of fractions of a chief orbit period by substituting $nT = 2\pi\tilde{T}$ (Equation (2) in Section 3.1)

$$\begin{bmatrix} \dot{x}_o \\ \dot{y}_o \\ \dot{z}_o \end{bmatrix} = n \begin{bmatrix} \frac{-4\tilde{S}+6\pi\tilde{T}\tilde{C}}{8-6\pi\tilde{T}\tilde{S}-8\tilde{C}} & \frac{2-2\tilde{C}}{8-6\pi\tilde{T}\tilde{S}-8\tilde{C}} & 0 & \frac{4\tilde{S}-6\pi\tilde{T}}{8-6\pi\tilde{T}\tilde{S}-8\tilde{C}} & \frac{-2+2\tilde{C}}{8-6\pi\tilde{T}\tilde{S}-8\tilde{C}} & 0 \\ \frac{-14+12\pi\tilde{T}\tilde{S}+14\tilde{C}}{8-6\pi\tilde{T}\tilde{S}-8\tilde{C}} & \frac{-\tilde{S}}{8-6\pi\tilde{T}\tilde{S}-8\tilde{C}} & 0 & \frac{2-2\tilde{C}}{8-6\pi\tilde{T}\tilde{S}-8\tilde{C}} & \frac{\tilde{S}}{8-6\pi\tilde{T}\tilde{S}-8\tilde{C}} & 0 \\ 0 & 0 & -\frac{\tilde{C}}{\tilde{S}} & 0 & 0 & \frac{1}{\tilde{S}} \end{bmatrix} \begin{bmatrix} x_o \\ y_o \\ z_o \\ x_f \\ y_f \\ z_f \end{bmatrix} \quad (110)$$

where $\tilde{T} = T/P$ $\tilde{S} = \sin(2\pi\tilde{T})$ $\tilde{C} = \cos(2\pi\tilde{T})$

If we choose units of relative velocity that are functions of time as a fraction of chief orbit radius as opposed to absolute time, we can use the transformation in Equation (78), Appendix F

$$\begin{bmatrix} \dot{\tilde{x}}_o \\ \dot{\tilde{y}}_o \\ \dot{\tilde{z}}_o \end{bmatrix} = \frac{2\pi}{n} \begin{bmatrix} \dot{x}_o \\ \dot{y}_o \\ \dot{z}_o \end{bmatrix} = 2\pi \begin{bmatrix} \frac{-4\tilde{S}+6\pi\tilde{T}\tilde{C}}{8-6\pi\tilde{T}\tilde{S}-8\tilde{C}} & \frac{2-2\tilde{C}}{8-6\pi\tilde{T}\tilde{S}-8\tilde{C}} & 0 & \frac{4\tilde{S}-6\pi\tilde{T}}{8-6\pi\tilde{T}\tilde{S}-8\tilde{C}} & \frac{-2+2\tilde{C}}{8-6\pi\tilde{T}\tilde{S}-8\tilde{C}} & 0 \\ \frac{-14+12\pi\tilde{T}\tilde{S}+14\tilde{C}}{8-6\pi\tilde{T}\tilde{S}-8\tilde{C}} & \frac{-\tilde{S}}{8-6\pi\tilde{T}\tilde{S}-8\tilde{C}} & 0 & \frac{2-2\tilde{C}}{8-6\pi\tilde{T}\tilde{S}-8\tilde{C}} & \frac{\tilde{S}}{8-6\pi\tilde{T}\tilde{S}-8\tilde{C}} & 0 \\ 0 & 0 & -\frac{\tilde{C}}{\tilde{S}} & 0 & 0 & \frac{1}{\tilde{S}} \end{bmatrix} \begin{bmatrix} x_o \\ y_o \\ z_o \\ x_f \\ y_f \\ z_f \end{bmatrix} \quad (111)$$

Finally, it is interesting to note that the y_o and y_f terms in the time-of-flight matrix are the negative of the other, thus we can substitute a Δy .

$$\begin{bmatrix} \dot{\tilde{x}}_o \\ \dot{\tilde{y}}_o \\ \dot{\tilde{z}}_o \end{bmatrix} = 2\pi \begin{bmatrix} \frac{-4\tilde{S}+6\pi\tilde{T}\tilde{C}}{8-6\pi\tilde{T}\tilde{S}-8\tilde{C}} & 0 & \frac{4\tilde{S}-6\pi\tilde{T}}{8-6\pi\tilde{T}\tilde{S}-8\tilde{C}} & 0 & \frac{-2+2\tilde{C}}{8-6\pi\tilde{T}\tilde{S}-8\tilde{C}} \\ \frac{-14+12\pi\tilde{T}\tilde{S}+14\tilde{C}}{8-6\pi\tilde{T}\tilde{S}-8\tilde{C}} & 0 & \frac{2-2\tilde{C}}{8-6\pi\tilde{T}\tilde{S}-8\tilde{C}} & 0 & \frac{\tilde{S}}{8-6\pi\tilde{T}\tilde{S}-8\tilde{C}} \\ 0 & -\frac{\tilde{C}}{\tilde{S}} & 0 & \frac{1}{\tilde{S}} & 0 \end{bmatrix} \begin{bmatrix} x_o \\ z_o \\ x_f \\ z_f \\ \Delta y \end{bmatrix} \quad (112)$$

where $\Delta y = y_f - y_o$

1.2 Final Relative Velocity

To calculate the velocities at the end of an arc, we start with the derivative of Equation (82) from Appendix G

$$\begin{aligned} \dot{x}_f &= \dot{x}(T) = \frac{\dot{x}_o}{n} \cos(nT) - \left[\frac{2\dot{y}_o}{n} + 3x_o \right] (-n) \sin(nT) \\ \dot{y}_f &= \dot{y}(T) = 2 \left[\frac{2\dot{y}_o}{n} + 3x_o \right] n \cos(nT) + \frac{2\dot{x}_o}{n} (-n) \sin(nT) - \frac{3}{2} n \left[\frac{2\dot{y}_o}{n} + 4x_o \right] \\ \dot{z}_f &= \dot{z}(T) = \frac{\dot{z}_o}{n} \cos(nT) + z_o (-n) \sin(nT) \end{aligned}$$

Preparing for matrix form

$$\dot{x}_f = \cos(nT)\dot{x}_o + 2\sin(nT)\dot{y}_o + 3n\sin(nT)x_o$$

$$\dot{y}_f = -2\sin(nT)\dot{x}_o + [-3 + 4\cos(nT)]\dot{y}_o + [-6n + 6n\cos(nT)]x_o$$

$$\dot{z}_f = \cos(nT)\dot{z}_o - n\sin(nT)z_o$$

yields ($S = \sin(nT)$, $C = \cos(nT)$)

$$\begin{bmatrix} \dot{x}_f \\ \dot{y}_f \\ \dot{z}_f \end{bmatrix} = \begin{bmatrix} C & 2S & 0 \\ -2S & -3 + 4C & 0 \\ 0 & 0 & C \end{bmatrix} \begin{bmatrix} \dot{x}_o \\ \dot{y}_o \\ \dot{z}_o \end{bmatrix} + \begin{bmatrix} 3nS & 0 & 0 \\ -6n + 6nC & 0 & 0 \\ 0 & 0 & -nS \end{bmatrix} \begin{bmatrix} x_o \\ y_o \\ z_o \end{bmatrix}$$

Substituting Equation (109), the first term is

$$\begin{bmatrix} C & 2S & 0 \\ -2S & -3 + 4C & 0 \\ 0 & 0 & C \end{bmatrix} n \begin{bmatrix} \frac{-4S+3nTC}{8-3nTS-8C} & \frac{2-2C}{8-3nTS-8C} & 0 & \frac{4S-3nT}{8-3nTS-8C} & \frac{-2+2C}{8-3nTS-8C} & 0 \\ \frac{-14+6nTS+14C}{8-3nTS-8C} & \frac{-S}{8-3nTS-8C} & 0 & \frac{2-2C}{8-3nTS-8C} & \frac{S}{8-3nTS-8C} & 0 \\ 0 & 0 & -\frac{C}{S} & 0 & 0 & \frac{1}{S} \end{bmatrix} \begin{bmatrix} x_o \\ y_o \\ z_o \\ x_f \\ y_f \\ z_f \end{bmatrix}$$

and the second term

$$n \begin{bmatrix} 3S & 0 & 0 & 0 & 0 & 0 \\ -6 + 6C & 0 & 0 & 0 & 0 & 0 \\ 0 & 0 & -S & 0 & 0 & 0 \end{bmatrix} \begin{bmatrix} x_o \\ y_o \\ z_o \\ x_f \\ y_f \\ z_f \end{bmatrix}$$

Multiplying out the first term and adding it to the second

$$\begin{aligned}
A_{11} &= \frac{C(-4S + 3nTC)}{8 - 3nTS - 8C} + \frac{2S(-14 + 6nTS + 14C)}{8 - 3nTS - 8C} + \frac{3S(8 - 3nTS - 8C)}{8 - 3nTS - 8C} \\
&= \frac{-4S + 3nT}{8 - 3nTS - 8C} \\
A_{12} &= \frac{C(2 - 2C)}{8 - 3nTS - 8C} + \frac{2S(-S)}{8 - 3nTS - 8C} + 0 = \frac{-2 + 2C}{8 - 3nTS - 8C} \\
A_{13} &= 0 + 0 = 0 \\
A_{14} &= \frac{C(4S - 3nT)}{8 - 3nTS - 8C} + \frac{2S(2 - 2C)}{8 - 3nTS - 8C} + 0 = \frac{4S - 3nTC}{8 - 3nTS - 8C} \\
A_{15} &= \frac{C(-2 + 2C)}{8 - 3nTS - 8C} + \frac{2S(S)}{8 - 3nTS - 8C} + 0 = \frac{2 - 2C}{8 - 3nTS - 8C} \\
A_{16} &= 0 + 0 = 0 \\
\\
A_{21} &= \frac{-2S(-4S + 3nTC)}{8 - 3nTS - 8C} + \frac{(-3 + 4C)(-14 + 6nTS + 14C)}{8 - 3nTS - 8C} + \frac{(-6 + 6C)(8 - 3nTS - 8C)}{8 - 3nTS - 8C} \\
&= \frac{2 - 2C}{8 - 3nTS - 8C} \\
A_{22} &= \frac{-2S(2 - 2C)}{8 - 3nTS - 8C} + \frac{(-3 + 4C)(-S)}{8 - 3nTS - 8C} + 0 = \frac{-S}{8 - 3nTS - 8C} \\
A_{23} &= 0 + 0 = 0 \\
A_{24} &= \frac{-2S(4S - 3nT)}{8 - 3nTS - 8C} + \frac{(-3 + 4C)(2 - 2C)}{8 - 3nTS - 8C} + 0 = \frac{-14 + 6nTS + 14C}{8 - 3nTS - 8C} \\
A_{25} &= \frac{-2S(-2 + 2C)}{8 - 3nTS - 8C} + \frac{(-3 + 4C)(S)}{8 - 3nTS - 8C} + 0 = \frac{S}{8 - 3nTS - 8C} \\
A_{26} &= 0 + 0 = 0 \\
\\
A_{31} &= 0 + 0 = 0 \\
A_{32} &= 0 + 0 = 0 \\
A_{33} &= C \frac{-C}{S} + (-S) \frac{S}{S} = -\frac{1}{S} \\
A_{34} &= 0 + 0 = 0 \\
A_{35} &= 0 + 0 = 0 \\
A_{36} &= C \frac{1}{S} + 0 = \frac{C}{S}
\end{aligned}$$

Thus the relative velocity at the end of a trajectory can be expressed as

$$\begin{bmatrix} \dot{x}_f \\ \dot{y}_f \\ \dot{z}_f \end{bmatrix} = n \begin{bmatrix} \frac{-4S+3nT}{8-3nTS-8C} & \frac{-2+2C}{8-3nTS-8C} & 0 & \frac{4S-3nTC}{8-3nTS-8C} & \frac{2-2C}{8-3nTS-8C} & 0 \\ \frac{2-2C}{8-3nTS-8C} & \frac{-S}{8-3nTS-8C} & 0 & \frac{-14+6nTS+14C}{8-3nTS-8C} & \frac{S}{8-3nTS-8C} & 0 \\ 0 & 0 & -\frac{1}{S} & 0 & 0 & \frac{C}{S} \end{bmatrix} \begin{bmatrix} x_o \\ y_o \\ z_o \\ x_f \\ y_f \\ z_f \end{bmatrix} \quad (113)$$

We can also express this in terms of fractions of a chief orbit period by substituting $nT = 2\pi\tilde{T}$ (Equation (2) in Section 3.1)

$$\begin{bmatrix} \dot{x}_f \\ \dot{y}_f \\ \dot{z}_f \end{bmatrix} = n \begin{bmatrix} \frac{-4\tilde{S}+6\pi\tilde{T}}{8-6\pi\tilde{T}\tilde{S}-8\tilde{C}} & \frac{-2+2\tilde{C}}{8-6\pi\tilde{T}\tilde{S}-8\tilde{C}} & 0 & \frac{4\tilde{S}-6\pi\tilde{T}\tilde{C}}{8-6\pi\tilde{T}\tilde{S}-8\tilde{C}} & \frac{2-2\tilde{C}}{8-6\pi\tilde{T}\tilde{S}-8\tilde{C}} & 0 \\ \frac{2-2\tilde{C}}{8-6\pi\tilde{T}\tilde{S}-8\tilde{C}} & \frac{-\tilde{S}}{8-6\pi\tilde{T}\tilde{S}-8\tilde{C}} & 0 & \frac{-14+12\pi\tilde{T}\tilde{S}+14\tilde{C}}{8-6\pi\tilde{T}\tilde{S}-8\tilde{C}} & \frac{\tilde{S}}{8-6\pi\tilde{T}\tilde{S}-8\tilde{C}} & 0 \\ 0 & 0 & -\frac{1}{\tilde{S}} & 0 & 0 & \frac{\tilde{C}}{\tilde{S}} \end{bmatrix} \begin{bmatrix} x_o \\ y_o \\ z_o \\ x_f \\ y_f \\ z_f \end{bmatrix} \quad (114)$$

where $\tilde{T} = T/P$ $\tilde{S} = \sin(2\pi\tilde{T})$ $\tilde{C} = \cos(2\pi\tilde{T})$

If we choose units of relative velocity that are functions of time as a fraction of chief orbit radius as opposed to absolute time, we can use the transformation in Equation (78), Appendix F

$$\begin{bmatrix} \dot{\tilde{x}}_f \\ \dot{\tilde{y}}_f \\ \dot{\tilde{z}}_f \end{bmatrix} = \frac{2\pi}{n} \begin{bmatrix} \dot{x}_f \\ \dot{y}_f \\ \dot{z}_f \end{bmatrix} = 2\pi \begin{bmatrix} \frac{-4\tilde{S}+6\pi\tilde{T}}{8-6\pi\tilde{T}\tilde{S}-8\tilde{C}} & \frac{-2+2\tilde{C}}{8-6\pi\tilde{T}\tilde{S}-8\tilde{C}} & 0 & \frac{4\tilde{S}-6\pi\tilde{T}\tilde{C}}{8-6\pi\tilde{T}\tilde{S}-8\tilde{C}} & \frac{2-2\tilde{C}}{8-6\pi\tilde{T}\tilde{S}-8\tilde{C}} & 0 \\ \frac{2-2\tilde{C}}{8-6\pi\tilde{T}\tilde{S}-8\tilde{C}} & \frac{-\tilde{S}}{8-6\pi\tilde{T}\tilde{S}-8\tilde{C}} & 0 & \frac{-14+12\pi\tilde{T}\tilde{S}+14\tilde{C}}{8-6\pi\tilde{T}\tilde{S}-8\tilde{C}} & \frac{\tilde{S}}{8-6\pi\tilde{T}\tilde{S}-8\tilde{C}} & 0 \\ 0 & 0 & -\frac{1}{\tilde{S}} & 0 & 0 & \frac{\tilde{C}}{\tilde{S}} \end{bmatrix} \begin{bmatrix} x_o \\ y_o \\ z_o \\ x_f \\ y_f \\ z_f \end{bmatrix} \quad (115)$$

Similar to the initial relative velocity, we can express this in terms of Δy

$$\begin{bmatrix} \dot{\tilde{x}}_f \\ \dot{\tilde{y}}_f \\ \dot{\tilde{z}}_f \end{bmatrix} = 2\pi \begin{bmatrix} \frac{-4\tilde{S}+6\pi\tilde{T}}{8-6\pi\tilde{T}\tilde{S}-8\tilde{C}} & 0 & \frac{4\tilde{S}-6\pi\tilde{T}\tilde{C}}{8-6\pi\tilde{T}\tilde{S}-8\tilde{C}} & 0 & \frac{2-2\tilde{C}}{8-6\pi\tilde{T}\tilde{S}-8\tilde{C}} \\ \frac{2-2\tilde{C}}{8-6\pi\tilde{T}\tilde{S}-8\tilde{C}} & 0 & \frac{-14+12\pi\tilde{T}\tilde{S}+14\tilde{C}}{8-6\pi\tilde{T}\tilde{S}-8\tilde{C}} & 0 & \frac{\tilde{S}}{8-6\pi\tilde{T}\tilde{S}-8\tilde{C}} \\ 0 & -\frac{1}{\tilde{S}} & 0 & \frac{\tilde{C}}{\tilde{S}} & 0 \end{bmatrix} \begin{bmatrix} x_o \\ z_o \\ x_f \\ z_f \\ \Delta y \end{bmatrix} \quad (116)$$

where $\Delta y = y_f - y_o$

Appendix J. T_{max} of the \hat{Z} Motion for a Circular Chief

The \hat{Z} motion is decoupled from the $\hat{X}\hat{Y}$ motion and can thus be treated separately. The linearized equation of motion is

$$\ddot{z} + n^2 z = 0$$

which is a harmonic oscillator. The solution to this differential equation is (Equation (94), Appendix G)

$$z(t) = \sqrt{\left(\frac{\dot{z}_o}{n}\right)^2 + z_o^2} \cos \left[nt - \tan^{-1} \left(\frac{\dot{z}_o}{nz_o} \right) \right]$$

The maximum and minimum z values are defined as follows

z_{\max} = furthestmost allowable z coordinate from the chief

z_{\min} = closest allowable z coordinate to the chief

Pulling the amplitude information from the above equation and setting it equal to

z_{\max}

$$\begin{aligned} z_{\max} &= \sqrt{\left(\frac{\dot{z}_o}{n}\right)^2 + z_o^2} \\ \dot{z}_o &= n\sqrt{z_{\max}^2 - z_o^2} = nz_o\sqrt{\left(\frac{z_{\max}}{z_o}\right)^2 - 1} \end{aligned}$$

or

$$\frac{\dot{z}_o}{nz_o} = \sqrt{\left(\frac{z_{\max}}{z_o}\right)^2 - 1} \tag{117}$$

Assume a cylinder is defined as shown in Figure 89 where h is half the height of the cylinder ($h > 0$) and β is the angle between the \hat{Z} axis and the vector from the chief to the center of the lobe. We wish to find the maximum time-of-flight (T_{\max}) between a starting position z_o and final position z_f . Assume that the deputy starts and stops

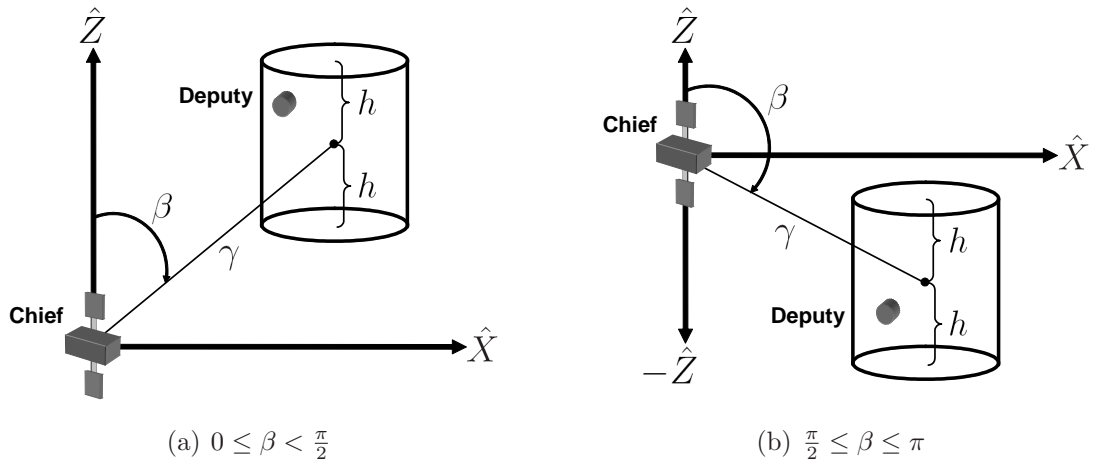


Figure 89: Cylindrical Lobe

at the same position, then

$$z_f = z_o = \sqrt{\left(\frac{\dot{z}_o}{n}\right)^2 + z_o^2} \cos \left[nT_{\max} - \tan^{-1} \left(\frac{\dot{z}_o}{nz_o} \right) \right]$$

Solving for T_{\max}

$$\begin{aligned} \cos^{-1} \left[\frac{z_o}{\sqrt{\left(\frac{\dot{z}_o}{n}\right)^2 + z_o^2}} \right] &= nT_{\max} - \tan^{-1} \left[\frac{\dot{z}_o}{nz_o} \right] \\ \cos^{-1} \left[\frac{1}{\sqrt{\left(\frac{\dot{z}_o}{nz_o}\right)^2 + 1}} \right] + \tan^{-1} \left[\frac{\dot{z}_o}{nz_o} \right] &= nT_{\max} \\ \cos^{-1} \left[\frac{1}{\sqrt{\left(\frac{\dot{z}_o}{nz_o}\right)^2 + 1}} \right] + \cos^{-1} \left[\frac{1}{\sqrt{\left(\frac{\dot{z}_o}{nz_o}\right)^2 + 1}} \right] &= nT_{\max} \end{aligned}$$

Collecting terms and substituting Equation (117)

$$T_{\max} = \frac{2}{n} \cos^{-1} \left[\frac{1}{\sqrt{\left(\frac{z_o}{nz_o}\right)^2 + 1}} \right] = \frac{2}{n} \cos^{-1} \left[\frac{1}{\sqrt{\left(\sqrt{\left(\frac{z_{\max}}{z_o}\right)^2 - 1}\right)^2 + 1}} \right] = \frac{2}{n} \cos^{-1} \left(\frac{z_o}{z_{\max}} \right)$$

Assume that the deputy enters the lobe at $z_o = z_{\min}$ and then, by Figure 89,

$$z_o = z_{\min} = \gamma \cos \beta - \varepsilon h \quad (118)$$

$$z_{\max} = \gamma \cos \beta + \varepsilon h \quad (119)$$

where

$$\varepsilon = \begin{cases} 1 & \text{if } 0 \leq \beta < \frac{\pi}{2} \\ -1 & \text{if } \frac{\pi}{2} \leq \beta \leq \pi \end{cases} \quad (120)$$

Thus

$$T_{\max} = \frac{2}{n} \cos^{-1} \left(\frac{\gamma \cos \beta - \varepsilon h}{\gamma \cos \beta + \varepsilon h} \right) = \frac{2}{n} \cos^{-1} \left(\frac{z_{\min}}{z_{\max}} \right) \quad (121)$$

where

$$0 \leq \left| \frac{\gamma \cos \beta - \varepsilon h}{\gamma \cos \beta + \varepsilon h} \right| \leq 1$$

The lower bound occurs when the cylinder is tangent to the orbital plane while the upper bound occurs when the cylinder has zero height. The range of the inverse cosine on the domain $[0, 1]$ is $\left[0, \frac{\pi}{2}\right]$, which means the domain of time-of-flight is $\left[0, \frac{1}{2}\right]$ (reference Figure 90).

These can also be written as functions of chief period in which the linearized equation of motion is

$$\ddot{\tilde{z}} + 4\pi^2 \tilde{z} = 0$$

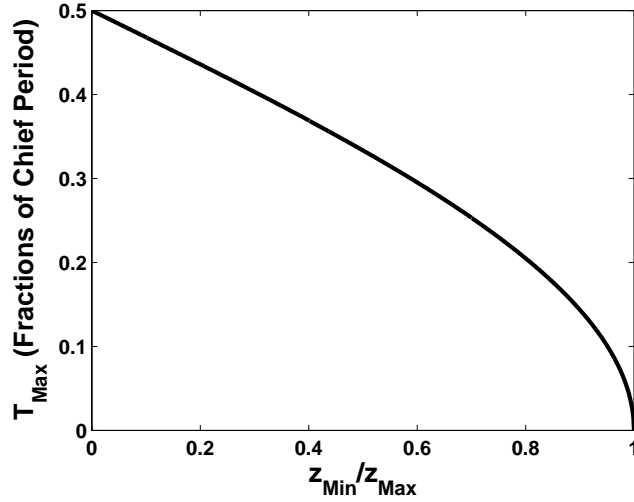


Figure 90: T_{\max} vs z_{\min}/z_{\max}

yielding a closed form solution of

$$\tilde{z}(\tilde{t}) = \frac{\dot{\tilde{z}}_o}{2\pi} \sin(2\pi\tilde{t}) + \tilde{z}_o \cos(2\pi\tilde{t})$$

Applying the harmonic addition theorem (Appendix A.3)

$$\tilde{z}(\tilde{t}) = \sqrt{\left(\frac{\dot{\tilde{z}}_o}{2\pi}\right)^2 + \tilde{z}_o^2} \cos\left[2\pi\tilde{t} - \tan^{-1}\left(\frac{\dot{\tilde{z}}_o}{2\pi\tilde{z}_o}\right)\right] \quad (122)$$

thus

$$\begin{aligned} \tilde{z}_{\max} &= \sqrt{\left(\frac{\dot{\tilde{z}}_o}{2\pi}\right)^2 + \tilde{z}_o^2} \\ \dot{\tilde{z}}_o &= 2\pi\sqrt{\tilde{z}_{\max}^2 - \tilde{z}_o^2} = 2\pi\tilde{z}_o\sqrt{\left(\frac{\tilde{z}_{\max}}{\tilde{z}_o}\right)^2 - 1} \end{aligned}$$

and the maximum time-of-flight is

$$\tilde{T}_{\max} = \frac{T_{\max}}{P} = \frac{1}{\pi} \cos^{-1}\left(\frac{\gamma \cos \beta - \varepsilon h}{\gamma \cos \beta + \varepsilon h}\right) = \frac{1}{\pi} \cos^{-1}\left(\frac{\tilde{z}_{\min}}{\tilde{z}_{\max}}\right) \quad (123)$$

Appendix K. The Derivation of ΔV

This research is founded on the assumption that the deputy satellite can perform impulsive burns to keep itself inside the defined lobe. Calculating the magnitude of those impulsive burns is therefore a key component of the cost function used in the optimization process. The following derivation finds the magnitude of the impulsive burn (ΔV).

K.1 The Derivation of ΔV^2

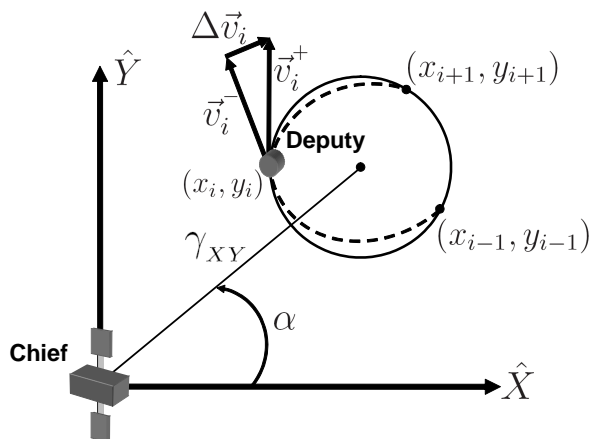


Figure 91: ΔV Derivation Setup

$\Delta \vec{v}_i$ is defined as the difference between the velocity before and after an impulsive thrust, that is, the instantaneous change in velocity required at the burn point [62] and is shown vectorially in Figure 91.

$$\Delta \vec{v}_i = \vec{v}_i^+ - \vec{v}_i^-$$

The \hat{Z} component completely decouples from the $\hat{X}\hat{Y}$ thus each will be addressed separately. In the orbit plane of the chief

$$\begin{aligned} \vec{v}_i^+ &= \dot{x}_i^+ \hat{X} + \dot{y}_i^+ \hat{Y} \\ \vec{v}_i^- &= \dot{x}_i^- \hat{X} + \dot{y}_i^- \hat{Y} \end{aligned}$$

Let the magnitude of the $\Delta\vec{v}$ vector be

$$\Delta V_i = \|\Delta\vec{v}_i\|_2 = \sqrt{(\dot{x}_i^+ - \dot{x}_i^-)^2 + (\dot{y}_i^+ - \dot{y}_i^-)^2}$$

The mathematics of the derivatives simplify somewhat if we remove the square root and deal with ΔV^2 . This will not adversely affect our ability to use ΔV in a cost function. Since ΔV is always a positive value, minimizing the square is equivalent to minimizing the square root.

$$\begin{aligned} \Delta V_i^2 &= (\dot{x}_i^+ - \dot{x}_i^-)^2 + (\dot{y}_i^+ - \dot{y}_i^-)^2 \\ &= \begin{bmatrix} \dot{x}_i^+ - \dot{x}_i^- & \dot{y}_i^+ - \dot{y}_i^- \end{bmatrix} \begin{bmatrix} \dot{x}_i^+ - \dot{x}_i^- \\ \dot{y}_i^+ - \dot{y}_i^- \end{bmatrix} \end{aligned} \quad (124)$$

where the velocity prior to the burn (Equation (113), Appendix I) is

$$\begin{bmatrix} \dot{x}_i^- \\ \dot{y}_i^- \end{bmatrix} = n \begin{bmatrix} \frac{-4S^- + 3nT^-}{8-3nT^-S^- - 8C^-} & \frac{-2+2C^-}{8-3nT^-S^- - 8C^-} & \frac{4S^- - 3nT^-C^-}{8-3nT^-S^- - 8C^-} & \frac{2-2C^-}{8-3nT^-S^- - 8C^-} & 0 & 0 \\ \frac{2-2C^-}{8-3nT^-S^- - 8C^-} & \frac{-S^-}{8-3nT^-S^- - 8C^-} & \frac{-14+6nT^-S^- + 14C^-}{8-3nT^-S^- - 8C^-} & \frac{S^-}{8-3nT^-S^- - 8C^-} & 0 & 0 \end{bmatrix} \begin{bmatrix} x_{i-1} \\ y_{i-1} \\ x_i \\ y_i \\ x_{i+1} \\ y_{i+1} \end{bmatrix}$$

where $T^- = T_{i-1,i}$, $S^- = \sin(nT_{i-1,i})$, $C^- = \cos(nT_{i-1,i})$ and the velocity after the burn (Equation (109), Appendix I)

$$\begin{bmatrix} \dot{x}_i^+ \\ \dot{y}_i^+ \end{bmatrix} = n \begin{bmatrix} 0 & 0 & \frac{-4S^++3nT^+C^+}{8-3nT^+S^+-8C^+} & \frac{2-2C^+}{8-3nT^+S^+-8C^+} & \frac{4S^+-3nT^+}{8-3nT^+S^+-8C^+} & \frac{-2+2C^+}{8-3nT^+S^+-8C^+} \\ 0 & 0 & \frac{-14+6nT^+S^++14C^+}{8-3nT^+S^+-8C^+} & \frac{-S^+}{8-3nT^+S^+-8C^+} & \frac{2-2C^+}{8-3nT^+S^+-8C^+} & \frac{S^+}{8-3nT^+S^+-8C^+} \end{bmatrix} \begin{bmatrix} x_{i-1} \\ y_{i-1} \\ x_i \\ y_i \\ x_{i+1} \\ y_{i+1} \end{bmatrix} \quad (125)$$

where $T^+ = T_{i,i+1}$, $S^+ = \sin(nT_{i,i+1})$, $C^+ = \cos(nT_{i,i+1})$. Let

$$\begin{bmatrix} \dot{x}_i^+ - \dot{x}_i^- & \dot{y}_i^+ - \dot{y}_i^- \end{bmatrix} = n \begin{bmatrix} x_{i-1} & y_{i-1} & x_i & y_i & x_{i+1} & y_{i+1} \end{bmatrix} R$$

Then

$$R = \begin{bmatrix} \frac{4S^- - 3nT^-}{8-3nT^-S^- - 8C^-} & & \frac{-2+2C^-}{8-3nT^-S^- - 8C^-} & & & & \\ & \frac{2-2C^-}{8-3nT^-S^- - 8C^-} & & \frac{S^-}{8-3nT^-S^- - 8C^-} & & & \\ \frac{-4S^++3nT^+C^+}{8-3nT^+S^+-8C^+} & -\frac{4S^- - 3nT^-C^-}{8-3nT^-S^- - 8C^-} & \frac{-14+6nT^+S^++14C^+}{8-3nT^+S^+-8C^+} & -\frac{-14+6nT^-S^-+14C^-}{8-3nT^-S^- - 8C^-} & & & \\ \frac{2-2C^+}{8-3nT^+S^+-8C^+} & -\frac{2-2C^-}{8-3nT^-S^- - 8C^-} & \frac{-S^+}{8-3nT^+S^+-8C^+} & -\frac{S^-}{8-3nT^-S^- - 8C^-} & & & \\ & \frac{4S^+ - 3nT^+}{8-3nT^+S^+-8C^+} & & \frac{2-2C^+}{8-3nT^+S^+-8C^+} & & & \\ & & \frac{-2+2C^+}{8-3nT^+S^+-8C^+} & & \frac{S^+}{8-3nT^+S^+-8C^+} & & \end{bmatrix} \quad (126)$$

We can also express this matrix in terms of fractions of a chief orbit period by substituting $nT = 2\pi\tilde{T}$ (Equation (2) in Section 3.1)

$$\tilde{R} = \begin{bmatrix} \frac{4\tilde{S}^- - 6\pi\tilde{T}^-}{8-6\pi\tilde{T}^- \tilde{S}^- - 8\tilde{C}^-} & \frac{-2+2\tilde{C}^-}{8-6\pi\tilde{T}^- \tilde{S}^- - 8\tilde{C}^-} \\ \frac{2-2\tilde{C}^-}{8-6\pi\tilde{T}^- \tilde{S}^- - 8\tilde{C}^-} & \frac{\tilde{S}^-}{8-6\pi\tilde{T}^- \tilde{S}^- - 8\tilde{C}^-} \\ \frac{-4\tilde{S}^+ + 6\pi\tilde{T}^+ \tilde{C}^+}{8-6\pi\tilde{T}^+ \tilde{S}^+ - 8\tilde{C}^+} - \frac{4\tilde{S}^- - 6\pi\tilde{T}^- \tilde{C}^-}{8-6\pi\tilde{T}^- \tilde{S}^- - 8\tilde{C}^-} & \frac{-14+12\pi\tilde{T}^+ \tilde{S}^+ + 14\tilde{C}^+}{8-6\pi\tilde{T}^+ \tilde{S}^+ - 8\tilde{C}^+} - \frac{-14+12\pi\tilde{T}^- \tilde{S}^- + 14\tilde{C}^-}{8-6\pi\tilde{T}^- \tilde{S}^- - 8\tilde{C}^-} \\ \frac{2-2\tilde{C}^+}{8-6\pi\tilde{T}^+ \tilde{S}^+ - 8\tilde{C}^+} - \frac{2-2\tilde{C}^-}{8-6\pi\tilde{T}^- \tilde{S}^- - 8\tilde{C}^-} & \frac{-\tilde{S}^+}{8-6\pi\tilde{T}^+ \tilde{S}^+ - 8\tilde{C}^+} - \frac{\tilde{S}^-}{8-6\pi\tilde{T}^- \tilde{S}^- - 8\tilde{C}^-} \\ \frac{4\tilde{S}^+ - 6\pi\tilde{T}^+}{8-6\pi\tilde{T}^+ \tilde{S}^+ - 8\tilde{C}^+} & \frac{2-2\tilde{C}^+}{8-6\pi\tilde{T}^+ \tilde{S}^+ - 8\tilde{C}^+} \\ \frac{-2+2\tilde{C}^+}{8-6\pi\tilde{T}^+ \tilde{S}^+ - 8\tilde{C}^+} & \frac{\tilde{S}^+}{8-6\pi\tilde{T}^+ \tilde{S}^+ - 8\tilde{C}^+} \end{bmatrix} \quad (127)$$

where

$$\begin{aligned} \tilde{T}^- &= \tilde{T}_{i-1,i} & \tilde{T}^+ &= \tilde{T}_{i,i+1} \\ \tilde{S}^- &= \sin(2\pi\tilde{T}_{i-1,i}) & \tilde{S}^+ &= \sin(2\pi\tilde{T}_{i,i+1}) \\ \tilde{C}^- &= \cos(2\pi\tilde{T}_{i-1,i}) & \tilde{C}^+ &= \cos(2\pi\tilde{T}_{i,i+1}) \end{aligned}$$

Finally ΔV_i^2 is

$$\Delta V_i^2 = n^2 \begin{bmatrix} x_{i-1} & y_{i-1} & x_i & y_i & x_{i+1} & y_{i+1} \end{bmatrix} R R' \begin{bmatrix} x_{i-1} \\ y_{i-1} \\ x_i \\ y_i \\ x_{i+1} \\ y_{i+1} \end{bmatrix} \quad (128)$$

where we can substitute \tilde{R} for R as desired. ΔV can also be expressed in terms of velocity as a function of fractions of a chief orbit period (see Appendix F). Starting

with Equation (124),

$$\begin{aligned}\Delta V_i^2 &= \begin{bmatrix} \frac{n}{2\pi}\dot{\hat{x}}_i^+ - \frac{n}{2\pi}\dot{\hat{x}}_i^- & \frac{n}{2\pi}\dot{\hat{y}}_i^+ - \frac{n}{2\pi}\dot{\hat{y}}_i^- \\ \frac{n}{2\pi}\dot{\hat{y}}_i^+ - \frac{n}{2\pi}\dot{\hat{y}}_i^- & \frac{n}{2\pi}\dot{\hat{x}}_i^+ - \frac{n}{2\pi}\dot{\hat{x}}_i^- \end{bmatrix} \\ &= \frac{n^2}{4\pi^2} \begin{bmatrix} \dot{\hat{x}}_i^+ - \dot{\hat{x}}_i^- & \dot{\hat{y}}_i^+ - \dot{\hat{y}}_i^- \\ \dot{\hat{y}}_i^+ - \dot{\hat{y}}_i^- & \dot{\hat{x}}_i^+ - \dot{\hat{x}}_i^- \end{bmatrix}\end{aligned}$$

This equation reduces to Equation (128) if we substitute Equations (111) and (115) but is useful if the pre- and post-scaled relative velocities are known.

K.2 Specific ΔV

It is useful to find a form of ΔV that is not dependent upon the chief's semi-major axis (or orbital radius for circular orbits). Therefore, define *specific* delta V ($\Delta\check{V}$) as

$$\begin{aligned}\Delta\check{V}_i^2 &= \frac{\Delta V_i^2}{n^2} = \begin{bmatrix} x_{i-1} & y_{i-1} & x_i & y_i & x_{i+1} & y_{i+1} \end{bmatrix} RR' \begin{bmatrix} x_{i-1} \\ y_{i-1} \\ x_i \\ y_i \\ x_{i+1} \\ y_{i+1} \end{bmatrix} \\ &= \frac{1}{4\pi^2} \begin{bmatrix} \dot{\hat{x}}_i^+ - \dot{\hat{x}}_i^- & \dot{\hat{y}}_i^+ - \dot{\hat{y}}_i^- \\ \dot{\hat{y}}_i^+ - \dot{\hat{y}}_i^- & \dot{\hat{x}}_i^+ - \dot{\hat{x}}_i^- \end{bmatrix}\end{aligned}\quad (129)$$

and the conversions between different types of ΔV are

$$\Delta\check{V}_i = \frac{\Delta V_i}{n} = \frac{\Delta\check{V}_i}{2\pi}\quad (130)$$

K.3 The Derivation of ΔV for \hat{Z} Motion

Since the \hat{Z} component of the deputy's motion decouples from $\hat{X}\hat{Y}$ plane, it can be treated separately. The instantaneous change in velocity at the burn points is [62]

$$\Delta V_i = \dot{z}_i^+ - \dot{z}_i^-$$

The relative velocity prior to the burn (\dot{z}_i^-) is the final relative velocity from the prior leg, and the relative velocity after the burn (\dot{z}_i^+) is the initial relative velocity of the next leg. These are defined by Equations (109) and (113)

$$\begin{aligned}\dot{z}_i^+ &= \dot{z}_o = -nz_o \frac{\cos(nT_i)}{\sin(nT_i)} + nz_f \frac{1}{\sin(nT_i)} \\ \dot{z}_i^- &= \dot{z}_f = -nz_o \frac{1}{\sin(nT_i)} + nz_f \frac{\cos(nT_i)}{\sin(nT_i)}\end{aligned}$$

Thus

$$\begin{aligned}\Delta V_i &= \left[-nz_o \frac{\cos(nT_i)}{\sin(nT_i)} + nz_f \frac{1}{\sin(nT_i)} \right] - \left[-nz_o \frac{1}{\sin(nT_i)} + nz_f \frac{\cos(nT_i)}{\sin(nT_i)} \right] \\ &= nz_o \left[\frac{1 - \cos(nT_i)}{\sin(nT_i)} \right] + nz_f \left[\frac{1 - \cos(nT_i)}{\sin(nT_i)} \right] \\ &= n(z_o + z_f) \tan \left(\frac{1}{2}nT_i \right)\end{aligned}$$

or in terms of chief orbit fractions by substituting Equation (2), Section 3.1

$$\Delta V_i = n(z_o + z_f) \tan \left(\pi \tilde{T}_i \right)$$

Note that ΔV is linear in z_o and z_f ; thus choosing

$$z_o = z_f = z_{\min}$$

will result in the minimum ΔV

$$\Delta V_i = 2nz_{\min} \tan\left(\pi\tilde{T}_i\right) \quad (131)$$

This substitution also allows the following reduction in the relative \hat{Z} direction velocities

$$\begin{aligned} \dot{z}_o &= nz_{\min} \frac{1 - \cos(nT_i)}{\sin(nT_i)} = nz_{\min} \tan\left(\frac{1}{2}nT_i\right) \\ \dot{z}_f &= -nz_{\min} \frac{1 - \cos(nT_i)}{\sin(nT_i)} = -nz_{\min} \tan\left(\frac{1}{2}nT_i\right) \end{aligned}$$

or in terms of chief orbit period

$$\begin{aligned} \dot{\tilde{z}}_o &= 2\pi\tilde{z}_{\min} \tan\left(\pi\tilde{T}_i\right) \\ \dot{\tilde{z}}_f &= -2\pi\tilde{z}_{\min} \tan\left(\pi\tilde{T}_i\right) \end{aligned}$$

Assume the total hover time (\tilde{T}_T) is given, the period of the \hat{Z} motion is constant (\tilde{P}_z), and that the entry conditions for the \hat{Z} motion is open, then the total number of burns required to keep the the deputy inside the lobe is

$$\# \text{ Burns} = \left\lfloor \frac{\tilde{T}_T}{\tilde{P}_z} \right\rfloor$$

and the ΔV required

$$\Delta V_Z = 2n \left\lfloor \frac{\tilde{T}_T}{\tilde{P}_z} \right\rfloor z_{\min} \tan\left(\pi\tilde{P}_z\right) \quad (132)$$

or, in terms of specific ΔV , (see Appendix K.2)

$$\Delta \check{V}_Z = \frac{\Delta V_Z}{n} = 2 \left\lfloor \frac{\tilde{T}_T}{\tilde{P}_z} \right\rfloor \tilde{z}_{\min} \tan\left(\pi\tilde{P}_z\right) \quad (133)$$

where $\lfloor \cdot \rfloor$ represents the floor function. Equation (132) converges to the continuous ΔV solution (Equation (137) in Appendix L) as \tilde{P}_z goes to zero and is proven below.

Let $\tilde{P}_z \rightarrow 0$. Using the small angle approximation,

$$\tan\left(\pi\tilde{P}_z\right) = \frac{\sin\left(\pi\tilde{P}_z\right)}{\cos\left(\pi\tilde{P}_z\right)} \approx \frac{\pi\tilde{P}_z}{1} = \pi\tilde{P}_z$$

Further, let \tilde{P}_z be an whole fraction of \tilde{T}_T where k_z is the number of \hat{Z} legs

$$\frac{1}{k_z}\tilde{T}_T = \tilde{P}_z$$

Then

$$\Delta V_Z = \left[\frac{\tilde{T}_T}{\frac{1}{k_z}\tilde{T}_T} \right] * 2nz_{\min} \left(\pi \frac{1}{k_z}\tilde{T}_T \right) = 2nz_{\min}\pi [k_z] \frac{1}{k_z}\tilde{T}_T$$

Since k_z is an integer

$$[k_z] = k_z$$

thus

$$\Delta V_Z = 2nz_{\min}\pi\tilde{T}_T$$

or in terms of specific ΔV

$$\Delta\check{V}_Z = \frac{\Delta V_Z}{n} = 2\check{z}_{\min}\pi\tilde{T}_T$$

which is the same as the continuous burn solution (Equation (137) in Appendix L).

The constraint on choosing k_z is

$$\frac{1}{k_z}\tilde{T}_T = \tilde{P}_z \leq \tilde{T}_{\max}$$

Solving for k_z

$$k_z \geq \frac{\tilde{T}_T}{\tilde{T}_{\max}}$$

since k_z is an integer

$$k_z = \left\lceil \frac{\tilde{T}_T}{\tilde{T}_{\max}} \right\rceil \quad (134)$$

where $\lceil \cdot \rceil$ represents the ceiling function. The total ΔV expended performing these optimal burns is therefore

$$\Delta V_Z = (k_z - 1) * 2nz_{\min} \tan \left(\pi \frac{1}{k_z} \tilde{T}_T \right) = 2nz_{\min} (k_z - 1) \tan \left(\frac{\pi \tilde{T}_T}{k_z} \right)$$

in specific ΔV

$$\Delta \check{V}_Z = 2\check{z}_{\min} (k_z - 1) \tan \left(\frac{\pi \tilde{T}_T}{k_z} \right)$$

or expressed in terms of the initial or final velocities in the \hat{Z} direction

$$\Delta V_Z = 2(k_z - 1)\dot{z}_o = -2(k_z - 1)\dot{z}_f$$

and in terms of velocities that are functions of the chief's period and specific ΔV

$$\Delta V_Z = 2(k_z - 1)\dot{\check{z}}_o \frac{n}{2\pi} = -2(k_z - 1)\dot{\check{z}}_f \frac{n}{2\pi}$$

Thus

$$\Delta \check{V}_Z = \frac{1}{\pi} (k_z - 1) \dot{\check{z}}_o = -\frac{1}{\pi} (k_z - 1) \dot{\check{z}}_f \quad (135)$$

Figure 92 represents an example plot of Equation (133). Note the sawtooth feature that is an artifact of the floor function and that the discrete solution converges to the continuous solution as $\tilde{P}_z \rightarrow 0$.

K.4 ΔV Expressed in the Inertial Frame

ΔV can also be expressed in inertial frame via

$$\Delta V = \hat{i}\hat{j}\hat{k}\dot{\vec{M}}^+ - \hat{i}\hat{j}\hat{k}\dot{\vec{M}}^-$$

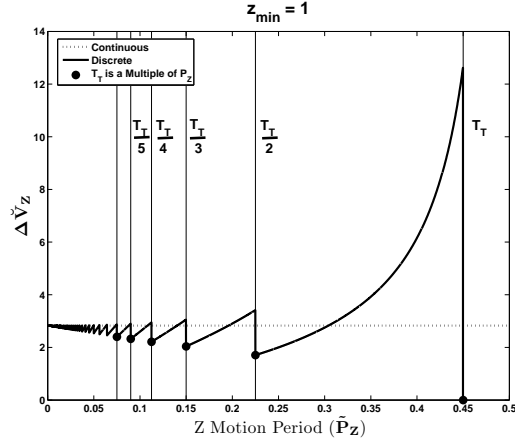


Figure 92: Notional $\Delta\check{V}$ vs Z Period

Substituting Equation (101)

$$\begin{aligned}
 \Delta V &= \left(C^{\text{R2I}} \begin{bmatrix} \dot{x}^+ - ny \\ \dot{y}^+ + nx \\ \dot{z}^+ \end{bmatrix} + \hat{i}\hat{j}\hat{k}\dot{\hat{L}} \right) - \left(C^{\text{R2I}} \begin{bmatrix} \dot{x}^- - ny \\ \dot{y}^- + nx \\ \dot{z}^- \end{bmatrix} + \hat{i}\hat{j}\hat{k}\dot{\hat{L}} \right) \\
 &= C^{\text{R2I}} \left(\begin{bmatrix} \dot{x}^+ - ny \\ \dot{y}^+ + nx \\ \dot{z}^+ \end{bmatrix} - \begin{bmatrix} \dot{x}^- - ny \\ \dot{y}^- + nx \\ \dot{z}^- \end{bmatrix} \right) \\
 &= C^{\text{R2I}} \begin{bmatrix} \dot{x}^+ - ny - \dot{x}^- + ny \\ \dot{y}^+ + nx - \dot{y}^- - nx \\ \dot{z}^+ - \dot{z}^- \end{bmatrix} \\
 &= C^{\text{R2I}} \begin{bmatrix} \dot{x}^+ - \dot{x}^- \\ \dot{y}^+ - \dot{y}^- \\ \dot{z}^+ - \dot{z}^- \end{bmatrix}
 \end{aligned}$$

Appendix L. The Continuous-Thrust Solution

As a benchmark with which to compare our optimal trajectories, the continuous-thrust solution is derived. We can quickly find the closed-form solution for a continuous-thrust controller attempting to keep the deputy at a specified point in the relative frame. Again, we expect the impulsive burn to be fuel-optimal compared to the continuous-thrust solution derived below. We want the velocities at this hover point to be zero

$$\dot{\tilde{x}} = 0 \quad \dot{\tilde{y}} = 0 \quad \dot{\tilde{z}} = 0$$

which reduces Equation (81), Appendix F to

$$\begin{aligned} \ddot{\tilde{x}} &= 4\pi(0) + 12\pi^2\tilde{x} = 12\pi^2\tilde{x} \\ \ddot{\tilde{y}} &= -4\pi(0) = 0 \\ \ddot{\tilde{z}} &= -4\pi^2\tilde{z} \end{aligned}$$

Since the $\ddot{\tilde{y}}$ equation is now zero, we need only worry about the accelerations in the \hat{X} and \hat{Z} directions. Integrating from zero to the total time-of-flight (\tilde{T}_T) yields the ΔV as a function of chief orbit period ($\Delta\tilde{V}_C$) required to keep the deputy hovering at a given $\tilde{x}_o, \tilde{y}_o, \tilde{z}_o$:

$$\begin{aligned} \Delta\tilde{V}_C &= \int_0^{\tilde{T}_T} |\ddot{\tilde{x}}|d\tilde{t} + \int_0^{\tilde{T}_T} |\ddot{\tilde{z}}|d\tilde{t} = \int_0^{\tilde{T}_T} 12\pi^2|\tilde{x}_o|d\tilde{t} + \int_0^{\tilde{T}_T} 4\pi^2|\tilde{z}_o|d\tilde{t} \\ &= \pi^2 (12|\tilde{x}_o| + 4|\tilde{z}_o|) \int_0^{\tilde{T}_T} d\tilde{t} = \pi^2 (12|\tilde{x}_o| + 4|\tilde{z}_o|) \tilde{T}_T \end{aligned}$$

where the subscript C represents “continuous”. To use this formulation, we must be careful not to pick lobe shapes that recouple the in-plane and out-of-plane components. Note that no claim is made that this is the optimal continuous-thrust solution; it will merely serve as a benchmark controller that is easily synthesized. The location of \tilde{x}_o and \tilde{z}_o is arbitrary but the smallest continuous $\Delta\tilde{V}$ is attained when \tilde{x}_o and \tilde{z}_o are at their minimum, thus \tilde{x}_{\min} and \tilde{z}_{\min} represent the point on the lobe that is

closest to the \hat{Y} axis and $\hat{X}\hat{Y}$ plane respectively:

$$\Delta\check{V}_C = (12\tilde{x}_{\min} + 4\tilde{z}_{\min}) \pi^2 \tilde{T}_T \quad (136)$$

If the lobe happens to intersect the \hat{Y} axis, then the optimal solution (for the linear CW case) is to stay on that \hat{Y} axis which is in fact the loci of equilibrium points and requires no expenditure of fuel. We can also express the continuous ΔV in terms of specific ΔV by applying the conversions in Equation (130), Appendix K

$$\Delta\check{V}_C = \left[\frac{1}{2\pi} \right] (12\tilde{x}_{\min} + 4\tilde{z}_{\min}) \pi^2 \tilde{T}_T = (6\tilde{x}_{\min} + 2\tilde{z}_{\min}) \pi \tilde{T}_T \quad (137)$$

The above equation works well if we assume the deputy starts at the minimum x and z values; however, in order to use this as a fair comparison, the ΔV needed to get into that position should also be included. Assume that the continuous-thrust solution starts at the same entry position and velocity as the discrete-thrust solution. The ΔV required to get to the \tilde{x}_{\min} position is $\Delta\check{V}_1^2$ is (from Equation (124) in Appendix K)

$$\Delta\check{V}_1^2 = \frac{1}{4\pi^2} [(\dot{\tilde{x}}_1^+ - \dot{\tilde{x}}_1^-)^2 + (\dot{\tilde{y}}_1^+ - \dot{\tilde{y}}_1^-)^2] = \frac{1}{4\pi^2} \begin{bmatrix} \dot{\tilde{x}}_1^+ - \dot{\tilde{x}}_1^- & \dot{\tilde{y}}_1^+ - \dot{\tilde{y}}_1^- \end{bmatrix} \begin{bmatrix} \dot{\tilde{x}}_1^+ - \dot{\tilde{x}}_1^- \\ \dot{\tilde{y}}_1^+ - \dot{\tilde{y}}_1^- \end{bmatrix}$$

Substituting Equation (110) in Appendix I

$$\begin{bmatrix} \dot{\tilde{x}}_1^+ - \dot{\tilde{x}}_1^- \\ \dot{\tilde{y}}_1^+ - \dot{\tilde{y}}_1^- \end{bmatrix} = \begin{bmatrix} \frac{-4\tilde{S}+6\pi\tilde{T}\tilde{C}}{8-6\pi\tilde{T}\tilde{S}-8\tilde{C}} & \frac{4\tilde{S}-6\pi\tilde{T}}{8-6\pi\tilde{T}\tilde{S}-8\tilde{C}} & \frac{-2+2\tilde{C}}{8-6\pi\tilde{T}\tilde{S}-8\tilde{C}} \\ \frac{-14+12\pi\tilde{T}\tilde{S}+14\tilde{C}}{8-6\pi\tilde{T}\tilde{S}-8\tilde{C}} & \frac{2-2\tilde{C}}{8-6\pi\tilde{T}\tilde{S}-8\tilde{C}} & \frac{\tilde{S}}{8-6\pi\tilde{T}\tilde{S}-8\tilde{C}} \end{bmatrix} \begin{bmatrix} \tilde{x}_1 \\ \tilde{x}_2 \\ \Delta\tilde{y} \end{bmatrix} - \begin{bmatrix} \dot{\tilde{x}}_1^- \\ \dot{\tilde{y}}_1^- \end{bmatrix}$$

where

$$\begin{aligned} \Delta\tilde{y} &= \tilde{y}_2 - \tilde{y}_1 \\ \tilde{S} &= \sin(2\pi\tilde{T}_{1,2}) \\ \tilde{C} &= \cos(2\pi\tilde{T}_{1,2}) \end{aligned}$$

Once at the \tilde{x}_{\min} position, the deputy must make a burn to cancel its relative velocity that is equal in magnitude but opposite in direction to the final velocity of the previous leg

$$\Delta\check{V}_2^2 = \frac{1}{4\pi^2} \|\dot{\tilde{x}}_2^- \hat{X} + \dot{\tilde{y}}_2^- \hat{Y}\|_2^2$$

where

$$\begin{bmatrix} \dot{\tilde{x}}_2^- \\ \dot{\tilde{y}}_2^- \end{bmatrix} = \begin{bmatrix} \frac{-4\tilde{S}+6\pi\tilde{T}}{8-6\pi\tilde{T}\tilde{S}-8\tilde{C}} & \frac{4\tilde{S}-6\pi\tilde{T}\tilde{C}}{8-6\pi\tilde{T}\tilde{S}-8\tilde{C}} & \frac{2-2\tilde{C}}{8-6\pi\tilde{T}\tilde{S}-8\tilde{C}} \\ \frac{2-2\tilde{C}}{8-6\pi\tilde{T}\tilde{S}-8\tilde{C}} & \frac{-14+12\pi\tilde{T}\tilde{S}+14\tilde{C}}{8-6\pi\tilde{T}\tilde{S}-8\tilde{C}} & \frac{\tilde{S}}{8-6\pi\tilde{T}\tilde{S}-8\tilde{C}} \end{bmatrix} \begin{bmatrix} \tilde{x}_1 \\ \tilde{x}_2 \\ \Delta\tilde{y} \end{bmatrix}$$

Appendix M. The Persistent Hover Orbit

The persistent hover orbit is a special type of repeating hover orbit that takes advantage of the equilibrium condition of the linear Clohessy-Wiltshire equations of motion. As presented in Section 3.2.2, let $\ddot{\tilde{x}} = \ddot{\tilde{y}} = \ddot{\tilde{z}} = \dot{\tilde{x}} = \dot{\tilde{y}} = \dot{\tilde{z}} = 0$. Then the Clohessy-Wiltshire equations reduce to

$$\begin{aligned} -12\pi^2\tilde{x} &= 0 \\ 4\pi^2\tilde{z} &= 0 \end{aligned}$$

Thus $\tilde{x} = 0$ and $\tilde{z} = 0$ without any restriction on \tilde{y} , meaning the entire \hat{Y} axis is an equilibrium solution. If the user-defined lobe is tangent to or contains within it any part of the \hat{Y} axis, then this becomes an ideal place for the deputy satellite to hover. In fact, finding a minimum-fuel solution to arrive and then remain on either the \hat{Y} axis itself (single point hovering orbit) or any 2x1 ellipse dictated by Equation (87), Appendix G, that is contained within the lobe. In the absence of linearization error and perturbations, the deputy could stay in this relative orbit indefinitely. Even with such nonlinearities present, it would take relatively little fuel to keep the deputy in this persistent orbit. Calculating those correction burns is not addressed in this research.

When investigating these unique persistently hovering orbits, two questions must be answered: 1) How do we define such a persistent orbit, and 2) How do we know a candidate persistent orbit fits within the lobe? The first question is relatively easy. Since the eccentricity of the hover orbit is required to be $\frac{\sqrt{3}}{2}$ and it must be centered along the \hat{Y} axis, only the center's y coordinate (b) and relative orbit size (ρ) are needed (reference Figure 93). The second question is answered via a numerical solution. For a given persistent hover orbit, each point is checked (to whatever resolution the user specifies) for breaches of the lobe boundary. This is accomplished by comparing the hover orbit radius (r_P) to the lobe's radius measured from the hover orbit center (r_L). If at any point, $r_P > r_L$, then the hover orbit is not acceptable.

Thus a numerical check can be done by sweeping ψ between 0 and 2π to the desired resolution and checking for $r_P > r_L$. Note that there is a singularity when ψ' passes through $\frac{\pi}{2}$ and $\frac{3\pi}{2}$, at which points

$$x_L = -r \cos \psi$$

The lobe radius can be calculated

$$r_L = y_L - b + r \sin \psi$$

but the persistent orbit radius is dependent on ψ' which is ill defined. Fortunately, these two points are co-linear with the semi-major axis

$$r_P = 2\rho$$

M.1 Maximum ρ and b

In order to search numerically for candidate persistent hover orbits, we need to bound both ρ and b . Referencing Figure 93, lobes potentially intersect the \hat{Y} axis at two points

$$\begin{aligned} y_{\text{Upper}} &= \gamma_{XY} \sin \alpha + r(\psi_U) \sin \psi_U \\ y_{\text{Lower}} &= \gamma_{XY} \sin \alpha + r(\psi_L) \sin \psi_L \end{aligned}$$

The largest possible ρ value is

$$\begin{aligned} 4\rho &< y_{\text{Upper}} - y_{\text{Lower}} \\ \rho &< \frac{r(\psi_U) \sin \psi_U - r(\psi_L) \sin \psi_L}{4} \end{aligned} \tag{138}$$

and the range of b by inspection is

$$b_{\max} = y_{\text{Upper}} = \gamma_{XY} \sin \alpha + r(\psi_U) \sin \psi_U$$

$$b_{\min} = y_{\text{Lower}} = \gamma_{XY} \sin \alpha + r(\psi_L) \sin \psi_L$$

Appendix N. The Teardrop Hover Orbit

This appendix develops a proof that the ΔV required to stay on a teardrop orbit is equivalent to hovering continuously at the time-averaged x coordinate of the teardrop. The results are equivalent to a similar derivation in [28]. A notional teardrop orbit and centroid location is shown in Figure 94.

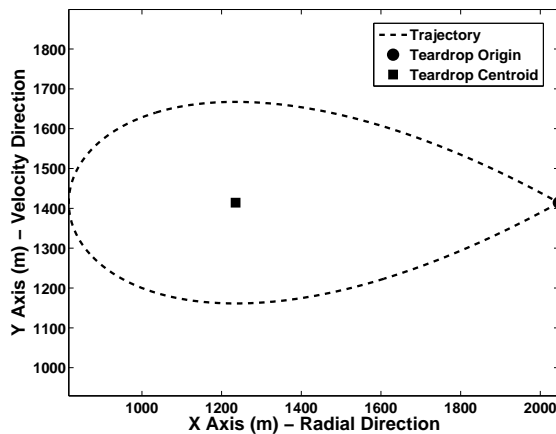


Figure 94: Notional Teardrop Orbit

Let the subscripts o and f represent initial and final conditions respectively. Noting the $\frac{1}{2\pi}$ scaling to convert to specific ΔV (Appendix K), the $\Delta\check{V}$ required for each cycle of a teardrop orbit is

$$\Delta\check{V} = \frac{1}{2\pi} \sqrt{(\dot{x}_o - \dot{x}_f)^2 + (\dot{y}_o - \dot{y}_f)^2} \quad (139)$$

Neglecting motion in the \hat{Z} direction, the relative velocities are calculated via Equations (112) and (116) from Appendix I.

$$\begin{bmatrix} \dot{\tilde{x}}_o \\ \dot{\tilde{y}}_o \end{bmatrix} = 2\pi \begin{bmatrix} \frac{-4\tilde{S}+6\pi\tilde{T}_{TD}\tilde{C}}{8-6\pi\tilde{T}_{TD}\tilde{S}-8\tilde{C}} & \frac{4\tilde{S}-6\pi\tilde{T}_{TD}}{8-6\pi\tilde{T}_{TD}\tilde{S}-8\tilde{C}} & \frac{-2+2\tilde{C}}{8-6\pi\tilde{T}_{TD}\tilde{S}-8\tilde{C}} \\ \frac{-14+12\pi\tilde{T}_{TD}\tilde{S}+14\tilde{C}}{8-6\pi\tilde{T}_{TD}\tilde{S}-8\tilde{C}} & \frac{2-2\tilde{C}}{8-6\pi\tilde{T}_{TD}\tilde{S}-8\tilde{C}} & \frac{\tilde{S}}{8-6\pi\tilde{T}_{TD}\tilde{S}-8\tilde{C}} \end{bmatrix} \begin{bmatrix} \tilde{x}_o \\ \tilde{x}_f \\ \Delta\tilde{y} \end{bmatrix}$$

$$\begin{bmatrix} \dot{\tilde{x}}_f \\ \dot{\tilde{y}}_f \end{bmatrix} = 2\pi \begin{bmatrix} \frac{-4\tilde{S}+6\pi\tilde{T}_{TD}}{8-6\pi\tilde{T}_{TD}\tilde{S}-8\tilde{C}} & \frac{4\tilde{S}-6\pi\tilde{T}_{TD}\tilde{C}}{8-6\pi\tilde{T}_{TD}\tilde{S}-8\tilde{C}} & \frac{2-2\tilde{C}}{8-6\pi\tilde{T}_{TD}\tilde{S}-8\tilde{C}} \\ \frac{2-2\tilde{C}}{8-6\pi\tilde{T}_{TD}\tilde{S}-8\tilde{C}} & \frac{-14+12\pi\tilde{T}_{TD}\tilde{S}+14\tilde{C}}{8-6\pi\tilde{T}_{TD}\tilde{S}-8\tilde{C}} & \frac{\tilde{S}}{8-6\pi\tilde{T}_{TD}\tilde{S}-8\tilde{C}} \end{bmatrix} \begin{bmatrix} \tilde{x}_o \\ \tilde{x}_f \\ \Delta\tilde{y} \end{bmatrix}$$

where \tilde{T}_{TD} is the time-of-flight of a cycle (i.e. period of the teardrop), $\tilde{S} = \sin(2\pi\tilde{T}_{TD})$, and $\tilde{C} = \cos(2\pi\tilde{T}_{TD})$. Since the initial and final coordinates occur at the apex of the teardrop,

$$\begin{aligned} \tilde{x}_o &= \tilde{x}_f \\ \Delta\tilde{y} &= \tilde{y}_o - \tilde{y}_f = 0 \end{aligned}$$

Letting $D = 8 - 6\pi\tilde{T}_{TD}\tilde{S} - 8\tilde{C}$,

$$\begin{bmatrix} \dot{\tilde{x}}_o \\ \dot{\tilde{y}}_o \end{bmatrix} = 2\pi \begin{bmatrix} \frac{-4\tilde{S}+6\pi\tilde{T}_{TD}\tilde{C}}{8-6\pi\tilde{T}_{TD}\tilde{S}-8\tilde{C}} & \frac{4\tilde{S}-6\pi\tilde{T}_{TD}\tilde{C}}{8-6\pi\tilde{T}_{TD}\tilde{S}-8\tilde{C}} \\ \frac{-14+12\pi\tilde{T}_{TD}\tilde{S}+14\tilde{C}}{8-6\pi\tilde{T}_{TD}\tilde{S}-8\tilde{C}} & \frac{2-2\tilde{C}}{8-6\pi\tilde{T}_{TD}\tilde{S}-8\tilde{C}} \end{bmatrix} \begin{bmatrix} \tilde{x}_o \\ \tilde{x}_o \end{bmatrix} = \frac{2\pi\tilde{x}_o}{D} \begin{bmatrix} -6\pi\tilde{T}_{TD}(1-\tilde{C}) \\ -12 + 12\pi\tilde{T}_{TD}\tilde{S} + 12\tilde{C} \end{bmatrix} \quad (140)$$

$$\begin{bmatrix} \dot{\tilde{x}}_f \\ \dot{\tilde{y}}_f \end{bmatrix} = 2\pi \begin{bmatrix} \frac{-4\tilde{S}+6\pi\tilde{T}_{TD}}{8-6\pi\tilde{T}_{TD}\tilde{S}-8\tilde{C}} & \frac{4\tilde{S}-6\pi\tilde{T}_{TD}\tilde{C}}{8-6\pi\tilde{T}_{TD}\tilde{S}-8\tilde{C}} \\ \frac{2-2\tilde{C}}{8-6\pi\tilde{T}_{TD}\tilde{S}-8\tilde{C}} & \frac{-14+12\pi\tilde{T}_{TD}\tilde{S}+14\tilde{C}}{8-6\pi\tilde{T}_{TD}\tilde{S}-8\tilde{C}} \end{bmatrix} \begin{bmatrix} \tilde{x}_o \\ \tilde{x}_o \end{bmatrix} = \frac{2\pi\tilde{x}_o}{D} \begin{bmatrix} 6\pi\tilde{T}_{TD}(1-\tilde{C}) \\ -12 + 12\pi\tilde{T}_{TD}\tilde{S} + 12\tilde{C} \end{bmatrix} \quad (141)$$

therefore

$$\begin{aligned} \dot{\tilde{x}}_o - \dot{\tilde{x}}_f &= \frac{2\pi\tilde{x}_o}{D} \left[-6\pi\tilde{T}_{TD}(1-\tilde{C}) - 6\pi\tilde{T}_{TD}(1-\tilde{C}) \right] = \frac{-24\pi^2\tilde{T}_{TD}\tilde{x}_o(1-\tilde{C})}{D} \\ \dot{\tilde{y}}_o - \dot{\tilde{y}}_f &= \frac{2\pi\tilde{x}_o}{D} \left[\left(-12 + 12\pi\tilde{T}_{TD}\tilde{S} + 12\tilde{C} \right) - \left(-12 + 12\pi\tilde{T}_{TD}\tilde{S} + 12\tilde{C} \right) \right] = 0 \end{aligned}$$

Substituting these into Equation (139) yields

$$\Delta\check{V} = \frac{1}{2\pi} \sqrt{\left(\frac{-24\pi^2\tilde{T}_{TD}\tilde{x}_o(1-\tilde{C})}{D}\right)^2 + (0)^2} = \frac{12\pi\tilde{T}_{TD}\tilde{x}_o(1-\tilde{C})}{8-6\pi\tilde{T}_{TD}\tilde{S}-8\tilde{C}}$$

We can set this equal to the continuous hover solution (Equation (137), Appendix L) and solve for the equivalent x coordinate (\tilde{x}_{eq}). This is the x position at which thrusting continuously would yield the same $\Delta\check{V}$ as thrusting at the apex of the teardrop.

$$\frac{12\pi\tilde{T}_{TD}\tilde{x}_o(1-\tilde{C})}{8-6\pi\tilde{T}_{TD}\tilde{S}-8\tilde{C}} = 6\tilde{x}_{\text{eq}}\pi\tilde{T}_{TD}$$

Solving for \tilde{x}_{eq} ,

$$\tilde{x}_{\text{eq}} = \frac{2(1-\tilde{C})\tilde{x}_o}{8-6\pi\tilde{T}_{TD}\tilde{S}-8\tilde{C}} \quad (142)$$

This equivalent x coordinate has a physical meaning. It is the time-averaged \hat{X} position of the deputy; a proof is presented below. The time-averaged \hat{X} position can be calculated via

$$\bar{x}_{TD} = \frac{1}{\tilde{T}_{TD}} \int_0^{\tilde{T}_{TD}} \tilde{x}(\tilde{t}) d\tilde{t} \quad (143)$$

where the x position is given by Equation (85a) in Appendix G:

$$\begin{aligned} x(t) &= (x_o - a) \cos(nt) + \frac{\dot{x}_o}{n} \sin(nt) + a \\ \tilde{x}(\tilde{t}) &= (\tilde{x}_o - a) \cos(2\pi\tilde{t}) + \frac{\dot{\tilde{x}}_o}{2\pi} \sin(2\pi\tilde{t}) + a \end{aligned}$$

and a is Equation (98a),

$$a = \frac{1}{\pi} \dot{y}_o + 4\tilde{x}_o$$

therefore the integral is,

$$\int_0^{\tilde{T}_{TD}} \tilde{x}(\tilde{t}) d\tilde{t} = \int_0^{\tilde{T}_{TD}} (\tilde{x}_o - a) \cos(2\pi\tilde{t}) d\tilde{t} + \int_0^{\tilde{T}_{TD}} \frac{\dot{\tilde{x}}_o}{2\pi} \sin(2\pi\tilde{t}) d\tilde{t} + \int_0^{\tilde{T}_{TD}} a d\tilde{t}$$

The first term reduces to:

$$\int_0^{\tilde{T}_{TD}} (\tilde{x}_o - a) \cos(2\pi\tilde{t}) d\tilde{t} = \frac{\tilde{x}_o - a}{2\pi} \left[\sin(2\pi\tilde{t}) \right]_0^{\tilde{T}_{TD}} = \frac{\tilde{x}_o - a}{2\pi} \sin(2\pi\tilde{T}_{TD})$$

The second term reduces to:

$$\int_0^{\tilde{T}_{TD}} \frac{\dot{\tilde{x}}_o}{2\pi} \sin(2\pi\tilde{t}) d\tilde{t} = -\frac{\dot{\tilde{x}}_o}{4\pi^2} \left[\cos(2\pi\tilde{t}) \right]_0^{\tilde{T}_{TD}} = -\frac{\dot{\tilde{x}}_o}{4\pi^2} (\cos(2\pi\tilde{T}_{TD}) - 1)$$

and the third term reduces to:

$$\int_0^{\tilde{T}_{TD}} a d\tilde{t} = a \left[\tilde{t} \right]_0^{\tilde{T}_{TD}} = a\tilde{T}_{TD}$$

Putting it all together and substituting for a ,

$$\begin{aligned} \int_0^{\tilde{T}_{TD}} \tilde{x}(\tilde{t}) d\tilde{t} &= \frac{\tilde{x}_o - a}{2\pi} \tilde{S} + \frac{\dot{\tilde{x}}_o}{4\pi^2} (1 - \tilde{C}) + a\tilde{T}_{TD} \\ &= \left(-\frac{1}{2\pi^2} \dot{y}_o - \frac{3}{2\pi} \tilde{x}_o \right) \tilde{S} + \frac{\dot{\tilde{x}}_o}{4\pi^2} (1 - \tilde{C}) + \left(\frac{1}{\pi} \dot{y}_o + 4\tilde{x}_o \right) \tilde{T}_{TD} \\ &= \left(4\tilde{T}_{TD} - \frac{3}{2\pi} \tilde{S} \right) \tilde{x}_o + \frac{1 - \tilde{C}}{4\pi^2} \dot{\tilde{x}}_o + \left(\frac{1}{\pi} \tilde{T}_{TD} - \frac{1}{2\pi^2} \tilde{S} \right) \dot{y}_o \\ &= \frac{8\pi\tilde{T}_{TD} - 3\tilde{S}}{2\pi} \tilde{x}_o + \frac{1 - \tilde{C}}{4\pi^2} \dot{\tilde{x}}_o + \frac{2\pi\tilde{T}_{TD} - \tilde{S}}{2\pi^2} \dot{y}_o \end{aligned}$$

Substituting Equation (140) for the initial relative velocities,

$$\begin{aligned} &\frac{8\pi\tilde{T}_{TD} - 3\tilde{S}}{2\pi} \tilde{x}_o + \frac{1 - \tilde{C}}{4\pi^2} \left(\frac{-2\pi\tilde{x}_o}{D} \right) 6\pi\tilde{T}_{TD}(1 - \tilde{C}) + \frac{2\pi\tilde{T}_{TD} - \tilde{S}}{2\pi^2} \left(\frac{2\pi\tilde{x}_o}{D} \right) (-12 + 12\pi\tilde{T}_{TD}\tilde{S} + 12\tilde{C}) \\ &\frac{1}{2\pi D} \left[(8\pi\tilde{T}_{TD} - 3\tilde{S}) D - 6\pi\tilde{T}_{TD}(1 - \tilde{C})^2 + (2\pi\tilde{T}_{TD} - \tilde{S}) (-24 + 24\pi\tilde{T}_{TD}\tilde{S} + 24\tilde{C}) \right] \tilde{x}_o \\ &\frac{1}{2\pi D} \left[16\pi\tilde{T}_{TD} - 16\pi\tilde{T}_{TD}\tilde{C} - 6\pi\tilde{T}_{TD}\tilde{S}^2 - 6\pi\tilde{T}_{TD}(1 - \tilde{C})^2 \right] \tilde{x}_o \\ &\frac{1}{2\pi D} \left[16\pi\tilde{T}_{TD}(1 - \tilde{C}) - 6\pi\tilde{T}_{TD}(\tilde{S}^2 + (1 - \tilde{C})^2) \right] \tilde{x}_o \\ &\frac{1}{2\pi D} \left[16\pi\tilde{T}_{TD}(1 - \tilde{C}) - 12\pi\tilde{T}_{TD}(1 - \tilde{C}) \right] \tilde{x}_o \\ &\frac{1}{2\pi D} \left[4\pi\tilde{T}_{TD}(1 - \tilde{C}) \right] \tilde{x}_o \end{aligned}$$

thus

$$\int_0^{\tilde{T}_{TD}} \tilde{x}(\tilde{t}) d\tilde{t} = \frac{2\tilde{T}_{TD}(1 - \tilde{C})\tilde{x}_o}{8 - 6\pi\tilde{T}_{TD}\tilde{S} - 8\tilde{C}}$$

The time-averaged x coordinate is therefore,

$$\bar{x}_{TD} = \frac{1}{\tilde{T}_{TD}} \int_0^{\tilde{T}_{TD}} \tilde{x}(\tilde{t}) d\tilde{t} = \frac{2(1 - \tilde{C})\tilde{x}_o}{8 - 6\pi\tilde{T}_{TD}\tilde{S} - 8\tilde{C}} \quad (144)$$

Comparing this result to Equation (142), we find that \tilde{x}_{eq} is in fact the time-averaged x coordinate and confirming that thrusting continuously at \bar{x}_{TD} requires the same amount of fuel as discretely thrusting at the teardrop apex to remain on the teardrop orbit. The specific ΔV per cycle is

$$\Delta\check{V}_{TD} = \frac{12\pi\tilde{T}_{TD}(1 - \tilde{C})\tilde{x}_o}{8 - 6\pi\tilde{T}_{TD}\tilde{S} - 8\tilde{C}} \quad (145)$$

Appendix O. The Truth Model

O.1 Propagation of the Truth Model

The truth model is based on the nonlinear inertial orbit equation

$$\ddot{\vec{d}} = -\frac{\mu}{\|\vec{d}\|_2^3} \vec{d} + \vec{a}_p$$

where

$$\|\vec{d}\|_2^3 = (X^2 + Y^2 + Z^2)^{\frac{3}{2}}$$

and \vec{v}_P represents the sum of the perturbation accelerations. Let the state (s) be

$$\vec{s}_i = \begin{bmatrix} X_i \\ Y_i \\ Z_i \\ \dot{X}_i \\ \dot{Y}_i \\ \dot{Z}_i \end{bmatrix}$$

then

$$\dot{\vec{s}}_i = \begin{bmatrix} \dot{X}_i \\ \dot{Y}_i \\ \dot{Z}_i \\ \ddot{X}_i \\ \ddot{Y}_i \\ \ddot{Z}_i \end{bmatrix} = \begin{bmatrix} 0 & 0 & 0 & 1 & 0 & 0 \\ 0 & 0 & 0 & 0 & 1 & 0 \\ 0 & 0 & 0 & 0 & 0 & 1 \\ -\frac{\mu}{\|\vec{d}_i\|_2^3} & 0 & 0 & 0 & 0 & 0 \\ 0 & -\frac{\mu}{\|\vec{d}_i\|_2^3} & 0 & 0 & 0 & 0 \\ 0 & 0 & -\frac{\mu}{\|\vec{d}_i\|_2^3} & 0 & 0 & 0 \end{bmatrix} \begin{bmatrix} X_i \\ Y_i \\ Z_i \\ \dot{X}_i \\ \dot{Y}_i \\ \dot{Z}_i \end{bmatrix} + \begin{bmatrix} 0 \\ 0 \\ 0 \\ a_{p_x} \\ a_{p_y} \\ a_{p_z} \end{bmatrix} \quad (146)$$

O.2 The J_2 Perturbation

Because gravity is a conservative force, it can be derived from the gradient of a scalar potential function [51]. Starting with Equation (55), Appendix C without any control inputs

$$\ddot{\vec{d}} = \frac{-\mu\vec{d}}{\|\vec{d}\|_2^3} + \vec{a}_p$$

Expanding in the inertial reference frame shown in Figure 84, Appendix C, and noting that $|\vec{d}| = d = \sqrt{X^2 + Y^2 + Z^2}$ where X , Y , and Z are the position of the satellite in the inertial frame $\hat{I}\hat{J}\hat{K}$,

$$\begin{aligned} \ddot{\vec{d}} = & \left[\frac{-\mu X}{[X^2 + Y^2 + Z^2]^{\frac{3}{2}}} + \vec{a}_{pI} \right] \hat{I} + \left[\frac{-\mu Y}{[X^2 + Y^2 + Z^2]^{\frac{3}{2}}} + \vec{a}_{pJ} \right] \hat{J} \\ & + \left[\frac{-\mu Z}{[X^2 + Y^2 + Z^2]^{\frac{3}{2}}} + \vec{a}_{pK} \right] \hat{K} \end{aligned}$$

Noting that

$$\begin{aligned} \frac{\partial}{\partial X} \left(\frac{\mu}{|\vec{d}|} + B \right) &= \left[\frac{\sqrt{X^2 + Y^2 + Z^2} * (0) - \mu[1/2(\sqrt{X^2 + Y^2 + Z^2})^{-1/2}]2X}{X^2 + Y^2 + Z^2} \right] + \vec{a}_{pI} \\ &= \frac{-\mu X}{[X^2 + Y^2 + Z^2]^{\frac{3}{2}}} + \vec{a}_{pI} \end{aligned}$$

where B is a potential function such that

$$\nabla B = \vec{a}_p$$

Similarly

$$\begin{aligned} \frac{\partial}{\partial Y} \left(\frac{\mu}{d} + B \right) &= \frac{-\mu Y}{[X^2 + Y^2 + Z^2]^{\frac{3}{2}}} + \vec{a}_{pJ} \\ \frac{\partial}{\partial Z} \left(\frac{\mu}{d} + B \right) &= \frac{-\mu Z}{[X^2 + Y^2 + Z^2]^{\frac{3}{2}}} + \vec{a}_{pK} \end{aligned}$$

Therefore the inertial acceleration is the gradient of the potential function $\frac{\mu}{d} + B$

$$\ddot{\vec{d}} = \nabla \left(\frac{\mu}{d} + B \right)$$

The B term comes about by modeling the Earth not as a point mass but as an oblate body with nonhomogeneous mass distribution (Figure 95) and is the sum of

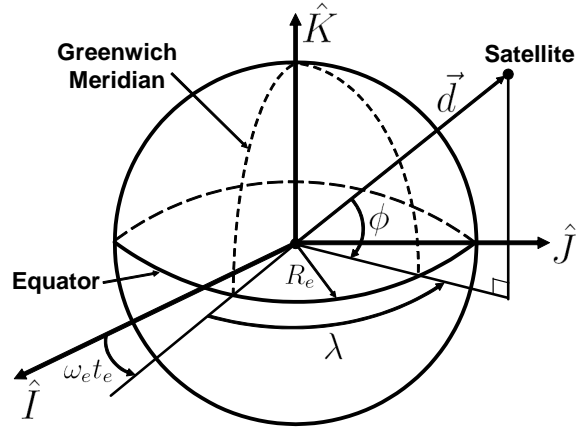


Figure 95: Oblate Earth Coordinate Frame

the infinite series

$$B = \frac{-\mu}{d} \left\{ \sum_{i=2}^{\infty} \left[\left(\frac{R_e}{d} \right)^i J_i P_i(\sin \phi) + \sum_{j=1}^n \left(\frac{R_e}{d} \right)^i (C_{ij} \cos \varphi + S_{ij} \sin \varphi) P_{ij}(\sin \phi) \right] \right\} \quad (147)$$

$$\varphi = j\lambda + \omega_e t_e$$

where R_e is the mean equatorial radius of the Earth, ϕ is the geocentric latitude of the satellite (measured from the equator), λ is the geographical longitude (measured from the prime meridian), d is the satellite position vector magnitude, ω_e is the rotation rate of the Earth, t_e is the time since the \hat{I} direction lined up with the Greenwich meridian, J_n is the zonal harmonic coefficients of order 0, P_n is a Legendre polynomial of degree n and order 0, P_{nm} is a Legendre polynomial of degree n and order m , C_{nm} is the tesseral harmonic coefficient for $n \neq m$, and S_{nm} is the sectorial harmonic coefficients for $n = m$.

Measurements of the zonal, tesseral and sectorial coefficients (J_n , C_{nm} , and S_{nm}) reveal that the J_2 term is at least 400 times larger than the next most significant term. Thus, for applications such as satellite reconfigurations which occur over relatively short time periods, all higher terms can be ignored. Using this assumption, Equation

(147) reduces to

$$B = \frac{-\mu}{d} \sum_{n=2}^2 \left[\left(\frac{R_e}{d} \right)^n J_n P_n(\sin \phi) \right] = \frac{-\mu}{d} \left(\frac{R_e}{d} \right)^2 J_2 P_2(\sin \phi) \quad (148)$$

where $J_2 = 0.0010826$ and the 2nd Legendre polynomial has the form [24]

$$P_2(X) = \frac{1}{2}(3X^2 - 1)$$

Using this Legendre polynomial in Equation (148)

$$B = \frac{-\mu}{d} \left(\frac{R_e}{d} \right)^2 J_2 \frac{1}{2} [3(\sin \phi)^2 - 1]$$

Defining the constant

$$A_{J_2} = \frac{1}{2} J_2 R_e^2$$

simplifies B to

$$B = A_{J_2} \left(\frac{-\mu}{d^3} [3(\sin \phi)^2 - 1] \right)$$

By geometry in Figure 95

$$\sin \phi = \frac{z}{d}$$

which means

$$B = A_{J_2} \left(\frac{-\mu}{d^3} \left[3 \frac{Z^2}{d^2} - 1 \right] \right) = \mu A_{J_2} \left(\frac{-3Z^2 + d^2}{d^5} \right)$$

Now that B is in cartesian coordinates, \vec{a}_{J_2} is found by taking the gradient of B

$$\vec{a}_{J_2} = \nabla B = \begin{bmatrix} \frac{\partial}{\partial X} B \\ \frac{\partial}{\partial Y} B \\ \frac{\partial}{\partial Z} B \end{bmatrix} = \mu A_{J_2} \begin{bmatrix} \frac{d^5(2d \frac{X}{d}) - (-3z^2 + d^2)5d^4 \frac{X}{d}}{d^{10}} \\ \frac{d^5(2d \frac{Y}{d}) - (-3z^2 + d^2)5d^4 \frac{Y}{d}}{d^{10}} \\ \frac{d^5(-6Z + 2d \frac{Z}{d}) - (-3Z^2 + d^2)5d^4 \frac{Z}{d}}{d^{10}} \end{bmatrix}$$

Simplifying

$$\vec{a}_{J_2} = \mu A_{J_2} \begin{bmatrix} \frac{15Z^2X}{d^7} - \frac{3X}{d^5} \\ \frac{15Z^2Y}{d^7} - \frac{3Y}{d^5} \\ \frac{15Z^3}{d^7} - \frac{9Z}{d^5} \end{bmatrix} = \frac{\mu J_2 R_e^2}{2} \begin{bmatrix} \frac{15Z^2X}{d^7} - \frac{3X}{d^5} \\ \frac{15Z^2Y}{d^7} - \frac{3Y}{d^5} \\ \frac{15Z^3}{d^7} - \frac{9Z}{d^5} \end{bmatrix} \quad (149)$$

0.3 Atmospheric Drag

Atmospheric drag is the second largest perturbation next to J_2 for satellites in near-Earth orbits [59]. Unfortunately, its effects are considerably harder to model accurately. Unknowns in atmospheric density, spacecraft ballistic coefficient, and relative velocity with respect to the atmosphere all contribute to errors in the model. However, a simple model will be employed in order to give a sense of its effects to hovering orbits. The standard equation for acceleration due to air drag is well documented in the literature [26, 50, 59]

$$\vec{a}_{\text{drag}} = -\frac{1}{2} \frac{C_D A}{m} \rho_d V^2 \frac{\vec{V}_{\text{rel}}}{\|\vec{V}_{\text{rel}}\|_2} = -\frac{1}{2} \frac{C_D A}{m} \rho_d V_{\text{rel}} \vec{V}_{\text{rel}}$$

where C_D is the coefficient of drag (and unitless), A is the area, m is the mass, ρ_d is the atmospheric density, and \vec{V}_{rel} is the satellite's velocity relative to the atmosphere and equal to

$$\vec{V}_{\text{rel}} = \vec{v} - \vec{v}_{\text{atmos}}$$

Due to the Earth's rotation, the atmosphere has a mean velocity of [59]

$$\vec{v}_{\text{atmos}} = \omega_{\oplus} \times \vec{M}$$

where \vec{M} is the inertial position vector of the satellite and the rotation of the Earth is $\omega_{\oplus} = 7.729 * 10^{-5} \frac{\text{rad}}{\text{s}}$. Higher order effects like local wind and density variations will be ignored in this simplified model.

The coefficient of drag, area, and mass are usually grouped into a single term called the ballistic coefficient (B_C)

$$B_C = \frac{m}{C_D A}$$

and typically have a range of [26]

$$0.515 \frac{\text{kg}}{\text{m}^2} < B_C < 437 \frac{\text{kg}}{\text{m}^2}$$

The last piece of the puzzle is a model of atmospheric density. Although a number of high fidelity stochastic models are available, we can get the accuracy we desire with the following exponential model [59]

$$\rho_d = \rho_o e^{\frac{h_o - h_d}{H}}$$

where ρ_o is the nominal density, h_o is the reference altitude, h_d is the deputy's altitude, and H is the scale height. The h_o and H values are determined by observations and are listed in Table 2 (verbatim from [59]). This model uses the U.S. Standard Atmosphere (1976) for 0 km, CIRA-72 for 25-500 km, and CIRA-72 with exospheric temperature, $T_\infty = 1000$ K for 500-1000 km. The atmospheric drag model as implemented in code is

$$\vec{a}_{\text{drag}} = -\frac{V_{\text{rel}}}{2B_C} \rho_o e^{\frac{h_o - h_d}{H}} \vec{V}_{\text{rel}} \quad (150)$$

Table 2: Atmospheric Model

Altitude h_d (km)	Reference Altitude h_o (km)	Nominal Density ρ_o (kg/m ²)	Scale Height H (km)	Altitude h_d (km)	Reference Altitude h_o (km)	Nominal Density ρ_o (kg/m ²)	Scale Height H (km)
0 – 25	0	1.225	7.249	150 – 180	150	2.070×10^{-9}	22.523
25 – 30	25	3.899×10^{-2}	6.349	180 – 200	180	5.464×10^{-10}	29.740
30 – 40	30	1.774×10^{-2}	6.682	200 – 250	200	2.789×10^{-10}	37.105
40 – 50	40	3.972×10^{-3}	7.554	250 – 300	250	7.248×10^{-11}	45.546
50 – 60	50	1.057×10^{-3}	8.382	300 – 350	300	2.418×10^{-11}	53.628
60 – 70	60	3.206×10^{-4}	7.714	350 – 400	350	9.518×10^{-12}	53.298
70 – 80	70	8.770×10^{-5}	6.549	400 – 450	400	3.725×10^{-12}	58.515
80 – 90	80	1.905×10^{-5}	5.799	450 – 500	450	1.585×10^{-12}	60.828
90 – 100	90	3.396×10^{-6}	5.382	500 – 600	500	6.967×10^{-13}	63.822
100 – 110	100	5.297×10^{-7}	5.877	600 – 700	600	1.454×10^{-13}	71.835
110 – 120	110	9.661×10^{-8}	7.263	700 – 800	700	3.614×10^{-14}	88.667
120 – 130	120	2.438×10^{-8}	9.473	800 – 900	800	1.170×10^{-14}	124.64
130 – 140	130	8.484×10^{-9}	12.636	900 – 1000	900	5.245×10^{-15}	181.05
140 – 150	140	3.845×10^{-9}	16.149	> 1000	1000	3.019×10^{-15}	268.00

$$\frac{\partial J}{\partial \psi_{k+1}} = \frac{\tilde{T}_T \frac{1}{\Delta \check{V}_C^2} \left[\frac{\partial(\Delta \check{V}_k^2)}{\partial \psi_{k+1}} \right] - 0}{\tilde{T}_T^2} = \frac{1}{\tilde{T}_T \Delta \check{V}_C^2} \left[\frac{\partial(\Delta \check{V}_k^2)}{\partial \psi_{k+1}} + \frac{\partial(\Delta \check{V}_F^2)}{\partial \psi_{k+1}} \right]$$

Note that how $\Delta \check{V}_1^2$ and its partial are calculated depends on the entry condition.

Let

$$\sum_{i=1}^k \Delta \check{V}_i^2 = \Delta \check{V}_{T^2}$$

the partials with respect to the times-of-flight are

$$\frac{\partial J}{\partial \tilde{T}_{1,2}} = \frac{\tilde{T}_T \frac{1}{\Delta \check{V}_C^2} \left[\frac{\partial(\Delta \check{V}_1^2)}{\partial \tilde{T}_{1,2}} + \frac{\partial(\Delta \check{V}_2^2)}{\partial \tilde{T}_{1,2}} \right] - \frac{1}{\Delta \check{V}_C^2} \Delta \check{V}_{T^2}(1)}{\tilde{T}_T^2} = \frac{1}{\tilde{T}_T \Delta \check{V}_C^2} \left[\frac{\partial(\Delta \check{V}_1^2)}{\partial \tilde{T}_{1,2}} + \frac{\partial(\Delta \check{V}_2^2)}{\partial \tilde{T}_{1,2}} - J \right] \quad (154)$$

noting that $J\tilde{T}_T = \frac{\Delta \check{V}_{T^2}}{\Delta \check{V}_C^2} \quad \vdots$

$$\frac{\partial J}{\partial \tilde{T}_{i,i+1}} = \frac{\tilde{T}_T \frac{1}{\Delta \check{V}_C^2} \left[\frac{\partial(\Delta \check{V}_i^2)}{\partial \tilde{T}_{i,i+1}} + \frac{\partial(\Delta \check{V}_{i+1}^2)}{\partial \tilde{T}_{i,i+1}} \right] - \frac{1}{\Delta \check{V}_C^2} \Delta \check{V}_{T^2}(1)}{\tilde{T}_T^2} = \frac{1}{\tilde{T}_T \Delta \check{V}_C^2} \left[\frac{\partial(\Delta \check{V}_i^2)}{\partial \tilde{T}_{i,i+1}} + \frac{\partial(\Delta \check{V}_{i+1}^2)}{\partial \tilde{T}_{i,i+1}} - J \right] \quad (155)$$

$$\vdots \quad \quad \quad \vdots \quad \quad \quad \vdots$$

$$\frac{\partial J}{\partial \tilde{T}_{k,k+1}} = \frac{\tilde{T}_T \frac{1}{\Delta \check{V}_C^2} \left[\frac{\partial(\Delta \check{V}_k^2)}{\partial \tilde{T}_{k,k+1}} \right] - \frac{1}{\Delta \check{V}_C^2} \Delta \check{V}_{T^2}(1)}{\tilde{T}_T^2} = \frac{1}{\tilde{T}_T \Delta \check{V}_C^2} \left[\frac{\partial(\Delta \check{V}_k^2)}{\partial \tilde{T}_{k,k+1}} + \frac{\partial(\Delta \check{V}_F^2)}{\partial \tilde{T}_{k,k+1}} - J \right]$$

The \tilde{T}_F term is nonzero in only one exit condition where it is set equal to $\tilde{T}_{1,2}$; therefore we do not need a partial with respect to \tilde{T}_F .

P.1 The Gradient of ΔV^2

A few preliminaries are required before taking the derivative of ΔV^2 . Examining the equation for R , (Equation (126), Appendix K) we see only a handful of repeated forms, thus finding the gradient is not as complex as it first seems. Let

$$\xi = 8 - 3nT \sin(nT) - 8 \cos(nT)$$

and its partial derivative with respect to time-of-flight is then

$$\frac{\partial \xi}{\partial T} = -3n^2T \cos(nT) - 3n \sin(nT) + 8n \sin(nT) = -3n^2T \cos(nT) + 5n \sin(nT)$$

Then the following partials are ($C = \cos(nT)$ and $S = \sin(nT)$)

$$\begin{aligned} \frac{\partial \left(\frac{4S-3nT}{\xi} \right)}{\partial T} &= \frac{(8 - 3nTS - 8C)(4nC - 3n) - (4S - 3nT)(-3n^2TC + 5nS)}{(8 - 3nTS - 8C)^2} \\ &= \frac{-44n + 56nC + 24n^2TS - 9n^3T^2C - 12nC^2}{(8 - 3nTS - 8C)^2} \end{aligned}$$

$$\begin{aligned} \frac{\partial \left(\frac{-2+2C}{\xi} \right)}{\partial T} &= \frac{(8 - 3nTS - 8C)(-2nS) - (-2 + 2C)(-3n^2TC + 5nS)}{(8 - 3nTS - 8C)^2} \\ &= \frac{6n^2T - 6nS + 6nSC - 6n^2TC}{(8 - 3nTS - 8C)^2} \end{aligned}$$

$$\begin{aligned} \frac{\partial \left(\frac{S}{\xi} \right)}{\partial T} &= \frac{(8 - 3nTS - 8C)nC - S(-3n^2TC + 5nS)}{(8 - 3nTS - 8C)^2} \\ &= \frac{-5n + 8nC - 3nC^2}{(8 - 3nTS - 8C)^2} \end{aligned}$$

$$\begin{aligned} \frac{\partial \left(\frac{4S-3nTC}{\xi} \right)}{\partial T} &= \frac{(8 - 3nTS - 8C)(nC + 3n^2TS) - (4S - 3nTC)(-3n^2TC + 5nS)}{(8 - 3nTS - 8C)^2} \\ &= \frac{-20n + 8nC + 24n^2TS + 12nC^2 - 9n^3T^2}{(8 - 3nTS - 8C)^2} \end{aligned}$$

$$\begin{aligned} \frac{\partial \left(\frac{-14+6nTS+14C}{\xi} \right)}{\partial T} &= \frac{(8 - 3nTS - 8C)(6n^2TC - 8nS) - (-14 + 6nTS + 14C)(-3n^2TC + 5nS)}{(8 - 3nTS - 8C)^2} \\ &= \frac{6nS - 6nSC + 6n^2TC - 6n^2T}{(8 - 3nTS - 8C)^2} \end{aligned}$$

altogether

$$\frac{\partial R}{\partial T^-} = \begin{bmatrix} \frac{-44n+56nC^-+24n^2T^-S^- -9n^3T^2-C^- -12nC^2-}{(8-3nT^-S^- -8C^-)^2} & \frac{6n^2T^- -6nS^-+6nS^-C^- -6n^2T^-C^-}{(8-3nT^-S^- -8C^-)^2} \\ \frac{-6n^2T^-+6nS^- -6nS^-C^-+6n^2T^-C^-}{(8-3nT^-S^- -8C^-)^2} & \frac{-5n+8nC^- -3nC^2-}{(8-3nT^-S^- -8C^-)^2} \\ \frac{20n-8nC^- -24n^2T^-S^- -12nC^2-+9n^3T^2-}{(8-3nT^-S^- -8C^-)^2} & \frac{-6nS^-+6nS^-C^- -6n^2T^-C^-+6n^2T^-}{(8-3nT^-S^- -8C^-)^2} \\ \frac{6n^2T^- -6nS^-+6nS^-C^- -6n^2T^-C^-}{(8-3nT^-S^- -8C^-)^2} & \frac{5n-8nC^-+3nC^2-}{(8-3nT^-S^- -8C^-)^2} \\ 0 & 0 \\ 0 & 0 \end{bmatrix} \quad (156)$$

$$\frac{\partial R}{\partial T^+} = \begin{bmatrix} 0 & 0 \\ 0 & 0 \\ \frac{20n-8nC^+ -24n^2T^+S^+ -12nC^2+ +9n^3T^2+}{(8-3nT^+S^+ -8C^+)^2} & \frac{6nS^+ -6nS^+C^+ +6n^2T^+C^+ -6n^2T^+}{(8-3nT^+S^+ -8C^+)^2} \\ \frac{-6n^2T^+ +6nS^+ -6nS^+C^+ +6n^2T^+C^+}{(8-3nT^+S^+ -8C^+)^2} & \frac{5n-8nC^+ +3nC^2+}{(8-3nT^+S^+ -8C^+)^2} \\ \frac{-44n+56nC^+ +24n^2T^+S^+ -9n^3T^2+C^+ -12nC^2+}{(8-3nT^+S^+ -8C^+)^2} & \frac{-6n^2T^+ +6nS^+ -6nS^+C^+ +6n^2T^+C^+}{(8-3nT^+S^+ -8C^+)^2} \\ \frac{6n^2T^+ -6nS^+ +6nS^+C^+ -6n^2T^+C^+}{(8-3nT^+S^+ -8C^+)^2} & \frac{-5n+8nC^+ -3nC^2+}{(8-3nT^+S^+ -8C^+)^2} \end{bmatrix} \quad (157)$$

if we want to express these partials in terms of \tilde{T} , we simply multiply both sides by

$$\frac{\partial T}{\partial \tilde{T}} = \frac{\partial \left(\frac{2\pi\tilde{T}}{n} \right)}{\partial \tilde{T}} = \frac{2\pi}{n}$$

and substitute $nT = 2\pi\tilde{T}$ from Equation (2), yielding

$$\frac{\partial \tilde{R}}{\partial \tilde{T}^-} = \begin{bmatrix} \frac{-88\pi+112\pi\tilde{C}^-+96\pi^2\tilde{T}^-\tilde{S}^- -72\pi^3\tilde{T}^2-\tilde{C}^- -24\pi\tilde{C}^2-}{(8-6\pi\tilde{T}^-\tilde{S}^- -8\tilde{C}^-)^2} & \frac{24\pi^2\tilde{T}^- -12\pi\tilde{S}^-+12\pi\tilde{S}^-\tilde{C}^- -24\pi^2\tilde{T}^-\tilde{C}^-}{(8-6\pi\tilde{T}^-\tilde{S}^- -8\tilde{C}^-)^2} \\ \frac{-24\pi^2\tilde{T}^-+12\pi\tilde{S}^- -12\pi\tilde{S}^-\tilde{C}^-+24\pi^2\tilde{T}^-\tilde{C}^-}{(8-6\pi\tilde{T}^-\tilde{S}^- -8\tilde{C}^-)^2} & \frac{-10\pi+16\pi\tilde{C}^- -6\pi\tilde{C}^2-}{(8-6\pi\tilde{T}^-\tilde{S}^- -8\tilde{C}^-)^2} \\ \frac{40\pi-16\pi\tilde{C}^- -96\pi^2\tilde{T}^-\tilde{S}^- -24\pi\tilde{C}^2-+72\pi^3\tilde{T}^2-}{(8-6\pi\tilde{T}^-\tilde{S}^- -8\tilde{C}^-)^2} & \frac{-12\pi\tilde{S}^-+12\pi\tilde{S}^-\tilde{C}^- -24\pi^2\tilde{T}^-\tilde{C}^-+24\pi^2\tilde{T}^-}{(8-6\pi\tilde{T}^-\tilde{S}^- -8\tilde{C}^-)^2} \\ \frac{24\pi^2\tilde{T}^- -12\pi\tilde{S}^-+12\pi\tilde{S}^-\tilde{C}^- -24\pi^2\tilde{T}^-\tilde{C}^-}{(8-6\pi\tilde{T}^-\tilde{S}^- -8\tilde{C}^-)^2} & \frac{10\pi-16\pi\tilde{C}^-+6\pi\tilde{C}^2-}{(8-6\pi\tilde{T}^-\tilde{S}^- -8\tilde{C}^-)^2} \\ 0 & 0 \\ 0 & 0 \end{bmatrix} \quad (158)$$

$$\frac{\partial \tilde{R}}{\partial \tilde{T}^+} = \begin{bmatrix} 0 & 0 \\ 0 & 0 \\ \frac{40\pi - 16\pi\tilde{C}^+ - 96\pi^2\tilde{T}^+\tilde{S}^+ - 24\pi\tilde{C}^{2+} + 72\pi^3\tilde{T}^{2+}}{(8-6\pi\tilde{T}^+\tilde{S}^+ - 8\tilde{C}^+)^2} & \frac{12\pi\tilde{S}^+ - 12\pi\tilde{S}^+\tilde{C}^+ + 24\pi^2\tilde{T}^+\tilde{C}^+ - 24\pi^2\tilde{T}^+}{(8-6\pi\tilde{T}^+\tilde{S}^+ - 8\tilde{C}^+)^2} \\ \frac{-24\pi^2\tilde{T}^+ + 12\pi\tilde{S}^+ - 12\pi\tilde{S}^+\tilde{C}^+ + 24\pi^2\tilde{T}^+\tilde{C}^+}{(8-6\pi\tilde{T}^+\tilde{S}^+ - 8\tilde{C}^+)^2} & \frac{10\pi - 16\pi\tilde{C}^+ + 6\pi\tilde{C}^{2+}}{(8-6\pi\tilde{T}^+\tilde{S}^+ - 8\tilde{C}^+)^2} \\ \frac{-88\pi + 112\pi\tilde{C}^+ + 96\pi^2\tilde{T}^+\tilde{S}^+ - 72\pi^3\tilde{T}^{2+}\tilde{C}^+ - 24\pi\tilde{C}^{2+}}{(8-6\pi\tilde{T}^+\tilde{S}^+ - 8\tilde{C}^+)^2} & \frac{-24\pi^2\tilde{T}^+ + 12\pi\tilde{S}^+ - 12\pi\tilde{S}^+\tilde{C}^+ + 24\pi^2\tilde{T}^+\tilde{C}^+}{(8-6\pi\tilde{T}^+\tilde{S}^+ - 8\tilde{C}^+)^2} \\ \frac{24\pi^2\tilde{T}^+ - 12\pi\tilde{S}^+ + 12\pi\tilde{S}^+\tilde{C}^+ - 24\pi^2\tilde{T}^+\tilde{C}^+}{(8-6\pi\tilde{T}^+\tilde{S}^+ - 8\tilde{C}^+)^2} & \frac{-10\pi + 16\pi\tilde{C}^+ - 6\pi\tilde{C}^{2+}}{(8-6\pi\tilde{T}^+\tilde{S}^+ - 8\tilde{C}^+)^2} \end{bmatrix} \quad (159)$$

We are now prepared to take the derivative of ΔV^2 with respect to the optimization variables. Applying the theorem found in Appendix A.4 and, taking the partial derivative with respect to the previous point,

$$\frac{\partial(\Delta V_i^2)}{\partial \psi_{i-1}} = 2n^2 \begin{bmatrix} x_{i-1} & y_{i-1} & x_i & y_i & x_{i+1} & y_{i+1} \end{bmatrix} RR' \begin{bmatrix} \frac{\partial x_{i-1}}{\partial \psi_{i-1}} \\ \frac{\partial y_{i-1}}{\partial \psi_{i-1}} \\ 0 \\ 0 \\ 0 \\ 0 \end{bmatrix} \quad (160)$$

where the partials of the positions are functions of the lobe shape. Equations (42) and (43) from Appendix B

$$x_i = \gamma \cos \alpha \sin \beta + \frac{\tau_x \tau_y \cos \psi_i}{\sqrt{\tau_y^2 \cos^2(\psi_i - \eta) + \tau_x^2 \sin^2(\psi_i - \eta)}}$$

$$y_i = \gamma \sin \alpha \sin \beta + \frac{\tau_x \tau_y \sin \psi_i}{\sqrt{\tau_y^2 \cos^2(\psi_i - \eta) + \tau_x^2 \sin^2(\psi_i - \eta)}}$$

The derivatives with respect to ψ are Equations (47) and (48) from Appendix B

$$\begin{aligned}\frac{\partial x_i}{\partial \psi_i} &= -r_i \sin \psi_i - r_i^3 \frac{\tau_x^2 - \tau_y^2}{2\tau_x^2 \tau_y^2} \sin(2\psi_i - 2\eta) \cos \psi_i \\ \frac{\partial y_i}{\partial \psi_i} &= r_i \cos \psi_i - r_i^3 \frac{\tau_x^2 - \tau_y^2}{2\tau_x^2 \tau_y^2} \sin(2\psi_i - 2\eta) \sin \psi_i \\ r_i &= \frac{\tau_x \tau_y}{\sqrt{\tau_y^2 \cos^2(\psi_i - \eta) + \tau_x^2 \sin^2(\psi_i - \eta)}}\end{aligned}$$

Similarly the partial derivative with respect to the current point is

$$\frac{\partial (\Delta V_i^2)}{\partial \psi_i} = 2n^2 \begin{bmatrix} x_{i-1} & y_{i-1} & x_i & y_i & x_{i+1} & y_{i+1} \end{bmatrix} RR' \begin{bmatrix} 0 \\ 0 \\ \frac{\partial x_i}{\partial \psi_i} \\ \frac{\partial y_i}{\partial \psi_i} \\ 0 \\ 0 \end{bmatrix} \quad (161)$$

and with respect to the next point:

$$\frac{\partial (\Delta V_i^2)}{\partial \psi_{i+1}} = 2n^2 \begin{bmatrix} x_{i-1} & y_{i-1} & x_i & y_i & x_{i+1} & y_{i+1} \end{bmatrix} RR' \begin{bmatrix} 0 \\ 0 \\ 0 \\ 0 \\ \frac{\partial x_{i+1}}{\partial \psi_{i+1}} \\ \frac{\partial y_{i+1}}{\partial \psi_{i+1}} \end{bmatrix} \quad (162)$$

Applying the theorem found in Appendix A.5, the partial derivative with respect to the previous time-of-flight is

$$\frac{\partial (\Delta V_i^2)}{\partial T_{i-1,i}} = 2n^2 \begin{bmatrix} x_{i-1} & y_{i-1} & x_i & y_i & x_{i+1} & y_{i+1} \end{bmatrix} R \frac{\partial R'}{\partial T^-} \begin{bmatrix} x_{i-1} \\ y_{i-1} \\ x_i \\ y_i \\ x_{i+1} \\ y_{i+1} \end{bmatrix} \quad (163)$$

and the partial with respect to the next time-of-flight

$$\frac{\partial (\Delta V_i^2)}{\partial T_{i,i+1}} = 2n^2 \begin{bmatrix} x_{i-1} & y_{i-1} & x_i & y_i & x_{i+1} & y_{i+1} \end{bmatrix} R \frac{\partial R'}{\partial T^+} \begin{bmatrix} x_{i-1} \\ y_{i-1} \\ x_i \\ y_i \\ x_{i+1} \\ y_{i+1} \end{bmatrix} \quad (164)$$

Recall that the partial derivatives of the cost function J requires the summation of two or three partials of $\Delta \check{V}$ with respect to ψ or \tilde{T} . When implementing these in an algorithm it becomes useful to construct the following matrices. The required summations are then simply the row sums.

	ΔV_1^2	ΔV_2^2	ΔV_3^2	ΔV_4^2	ΔV_5^2	...	ΔV_{k-2}^2	ΔV_{k-1}^2	ΔV_k^2	ΔV_F^2
ψ_1	$\frac{\partial(\Delta V_1^2)}{\partial\psi_1}$	$\frac{\partial(\Delta V_2^2)}{\partial\psi_1}$	0	0	0	...	0	0	$\frac{\partial(\Delta V_k^2)}{\partial\psi_1}$	$\frac{\partial(\Delta V_F^2)}{\partial\psi_1}$
ψ_2	$\frac{\partial(\Delta V_1^2)}{\partial\psi_2}$	$\frac{\partial(\Delta V_2^2)}{\partial\psi_2}$	$\frac{\partial(\Delta V_3^2)}{\partial\psi_2}$	0	0	...	0	0	0	0
ψ_3	0	$\frac{\partial(\Delta V_2^2)}{\partial\psi_3}$	$\frac{\partial(\Delta V_3^2)}{\partial\psi_3}$	$\frac{\partial(\Delta V_4^2)}{\partial\psi_3}$	0	...	0	0	0	0
ψ_4	0	0	$\frac{\partial(\Delta V_3^2)}{\partial\psi_4}$	$\frac{\partial(\Delta V_4^2)}{\partial\psi_4}$	$\frac{\partial(\Delta V_5^2)}{\partial\psi_4}$...	0	0	0	0
ψ_5	0	0	0	$\frac{\partial(\Delta V_4^2)}{\partial\psi_5}$	$\frac{\partial(\Delta V_5^2)}{\partial\psi_5}$...	0	0	0	0
\vdots	\vdots	\vdots	\vdots	\vdots	\vdots	\ddots	\vdots	\vdots	\vdots	\vdots
ψ_{k-2}	0	0	0	0	0	...	$\frac{\partial(\Delta V_{k-2}^2)}{\partial\psi_{k-2}}$	$\frac{\partial(\Delta V_{k-1}^2)}{\partial\psi_{k-2}}$	0	0
ψ_{k-1}	0	0	0	0	0	...	$\frac{\partial(\Delta V_{k-2}^2)}{\partial\psi_{k-1}}$	$\frac{\partial(\Delta V_{k-1}^2)}{\partial\psi_{k-1}}$	$\frac{\partial(\Delta V_k^2)}{\partial\psi_{k-1}}$	0
ψ_k	0	0	0	0	0	...	0	$\frac{\partial(\Delta V_{k-1}^2)}{\partial\psi_k}$	$\frac{\partial(\Delta V_k^2)}{\partial\psi_k}$	$\frac{\partial(\Delta V_F^2)}{\partial\psi_k}$
ψ_{k+1}	0	0	0	0	0	...	0	0	$\frac{\partial(\Delta V_k^2)}{\partial\psi_{k+1}}$	$\frac{\partial(\Delta V_F^2)}{\partial\psi_{k+1}}$

The last two entries in the ψ_1 row are nonzero only in the repeating hovering orbit exit condition. The partials with respect to time-of-flight

	ΔV_1^2	ΔV_2^2	ΔV_3^2	ΔV_4^2	ΔV_5^2	...	ΔV_{k-2}^2	ΔV_{k-1}^2	ΔV_k^2	ΔV_F^2
$T_{1,2}$	$\frac{\partial(\Delta V_1^2)}{\partial T_{1,2}}$	$\frac{\partial(\Delta V_2^2)}{\partial T_{1,2}}$	0	0	0	...	0	0	0	$\frac{\partial(\Delta V_k^2)}{\partial T_{1,2}}$
$T_{2,3}$	0	$\frac{\partial(\Delta V_2^2)}{\partial T_{2,3}}$	$\frac{\partial(\Delta V_3^2)}{\partial T_{2,3}}$	0	0	...	0	0	0	0
$T_{3,4}$	0	0	$\frac{\partial(\Delta V_3^2)}{\partial T_{3,4}}$	$\frac{\partial(\Delta V_4^2)}{\partial T_{3,4}}$	0	...	0	0	0	0
$T_{4,5}$	0	0	0	$\frac{\partial(\Delta V_4^2)}{\partial T_{4,5}}$	$\frac{\partial(\Delta V_5^2)}{\partial T_{4,5}}$...	0	0	0	0
$T_{5,6}$	0	0	0	0	$\frac{\partial(\Delta V_5^2)}{\partial T_{5,6}}$...	0	0	0	0
\vdots	\vdots	\vdots	\vdots	\vdots	\vdots	\ddots	\vdots	\vdots	\vdots	\vdots
$T_{k-2,k-1}$	0	0	0	0	0	...	$\frac{\partial(\Delta V_{k-2}^2)}{\partial T_{k-2,k-1}}$	$\frac{\partial(\Delta V_{k-1}^2)}{\partial T_{k-2,k-1}}$	0	0
$T_{k-1,k}$	0	0	0	0	0	...	0	$\frac{\partial(\Delta V_{k-1}^2)}{\partial T_{k-1,k}}$	$\frac{\partial(\Delta V_k^2)}{\partial T_{k-1,k}}$	0
$T_{k,k+1}$	0	0	0	0	0	...	0	0	$\frac{\partial(\Delta V_k^2)}{\partial T_{k,k+1}}$	$\frac{\partial(\Delta V_F^2)}{\partial T_{k,k+1}}$

Appendix Q. MATLAB[®] Algorithm

The following appendix contains pseudocode for the MATLAB[®] routine used to produce the results presented.

1. Description: Finds and plots the solution for staying the defined lobe while minimizing the total ΔV used per unit of time.
2. Inputs
 - (a) Entry/Exit Condition
 - (b) Lobe Parameters: $\alpha, \beta, \gamma, h, \tau_x, \tau_y, \eta$
 - (c) Chief Orbit Parameters (for elliptical orbits only)
 - (d) ψ Initial Conditions (determines number of legs)
3. Algorithm
 - (a) Load constraint data if available
 - (b) Calculate mean motion and period of chief (for elliptical chiefs)
 - (c) Calculate \hat{Z} information
 - i. $\tilde{z}_{\min} = \gamma \|\cos \beta\| - h$ $\tilde{z}_{\max} = \gamma \|\cos \beta\| + h$
 - ii. Max \hat{Z} period = $\tilde{T}_z = \frac{1}{\pi} \cos^{-1}(\tilde{z}_{\min}/\tilde{z}_{\max})$
 - (d) Calculate lobe parameters: $\tilde{x}_{\min}, \psi_{\tilde{x}_{\min}}, \tilde{y}_{\tilde{x}_{\min}}$
 - (e) Construct the initial condition for the nonlinear programming algorithm (set $\tilde{T} = 0.01$ chief orbit fractions for all)
 $[\psi_1, \psi_2, \dots, \psi_k, \tilde{T}_{1,2}, \tilde{T}_{2,3}, \dots, \tilde{T}_{k,k+1}]$
 - (f) Run FMINCON
 - (g) Calculate number of legs (k_z) in the \hat{Z} direction: $\left\lfloor \frac{\tilde{T}_T}{\tilde{T}_z} \right\rfloor$
 - (h) Generate thrust locations and the time-of-flight between them
 - (i) Propagate the trajectory between thrust locations
 - (j) Plot data

Bibliography

1. “DART Rendezvous Vehicle Fact Sheet,” May 2006. <http://www.orbital.com/AdvancedSpace/DART/index.html>.
2. Alfriend, K.T. and H. Yan. “Evaluation and Comparison of Relative Motion Theories,” *Journal of Guidance, Control, and Dynamics*, 28(2):254–261, March-April 2005.
3. Alfriend, K.T., H. Yan, and S.R. Vadali. “Nonlinear Considerations in Satellite Formation Flying.” *AIAA/AAS Astrodynamics Specialists Conference*. Monterey, CA, August 2002.
4. Broschart, Stephen B. and Daniel J. Scheeres. “Control of Hovering Spacecraft Near Small Bodies: Application to Asteroid 25143 Itokawa,” *Journal of Guidance, Control, and Dynamics*, 28(2):343–354, March-April 2005.
5. Broucke, Roger A. “Solution of the Elliptic Rendezvous Problem with the Time as Independent Variable,” *Journal of Guidance, Control, and Dynamics*, 26(4):615–621, July-August 2003.
6. Burns, Rich, Craig McLaughlin, Jesse Leitner, and Maurice Martin. *TechSat 21: Formation Design, Control, and Simulation*. In-house, Air Force Research Laboratory, Space Vehicles Directorate, Kirtland AFB, NM, 2000.
7. Carter, Thomas and Mayer Humi. “Clohessy-Wiltshire Equations Modified to Include Quadratic Drag,” *Journal of Guidance, Control, and Dynamics*, 25(6):1058–1063, November-December 2002.
8. Clohessy, W.H. and R.S. Wiltshire. “Terminal Guidance System for Satellite Rendezvous,” *Journal of the Aerospace Sciences*, 27(9):653–659, September 1960.
9. D’Amico, Simone and Oliver Montenbruck. “Proximity Operations of Formation-Flying Spacecraft Using an Eccentricity/Inclination Vector Separation,” *Journal of Guidance, Control, and Dynamics*, 29(3):554–563, May-June 2006.
10. Department of the Air Force (DAF). “Roles, Missions, and Functions of Air and Space Power,” AFDD 1, Air Force Basic Doctrine, Chapter 4, Washington: HQ USAF, November 2003.
11. Duan, Xiaodong and Peter M. Bainum. “Low-Thrust Autonomous Control for Maintaining Formation and Constellation Orbits.” *AIAA/AAS Astrodynamics Specialists Conference*. Providence, RI, August 2004.
12. Gabern, Frederic, Wang S. Koon, and Jerrold E. Marsden. “Parking a Spacecraft near an Asteroid Pair,” *Journal of Guidance, Control, and Dynamics*, 29(3):544–553, May-June 2006.

13. Gim, Dong-Woo and Kyle T. Alfriend. "State Transition Matrix of Relative Motion for the Perturbed Noncircular Reference Orbit," *Journal of Guidance, Control, and Dynamics*, 26(6):956–971, November-December 2003.
14. Guibout, V.M. and D.J. Scheeres. "Solving Relative Two-Point Boundary Value Problems: Spacecraft Formation Flight Transfers Application," *Journal of Guidance, Control, and Dynamics*, 27(4):693–704, July-August 2004.
15. Gurfil, Pini and Konstantin V. Kholshchikov. "Distances on the Relative Spacecraft Motion Manifold." *AIAA Guidance, Navigation, and Control Conference and Exhibit*. San Francisco, CA, August 2005.
16. Hill, G.W. "Researches in the Lunar Theory," *American Journal of Mathematics*, 1:5–26, 1878.
17. Hope, Alan S. and Aaron J. Trask. "Pulsed Thrust Method for Hover Formation Flying." *AIAA/AAS Astrodynamics Specialists Conference*. Big Sky, Montana, August 2003.
18. Hu, W. and D.J. Scheeres. "Spacecraft Motion About Slowly Rotating Asteroids," *Journal of Guidance, Control, and Dynamics*, 25(4):765–775, July-August 2002.
19. Humi, Mayer and Thomas Carter. "Rendezvous Equations in a Central-Force Field with Linear Drag," *Journal of Guidance, Control, and Dynamics*, 25(1):74–79, January-February 2002.
20. Inalhan, Gorkan, Michael Tillerson, and Jonathan P. How. "Relative Dynamics and Control of Spacecraft Formations in Eccentric Orbits," *Journal of Guidance, Control, and Dynamics*, 25(1):48–59, January-February 2002.
21. Irvin, David J. *A Study of Linear vs. Nonlinear Control Techniques for the Reconfiguration of Satellite Formations*. Master's Thesis, Graduate School of Engineering and Management, Air Force Institute of Technology (AETC), Wright-Patterson AFB, OH, March 2001. AFIT/GA/ENY/01M-02.
22. Karlgaard, Christopher D. and Frederick H. Lutze. "Second-Order Relative Motion Equations," *Journal of Guidance, Control, and Dynamics*, 26(1):41–49, January-February 2003.
23. Kasdin, Pini Gurfil N. Jeremy. "Nonlinear Modeling of Spacecraft Relative Motion in the Configuration Space," *Journal of Guidance, Control, and Dynamics*, 27(1):154–157, January-February 2004.
24. Kreyszig, Erwin. *Advanced Engineering Mathematics*. John Wiley and Sons, Inc., New York, NY, seventh edition, 1993.
25. Lane, Christopher and Penina Axelrad. "Formation Design in Eccentric Orbits Using Linearized Equations of Relative Motion," *Journal of Guidance, Control, and Dynamics*, 29(1):146–160, January-February 2006.

26. Larson, Wiley J and James R. Wertz. *Space Mission Analysis and Design*. Microcosm Inc., Torrance, CA, second edition, 1992.
27. Leonard, C.L., W.M. Hollister, and E.V. Bergmann. "Orbital Formationkeeping with Differential Drag," *Journal of Guidance, Control, and Dynamics*, 12(1):108–113, January-February 1989.
28. Lovell, T. Alan and Denise L. Brown. "Impulsive-Hover Satellite Trajectory Design for Rendezvous and Proximity Operation Missions." *AAS Rocky Mountain Guidance, Navigation, and Control Conference*. American Astronautical Society, Breckenridge, CO, February 2007.
29. Lovell, T. Alan and Mark V. Tollefson. "Calculation of Impulsive Hovering Trajectories via Relative Orbit Elements." *AIAA/AAS Astrodynamics Specialists Conference*. Lake Tahoe, CA, August 2005.
30. Lovell, T. Alan and Steven G. Tragesser. "Guidance for Relative Motion of Low Earth Orbit Spacecraft Based on Relative Orbit Elements." *AIAA/AAS Astrodynamics Specialists Conference*. Providence, RI, August 2004.
31. Martin, Maurice and Michael J. Stallard. "Distributed Satellite Missions and Technologies - The TechSat 21 Program." *AIAA Space Technology Conference and Exposition*. American Institute of Astronautics and Aeronautics, Albuquerque, NM, 1999.
32. Massey, Timothy and Yuri Shtessel. "Continuous Traditional and High-Order Sliding Modes for Satellite Formation Control," *Journal of Guidance, Control, and Dynamics*, 28(4):826–831, July-August 2005.
33. Maybeck, Peter S. *Stochastic Models, Estimation, and Control: Volume 1*. Navtech Book and Software Store, Arlington, VA, first edition, 1994.
34. Milam, Mark B., Nicolas Petit, and Richard M. Murray. "Constrained Trajectory Generation for Micro-Satellite Formation Flying." *AIAA Guidance, Navigation, and Control Conference*. Montreal, Canada, August 2001.
35. Mishne, David. "Formation Control of Satellites Subject to Drag Variations and J_2 Perturbations," *Journal of Guidance, Control, and Dynamics*, 27(4):685–692, July-August 2004.
36. Mitchell, Jason W. and David L. Richardson. "Invariant Manifold Tracking for First-Order Nonlinear Hill's Equations," *Journal of Guidance, Control, and Dynamics*, 26(4):622–627, July-August 2003.
37. Mullins, Larry D. "Initial Value and Two Point Boundary Value Solutions to the Clohessy-Wiltshire Equations," *The Journal of the Astronautical Sciences*, 40(4):487–501, October-December 1992.
38. Newton, Issac. *The Principia*. Prometheus Books, Amherst, NY, 1995.

39. Orbital Sciences Corporation. "Demonstration of Autonomous Rendezvous Technology (DART) Fact Sheet," 2000.
40. Orbital Sciences Corporation. "Orbital Express Space Operations Architecture," March 2006. <http://www.darpa.mil/ucar/programs/oe.htm>.
41. Paiewonsky, Bernard and Peter J. Wood. "Three-Dimensional Time-Optimal Rendezvous," *Journal of Spacecraft*, 3(11):1577–1584, November 1966.
42. Palmer, Phil. "Optimal Relocation of Satellites Flying in Near-Circular-Orbit Formations," *Journal of Guidance, Control, and Dynamics*, 29(3):519–526, May-June 2006.
43. Richardson, David L. and Jason W. Mitchell. "A Third-Order Analytical Solution for Relative Motion with a Circular Reference Orbit." *AAS/AIAA Space Flight Mechanics Meeting*. American Astronautical Society, San Antonio, TX, January 2002.
44. S. Sawai, D.J. Scheeres and S.B. Broshcart. "Control of Hovering Spacecraft Using Altimetry," *Journal of Guidance, Control, and Dynamics*, 25(4):786–795, July-August 2002.
45. Schaub, Hanspeter. "Relative Orbit Geometry Through Classical Orbit Element Differences," *Journal of Guidance, Control, and Dynamics*, 27(5):839–848, September-October 2004.
46. Schaub, Hanspeter and Kyle T. Alfriend. "Hybrid Cartesian and Orbit Element Feedback Law for Formation Flying Spacecraft," *Journal of Guidance, Control, and Dynamics*, 25(2):387–393, March-April 2002.
47. Schweighart, Samuel A. and Raymond J. Sedwick. "High-Fidelity Linearized J_2 Model for Satellite Formation Flight," *Journal of Guidance, Control, and Dynamics*, 25(6):1073–1080, November-December 2002.
48. Schweighart, Samuel A. and Raymond J. Sedwick. "Cross-Track Motion of Satellite Formations in the Presence of J_2 Disturbances," *Journal of Guidance, Control, and Dynamics*, 28(4):824–826, July-August 2005.
49. Seo, John Sang-Pil. *Analytical Solution for Low-Thrust Minimum Time Control of a Satellite Formation*. Ph.D. dissertation, Graduate School of Engineering and Management, Air Force Institute of Technology (AETC), Wright-Patterson AFB OH, September 2004. AFIT/DS/ENY/04-04.
50. Serway, Raymond A. *Physics for Scientists and Engineers with Modern Physics*. Saunders College Publishing, Philadelphia, PA, second edition, 1983.
51. Sidi, Marcel J. *Spacecraft Dynamics and Control*. Cambridge University Press, New York, NY, first edition, 1997.
52. Space Vehicles Directorate. "XSS-11 Micro Satellite," December 2005. <http://www.vs.af.mil/FactSheets/XSS11-MicroSatellite.pdf>.

53. Tallarida, Ronald J. *Pocket Book of Integrals and Mathematical Formulas*. Chapman & Hall/CRC, New York, NY, third edition, 1999.
54. Thomas, Stephanie J., Joseph B. Mueller, and Michael A. Paluszek. "Formations for Close-Orbiting Escort Vehicles." *AIAA 1st Intelligent Systems Technical Conference*. American Institute of Astronautics and Aeronautics, Chicago, IL, September 2004.
55. Vadali, S.R., H. Schaub, and K.T. Alfriend. "Initial Conditions and Fuel-Optimal Control for Formation Flying of Satellites." *AIAA Guidance, Navigation, and Control Conference*. Portland, OR, August 1999.
56. Vadali, S.R., S.S. Vaddi, K. Naik, and K.T. Alfriend. "Control of Satellite Formations." *AIAA Guidance, Navigation, and Control Conference*. Montreal, Canada, August 2001.
57. Vaddi, S.S., Srinivas R. Vadali, and Kyle T. Alfriend. "Formation Flying: Accommodating Nonlinearity and Eccentricity Perturbations," *Journal of Guidance, Control, and Dynamics*, 26(2):214–223, March-April 2003.
58. Vaddi, S.S., K.T. Alfriend, S.R. Vadali, and P. Sengupta. "Formation Establishment and Reconfiguration Using Impulsive Control," *Journal of Guidance, Control, and Dynamics*, 28(2):262–268, March-April 2005.
59. Vallado, David A. *Fundamentals of Astrodynamics and Applications*. Microcosm Press, El Segundo, CA, second edition, 2001.
60. Vignal, Pierre and Henry Pernicka. "Low-Thrust Spacecraft Formation Keeping," *Journal of Spacecraft and Rockets*, 43(2):466–475, March-April 2006.
61. Weisstein, Eric W. "Harmonic Addition Theorem," May 2004. <http://mathworld.wolfram.com/HarmonicAdditionTheorem.html>. MathWorld—A Wolfram Web Resource.
62. Wie, Bong. *Space Vehicle Dynamics and Control*. American Institute of Aeronautics and Astronautics, Inc., Reston, VA, first edition, 1998.
63. Wiesel, William E. *Spaceflight Dynamics*. Irwin McGraw-Hill, Boston, MA, second edition, 1997.
64. Wiesel, William E. "Relative Satellite Motion About an Oblate Planet," *Journal of Guidance, Control, and Dynamics*, 25(4):776–785, July-August 2002.
65. Wiesel, William E. "Optimal Impulsive Control of Relative Satellite Motion," *Journal of Guidance, Control, and Dynamics*, 26(1):74–78, January-February 2003.
66. Williams, Trevor and Zhong-Sheng Wang. "Solar Radiation Pressure and Formation-Keeping in Highly Elliptical Orbits." *AIAA/AAS Astrodynamics Specialist Conference*. Monterey, CA, August 2002.

67. Yamanaka, Koji and Finn Ankersen. "New State Transition Matrix for Relative Motion on an Arbitrary Elliptical Orbit," *Journal of Guidance, Control, and Dynamics*, 25(1):60–66, January-February 2002.
68. Yeh, Hsi-Han, Eric Nelson, and Andrew Sparks. "Nonlinear Tracking Control for Satellite Formations," *Journal of Guidance, Control, and Dynamics*, 25(2):376–386, March-April 2002.

REPORT DOCUMENTATION PAGE

Form Approved
OMB No. 0704-0188

The public reporting burden for this collection of information is estimated to average 1 hour per response, including the time for reviewing instructions, searching existing data sources, gathering and maintaining the data needed, and completing and reviewing the collection of information. Send comments regarding this burden estimate or any other aspect of this collection of information, including suggestions for reducing this burden to Department of Defense, Washington Headquarters Services, Directorate for Information Operations and Reports (0704-0188), 1215 Jefferson Davis Highway, Suite 1204, Arlington, VA 22202-4302. Respondents should be aware that notwithstanding any other provision of law, no person shall be subject to any penalty for failing to comply with a collection of information if it does not display a currently valid OMB control number. **PLEASE DO NOT RETURN YOUR FORM TO THE ABOVE ADDRESS.**

1. REPORT DATE (DD-MM-YYYY) 11-09-2007		2. REPORT TYPE Doctoral Dissertation		3. DATES COVERED (From — To) Sep 2004 — Sep 2007	
4. TITLE AND SUBTITLE Optimal Control Strategies for Constrained Relative Orbits				5a. CONTRACT NUMBER	
				5b. GRANT NUMBER	
				5c. PROGRAM ELEMENT NUMBER	
6. AUTHOR(S) Irvin Jr., David J., Major, USAF				5d. PROJECT NUMBER 07-298	
				5e. TASK NUMBER	
				5f. WORK UNIT NUMBER	
7. PERFORMING ORGANIZATION NAME(S) AND ADDRESS(ES) Air Force Institute of Technology Graduate School of Engineering and Management (AFIT/EN) 2950 Hobson Way WPAFB OH 45433-7765				8. PERFORMING ORGANIZATION REPORT NUMBER AFIT/DS/ENY/07-03	
9. SPONSORING / MONITORING AGENCY NAME(S) AND ADDRESS(ES) AFRL/VS Attn: Dr. T. Alan Lovell 3550 Aberdeen Ave, SE Kirtland AFB, NM 87117-5776 DSN: 263-4132				10. SPONSOR/MONITOR'S ACRONYM(S)	
				11. SPONSOR/MONITOR'S REPORT NUMBER(S)	
12. DISTRIBUTION / AVAILABILITY STATEMENT Approved for public release; distribution unlimited.					
13. SUPPLEMENTARY NOTES					
14. ABSTRACT The US Air Force's ability to protect space assets is enhanced by a proficiency in satellite proximity operations and Space Situational Awareness (SSA). In pursuit of that proficiency, this research develops a key capability of interest to mission planners; the ability of a deputy satellite to "hover" within a defined volume fixed in the vicinity of a chief satellite for an extended period of time. This research finds optimal trajectories, produced with discrete-thrusts, that minimize fuel spent per unit time and stay within the user-defined volume, thus providing a practical hover capability in the vicinity of the chief. The work assumes the Clohessy-Wiltshire closeness assumption between the deputy and chief is valid, however, elliptical chief orbits are allowed. Using the new methodology developed in this work, feasible closed and non-closed relative orbits are found and evaluated based on a fuel criterion and compared to an easily calculated continuous-thrust baseline. It is shown that in certain scenarios the discrete-thrust solution provides the lowest overall fuel cost. These scenarios are generally constrained to a smaller total time-of-flight. A simple check is proposed that enables the mission planner to make the correct strategy choice.					
15. SUBJECT TERMS counterspace, space situational awareness, hovering satellites, relative satellite motion, proximity operations, trajectory optimization, teardrop orbits.					
16. SECURITY CLASSIFICATION OF:			17. LIMITATION OF ABSTRACT UU	18. NUMBER OF PAGES 227	19a. NAME OF RESPONSIBLE PERSON Dr. Richard G. Cobb (ENY)
a. REPORT U	b. ABSTRACT U	c. THIS PAGE U			19b. TELEPHONE NUMBER (include area code) (937) 255-3636, ext. 4559